Reactivity of Highly Unsaturated Molecules – Investigation of the Photo-Oxidation of Bitumen & Chemistry of Propargyl Carbocations

By
Matthew Joshua Joseph Laprade

A Thesis Submitted to
Saint Mary's University, Halifax, Nova Scotia
in Partial Fulfillment of the Requirements for
the Degree of Master of Science in Applied Science

December 2020, Halifax, Nova Scotia

Approved:	Dr. Jason A. C. Clyburne Supervisor Departments of Chemistry & Environmental Science
Approved:	Dr. Jason Masuda Acting Supervisor Supervisory Committee Member Department of Chemistry
Approved:	Dr. Anne Dalziel Supervisory Committee Member Department of Biology
Approved:	Dr. Matthias Bierenstiel External Examiner Department of Chemistry Cape Breton University

December 16, 2020

Reactivity of Highly Unsaturated Molecules –
Investigation of the Photo-Oxidation of Bitumen
&
Chemistry of Propargyl Carbocations

By Matthew Joshua Joseph Laprade

Abstracts

Investigation of the Photo-Oxidation of Bitumen

Highly unsaturated organic molecules, commonly referred to as porphyrins, within bitumen are oxidized when exposed to sunlight. These photo-oxidized porphyrins influence the chemical and physical properties of the bitumen. The generation of these oxidized porphyrins have been monitored using infrared spectroscopy (IR), nuclear magnetic resonance (NMR), gas chomatography/mass spectrometry (GCMS), and saturate, aromatic, resin and asphaltene (SARA) analyses.

Chemistry of Propargyl Carbocations

Highly unsaturated organic molecules are very reactive and readily undergo addition reactions. The reactivity of unsaturated molecules will be further modified by the inclusion of a carbocationic center. For instance, the reactivity of an alkyne is believed to increase with the presence of an adjacent carbocation; a structure referred to as a propargyl carbocation. The carbocation will withdraw electron density, causing the alkyne carbon to form a dipole moment and become highly reactive. We have been able to isolate several stable propargyl carbocations and made preliminary investigations into their chemistry.

December 16, 2020

The contents of this thesis have been divided into two separate parts, with permission from Saint Mary's University. Each part is to be treated as its own self-enclosed thesis, with no relation to each other, even though there may be overlaps in the underlying chemistry.

Acknowledgements

The first person I'd like to thank is my supervisor, Dr. Jason Clyburne. I cannot thank him enough for all the support and experiences he has given me over the years that I have had the pleasure of working with him. When I first joined his research group as an undergraduate, I was shocked and surprised that he was willing to take and train someone like me. I had no idea that I would end up where I am. Even though his health had deteriorated in the last year of my studies, he still made efforts to support me. He has helped me to not only become a trained researcher but, has also provided the framework for substantial personal growth.

I would also like to thank the other members of the Clyburne research group, especially Robert Riley, Katrina Turrie, and Michael Land who have assisted with a few parts of this project. Michael Land especially for his help in reading, corrections, and letting me know every time I am completely wrong in my chemistry (which was a lot). Logan Cox, though not an official member of the Clyburne research group, was training to become a member before the COVID-19 outbreak, and his help on this project was appreciated.

Although he was not on my supervisory committee, Dr. Jason Masuda also deserves acknowledgment for allowing me to use materials, chemicals, and his glove-box. Dr. Masuda also was the acting superior for me when Dr. Clyburne became ill, and thus also assisted with the explanation of chemistry concepts. Additionally, the Saint Mary's technicians, have been incredible while working in the chemistry department; a special thanks to Alyssa Doué, as she is the person I look to first whenever I needed to find a chemical.

A special "thank you" goes to my supervisory committee, Dr. Anne Dalziel and Dr. Jason Masuda, for helping to guide me though this degree, despite all of the events that made it difficult. Also, to my external examiner, Dr. Matthias Bierenstiel, for taking the time to read this thesis. I am also grateful to the Faculty of Graduate Studies and Research for providing funding over the last two years.

Finally, Dr. Katherine Robertson is someone who I cannot thank enough for all of her hard work and assistance with this thesis. All of the structural refinements, and all of the crystallographic data collections within this thesis were performed by Dr. Robertson. Not only this, but Dr. Robertson had sacrificed an incredible amount of hours, sleep, meals, and time in order to help me by editing my thesis at every step. Words cannot express how substantially she had helped me, and how much thanks I, whom she has started referring to as "Stupid Matthew", have for everything she has done.

Table of Contents

List of Figures

List of Tables and Graphs

Introduction

Bitumen, a class of heavy oil, is composed of a mixture of complex hydrocarbons, compounds with multiple aromatic rings containing heteroatoms (N, O, S) and metals (V, Al, Fe, & Ni).[1,2,3] More than 2 trillion barrels of bitumen are estimated to be extractable from the Earth;[4] with this meeting about 33% of the world's current oil demands.[5] Bitumen is of great importance to Canada where it is extracted in northern Alberta. There is an estimated 1.75 trillion barrels of bitumen in Alberta, with only about 15% of that being proven heavy oil reserves.[6] Bitumen is highly viscous and produces toxic effects when it is spilled due to the presence of naphthenic acids,[7] which occur at concentrations ranging from 0-3%,[8-11] and other toxic organic compounds. Of particular interest in this work is what happens to these compounds in the event of a marine oil spill. Spilled bitumen is affected by environmental factors, such as exposure to water, heat, and sunlight. For example, it has been well documented that heavy oils and bitumen oxidize in the presence of water and sunlight.[12,13] This creates chemical reactions within the bitumen that then impact the water systems where the spill has occurred.

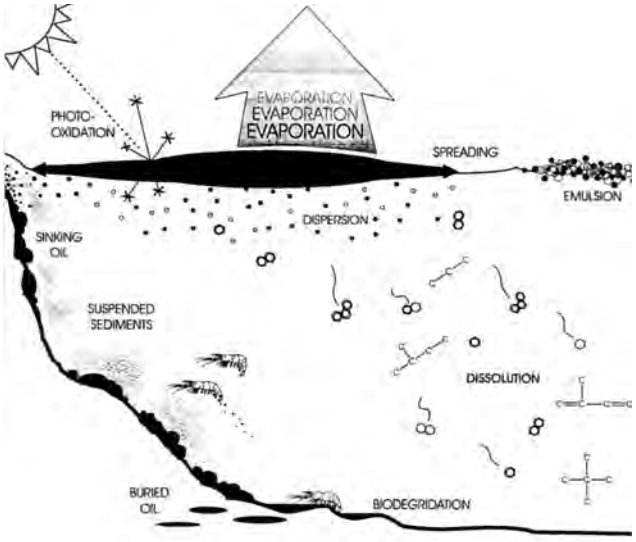

Figure 1: Diagram showing five of the major oil weathering processes available to oil spilled in the environment.[14]

This study concerns the photochemical oxidation of crude petroleum products in both the presence and absence of sunlight. Surface spills were prepared and tested on freshwater model systems and these were subsequently exposed to either natural or artificial sunlight. The weather, which includes the amount of sunlight, was carefully monitored. Exposure of these materials to sunlight caused them to naturally weather. The term "weathering" refers to the changes that occur to oil as it spends time in the environment.[14] After oil is released, it undergoes a wide variety of physical, chemical, and biological processes that begin to transform the oil almost immediately. This process is affected by the spill location, surrounding air and water temperatures, wave activity, wind, and other factors, such as the presence of particulates or sediment in the water.[14] There are eight main weathering processes that can occur:[15] spreading, evaporation, dispersion, emulsification, dissolution, oxidation, sedimentation and sinking, and biodegradation. In this report, weathered bitumen refers primarily to samples that were

subjected to the process of evaporation. The experiments carried out focused on oxidative processes occurring within bitumen.

The oxidation products[12,13] formed in the experimental samples were monitored by studying the composition of the water and the surface layer bitumen in the model spill systems. Oxidation of organic materials typically yields polar molecules, which are more soluble in water than are their nonpolar precursors. Using gas chomatography, coupled with mass spectrometry, we also attempted to identify structures for the oxidation products being formed. The primary method used to assess the oxidation of the surface layer was infrared spectroscopy. After isolation of the surface layer, new spectroscopic features attributable to oxidized products were located and identified. For instance, the carbonyl stretching frequency[16] (ca. 1700 cm^{-1}) was monitored and compared to either the normalized absorbance of the C-H stretching frequency[16] (ca. 3000 cm^{-1}), or to the C=C stretching vibration for aromatic carbons[16] (ca. 1605 cm^{-1}) by taking the ratio of the integrated areas of these functional group peaks. It was important to take a ratio instead of the absolute values of the integrations as the intensities of the peaks are subject to change depending on where the measurement is taken on the sample. By using a ratio, any relative increases or decreases in intensity are compensated for, as the peaks remain proportional to each other, provided that there has not been a reaction.

The carbonyl stretching frequency[16] (ca. 1700 cm^{-1}) and the C=C stretching vibration for aromatic carbons[16] (ca. 1605 cm^{-1}), were chosen for this work as they are quite well separated in the infrared spectrum of bitumen. A reduction in the intensities of the C-H stretching or C=C stretching modes would indicate that an addition reaction had occurred in the sample during the weathering process, disrupting these functional groups.

A concurrent increase in the intensity of the carbonyl stretching vibration (ca. 1700 cm^{-1}) would indicate that this disruption was due to the addition of oxygen. A measured increase in this ratio allows the rate of oxidation of the surface products to be determined.

According to Ward *et al*.,[12,13] bitumen can be photo-oxidized all the way to CO_2. If this were to occur, a decrease in the above ratio might be observed, as more oxygenated carbons would be escaping the system than alkenyl carbons. It is important to note, however, that this ratio might also remain unchanged after photo-oxidation to CO_2. This is because it is not yet clear which components of bitumen are oxidized to CO_2 and whether the CO_2 comes directly from the oxidative process. Still, it is likely that the carbonyl to alkenyl ratio will decrease, as the aromatic components that form the original oxidative products should also be able to be oxidized all the way to CO_2.

A component of bitumen that may also accelerate photo-oxidation in porphyrin rings. These porphyrin rings are believed to be derived from the chlorophyll of plant matter that eventually formed the bitumen. There are five main porphyrins that have been identified by mass spectrometry in bitumen samples:[17-19] etioporphyrins (Etio), deoxophylloerthoetioporphyrin (DPEP), tetrahydrobenzoDPEP (THBD), benzo (rahodo) Etio and benzo (rhodo) DPEP (Figure 2). In bitumen, the porphyrins primarily reside in the asphaltene fraction, but are also able to exist as resins depending on their polarity. The more polar the porphyrins are, the more likely they are to be with the asphaltenes in bitumen.

Porphyrin rings could be a contributing factor in the photo-oxidation of bitumen; they have can react with metals present in bitumen to form metalloporphyrins.[17-19] The

coordinated metal center can then undergo oxidative addition with molecular oxygen to form a stable intermediate, with oxygen in place to react with hydrocarbons. This idea is supported in the literature, as such complexes have been used as photocatalytic materials to form carbonyl complexes.[20-23] One example is the heme group, which contains an iron-porphyrin complex, and which coordinates oxygen and carbon dioxide for cellular carriage in the human body. The heme group is responsible for providing oxygen for cellular respiration, and contributes to the catalytic activities of many enzymes as cofactors. Reactions with metalloporphyrins can produce oxidised species in good yields and with wide selectively[20-24] The formation of alcohols, aldehydes, ketones, carboxylic acids, and even peroxides can result, not only in unsaturated or aromatic systems, but also in systems where the site of nucleophilic attack is fully saturated. Metalloporphyrins are also known to be potent photosensitizers.[20,24]

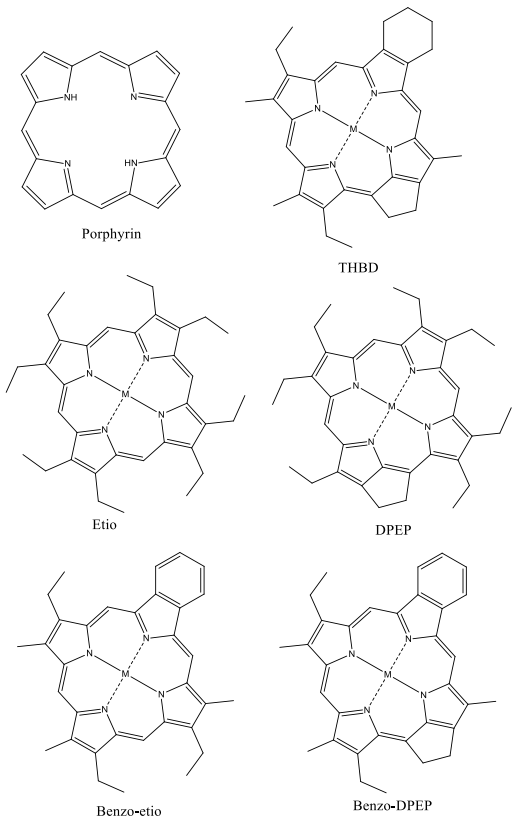

Figure 2: Structures of porphyrin rings commonly found in bitumen, as identified using mass spectrometry.[17-19]

The metalloporphyrin hemin (Figure 3) was chosen as a model for the naturally occurring metalloporphyrins present in bitumen since it is similar in structure to the porphyrins in Figure 2, along with it being inexpensive. Hemin does, however, also have salt-like properties as it has a chloride anion coordinating to the iron center. It also has two carbonyls and two hydroxyls within the structure, while the more common porphyrins in bitumen (Figure 2) do not. This creates the potential problem of overlapping carbonyl peaks, when studying bitumen using infrared spectroscopy. Typically, vanadium and nickel are the most common metal centers found in the metalloporphyrins of bitumen, although iron is also a common metal center as well.[25]

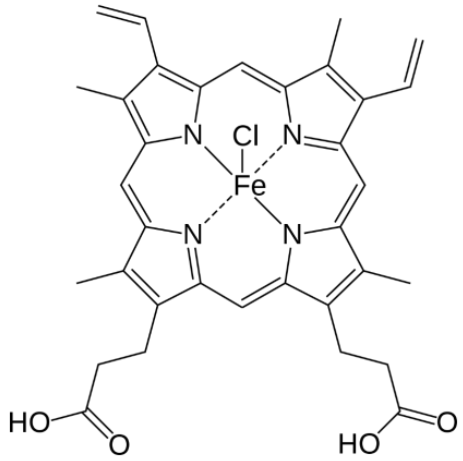

Figure 3: Structure of the metalloporphyrin hemin.

Infrared spectroscopy (IR) was used to observe changes in the experimental bitumen samples, as it was quick, simple, and allowed easy monitoring of functional group differences between trials/samples. The target peaks to follow were determined to be those at 1604 cm^{-1} and 1700 cm^{-1}, which are for conjugated aromatics (ν(C=C) of conjugated aromatics) and carbonyl groups (ν(C=O)), respectively.[27] These IR peaks were integrated using OPUS software[26] and the baseline profile method. A ratio was calculated using the integration of the 1700 cm^{-1} carbonyl peak over the integration of the 1604 cm^{-1} C=C alkenyl peak. The peak at 1700 cm^{-1} likely arises from the formation of oxidative products, therefore if the ratio between these peaks increases, the number of non-volatile oxidative products should be increasing. If it decreases, then the number of oxidative products should be decreasing, either by leaving the system due to volatility or after being fully oxidized to CO_2. The reverse holds true for the peak at 1604 cm^{-1} attributed to the C=C conjugated aromatics. If this peak increases, the ratio of oxidative products to non-oxidized products will decrease.

Athabasca bitumen will be the primary source of material used in these experiments due to its ready availability. Both unprocessed Athabasca bitumen and a commercial dilbit blend made from Athabasca bitumen, Access Western Blend, will be studied. The question as to whether there might be a difference between bitumen types was raised, so Mesa bitumen will also be tested, in certain of the experiments, and its results compared with those of the Athabasca bitumen. Mesa bitumen is a bitumen from Venezuela that is less viscous and has a lower sulfur content compared to Athabasca bitumen.

Section 1: Initial testing using infrared spectroscopy

Experiment One

Before more detailed experiments were undertaken, it was important to see how bitumen would behave in small scale experiments and what could be determined, if anything, after bitumen had been exposed to full spectrum light. Infrared spectroscopy (IR) was chosen as the technique to be used to monitor the bitumen, as it was quick, simple, and allowed easy observation of functional group changes between trials/samples. We were curious to see if the bitumen samples would undergo oxidation when exposed to natural and artificial ultra-violet (UV) light (~100-400 nm), which would result in a growth of the peak arising from the C=O carbonyl stretching vibration (ca. 1700 cm^{-1}) in the IR spectra of the samples as they aged.

Initial experiments were conducted with Athabasca bitumen and Access Western Blend (AWB) bitumen. The Athabasca bitumen (2 g) was always diluted with hexanes (10 mL) before use to make it less viscous and more manageable. AWB bitumen, is a commercially prediluted dilbit blend also containing Athabasca bitumen. It was provided by the Bedford Institute of Oceanography and used without further dilution, unless otherwise noted. Each sample was deposited onto NaCl plates and allowed to dry for a few min. The IR spectra were then recorded, to be used as both a control and a blank (Figure 4). The spectra for both diluted Athabasca bitumen and the Access Western Blend were relatively similar, with the exception of an extremely prominent OH stretching vibration (~3400 cm^{-1}) in the AWB sample. Due to this, the spectra for AWB are not shown here, although AWB bitumen was used for later experiments due to its

greater availability and ease of use compared to the Athabasca bitumen. The type of bitumen used in an experiment is always specifically noted.

Each sample was then placed under a full-spectrum growing light (used as a model for sunlight) for 3 h. After this time, the IR spectra were again recorded with the NaCl plates oriented in the same way as in the first runs. In the original spectrum of diluted Athabasca bitumen (Figure 4), a broad peak at 1640 cm^{-1}, which is attributed to the presence of volatile alkenyl-containing compounds (ν(C=C) of isolated alkene bonds),[27] covered the target peaks at 1600 cm^{-1} and 1700 cm^{-1}, which are assigned to conjugated aromatics (ν(C=C) of conjugated aromatics) and carbonyl groups (ν(C=O)), respectively.[27] Evidence that the 1640 cm^{-1} is broad enough to cover the target peaks can be seen in Figure 4. The presence of a twinned peak can be seen in the spectrum of the bitumen control; it can almost be resolved into a ν(C=C) peak of conjugated aromatic alkene bonds (1600 cm^{-1}) and the 1640 cm^{-1} peak. While the peak associated with ν(C=C) of conjugated alkene bonds is strong enough to be somewhat resolved from the isolated alkenyl C=C peak, any peaks associated with ν(C=O) of carbonyl groups at 1700 cm^{-1} are either not intense enough to be resolved or are not present in the original control sample.

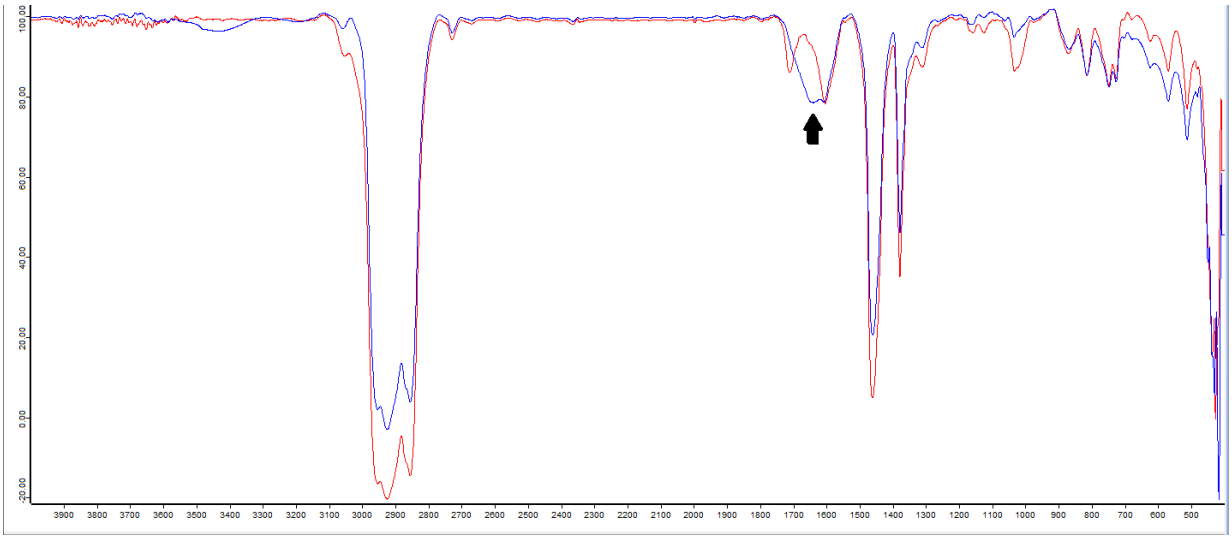

Figure 4A: Stacked infrared spectra of Athabasca bitumen deposited on a NaCl plate. Bitumen control (blue) measured immediately and then again after being exposed to UV light for 3 h (red).

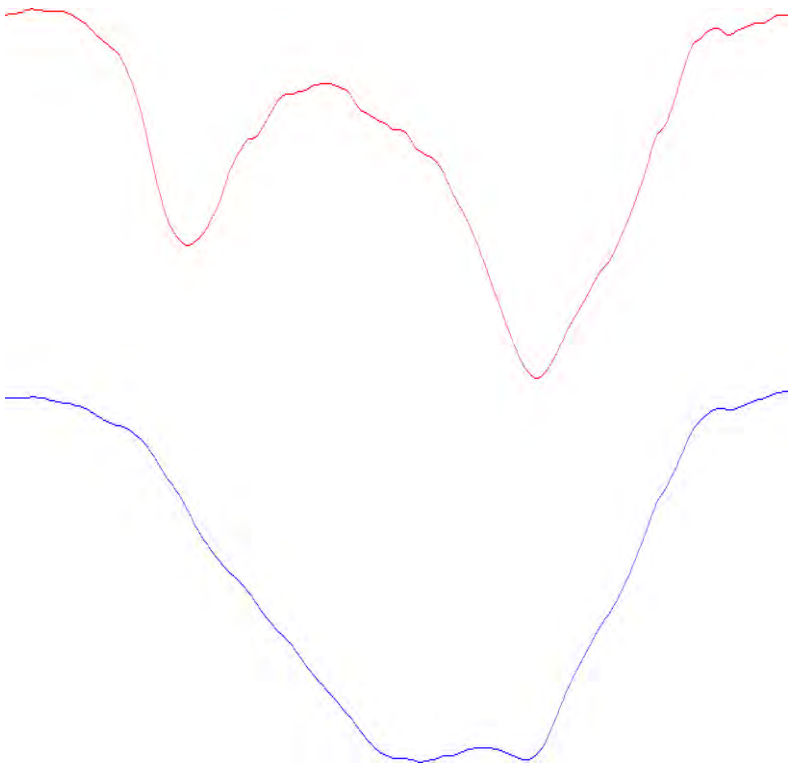

Figure 4B: Infrared spectra of Athabasca bitumen deposited on a NaCl plate focussed on the 1750-1500 cm^{-1} region. Bitumen control (bottom) measured immediately and then again after being exposed to UV light for 3 h (top).

Upon prolonged exposure to light and the open atmosphere, the peak at 1640 cm^{-1} has disappeared from the spectrum of the 3-h sample, which uncovers a peak at 1600 cm^{-1}. A peak at 1700 cm^{-1} also visible in the spectrum of the 3-h sample, may or may not have been an unresolved peak hidden by the 1640 cm^{-1} peak in the original spectrum. The 1640 cm^{-1} peak is attributed to volatile alkenyl-containing compounds (ν(C=C) of isolated alkene bonds).[27] These compounds escape the bitumen sample, either with or without oxidation, which allows the 1600 cm^{-1} peak for ν(C=C) arising from conjugated aromatics to be seen. The concurrent appearance of the peak at 1700 cm^{-1}, is indicative of the presence of carbonyl complexes.[16] As this peak appears to be more intense in the spectrum run after exposure to the UV light, it seems likely that the concentration of oxidized compounds in the sample has increased. It was not yet certain if the peak at 1700 cm^{-1} was being directly generated from the volatile alkenyl compounds (peak at 1640 cm^{-1}), or if it was attributable to the photo-oxidation of a different bitumen component. This idea was tested by having a sample of bitumen kept in darkness for the same amount of time as a sample of bitumen was placed under the growing light in a subsequent experiment.

The initial IR determination for the control bitumen sample in this, and some of the other experiments, revealed extremely prominent OH stretching vibrations (~3400 cm^{-1}) (see Figure 6 or 8 for an example). These peaks are only sometimes present, only for the bitumen samples at time = 0, and are not ever present at longer times thereafter. These peaks are believed to be associated with trace amounts of water that has formed an emulsion with the non-polar volatile hydrocarbons in the bitumen. Though undiluted typically does not contain any volatiles due to them having degraded, the bitumen was

diluted with hexanes, which would account for the presence of these volatiles. The origin of the water is not clear. It may come from water in the bitumen (possibly absorbed from the atmosphere), or it may be added with the hexanes used for dilution of the samples. Whatever its origin, the water emulsion must be liberated from the bitumen when the volatile aromatics dissipate. It is unlikely that this water is from the presence of alcohols in the samples as there are no associated C-O stretching vibrations (~1100 cm^{-1}) observed in the IR spectra.

Experiment Two

A slight variation of this experiment was then run, this time with duplicate samples of Athabasca bitumen. One sample was left in the dark, to act as a comparison and control for the second, light-exposed sample (Figure 5). The samples were made in the same manner as the first, but using only the bulk Athabasca bitumen diluted with hexanes. IR spectra of both samples were measured, then one was placed under the grow light, while the other was placed in the dark, with both open to air, for 3 hs. After the 3 h, the IR spectra were measured again.

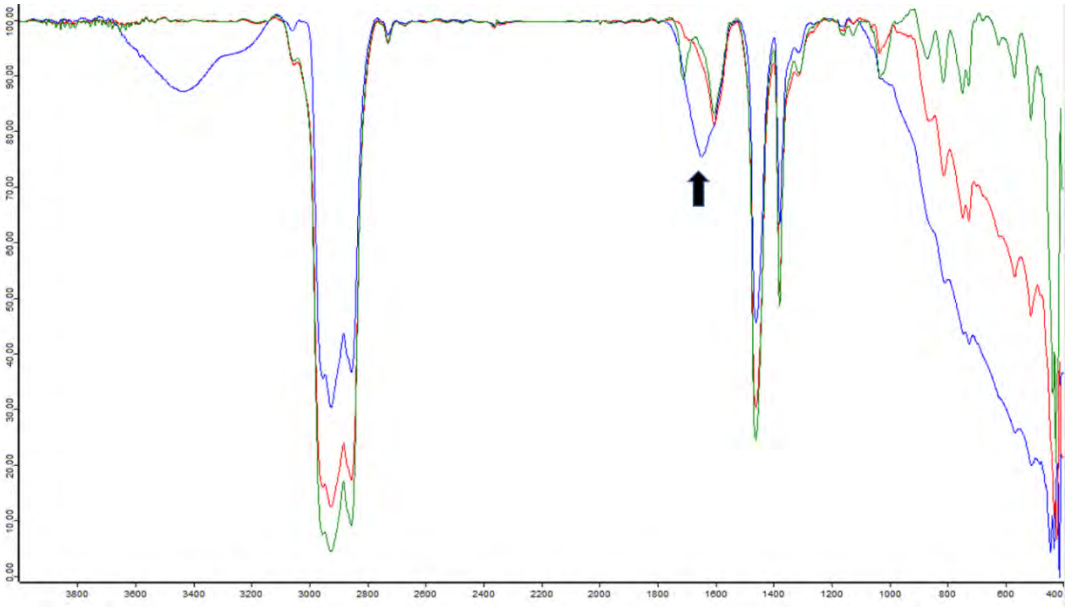

Figure 5A: Stacked infrared spectra of bitumen deposited on a NaCl plate. Bitumen control (blue) measured immediately and then again after being kept in the dark for 3 h (red), or after being exposed to a full spectrum grow light for 3 h (green).

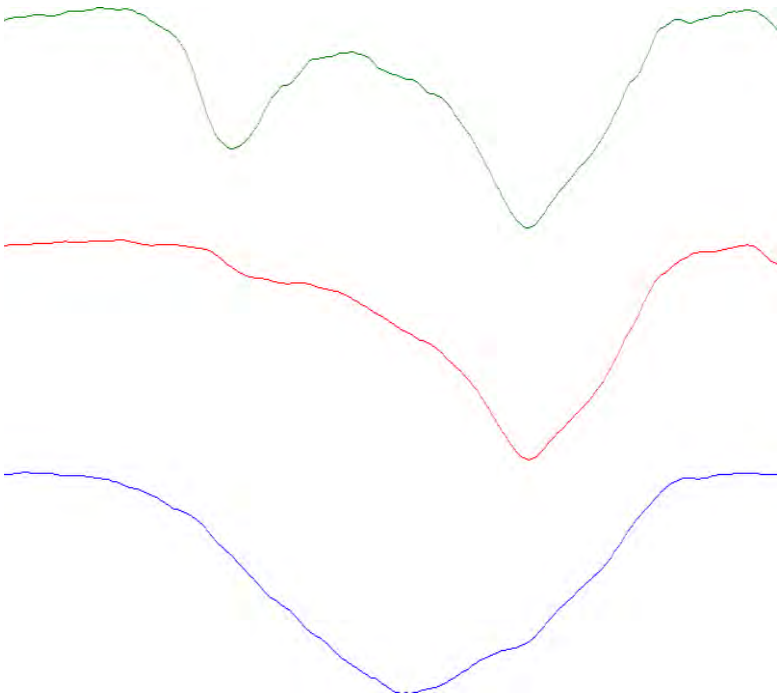

Figure 5B: Infrared spectra of Athabasca bitumen deposited on a NaCl plate focussed on the 1750-1500 cm^{-1} region. Bitumen control (bottom; blue) measured immediately and then again after being kept in the dark for 3 h (middle; red) or after being exposed to a full spectrum grow light for 3 h (top; green).

The initial control sample had a similar spectrum to that shown in Figure 4 for the control bitumen. Only a single large peak at 1640 cm^{-1}, associated with volatile aromatic compounds, was observed. This time however, the 1640 cm^{-1} peak disappeared from the IR spectrum of both the sample exposed to the growing light for 3 hs and from that of the sample that was kept in the dark. This suggests that the alkene-containing compounds within the bitumen sample are volatile enough to escape the system completely when it is left undisturbed for a period of time open to the air. Once the 1640 cm^{-1} peak was eliminated from the IR spectrum of the dark sample (and also from that of the light sample) a C=C stretching vibration at 1600 cm^{-1} arising from conjugated aromatic carbons was observed. This means that this signal must have been hidden by the 1640 cm^{-1} peak in the initial experiments, and is not a new product of a photo-oxidation reaction. The sample that was exposed to the growing light, like the sample in Figure 4, did show growth of a carbonyl peak at 1700 cm^{-1}. This indicates that the majority of the oxidative products are formed from UV light exposure, as the sample kept in the dark had only a tiny shoulder peak that might be attributable to oxidative product formation. It could be that bitumen itself is naturally reactive with oxygen, just at a significantly slower rate with no UV light present, or bitumen may naturally contain small amounts of oxygenated components which are obscured by the 1640 cm^{-1} peak in the original spectra. The earlier presented idea that the peak at 1600 cm^{-1} is generated from the photo-oxidation of the peak at 1640 cm^{-1} is unlikely; instead, it must be that the 1640 cm^{-1} is just obscuring this peak. This is consistent with the observation that the dark sample also shows the disappearance of the 1640 cm^{-1} peak without showing the appearance of a significant carbonyl peak at 1700 cm^{-1}. Instead of an oxidation-reduction reaction

occurring, the conjugated aromatic compounds present within the bitumen, as seen from the peak at 1600 cm^{-1}, must be reacting with oxygen in the presence of UV light to produce the carbonyl compounds giving rise to the more intense peak at 1700 cm^{-1}. In order to confirm these ideas, this experiment was repeated, with the same results being observed.

The results of the initial experiments suggested that the bitumen samples were undergoing a chemical change in the presence of the UV radiation provided by the full spectrum grow light. The bitumen samples that were left in the dark did not show any appreciable growth of the carbonyl peak at 1700 cm^{-1}. The bitumen samples do appear to contain volatile compounds. The peak arising from the more isolated C=C bonds (1640 cm^{-1}) disappeared from the IR spectra of both the samples exposed to UV light and the samples that were kept in darkness, if they were left open to the atmosphere. Separation and determination of these volatiles will be discussed in Section 4.

A few questions were raised with these initial experiments:

- What is the rate of photo-oxidation and is there a difference in the rate of oxidation between natural and artificial light? (see Section 2)
- Does bitumen interact differently with UV light in the presence of water, as suggested by the work of Ward *et al.*?[12,13] (see Section 3)
- Can bitumen be oxidized all the way to CO_2 as described by Ward *et al.*?[12,13] (see Section 5)

Section 2: Photo-oxidation rate determination

Experiment One

The results of the previous IR experiments (Section 1, experiment 2) suggested that bitumen was being photo-oxidized in the presence of UV light. We thus proceeded with more in-depth studies. Before that, it was necessary to know how long it would take bitumen to be oxidized under the UV light being employed.

A time trial to determine the rate of the photo-oxidation of bitumen was devised (Figures 7 and 8). The experiment mirrored the previous experiments in Section 1, except the sample of Athabasca bitumen was removed from the light every 20 min and its IR spectrum recorded. The intensity of the grow light (~10000 ± 1000 lux, Figure 6) was monitored over the entire course of the experiment. It is important to note that CO_2 was not controlled in these experiments. The infrared spectrometer was not purged with dry nitrogen between trials, so any CO_2 peaks visible (asymmetric stretching modes of gas phase CO_2 at ~2340 cm^{-1})[28] in the spectra likely arise, at least in part, from atmospheric contamination.

The results showed a steady decrease in the peak at 1640 cm^{-1} and the concomitant appearance of the peak at 1600 cm^{-1}. It was not until the 60-min mark that a peak at 1700 cm^{-1} became visible in the spectrum; this peak continued to grow in strength for the remainder of the time trial (120 min), presumably as the sample underwent photo-oxidation.

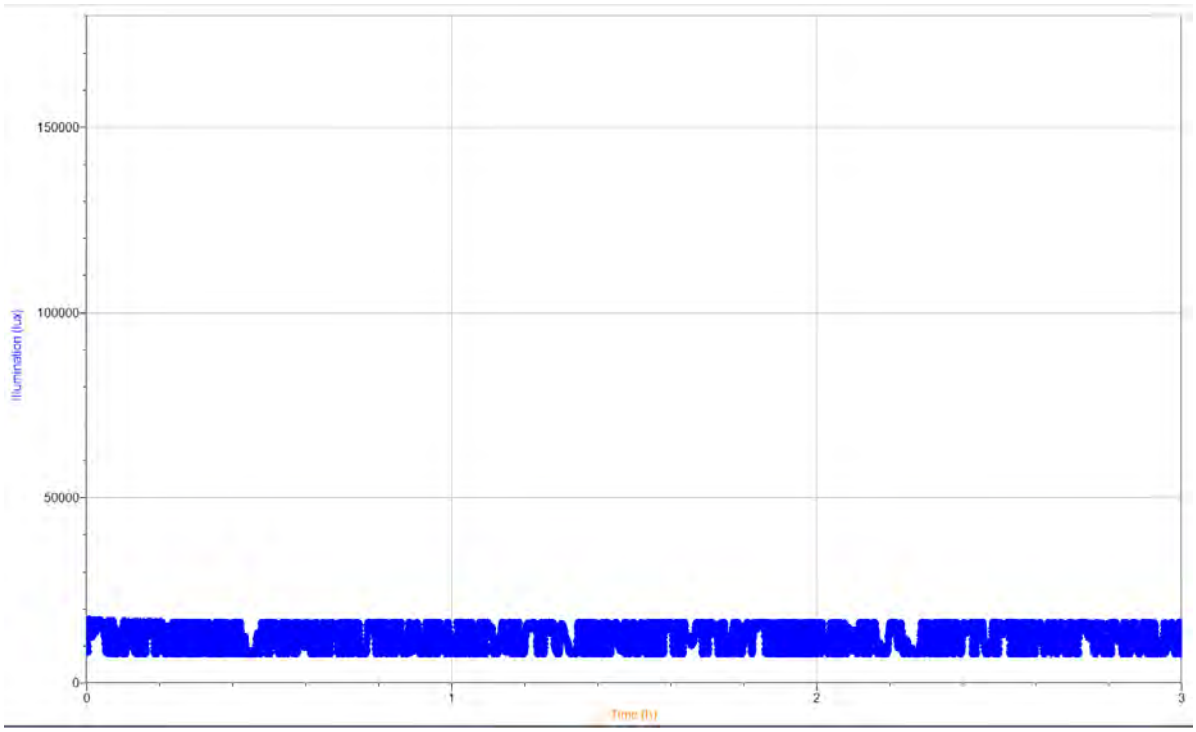

Figure 6: Measurement of the growing light intensity (in Lux) recorded over the course of 3 h.

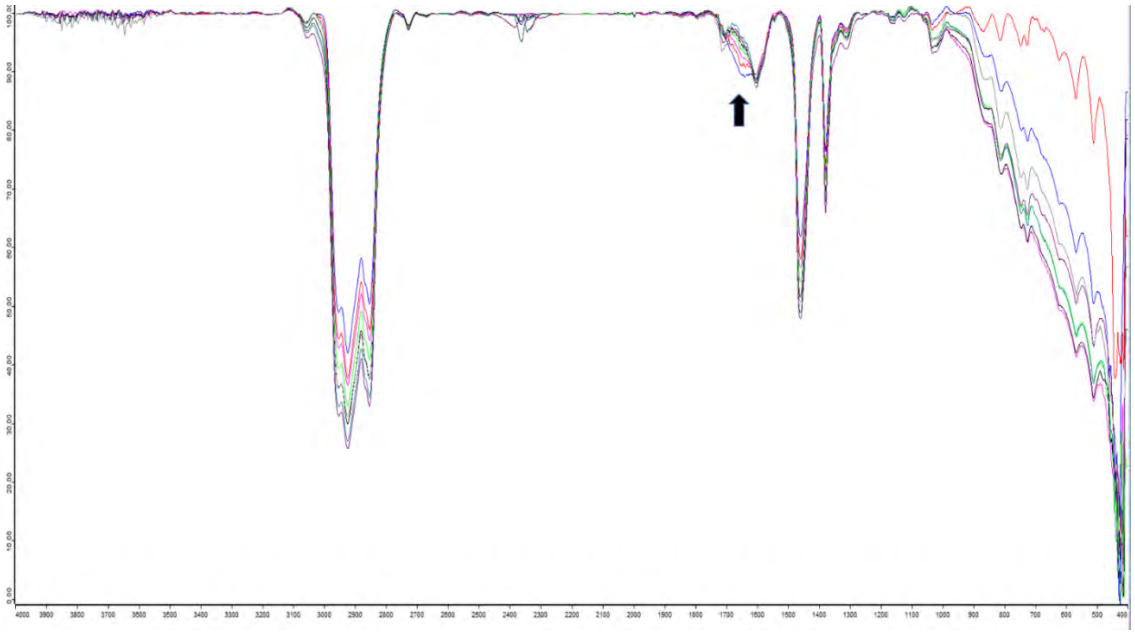

Figure 7: Infrared spectra of Athabasca bitumen deposited on a NaCl plate. Spectra of the same sample recorded at different times under the grow light (Figure 8 A and B). Stacked view to show differences arising from exposure to the light for varying times.

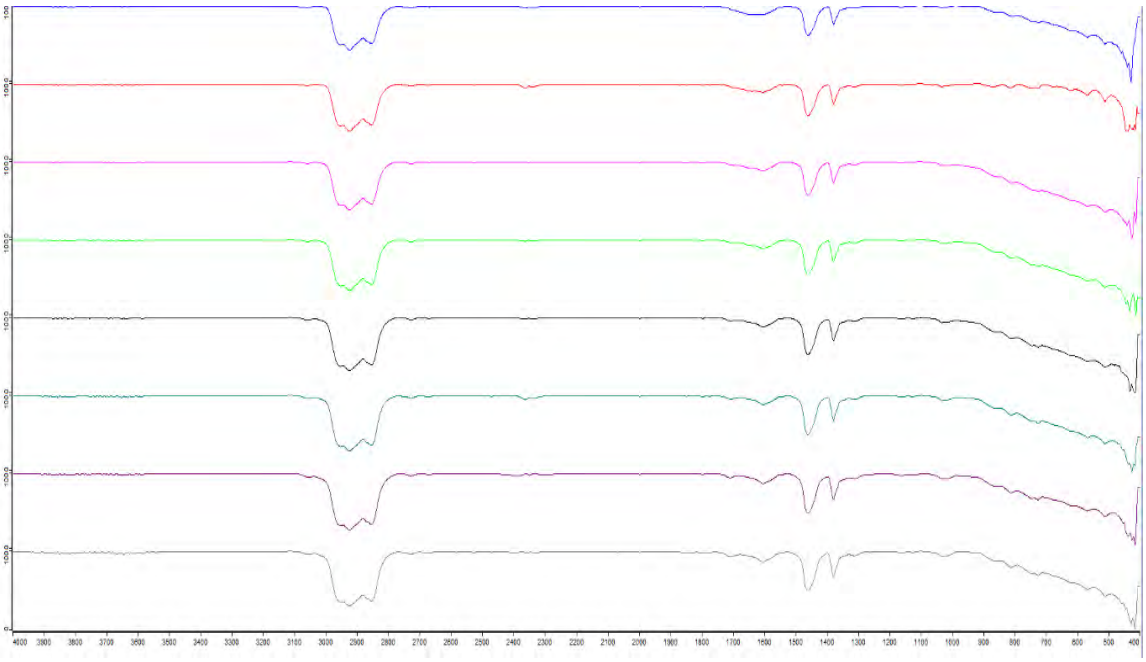

Figure 8A: Infrared spectra of Athabasca bitumen deposited on a NaCl plate. Spectra of the same sample recorded after different times under the grow light: the bitumen control at time 0 min (blue), 10 min (red), 20 min (magenta), and then increasing by 20-min intervals for each respective spectrum until the final spectrum (120 min).

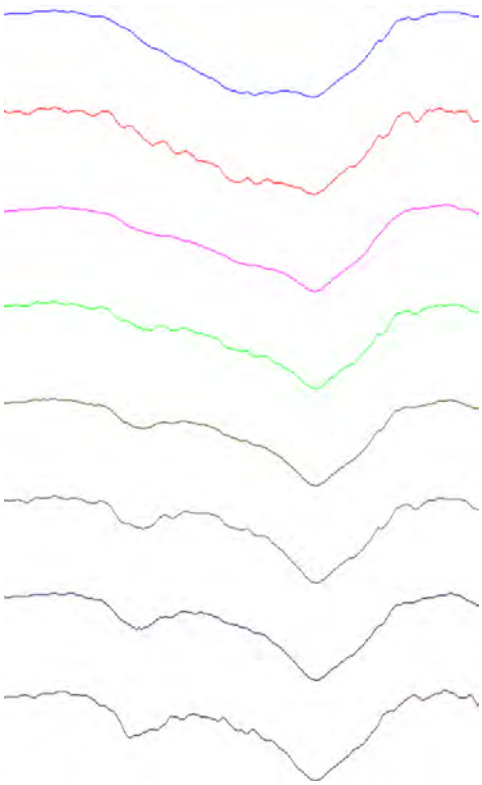

Figure 8B: Infrared spectra of Athabasca bitumen deposited on a NaCl plate focussed on the 1750-1500 cm^{-1} region. Spectra of the same sample recorded after different times under the grow light: the bitumen control at time 0 min (top), 10 min (second), 20 min (third), and then increasing by 20-min intervals for each respective spectrum until the final spectrum (120 min).

Experiment Two

The oxidation of bitumen with natural sunlight was then compared to the results obtained using the grow light. The intensity of sunlight should be about ten times greater than the intensity of our growing light (see Figure 16 in Section 3). Thus, it was believed that this sample would not only give a more intense carbonyl peak in the IR, with respect to the grow light samples, but also that the oxidation would occur more quickly.

Two similar experiments were done, and the results compared; one was run in the sun and one in the dark. The samples were made in a similar manner to the first sample

placed under the growing light, using bitumen from the same batch of Athabasca bitumen dissolved in hexanes. One sample was placed in the dark and sampled every 20 min, while one was placed in the sun and was retrieved for sampling also every 20 min. Each run was continued for a total of 3 h.

The sample that was kept in the dark showed only the disappearance of the peak at 1640 cm^{-1}, which likely indicated evaporation of volatile compounds. No other significant change was observed in the IR spectra over the course of the 3 h of sampling (Figure 9). The sample exposed to the sun at first showed no differences in the IR spectra when compared to those of the dark sample. At the 80-min mark, however, a peak appeared at about 1700 cm^{-1} and it grew rapidly in strength for the remainder of the time trial (Figure 9).

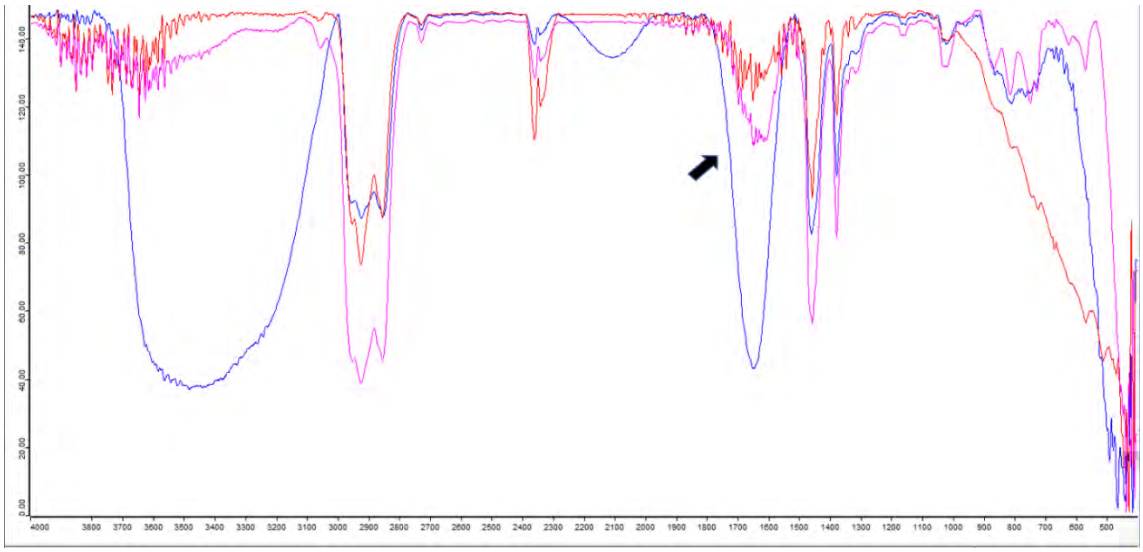

Figure 9A: Stacked infrared spectra used in the determination of the rate of photo-oxidation of bitumen deposited on a NaCl plate. Spectra taken of the same sample at different times while it was kept in the dark stacked view to show differences in exposure to light: blue is 0 min, red is 80 min, and pink is 180 min. The large fluctuations in the intensities are at least partially due to different orientations of the NaCl plate and to sample drying. The large peak at ~3400 cm-1 is attributed to a volatile OH-containing species and/or water in the initial control sample.

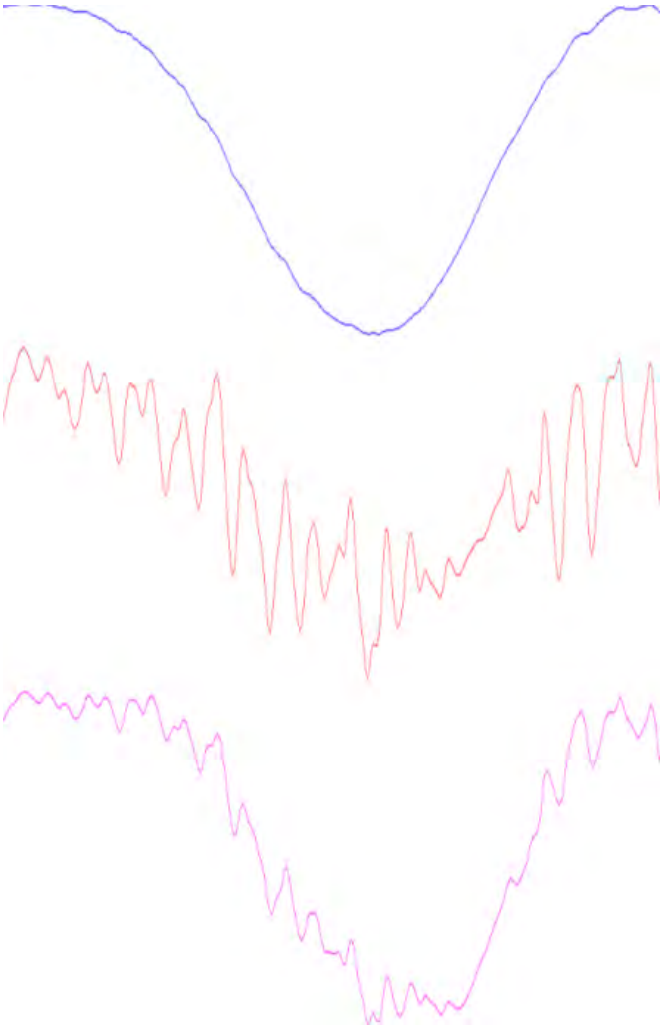

Figure 9B: Infrared spectra used for the determination of the rate of photo-oxidation of Athabasca bitumen deposited on a NaCl plate focussed on the 1750-1500 cm^{-1} region. Spectra taken of the same sample at different times while it was kept in the dark. Stacked view to show differences in exposure to light: 0 min (top), 80 min (middle), 180 min (bottom). Some of the large fluctuations in the overall intensities are due to different orientations of the NaCl plate and to sample drying. The large peak at ~3400 cm^{-1} is attributed to a volatile OH-containing species and/or water in the initial control sample.

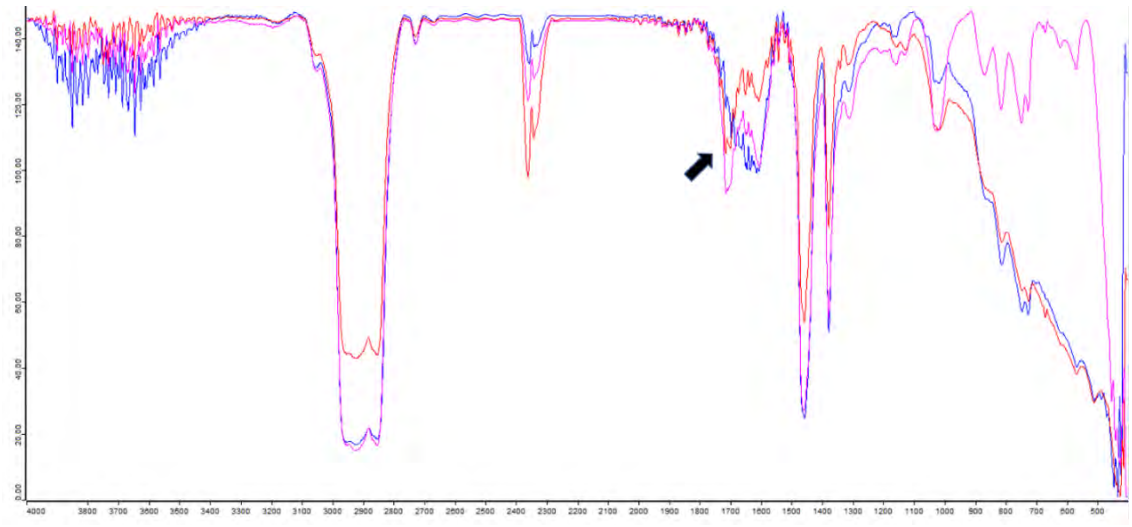

Figure 10A: Stacked infrared spectra used for the determination of the rate of photo-oxidation of Athabasca bitumen deposited on a NaCl plate. Spectra taken of the same sample at different times while it was being kept under sunlight. Stacked view to show differences in exposure to light: blue is 0 min, red is 80 min, and pink is 180 min.

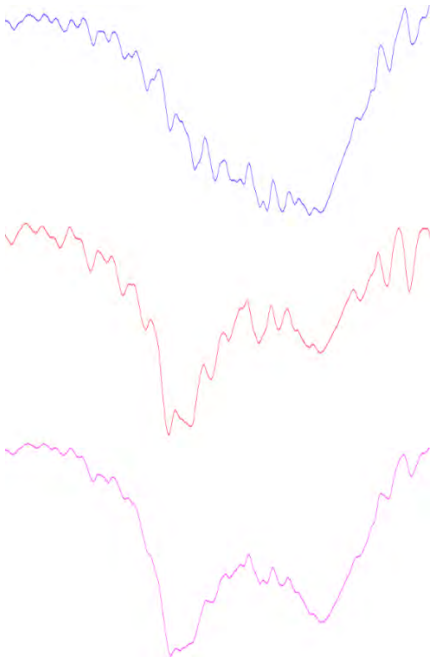

Figure 10B: Infrared spectra used for the determination of the rate of photo-oxidation of Athabasca bitumen deposited on a NaCl plate focussed on the 1750-1500 cm^{-1} region. Spectra taken of the same sample at different times for the sample kept under sunlight. Stacked view to show differences in exposure to light: 0 min (top), 80 min (middle), 180 min (bottom).

It was surprising that the oxidation in the sun took longer to begin, when compared to that of the growing light sample, 80 min versus 60 min, respectively. Again, the luminance of the sunlight was not recorded over the course of this experiment, but it was measured to average 100000 ± 5000 lux in other experiments, making it about 10 times stronger than the grow light (Figure 6). The sample under the growing light may have oxidized more quickly due to the thickness of the bitumen deposited onto the NaCl plate; if a thinner layer had been deposited, relative to the sun sample, it might have oxidized more quickly. Another explanation could be that the full spectrum growing light has a higher percentage of UV light compared to the sun, as the growing light does not have the atmosphere to act as a UV filter. Clearly, the sample that was placed in the sun did produce a significantly larger peak at 1700 cm^{-1} after 3 h, with respect to the growing light sample. This is most likely due to the 10 times greater intensity of the sun compared to the growing light.

Experiment Thee

An experiment was performed to test the photo-oxidation effects that an introduced porphyrin might have on the bitumen. It was hypothesized that such compounds should act as photocatalysts. This would increase the amount of carbonyl-containing complexes formed within the bitumen, as well as perhaps promote complete oxidation to CO_2. This idea of porphyrin rings being used as a photocatalytic material to form carbonyl complexes in bitumen is supported by previously published literature[20-24].

Part One: Investigation of Hemin

An IR spectrum of pure hemin was first recorded (Figure 11). The hemin sample was also exposed to a growing light for a period of 6 h to ensure that it did not react under UV light. After 6 hours of exposure, there was no observed change in its IR spectrum.

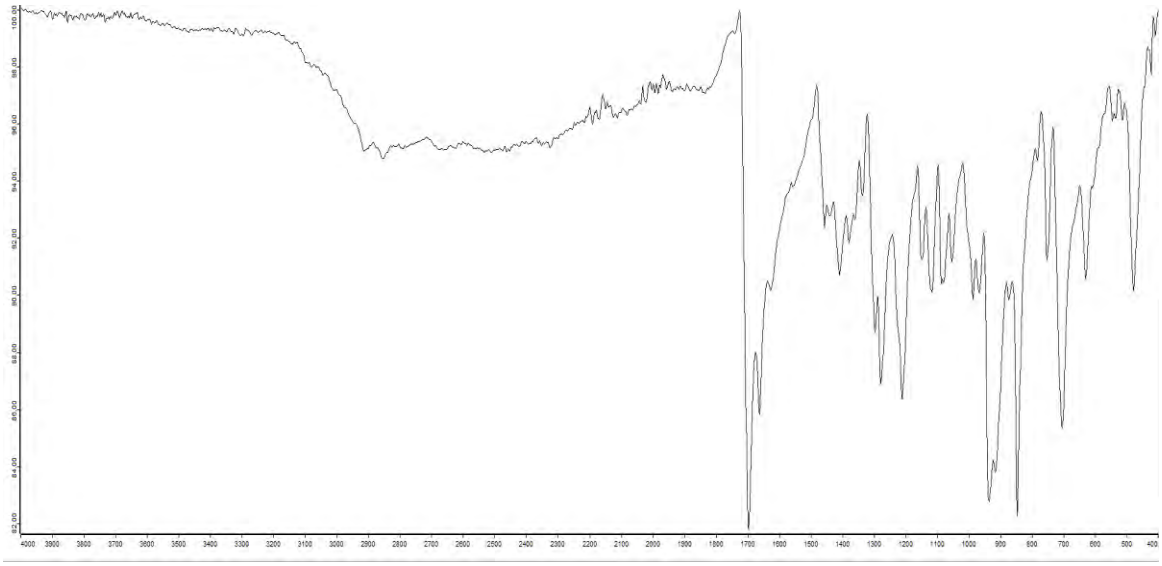

Figure 11: IR spectrum of hemin recorded on a Bruker Alpha Spectrometer with ATR.

Hemin does contain carbonyl groups and thus has IR peaks within the target region being studied for bitumen. An experiment was devised to try and determine the impact hemin would have on the IR integrations to be used in the second part of this experiment. Hemin was added to nujol oil in a 5% w/w mixture to mimic the spiked bitumen samples. This sample was deposited onto a NaCl plate. As it did not dry upon exposure to air like the bitumen samples, it was pressed into a thin film with another NaCl plate. The sample was placed under a growing light for a total period of two hours. Its IR spectrum was recorded at the same time intervals as those used for the Mesa bitumen samples (in the experiment which follows). Each time the sample was placed

under the growing light, the NaCl plates were separated to allow exposure to the atmosphere as in the bitumen samples.

The hemin nujol sample did not show any evidence of photoreaction (Figure 12). There was an observed increase in the intensity of the peak at 1600 cm^{-1} but it is unlikely that it was due to photo-oxidation. There is no evidence of porphyrins oxidizing or decomposing in the presence of UV light in the literature,[21-25,27,29] and these materials are used as photo-catalysts. It is possible that the NaCl plates were contaminated by perspiration, as the plates for the 90- and 120-min trials were handled without gloves. Perspiration does have a major peak[30] in the IR at 1580 cm^{-1}.

There was a prominent IR peak at 1700 cm^{-1}, from ν(C=O) of its carbonyl groups, and a similar size peak at 1660 cm^{-1}, arising from ν(C=C) of its alkene bonds. The ratio between the hemin C=O peak at 1700 cm^{-1} and the peak at 1660 cm^{-1} was calculated at the different sampling times and the results are shown in Figure 13. From this, it can be seen that the relative sizes of the two peaks remain consistent within the different IR spectra. This implies that there was no direct reaction of the hemin in the presence of UV light. The integration of one peak is roughly equal to the other since the measured ratio remains consistently close to unity. This might allow separation of the hemin CO peak from that of bitumen, since both will be present in the hemin spiked Mesa bitumen samples (Figures 16 and 17). However, these peaks are largely unresolved in those samples, so it will be difficult to determine just how much each peak will contribute to the integration values. It is thus unlikely that separation of the hemin contributions from the Mesa bitumen contributions will be possible. It must then be noted that all of the

ratios for all hemin spiked bitumen samples will have a contribution from the added hemin.

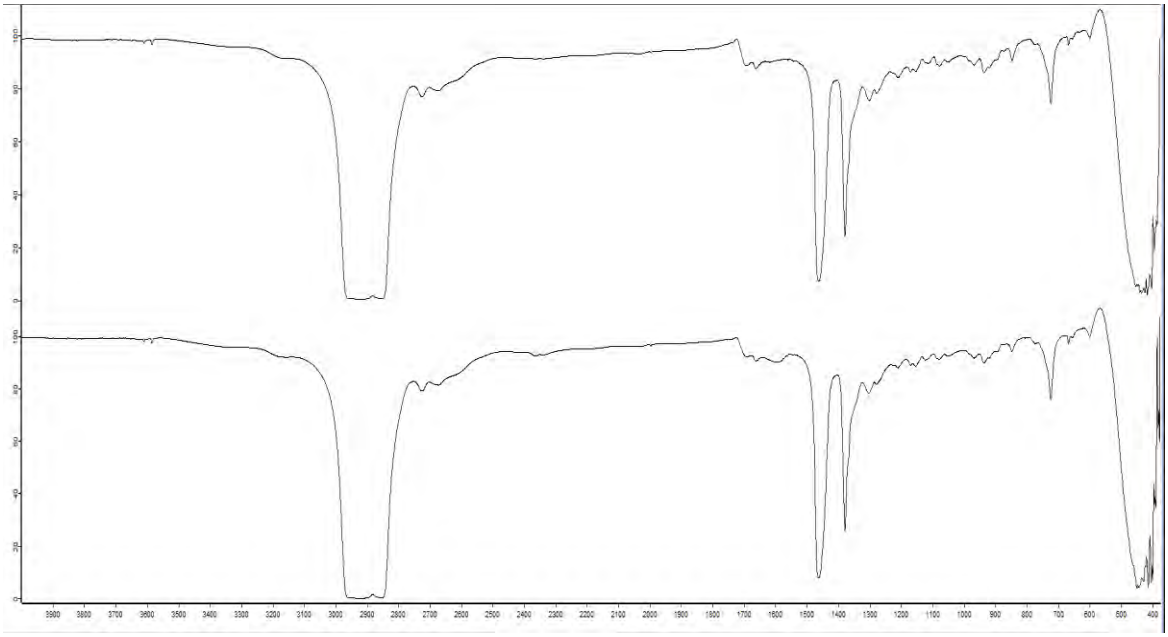

Figure 12A: Infrared spectra of hemin in nujol 5% w/w, before exposure to the growing light (top) and after 120 min of exposure to the growing light (bottom).

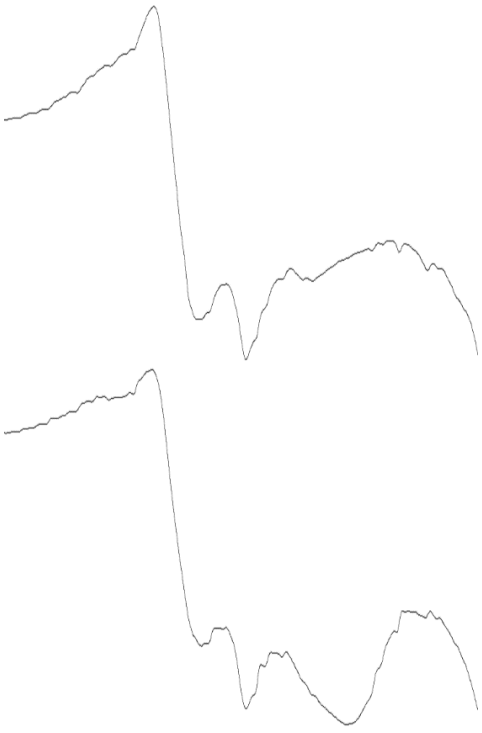

Figure 12B: Infrared spectra of hemin in nujol 5% w/w focussed on the 1750-1500 cm^{-1} region, before exposure to the growing light (top) and after 120 min of exposure to the growing light (bottom).

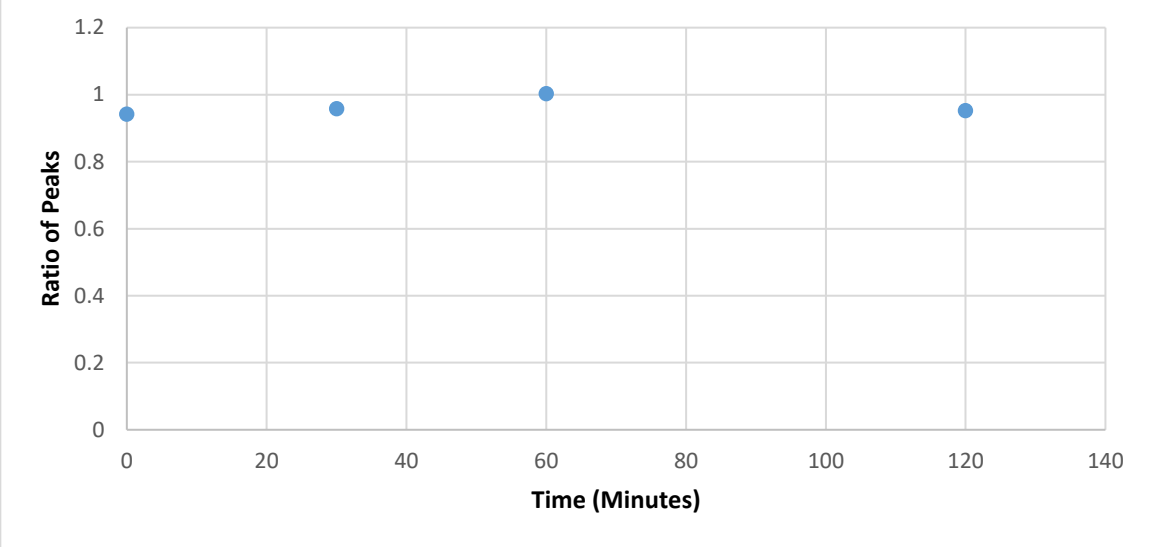

Figure 13: Ratio of the 1700 cm^{-1} (ν(C=O) peak over the 1660 cm^{-1} (ν(C=C) peak from integration of the IR spectra for the nujol plus hemin samples. Data for the 90-min mark was lost and thus had to be omitted.

Part Two: Bitumen Samples Spiked with Hemin

As in the previous tests, samples of bitumen were deposited onto NaCl plates and allowed to dry. Four samples were made using Mesa bitumen, half of which were spiked with hemin such that it was 5% w/w. One of each type of sample was placed into darkness while the other was placed into direct sunlight. The IR spectra of the samples were recorded every 30 min for 2 hours. This experiment utilized Mesa bitumen, so it also tested if another type of bitumen would produce similar results to Athabasca bitumen upon sun exposure. In order to determine whether there was any difference between the samples, a ratio of the integrations of specific IR peaks was calculated, to give a relative value that would be relatable between samples.

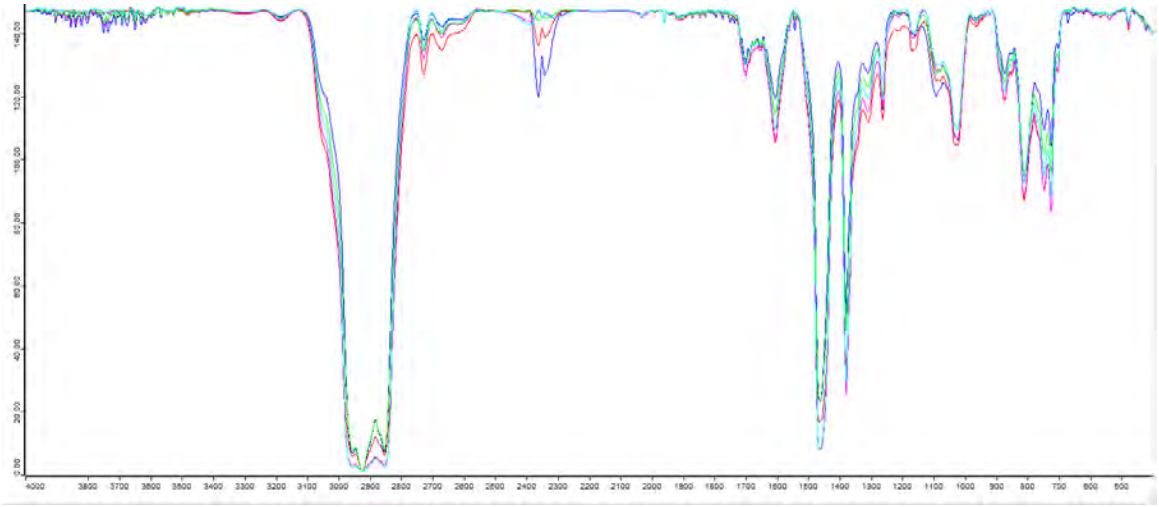

Figure 14A: Overlaid infrared spectra for a sample of photo-oxidized Mesa bitumen deposited on a NaCl plate left in the dark and sampled every 30 min for a total of 2 h.

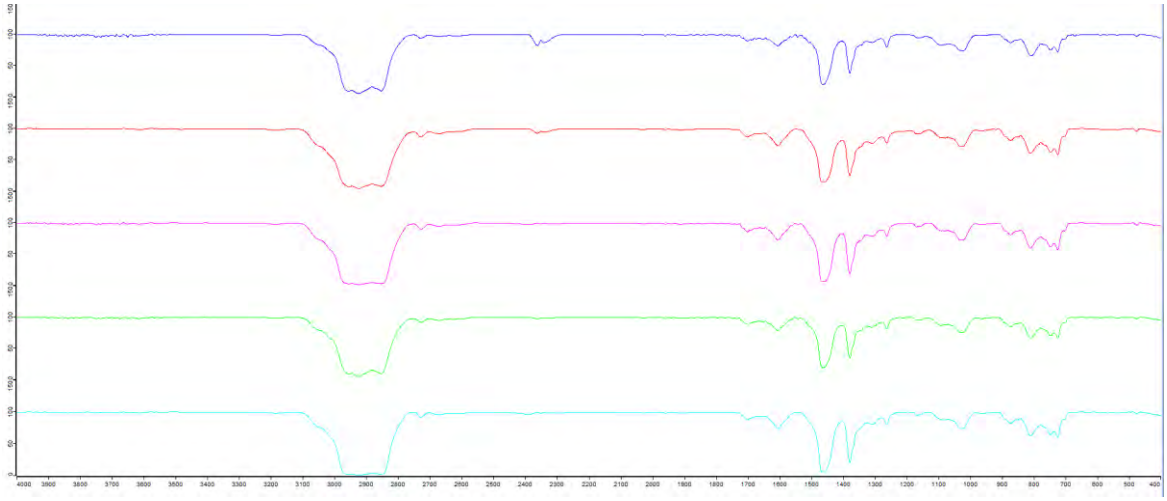

Figure 14B: Stacked infrared spectra for a sample of photo-oxidized Mesa bitumen deposited on a NaCl plate (dark control). Bitumen control time 0 min (top), increasing by 30-min intervals for each respective spectrum below ending with 120 min (bottom).

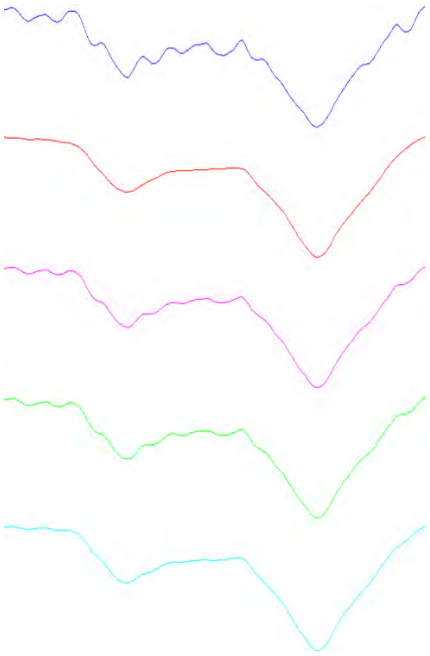

Figure 14C: Stacked infrared spectra for a photo-oxidized sample of Mesa bitumen deposited on a NaCl plate (dark control) focussed on the 1750-1500 cm^{-1} region. Bitumen control time 0 min (top), increasing by 30-min intervals for each respective spectrum below ending with 120 min (bottom).

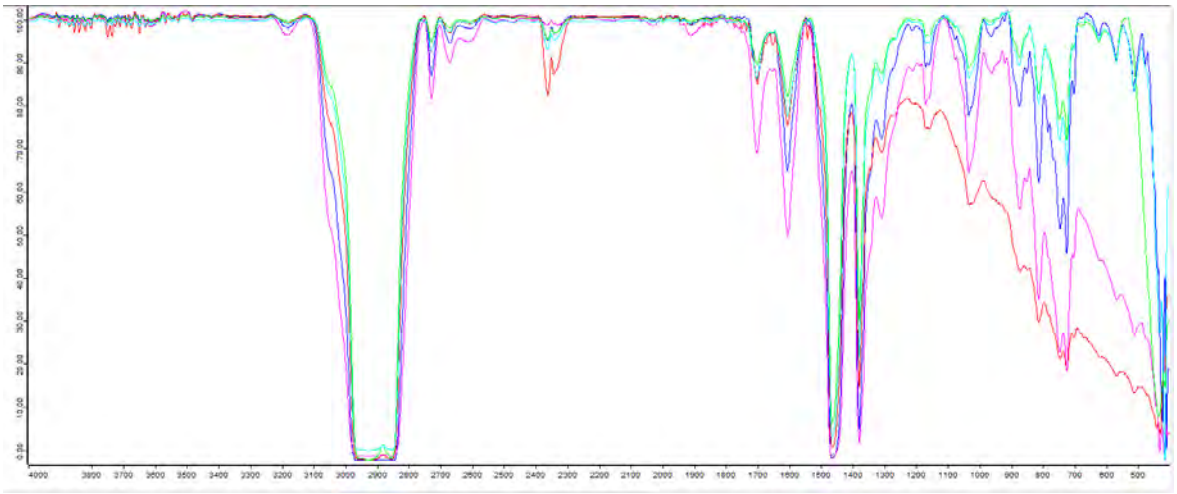

Figure 15A: Overlaid infrared spectra for the photo-oxidation of Mesa bitumen left in the sun and sampled every 30 min for a total of 2 h.

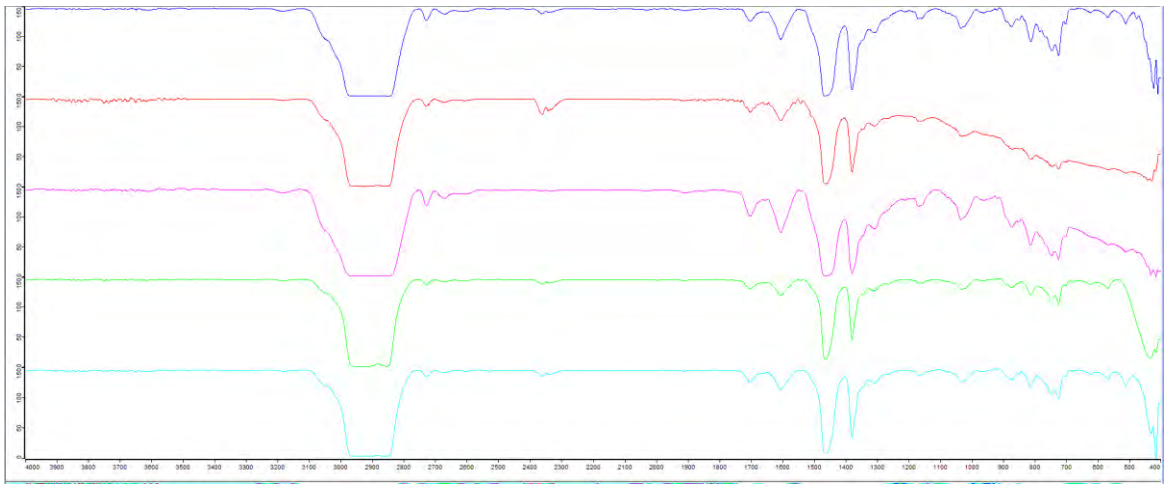

Figure 15B: Stacked infrared spectra for the photo-oxidation of Mesa bitumen (sun control). Bitumen control of time 0 min (top), increasing by 30-min intervals for each respective spectrum below it and ending with 120 min (bottom).

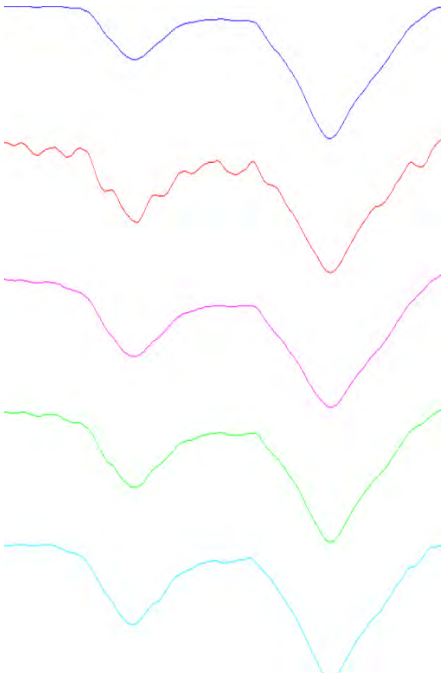

Figure 15C: Infrared spectra for the photo-oxidation of Mesa bitumen (sun control) focussed on the 1750-1500 cm^{-1} region. Bitumen control of time 0 min (top), increasing by 30-min intervals for each respective spectrum below it and ending with 120 min (bottom).

For the Figures 15, it should be noted that the peaks at 1700 cm^{-1} and 1600 cm^{-1} are significantly larger at the 60-min mark compared to the other time points; these then shink again as the experiment progresses. This could be a true experimental observation. However, it is more likely attributable to the sample accidentally having been measured in a different location for this time, compared to the others. If one position had a higher density of bitumen deposited onto the NaCl plate relative to the other, this would artificially create higher intensities in the spectra of those samples. However, the ratio between the peaks at 1700 cm^{-1} and 1600 cm^{-1} would remain internally consistent. From Table 1 and Graph 1, it can be seen that the ratio remains stable within the error range.

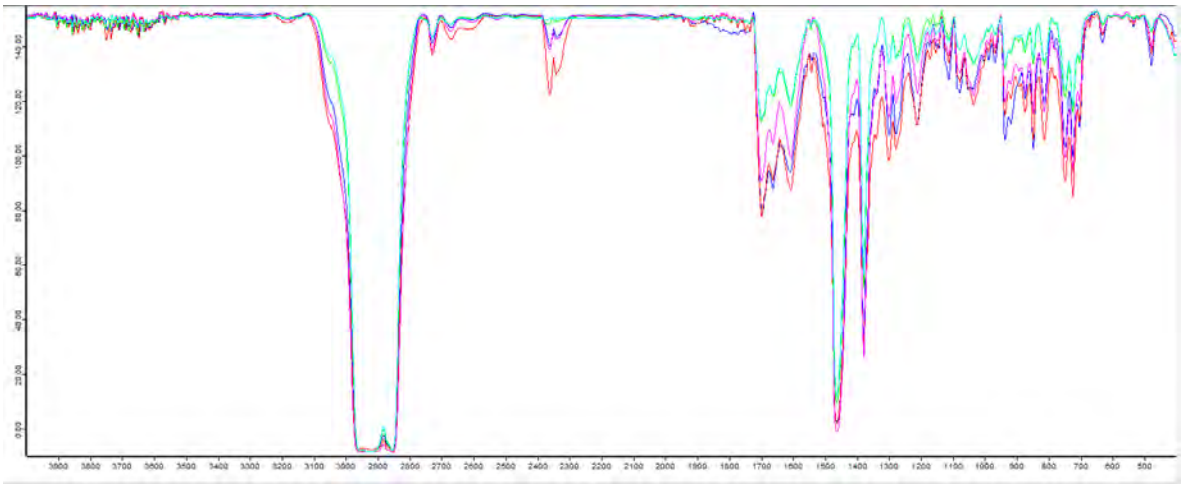

Figure 16A: Overlaid infrared Spectra for the photo-oxidation of hemin spiked Mesa bitumen left in the dark and sampled every 30 min for a total of 2 h.

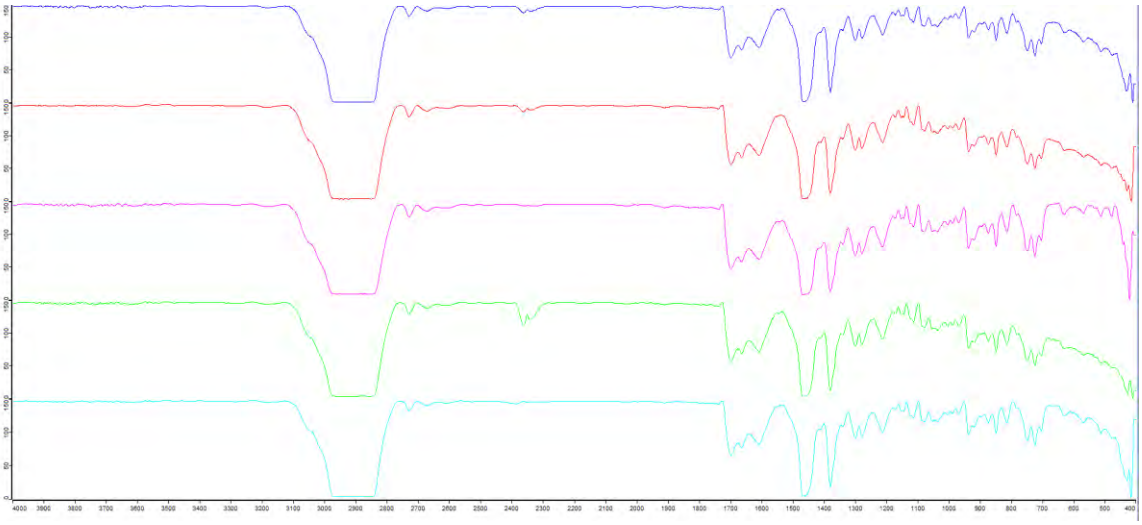

Figure 16B: Stacked infrared spectra for the photo-oxidation of the hemin spiked Mesa bitumen dark sample. Bitumen control of time 0 min (top), increasing by 30-min intervals for each respective spectrum below ending with 120 min (bottom).

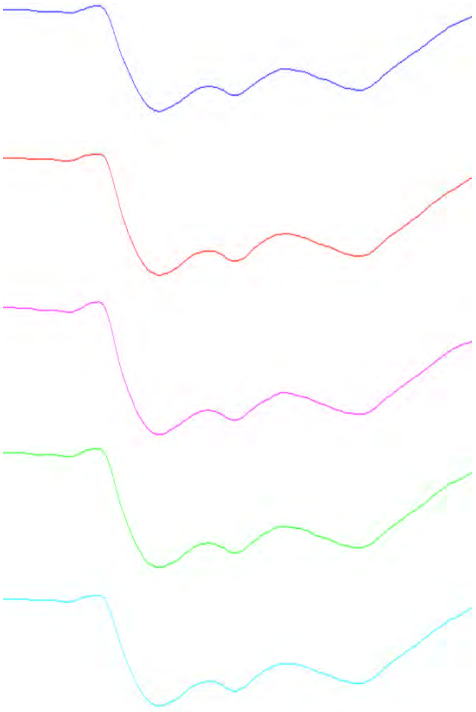

Figure 16C: Stacked infrared Spectra for the photo-oxidation of the hemin spiked Mesa bitumen dark sample focussed on the 1750-1500 cm^{-1} region. Bitumen control of time 0 min (top), increasing by 30-min intervals for each respective spectrum below ending with 120 min (bottom).

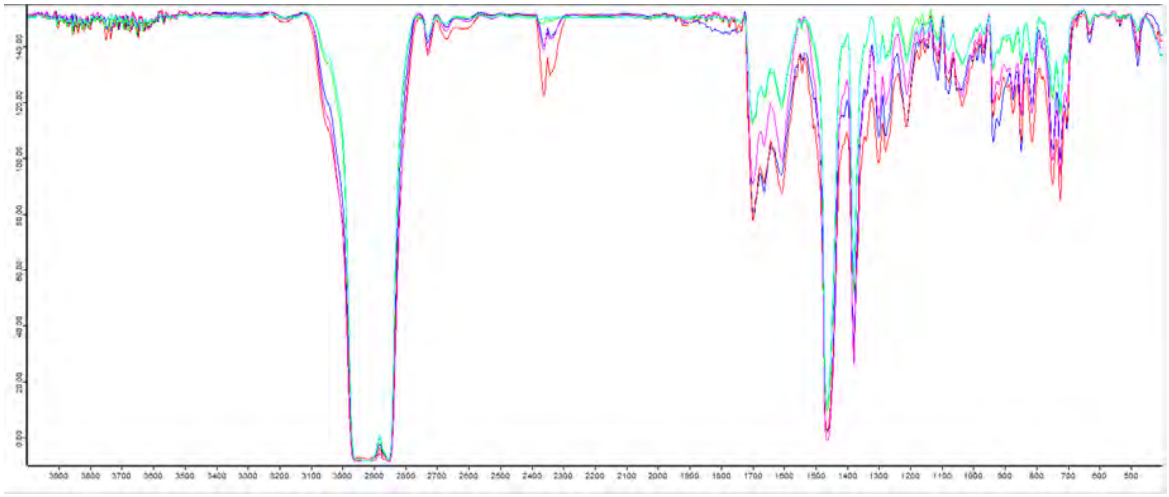

Figure 17A: Overlaid infrared spectra for the photo-oxidation of hemin spiked Mesa bitumen left in the sun and sampled every 30 min for a total of 2 h.

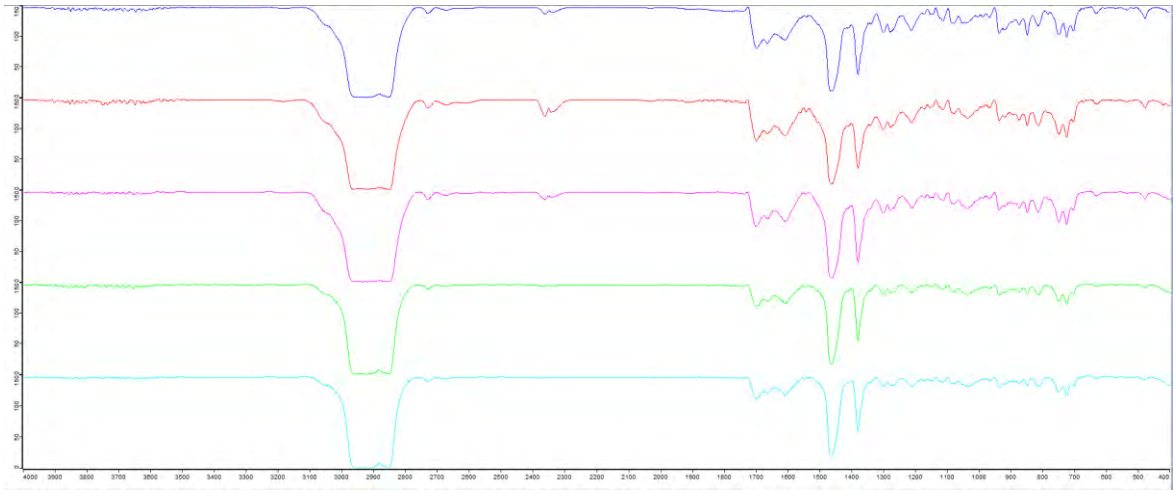

Figure 17B: Stacked infrared Spectra for the photo-oxidation of the hemin spiked Mesa bitumen sunlight sample. Bitumen Control of time 0 min (top), increasing by 30-min intervals for each respective spectrum below ending with 120 min (bottom).

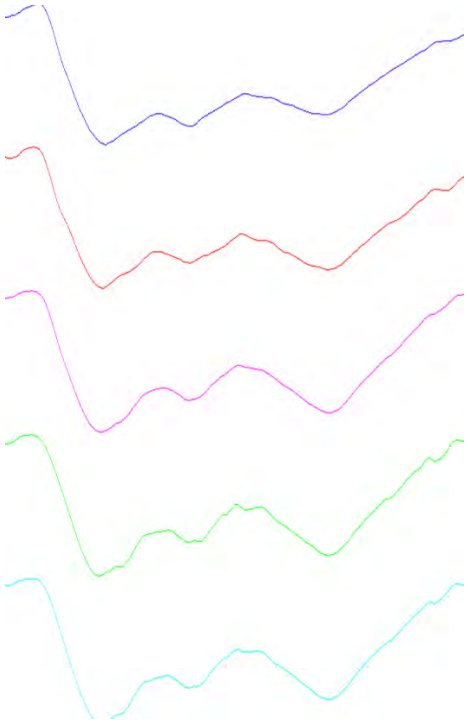

Figure 17C: Stacked infrared spectra for the photo-oxidation of the hemin spiked Mesa bitumen sunlight sample focussed on the 1750-1500 cm^{-1} region. Bitumen control of time 0 min (top), increasing by 30-min intervals for each respective spectrum below ending with 120 min (bottom).

It is important to note that the Mesa bitumen samples show no evidence of water or volatile hydrocarbons in their IR spectra, which is unlike the diluted Athabasca bitumen used in Section 1 and earlier in Section 2. This may be because the Mesa bitumen was not diluted like the previous bitumen samples had been, and thus its samples had less available volatiles. Another explanation could be that the Mesa bitumen used was significantly older than the Athabasca bitumen; the additional aging could have provided time for any volatiles that were originally present in it to have escaped.

As can be seen from the spectra of the dark sample (Figure 14), there is must be a small amount of a carbonyl containing component, which remains relatively constant, within the sample. Whether this has arisen from oxidation due to the sample's age, or if it

occurred naturally within the sample, is not certain. From Figure 14A, is can be seen that there is little to no fluctuation within the spectra over the course of the experiment. The average ratio for the integration of the peak at 1700 cm^{-1} over that at 1600 cm^{-1} for the dark control spectra is 0.44 ± 0.05. This standard deviation can also be used as a base measure of the error in the overall experiment; while the control spectra show minimal changes over time, there are small fluctuations observed in the ratio. For both the dark and sun control samples, once the 30-min mark is reached the samples and their calculated ratios are very stable. With the initial measurement removed from each series, the Mesa dark sample control has an average value and standard deviation of 0.42 ± 0.02 and the sun sample control has respective values of 0.50 ± 0.01. This suggests that a small amount of oxidation did occur in the sun sample, even in the absence of hemin.

Stacking the sun control sample IR spectra (Figure 15) clearly shows that the carbonyl peak increases in intensity over the course of the experiment. This implies that the Mesa bitumen has been photo-oxidized in the presence of UV light, just like the previous bitumen samples were. The lack of volatile hydrocarbons (no peak observed at 1640 cm^{-1}) also shows that these are not the components within the bitumen that are being photo-oxidized, instead it confirms that is the conjugated aromatic structures within the bitumen that undergo photo-oxidation. However, since the integrated peak ratio of the sun sample also remained relatively constant over the course of the experiment, the intensity of the C=C aromatic peak must have increased proportionally with the observed increase of the C=O peak.

Table 1: Ratios of the integration for the carbonyl peak over that of the alkenyl peak in the IR spectra of the hemin spiked bitumen samples

Sample	0 min	30 min	60 min	90 min	120 min

Mesa Dark Control	0.52	0.42	0.42	0.45	0.41
Mesa Sun Control	0.32	0.50	0.52	0.51	0.49
Mesa + Hemin Dark†	0.76	0.67	0.64	0.68	0.74
Mesa + Hemin Sun†	0.67	0.63	0.73	0.74	0.76

†integration values are increased relative to the controls due to the additional carbonyl peaks arising from the hemin addition

Graph 1: Ratio of C=O over C=C Integrations for peaks in the IR Spectra of the Mesa samples

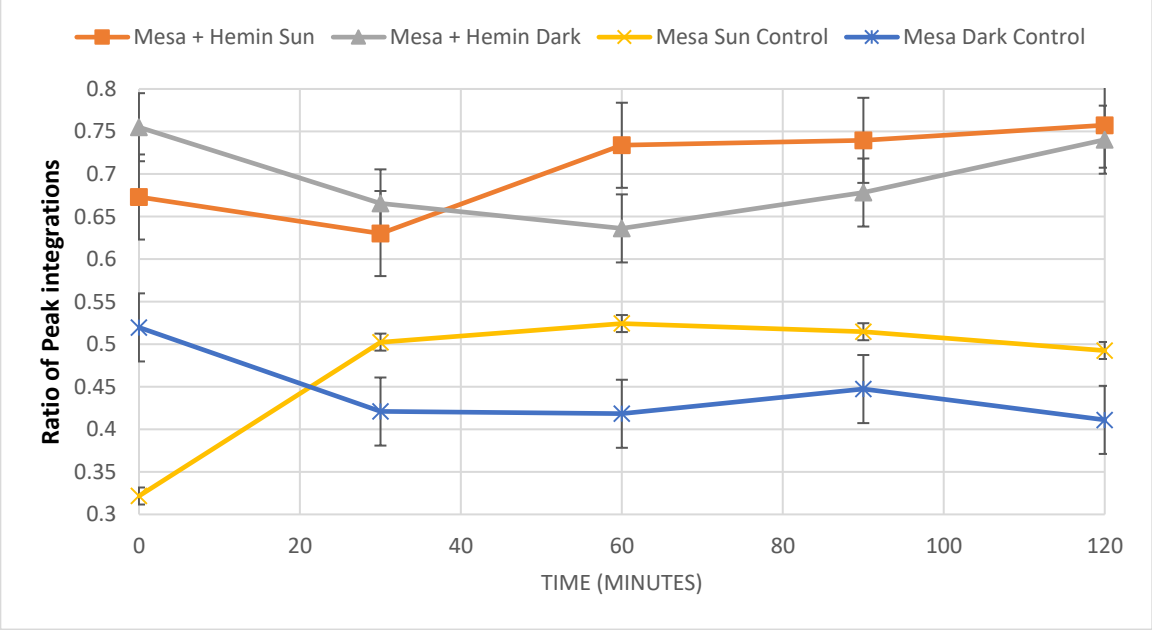

There are several interesting observations that can be made after looking at the data for the hemin spiked samples in Table 1. Error bars, equal to the standard deviation for each sample, have been added to Graph 1. What is immediately noticeable is that the hemin spiked samples consistently have a larger integration ratio with respect to the control Mesa samples. This must be due, at least in part, to the presence of carbonyl groups in the hemin itself. The average change observed in the ratios of the dark samples on the addition of hemin is the same as that observed for the light samples. This suggests that, in both type of sample, the difference arises only from the addition of hemin to the sample.

The Mesa dark control and the Mesa hemin dark sample appear to behave similarly. Though the average ratio value is increased for the hemin dark sample compared to the dark control (0.44 vs. 0.70 respectively), they both have about the same standard deviation. This likely implies that there is not much change between the samples other than the increased ratio due to the presence of hemin carbonyls. The peaks of interest in the dark hemin spectra do increase more over time than do the peaks in that of the dark control. The fact that the ratio is relatively stable suggests that they are increasing in a proportional way.

The average ratio is also larger for the hemin sun sample compared to the sun control (0.72 vs. 0.50 respectively). This difference in the averaged integrated ratios is the same as was observed for the dark samples, which again implies that it arises from adding hemin to the bitumen sample rather than from their photo-oxidation. As in the dark hemin sample, the peaks of interest in the actual IR spectra appear to strengthen in a concerted

fashion leaving the ratio relatively constant. However, if one looks only at the hemin sun curve in Graph1, there does appear to be a gradual increase in the integrated ratio with time spent in the sun. This suggests that a small amount of photo-oxidation may have occurred in the hemin sun sample.

Overall, the dark and light samples, with and without added hemin, have integrated ratios that are quite stable over time and that generally vary only in amount that can be attributed to having added hemin to some samples. Little proof of photo-oxidation was obtained from this experiment. However, it did not reliably account for the possibility of the bitumen having been oxidized all the way to CO_2. The introduction of a metalloporphyrin is known to act as a photo-catalyst for oxidation in literature,[20-24] but it is unclear whether or not this process can cause oxidation all the way to CO_2.

The results of these experiments show that photo-oxidation does occur in Athabasca bitumen with the use of a growing light. This oxidation could be monitored using IR spectroscopy of the bitumen samples over the course of the thee-hour experiment. A carbonyl peak (~1700 cm^{-1}) appeared in the spectrum after approximately 60 min. Photo-oxidation was also observed when the sun was used as the light source for the photo-oxidations. It required 80 min before the Athabasca bitumen began to show evidence of the carbonyl peak in IR. This was surprising as the intensity of the sun was about 10 times greater than that of the growing light. Perhaps the sample under the growing light may have oxidized more quickly due to a thinner layer having been deposited onto the NaCl plate relative to the sun experiment. Or, perhaps the full spectrum growing light has a higher percentage of UV light compare to the sun, as the growing light does not have the atmosphere to act as a UV filter.

The effects of the addition of the metalloporphyrin hemin to bitumen were also explored. First, hemin was shown to be chemically unaltered under exposure to UV light over the time lengths of the IR experiments. Mesa bitumen samples spiked with hemin did not show any significant photo-oxidation; the samples left in the sun were no different from the samples left in darkness, as judged from the ratio of the C=O peak to C=C peak in the IR. The Mesa bitumen samples that were not spiked with hemin, however, showed a distinct photo-oxidation in the sun sample relative the sample left in darkness. This at least demonstrated that photo-oxidation occurs in different varieties of bitumen.

Section 3: Bitumen on water

Experiment One

Samples of diluted Athabasca bitumen, 2 g dissolved in 10 mL hexanes, were deposited onto the surface of 10 mL of aliquots of water in regular increments of 0.25, 0.50, and 1.00 mL. These samples were carefully sealed to the air and handled so as not to cause mixing of the layers. Two sets of thee samples each were prepared. One set was placed under the growing light, while the other was sealed and placed in darkness. They were allowed to sit undisturbed for 3 hs. The IR spectra of the 1.0 mL samples (dark and light) were recorded after depositing a small amount of bitumen onto a NaCl plate with a glass stir rod.

Next, 5 mL of the water layer was pipetted out of each of the 0.5 mL and 1.0 mL samples. The water was shaken with 10 mL dichloromethane (DCM) for 5 min in order to extract organic compounds that might have entered the water layer. The DCM extracts were taken for Liquid Chomatography–Mass Spectrometry (LC-MS), and Ultraviolet–Visible spectroscopy (UV-vis) analyses. The DCM samples were passed though a High-Performance Liquid Chomatograph (HPLC) with a ZDRBAX Eclipse XDB-C18 column. There was no evidence of leeching of the bitumen into the water layer as no peaks were seen in the elution and MS data did not reveal anything different from the solvent mobile phase blank.

The UV-Visible Spectrophotometer was blanked using DCM in a 1 cm path-length quartz cuvette, which had been rinsed 3 times with DCM beforehand. A sample was then dispensed into the cuvette and measured across the wavelength range of 200-1200 nm. The UV-Vis data could not be used to monitor the leeching of hydrocarbons

into the aqueous layer, as the absorbance of the samples was off the scale, even after a dilution of 1:160000. It is important to note that not having spectroscopic evidence of bitumen leeching into the aqueous layer, and leeching of bitumen into the aqueous layer not occurring, are not the same thing. From the photographs in Figures 18 and 19 below, it can be seen that the aqueous layers are either obviously discoloured or have dispersed droplets of bitumen thoughout the aqueous layer, depending on the sample. These figures alone show distinct interactions between bitumen and the aqueous layer, however, the spectroscopic and spectrometric analyses we tried did not give any tangible results that could be used for compound identification.

Experiment Two

Another experiment was devised such that the samples would be left open to the air instead of sealed. Triplicate samples of 0.5 mL and 1.0 mL of AWB bitumen were deposited onto the surface of 10 mL of water in scintillation vials. Thee trials were made: samples sealed to air left under darkness for 24 hs, samples open to air left under darkness for 24 hs, and samples open to the air left under a growing light for 24 hs. Sealed to air samples to be left under the growing light were not prepared. Not only would sealing block the UV light from hitting the bitumen, but it would also reduce the amount of oxygen reaching the sample. From the previous experiments run, it was believed that the bitumen reacts with atmospheric oxygen, and thus making sealed samples would hinder their photo-oxidation. The IR of each bitumen sample was recorded (Figures 20 and 21) by depositing a small amount of bitumen onto a NaCl plate

with a glass stir rod. The bitumen layers of the 0.5 and 1.0 mL sealed dark samples and the related dark samples left the open to the air had identical IR spectra.

Once the 24-h experiment was complete, the samples were thoroughly mixed at regular intervals, to promote leeching of bitumen components into the aqueous layer. This was done using alternating methods of shaking, manual shaking for 5-min intervals and then using a vortex mixer at 5-min intervals. Samples were mixed like this for a total of 30-min. By the end of the mixing period, the bitumen samples that had been kept in the dark expanded and become "gel-like" upon shaking (Figure 18), In contrast, the light samples formed smaller droplets of bitumen that dispersed thoughout the water on shaking; these would slowly recollect at the water surface, but never completely (Figure 19, top). The samples were also observed under UV light to see if there were any noticeable differences (Figure 19, bottom). The light samples did not fluoresce under the lamp, while the dark samples did. This may indicate that the light samples had lost aromaticity, which decreased the fluorescence of the bitumen. The IR spectra of the 0.5- and 1.0-mL bitumen open to air, dark and light samples were recorded (Figures 20 and 21). The bitumen layer of the 0.5 and 1.0 mL sealed dark samples were also tested but their spectra were no different than those of the open to air dark samples.

Once the bitumen had settled as much as possible after mixing, so that any floating particles would not be taken up, the water layers were extracted. 5 mL of the water layer was removed from each sample vial and washed with 10 mL DCM in order to extract any hydrocarbons from the aqueous layer.

No tangible evidence of hydrocarbon leeching was found after testing the samples using both LC-MS and UV-Vis methods. The LC-MS data did show that there was some

hydrocarbon leeching into the aqueous layer. Some compounds were eluted just after the solvent peak in the light samples but not in the dark ones. The peaks appeared before the 5-min mark, indicating that they were polar in nature, which is possible evidence for photo-oxidation having occurred on exposure to light. This being said, the data did not provide any information useful for compound identification because of a lack of resolution between signals. The data for aqueous layer leeching has thus not been included here.

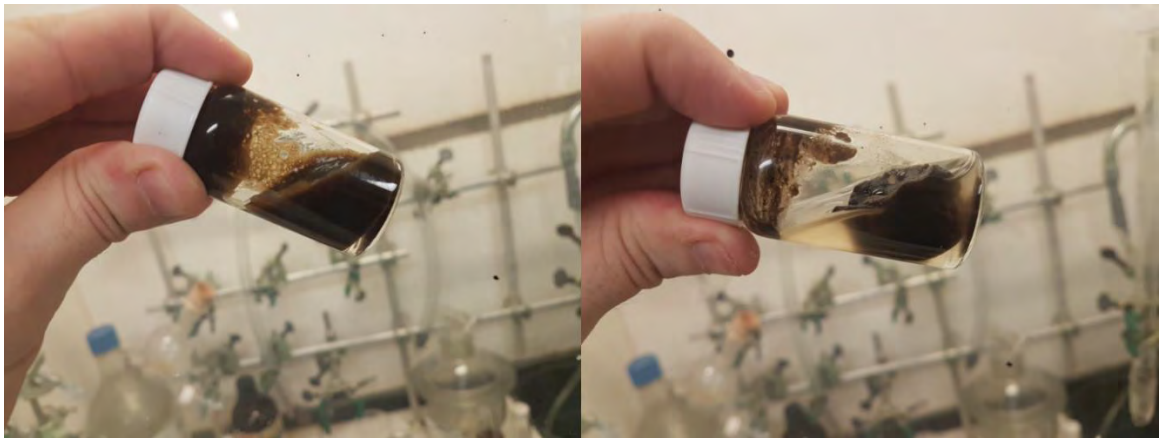

Figure 18: Demonstration of the "gelling" effect of bitumen in water left in the dark.

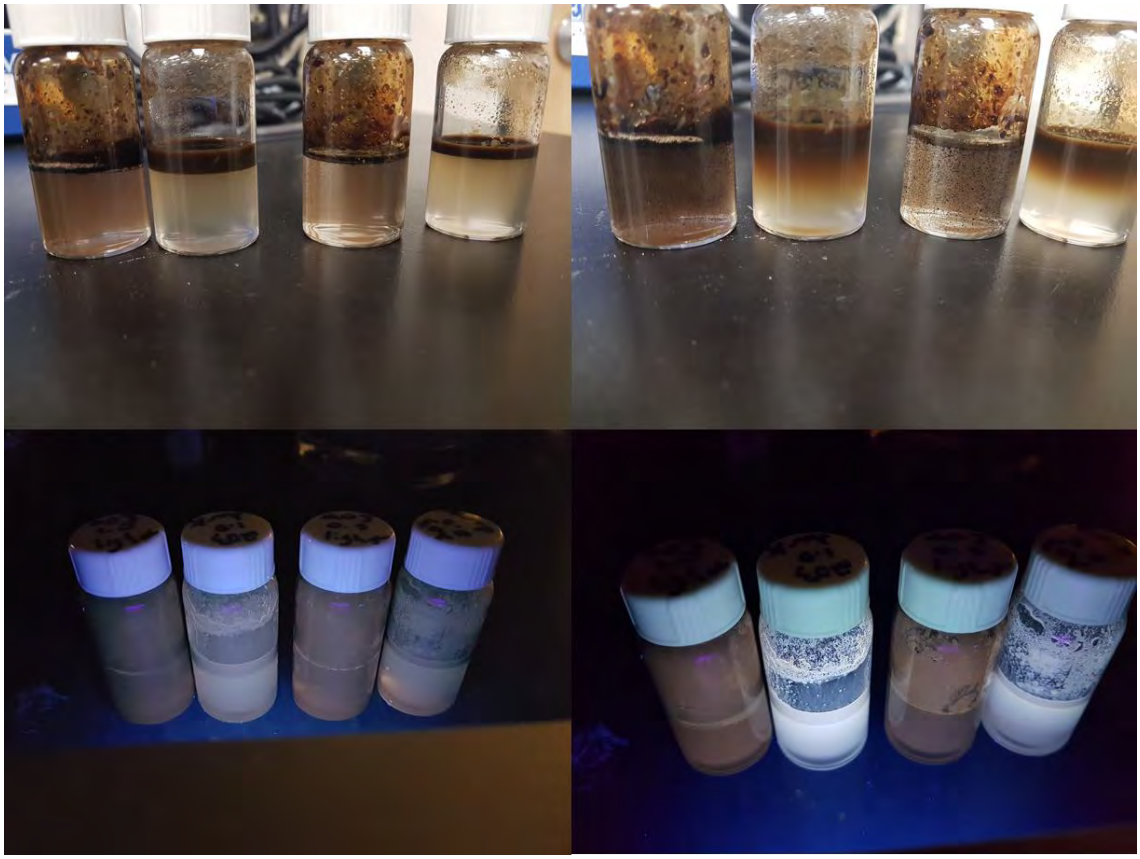

Figure 19: Bitumen on 10 mL water samples left open to air (bitumen volumes as given in the captions) from left to right: 1.0 mL Light, 1.0 mL Dark, 0.5 mL Light, and 0.5 mL Dark. Bitumen settled on water level (top left), bitumen shaken and allowed to settle for 1 min (top right), samples under short wave UV light 254 nm (bottom left), samples under long wave UV light 365 nm (bottom right). Bitumen dark samples sealed to air have been omitted as they were no different from the respective open to air dark samples.

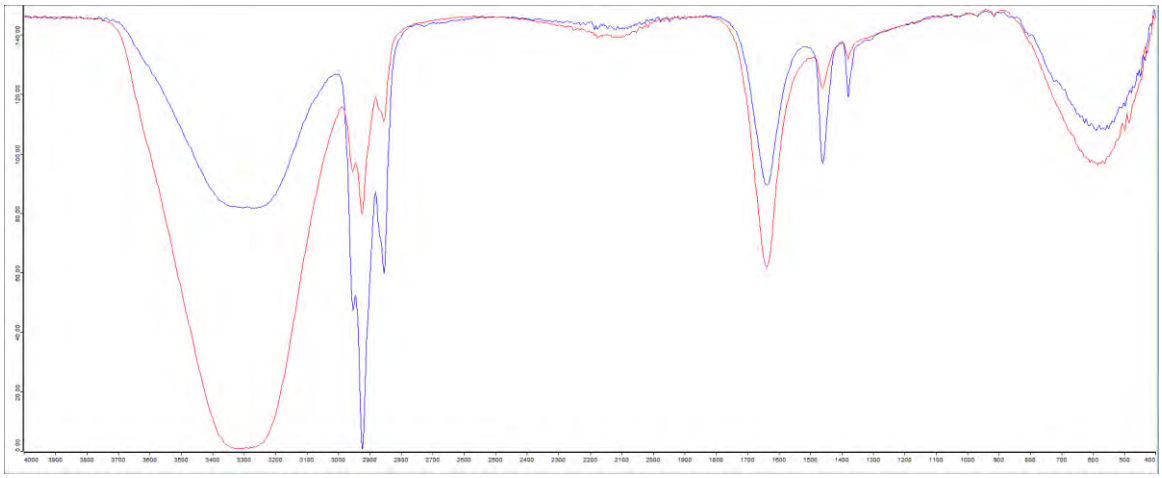

Figure 20: Infrared Spectra for the 0.5 mL samples of bitumen on water left under their respective conditions for 3 h. Bitumen left open in the dark (blue), bitumen left open to the air and placed under the growing light (red). Large peak at ~3400 cm^{-1} attributed to volatile OH-containing species and/or water. Samples run on a NaCl plate.

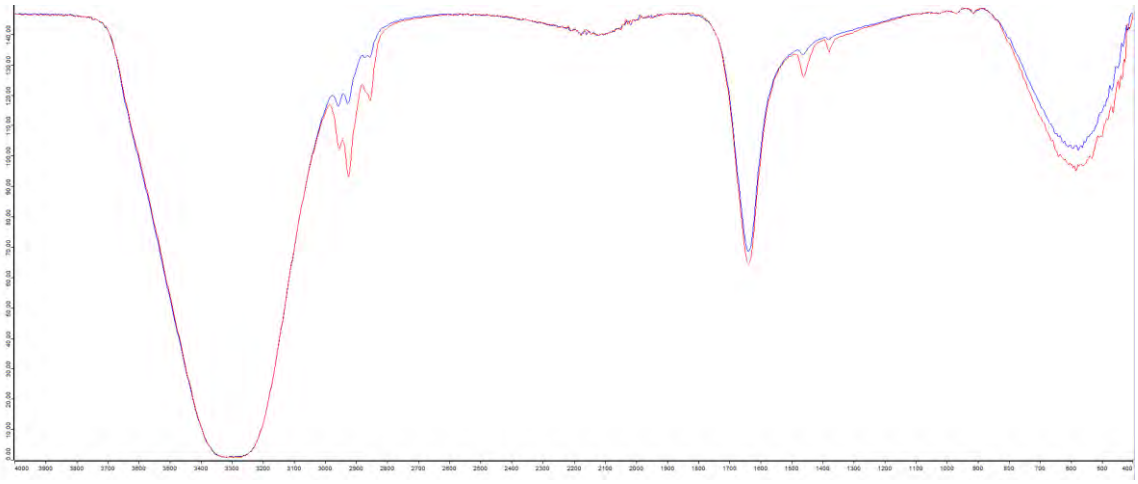

Figure 21: Infrared Spectra for the 1.0 mL samples of bitumen on water left under their respective conditions for 3 h. Bitumen left open in the dark (blue), bitumen left open to the air under the growing light (red). Large peak at ~3400 cm^{-1} attributed to volatile OH-containing species and/or water. Samples run on a NaCl plate.

It is unclear why the spectra in Figures 20 and 21 show only the 1640 cm^{-1} peak related to isolated alkenyl C=C bonds. They all clearly show strong ν(OH) stretching vibrations, suggesting that the IR samples run were wet. The 0.5 mL samples do show differences between the light and dark samples, whereas the 1.0 mL light and dark

spectra show only very minor differences. The 0.5 mL dark samples have a greater CH stretching vibration in the 2900 cm^{-1} region and a reduced water peak in the 3400 cm^{-1} region compared to the light sample. It also has peaks at 1640 and 1500 cm^{-1} of roughly the same size, while in the spectra of the light sample the 1640 cm^{-1} peak is significantly larger than that at 1500 cm^{-1}. Between the light and dark 1.0 mL samples, there is very little difference other than a reduction in the CH stretching peak at 2900 cm^{-1}. A possible idea is that the water has prevented the volatile components from leaving the system as had been seen in the IR analysis of the bitumen samples in Sections 1 and 2. It is also possible that the heavy agitation of the samples caused the more polar components of the bitumen to enter into the aqueous phase (or at least separate onto the aqueous phase) away from the more non-polar components. Either of these processes, in addition to any photo-oxidation that might have occurred and varying amounts of water in the different samples, could have affected the IR spectra collected in this experiment.

Experiment Thee

A similar experiment was then carried out but adding the sun as an additional light source. Thee sets of samples were made up and all were left open to air - light, dark, and sun - for a total of 3 h. The samples were made in the same manner as before, with set amounts of AWB bitumen (0.5 and 1.0 mL) deposited on 10 mL of water, for six samples total. The two light samples were placed under a growing light, while the two sun and two dark samples were placed onto a green roof. The dark samples were left open to air but were doubly shielded from the sun with aluminium foil and a secondary holding vessel also wrapped in aluminium foil. In this way, the dark samples could be left in the

same atmospheric conditions as the sun samples without being exposed to light. The top of the tin foil wrapping was left open but shaped into a gooseneck to prevent light exposure. The intensity (in Lux) of both the growing light and the sun were measured for the entirety of the 3-h experiment, with measurements taken every 2 seconds (Figure 22). The growing light intensity did not change from that shown in Figure 6.

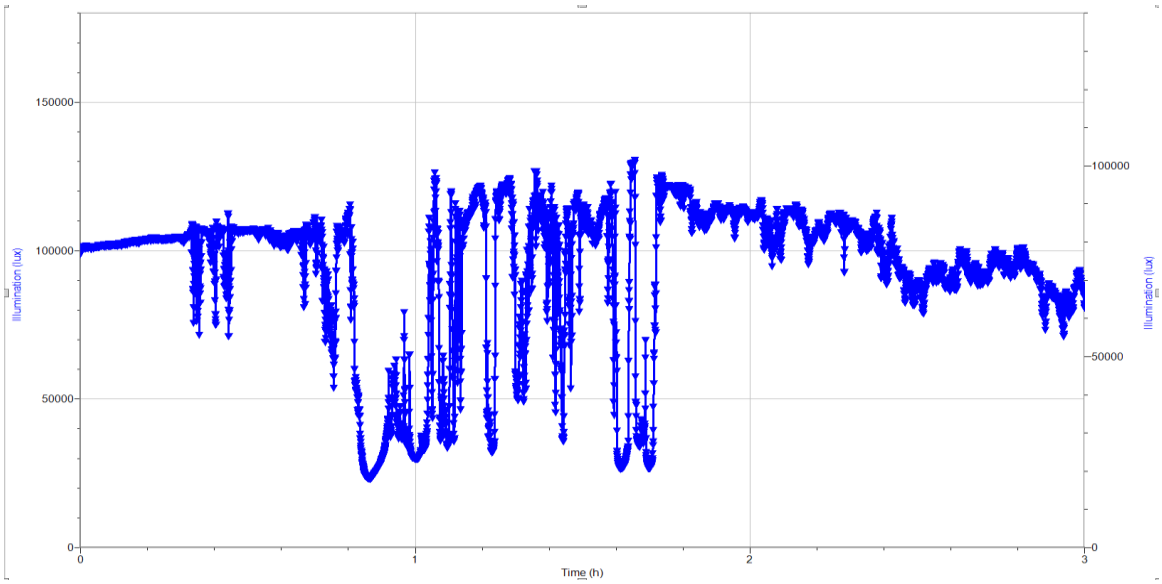

Figure 22: Measurement of the recorded intensity (in Lux) of the sun over the 3-h duration of the experiment.

The samples were sealed and moved carefully, so as to not mix the phases more than necessary. Leeching experiments were not run as the necessary equipment was no longer available. This time, it was noticed between the trials that the sun samples had developed a "film" on top of the water. The bitumen itself would collect into clumps on top of the water layer, but wherever the bitumen did not cover, a thin translucent layer of film was visible on the water surface. The samples were examined under a UV lamp, but nothing unusual was observed. The "film" part of the sun samples was isolated and separated for its own testing. It will be referred to as the "film" sample from now on.

The samples from the green roof (the 0.5- and 1.0-mL sun, dark and "film" samples) and from under the growing light were studied, first with IR (Figures 23 and 24). All of the bitumen samples showed two distinct peaks at 1600 cm^{-1} and 1700 cm^{-1} in their respective IR spectra. This implies that all of the samples underwent photo-oxidation over the thee hours. The layers of aluminium foil covering the dark samples may have increased their internal temperature upon exposure to sunlight, causing them to "bake" in the sun and thus oxidize in this way. Further experiments will need to be conducted to see if this was the case. The carbonyl peak (ν(C=O)) at 1700 cm^{-1} was visible in all spectra but it was slightly smaller in the dark samples and larger in the sun samples. All of the spectra also showed the peak at 1600 cm^{-1}, also seen in previous experiments, assigned to the C=C stretching vibrations of conjugated aromatic systems.

Even more noticeable was the size difference of the 1640 cm^{-1} isolated alkenyl C=C stretching peak in comparison to those in the spectra reported in previous sections. In particular, the IR spectra of the "film" components (separated from the sun samples) are very different from all of the other samples run in this experiment. In addition to distinct peaks arising from ν(OH) and ν(CO) vibrations, the film spectra show relatively large peaks at ~1640 cm^{-1} assigned to isolated alkenyl C=C stretching vibrations. In the film spectra the 1640 cm^{-1} ν(C=C) peak is large enough to almost completely hide the ν(C=C) conjugated aromatic peak at 1600 cm^{-1}. From the results of previous experiments, we have suggested that this signal arises from the more volatile components of the bitumen. Here, it appears that these components are moving out of the bitumen bulk and moving into the film layer which has formed on the surface of the water layer. The fact that the film separates from the overall non-polar bitumen indicates that it must be more

polar in nature. This is confirmed by the spectroscopic data, as the film does have much larger signal strengths in the 1700 cm^{-1} C=O region being monitored for oxidation.

Not only did the volatile compounds not disappear, like they had in the experiments described previous sections, but the film layer may be a potential surfactant[i], holding on to these compounds. The film would become too polar to remain in the non-polar bitumen, thus separating from it. However, the film must also be too non-polar to mix with the aqueous layer, which is why it remains on the surface and recollects after being dispersed by agitation. The film, acting as a surfactant, is essentially a phase of its own, having a polarity mid-way between those of the non-polar bitumen and polar aqueous layers. This might also explain why the film has such a large ν(OH) peak at ~3400 cm^{-1} while the other samples do not. The film was able to interact with the water and disperse thoughout it, but it was not miscible. The film therefore would have a much larger surface area that would come into contact with the water, while the rest of the bitumen would clump and be hydrophobic. It is possible that this peak could be attributed to compounds containing alcohol functional groups formed on contact with water, but it is more likely to be attributable to water itself being present in the film sample. The film layers were very thin and difficult to separate cleanly from the water in the sun samples,

[i] Possessing both polar and non-polar functional groups.

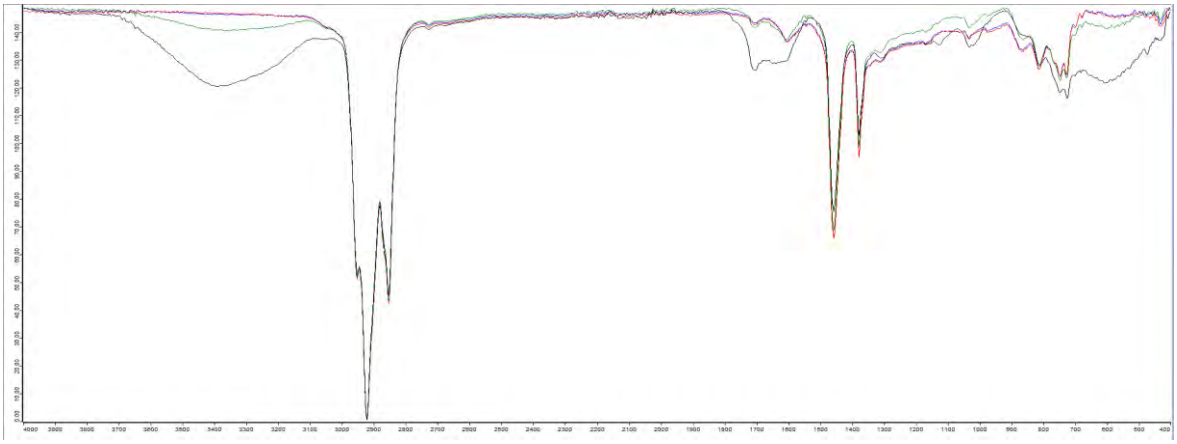

Figure 23A: Infrared Spectra for the photo-oxidized samples of 0.5 mL bitumen on water left under their respective conditions for 3 h. Bitumen left in the dark (blue), bitumen left under the growing light (red), bitumen left under the sun (green), and the bitumen "film" which formed on top of the water layer in the sun sample (black). Large peak at ~3400 cm^{-1} attributed to volatile OH-containing species and/or water.

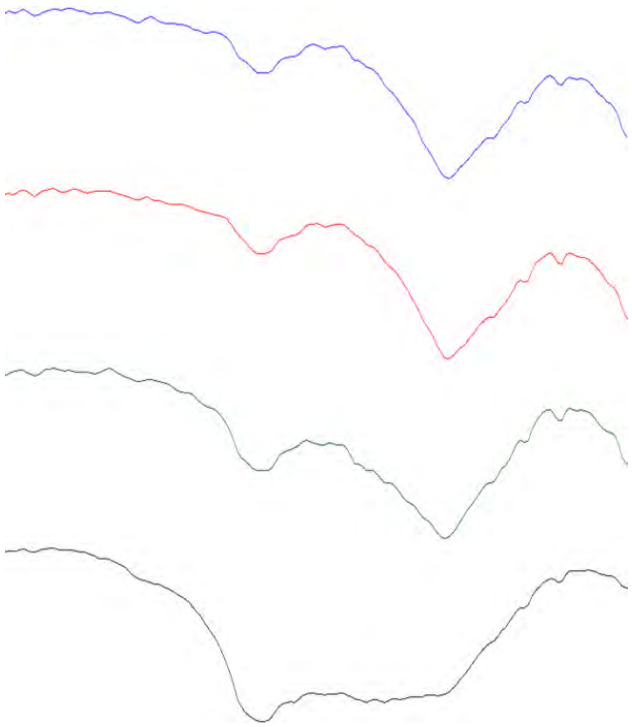

Figure 23B: Infrared Spectra for the photo-oxidized samples of 0.5 mL bitumen on water left under their respective conditions for 3 h focussed on the 1750-1500 cm^{-1} region. Bitumen left in the dark (blue), bitumen left under the growing light (red), bitumen left under the sun (green), and the bitumen "film" which formed on top of the water layer in the sun sample (black).

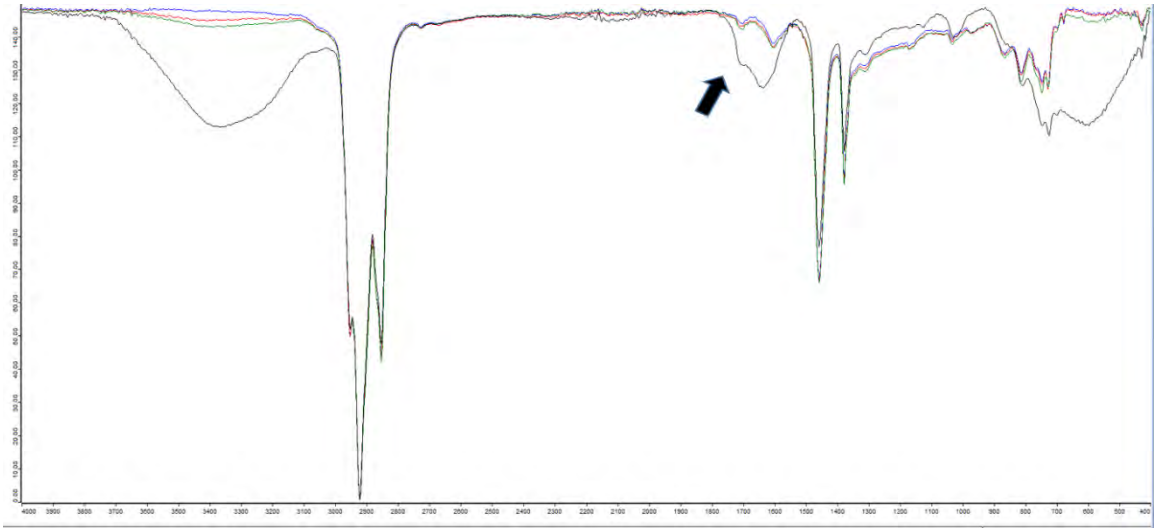

Figure 24A: Infrared Spectra for the photo-oxidized samples of 1.0 mL bitumen on water left under their respective conditions for 3 h. Bitumen left in the dark (blue), bitumen left under the growing light (red), bitumen left under the sun (green), and the bitumen "film" which formed on top of the water layer in the sun sample (black). Large peak at ~3400 cm^{-1} attributed to volatile OH-containing species and/or water.

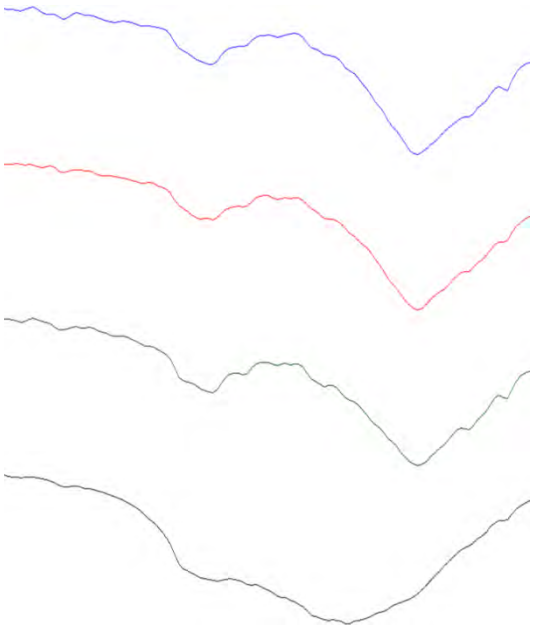

Figure 24B: Infrared Spectra for the photo-oxidized samples of 1.0 mL bitumen on water left under their respective conditions for 3 h focussed on the 1750-1500 cm^{-1} region. Bitumen left in the dark (blue), bitumen left under the growing light (red), bitumen left under the sun (green), and the bitumen "film" which formed on top of the water layer in the sun sample (black).

Since other techniques were not available, Nuclear Magnetic Resonance (NMR) was used to try and find differences between the light, dark, sun and film samples. Only the 0.5 mL samples were dissolved in $CDCl_3$ and measured with ^1H NMR (calibrated with TMS); other methods were also run later for selected samples. The spectrum of the original AWB bitumen has also been included for comparison purposes.

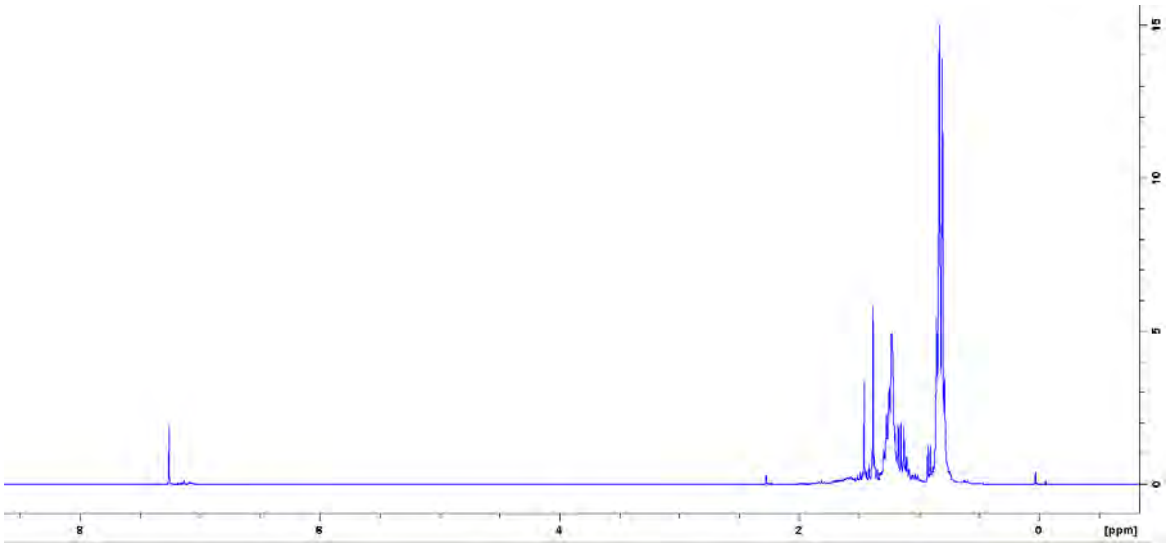

Figure 25: ^1H NMR spectrum of unaltered AWB bitumen, run in $CDCl_3$.

The NMR spectrum of the AWB bitumen shows signals arising from aliphatic protons in the region from 0.7 - 1.5 ppm. The large signal at 0.8 ppm is thought to arise from aliphatic CH_3 groups, most likely from straight chain alkanes,[31,32] while the signals in the range from 1.2 - 1.5 ppm are likely from the CH_2 groups of aliphatic rings.[31,32] A signal attributable to water is not observed in the unaltered sample (1.56 ppm), which indicates that the water in the experimental samples is likely from the bitumen sitting on the water surface. There is a very small region of signals at 7.00 ppm assigned to aromatic compounds, though it is difficult to see in this spectrum next to the $CDCl_3$ peak at 7.26 ppm.

The ^{1}H NMR spectrum of the experimental dark sample (Figures 26 and 27) is very similar to the spectrum of AWB bitumen (Figure 25 above). The main difference observed was a reduction in the signal heights in the dark sample. Signals are no longer observed at 1.45, 1.38, or 1.16 ppm, which can be explained by a loss of resolution. The peaks are broader in the dark sample, likely due to its exposure to the water. It is also possible that some compounds have actually leeched completely into the water layer from the bitumen. This would also cause the same type of discrepancies between the spectra of the unaltered AWB bitumen and the dark sample.

The experimental samples had quite similar spectra, however, there were a few notable differences (Figures 26, 27, and 28). A small peak was observed next to the TMS peak, 0.08 ppm, in the dark and light samples. This peak was not present, however, in either the sun or sun film samples. This peak has been attributed to terminal aliphatic CH_3 protons,[31,32] which might help to explain why it is present in the samples that have undergone less photo-oxidation. If this terminal CH_3 is a potential site of oxidation, to form aldehydes and carboxylic acids, then it should decrease in intensity upon exposure to sunlight. It is important to note, however, that silicone grease in $CDCl_3$ also gives rise to a signal with this chemical shift, although exposure to this contaminant is unlikely.

There was a general decrease in the signal intensities in the sun film sample, relative to the spectra of the other samples, but this may just have been attributable to it being more dilute than the other thee. An integration of the signals, with the broad doublet at 0.9 ppm calibrated to 1 in all of the spectra, confirmed that this was just a dilution issue.

The next difference between the spectra was a broad signal which was observed in only some of the samples at 1.62 ppm. This signal is heavily reduced in the sun sample, with respect to the dark and light samples, to the point that it is almost indistinguishable from the baseline in the sun spectrum. In the sun film sample, however, the same signal has been shifted upfield slightly to 1.59 ppm and is significantly greater in intensity in comparison to the other samples. This peak has been attributed to the presence of water (which appears at 1.56 ppm in $CDCl_3$). The sun sample no longer contains this signal as the water giving rise to it has been separated out when the film layer was removed. This matches the results from the IR runs (Figure 23 and 24), where a broad ν(OH) peak was observed in the film spectra. There is still the potential that this signal is associated with the formation of oxidative products (alcohols). However, integration of the peaks in the film spectra shows that this peak does not arise solely from the formation of alcoholic products. It remains more likely that it is attributable to the presence of water in the sample.

The last major difference between the samples is the observation of a signal at 4.41 ppm which varies in intensity. This signal is usually rather small and broad. It is not observed at all in the dark spectrum or in the bitumen sun spectrum. In the light sample it is small, while in the sun film spectrum, where it has been shifted downfield to 4.60 ppm, it is significantly larger. The difference in the integration of the film sample signal compared to the light signal is a factor 40. The fact that the signal is not observed in the sun sample, is again unsurprising, it was likely removed when the film was separated from the bulk sun sample. A signal with a chemical shift of roughly 4.5 ppm has been attributed to the presence of alcohols, phenols, and aromatic ethers in the bitumen

literature.[31,32] Our results suggest that sunlight and the growing light are both able produce such compounds in the bitumen samples. The growing light sample, however, has a significantly smaller signal compared to the film sample as the growing light is not as intense as direct sunlight. This signal does not appear in the NMR of the dark sample suggesting that it did not contain, and has not formed, any of these compounds.

Furthermore, these hydroxyl and alkoxyl compounds must separate from the non-polar bitumen upon reaching a high enough concentration, a level that was not achieved by the growing light in the experimental timeframe. These hydroxyl and alkoxyl compounds migrate to form the film on the surface of the water which was isolated from the sun sample. The fact that this signal is not present in the sun sample spectrum further emphasises the idea that polar compounds formed in the sun sample have separated out of the bitumen and into the film. Although there are more hydroxyl and alkoxyl containing compounds within the film, compared to the other samples, the NMR of the film still reveals that much of its composition must still be non-polar bitumen, being largely unchanged relative to the other spectra. This furthers the previous idea that the film is a potential surfactant. It has too many polar compounds to be fully miscible with the bitumen layer, but it also has too many non-polar compounds to be fully miscible with the aqueous layer.

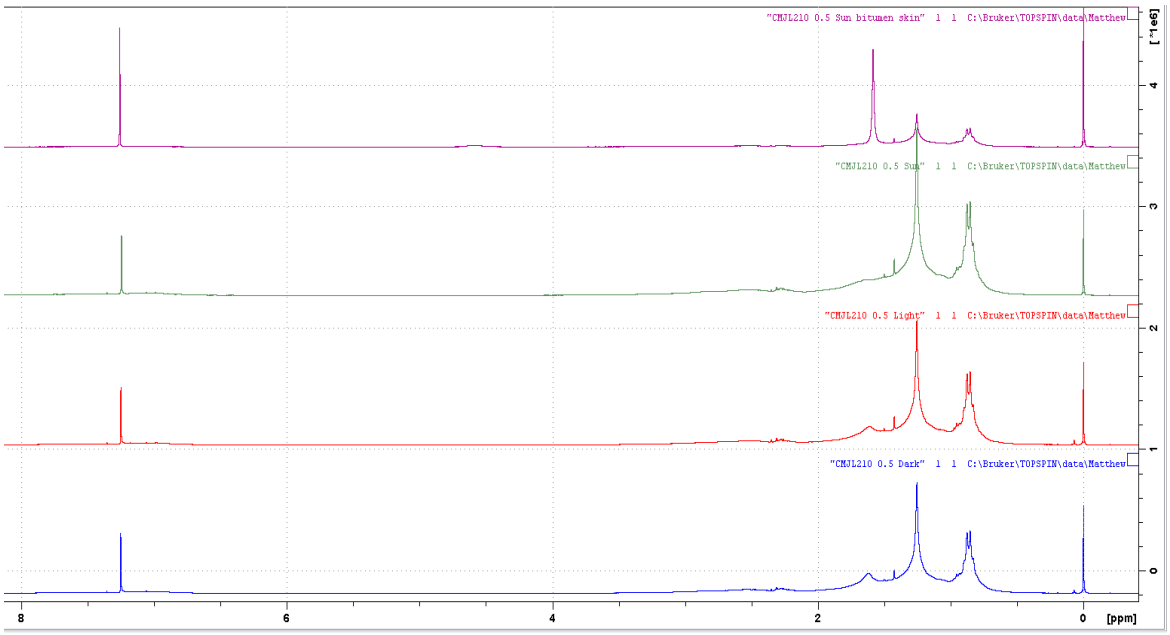

Figure 26: ^{1}H NMR Spectra for the samples of photo-oxidized bitumen on water left under their respective conditions for 3 h. Bitumen left in the dark (bottom), bitumen left under the growing light (middle bottom), bitumen left under the sun (middle top), and the bitumen "film" formed on top of the water layer in the sun sample (top).

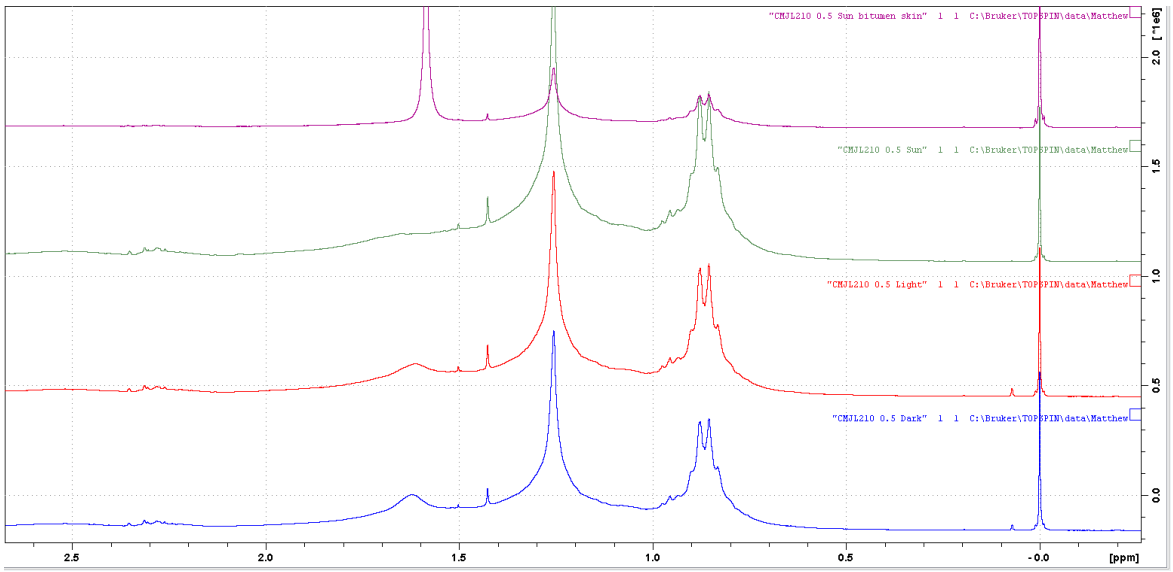

Figure 27: ^{1}H NMR spectra showing expansion of the 0.0 - 2.5 ppm chemical shift range for the photo-oxidized samples of bitumen left on water under their respective conditions for 3 h. Bitumen left in the dark (bottom), bitumen left under the growing light (middle bottom), bitumen left under the sun (middle top), and the bitumen "film" formed on top of the water layer in the sun sample (top).

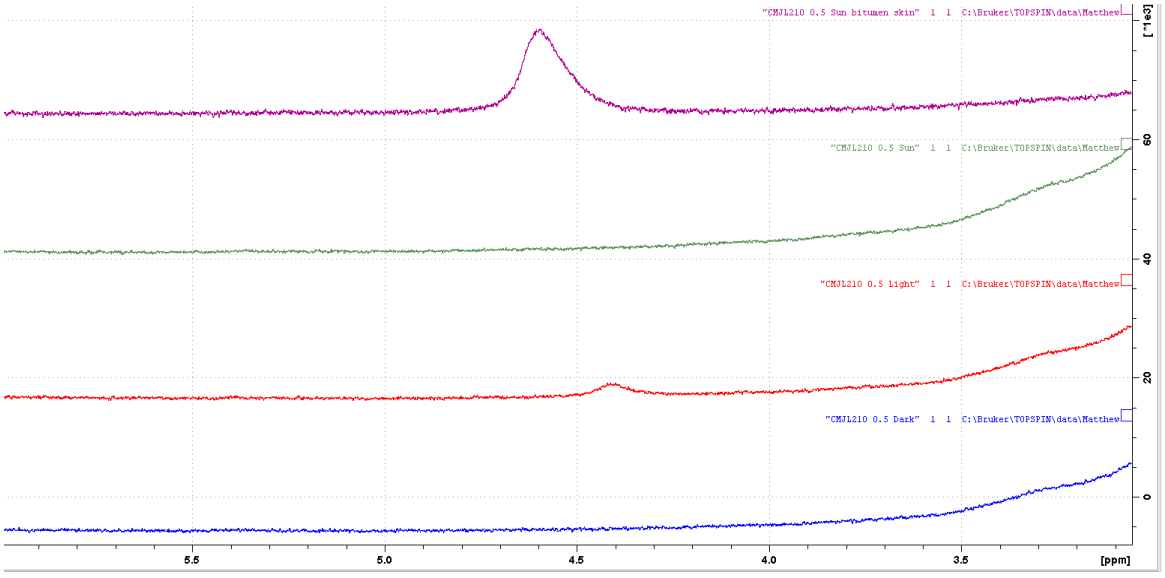

Figure 28: ^{1}H NMR spectra showing expansion of the 3 - 6 ppm chemical shift range for the photo-oxidized samples of bitumen on water left under their respective conditions for 3 h. Bitumen left in the dark (bottom), bitumen left under the growing light (middle bottom), bitumen left under the sun (middle top), and the bitumen "film" formed on top of the water layer in the sun sample (top).

Experiment Four

Another experiment was run in a similar manner to the AWB bitumen on water experiments. For each sample, 2 mL of water was added to a quartz cuvette (so that UV light would not be obstructed), followed by 0.05 mL of AWB bitumen layered carefully onto the water surface. 10 identical samples were made and 9 of those were placed into the sun, while one was stored in a separate dark location where it was kept as a control. The intensity of the sun was recorded thoughout the experiment (Figure 29). Seven samples were sealed off from the air with rubber septa to keep the headspace unchanged (one of these was the dark control) and thee were left open to the air. The 6 sealed samples were kept in the sun for varying amounts of time as a way to measure the rate of photo-oxidation. They were removed from the sun exposure in 30-min increments such

that the total experiment took 3 hours. The thee open to air samples were removed in 1-hour increments and sealed with rubber septa for storage until the next experiment. The samples were kept sealed until the head space analyses could be carried out using Solid Phase Microextraction (SPME, see section 4) (Figure 30). Afterwards, the IR spectra of the samples were recorded, and those samples showing major differences were additionally studied using ^{1}H and/or ^{13}C NMR.

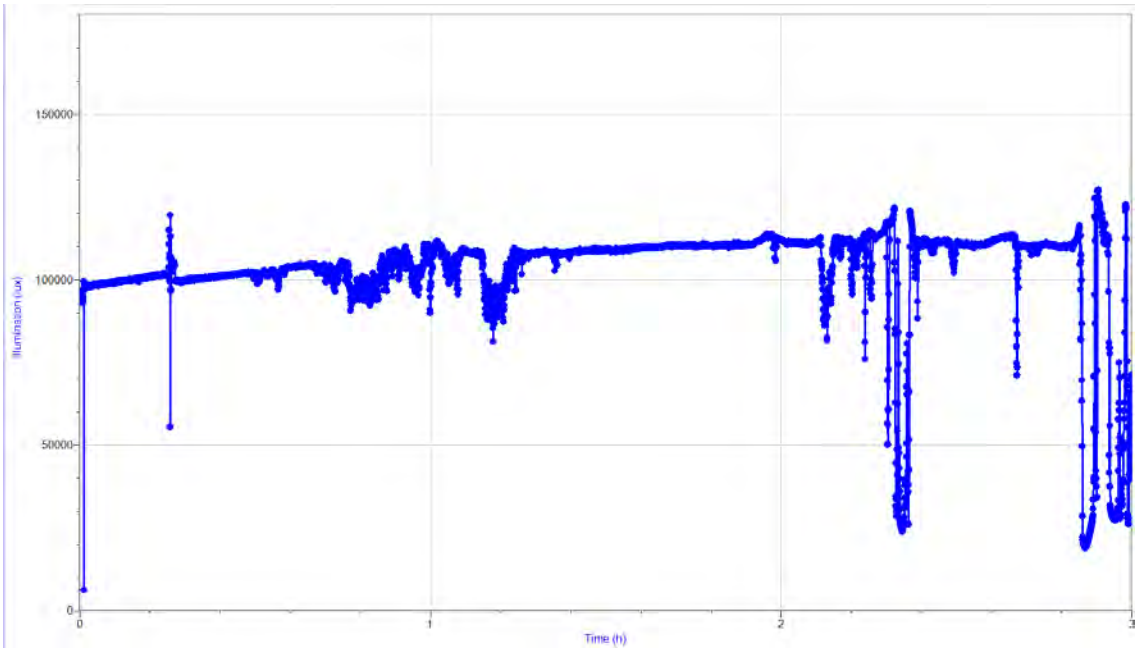

Figure 29: Measurement of the recorded intensity of the sun (in Lux) for the quartz cuvette experiment.

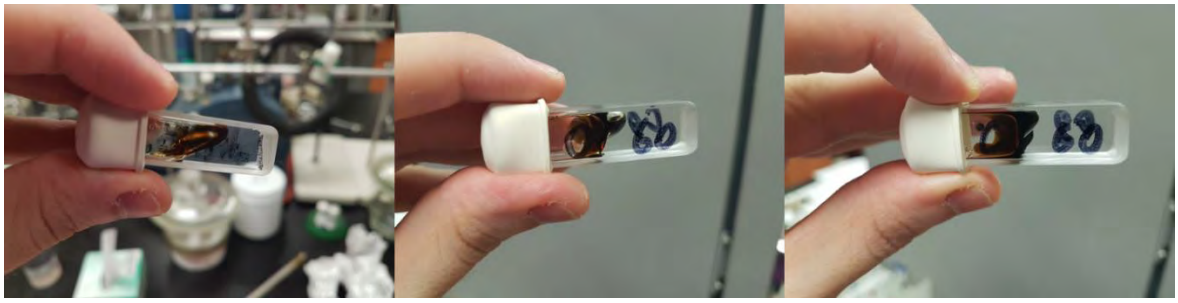

Figure 30: Visual comparison of bitumen on water samples photo-oxidized in the sun. Bitumen control left in the dark (left), bitumen open to the air and in the sun for 60 min (middle), bitumen sealed and in the sun for 60 min (right).

SPME of the samples (see section 4) revealed that they had been inconsistently oxidized. This was further supported by the ^{1}H NMR spectra of the samples, which showed signals of varying intensities at ~4.8 ppm (Figures 31-34). Signals in this region are often assigned to petroleum ethers and oxidative products within bitumen and heavy oils.[32] Figures 31 and 32 show the bitumen samples that were exposed to the atmosphere. There is next to no difference in the aliphatic region of the spectra compared to the dark control sample, but there are signals present at 4.8 ppm in all thee spectra. The signal at 120 min is difficult to see, as it is broad on the scale used in Figure 32, but it is present at 4.9 ppm. The size of these signals steadily increases with time, with that at 180 min being the largest, suggesting that more of these products form with longer sun exposure. An integration of the signals, with the broad doublet at 0.9 ppm calibrated to 1 in all of the spectra, showed that the peak at 4.9 ppm increased substantially with each hour, from 0.015 at 60 min, to 0.021 at 120 min, and 0.068 at 180 min.

Figures 33 and 34 show the spectra of the bitumen samples that were sealed from the atmosphere. There is next to no difference in the aliphatic region of the spectra compared to the dark control sample, but there are quite different signals present at 4.8

ppm in most of the spectra. In Figure 34, a signal is present at 4.8 ppm in the 90-min spectrum, but it is small and broad on the presented scale. A broad signal is also present in the 30-min sample at 5.1 ppm which is difficult to distinguish on the presented scale. This is likely evidence of inconsistent photo-oxidation in these samples. For example, the 90- and 180-min spectra have small signals in this region, while the 60- and 150-min spectra have much larger signals. An integration of the signals, with the broad doublet at 0.9 ppm calibrated to 1 in all of the spectra showed wildly varying intensities of the signals in the 4.9 ppm region: 180 min had the smallest signal with an integration of 0.007, while 150 min had the largest with an integration of 0.122. This discrepancy may have arisen because some samples received more sunlight than others, creating varying degrees of photo-oxidation within the series. These samples were sealed inside quartz cuvettes as it was thought quartz would not block the UV light like glass does. This, however, does not seem to have been the case, instead the septa used appear to have stopped sunlight from reaching the bitumen, in varying amounts depending on their position. It is unknown why the signal at 4.9 ppm is shifting position with the varying time intervals, or why it is changing in breadth, but this is likely related to the amount of water present in the sample. Again, these are the same samples used in the SPME analyses (in the following section) and the inconsistent photo-oxidation likely affects those results as well.

It was not noticed if a film appeared in this experiment, as it had in the previous experiment, since it was conducted in a quartz cuvette. The surface area of the water layer was much smaller compared to that area in the scintillation vial, in which the film was

discovered. If such a layer was generated, it may not have had enough room to separate from the bulk bitumen in the cuvette.

In our samples these signals of interest did not increase steadily with time, instead they appeared after the 90 min mark and inconsistently at that. For instance, a large signal was observed in the spectrum of the sample sealed for 150 min, but not in that of the sample sealed for 180 min. The 180 min sample that was open to the atmosphere also had a strong signal in that region. In this experiment, the samples were setup in a circular configuration around a central stand, so some samples were probably exposed to more sunlight than others. This might explain why the NMR results were inconsistent and why the samples in this experiment were not observed to form “films” under circumstances where they had in the previous experiment. If the samples did not get consistent light from the sun relative to each other, they would have behaved differently, thus leading to the inconsistent results being observed. It was believed that performing these experiments at midday would help to average out the amount of sunlight each sample was exposed to. This is also why quartz vessels were chosen for the experiments, as it would not block the UV light like glass would. This, however, does not seem to have been the case. It appears that samples that were left uncovered, with an unobscured top, directly facing the sun were the most photo-oxidized; therefore, these results other than producing the SPME samples, should not be over interpreted. These inconsistent results should also be remembered when examining the SPME data since it too was generated from these samples.

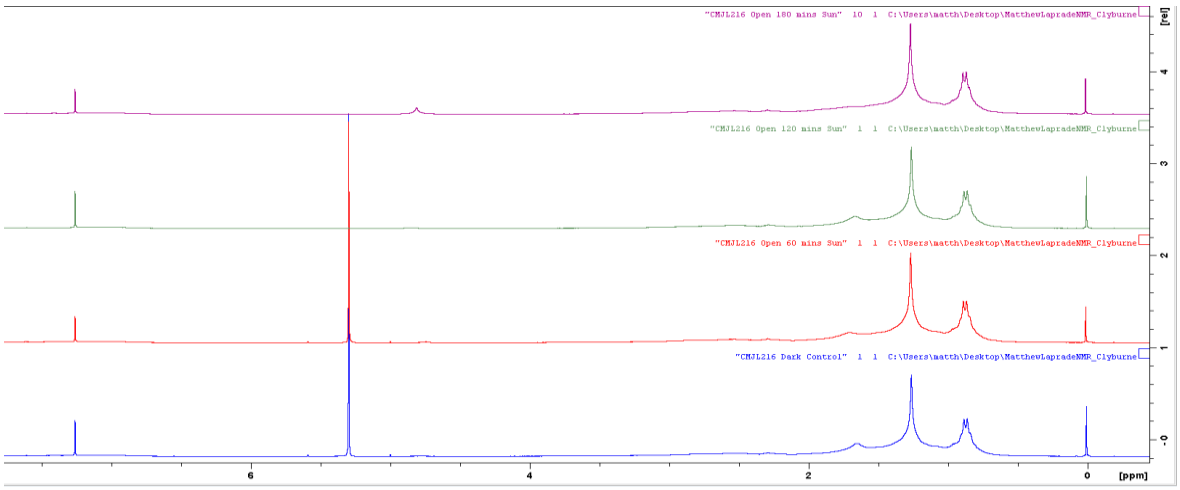

Figure 31: ^{1}H NMR spectra for Section 3 experiment 4, open to air samples. Bitumen left in the dark (bottom), bitumen open in sunlight 60 min (middle bottom), bitumen open in sunlight 120 min (middle top), bitumen open in sunlight 180 min (top). The large peak at 5.3 ppm in the bottom two spectra are attributed to DCM contamination.

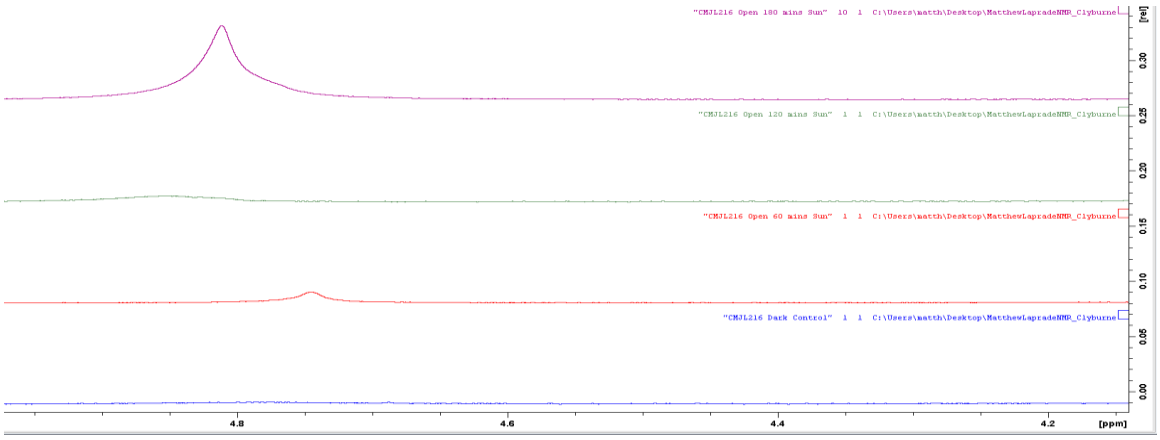

Figure 32: ^{1}H NMR spectra for Section 3 experiment 4, open to air samples showing expansion of the 4-5 ppm region. Bitumen left in the dark (bottom), bitumen open in sunlight 60 min (middle bottom), bitumen open in sunlight 120 min (middle top), bitumen open in sunlight 180 min (top). A peak is present at 4.8 ppm in middle top spectrum, but it is very broad and hard to distinguish at this scale.

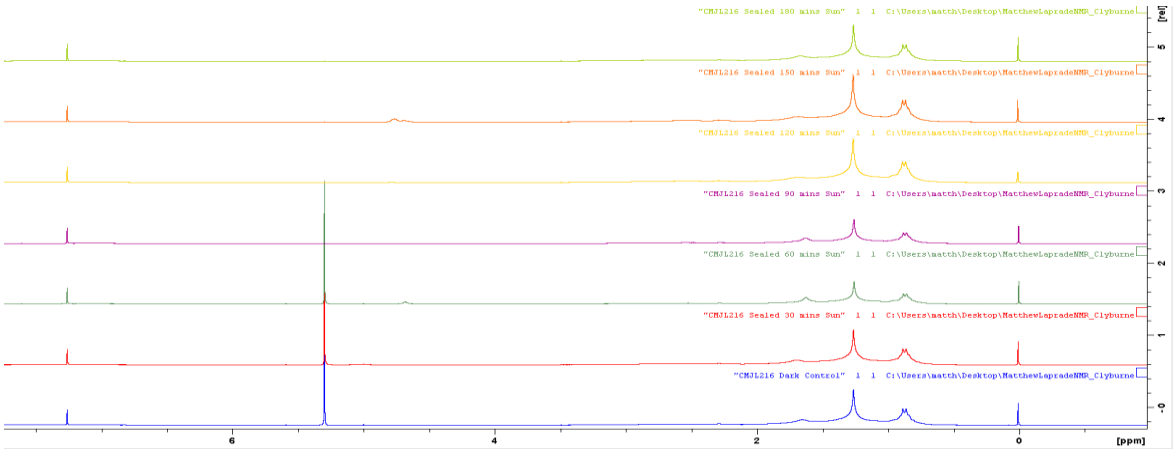

Figure 33: ^{1}H NMR spectra for Section 3 experiment 4, sealed to air samples. Bitumen left in the dark (bottom), bitumen sealed in sunlight samples increasing by 30 min internals from bottom to top until final time of 180 min. The large peak at 5.3 ppm in the bottom two spectra are attributed to DCM contamination.

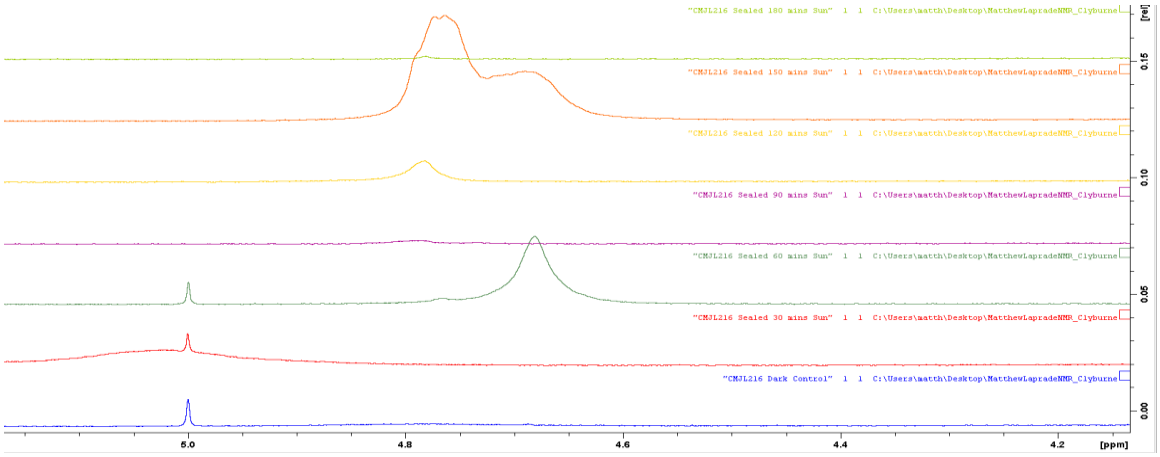

Figure 34: ^{1}H NMR Spectra for Section 3 experiment 4, sealed to air samples expansion of the 4-5.5 ppm region. Bitumen left in the dark (bottom), bitumen sealed in sunlight samples increasing by 30 min internals from bottom to top until final time of 180 min. The peak at 5.0 ppm in the bottom thee spectra are attributed to satellite DCM contamination. A peak is present at 4.8 ppm in the 90-min spectrum, but is small and broad at this scale. There is a broad peak in the 30-min sample at 5.1 ppm which is difficult to distinguish at this scale.

The results of these experiments show that bitumen layered on a water surface can be photo-oxidized. Exposure to water alone (no light) caused the bitumen to change its physical properties, where it expanded and became “gel-like”. In combination with a

period of photo-oxidization, for as short as 3 hours, this effect was not observed. Instead, the bitumen formed smaller droplets that dispersed though the water upon agitation. The LC-MS data did show that there was some hydrocarbon leeching into the aqueous layer. Some compounds were eluted just after the solvent peak in the light samples but not in the dark ones. The peaks appeared before the 5-min mark, indicating that they were polar in nature, which is possible evidence for photo-oxidation having occurred on exposure to light. This being said, the data did not provide any information useful for compound identification because of a lack of resolution between the signals.

It was observed that exposure to sun light, for a period of 3 hours, caused some of the bitumen samples to form a thin film on the surface of the water layer. The fact that the film separated from the overall non-polar bitumen indicated that it must be more polar in nature. This was confirmed by the spectroscopic data, as the film samples did have much larger signal strengths in the 1700 cm^{-1} C=O region of the IR spectra, which was being monitored for evidence of oxidation. In the ^{1}H NMR spectrum the same sun film sample showed a relatively large signal at 4.6 ppm that was attributed to the presence of polar molecules such as alcohols and ethers. It is believed that this film was too polar to remain in the non-polar bitumen, thus separating from it. However, the film must also have been too non-polar to mix with the aqueous layer, which is why it remains on the surface and recollects after being dispersed by agitation.

Section 4: The determination of volatile components in Bitumen using Solid Phase Microextraction

Experiment One

This experiment was aimed to determine what volatile compounds might be present in the photo-oxidized bitumen samples. It was devised as these compounds were not leeching into water, and it was thought that they might instead be escaping into the gas phase. About 15 mL of AWB bitumen was placed in a round bottom flask. This flask was connected to a fractional distillation apparatus (joints sealed with H_2SO_4) and then boiled at 100°C. Gas fractions from the flask were collected at 5-min intervals. This was done using 15 mL round bottom flasks which were attached to the apparatus after the condenser sequentially over each time interval. Once a given time interval had elapsed, the flask was detached and immediately sealed with a glass stopper and Parafilm. For the first 10-15 min, the bitumen sample boiled heavily. After this time, the bubbling became much less violent and nothing occurred again until the 30-min mark when the entire apparatus became filled with smoke. This lasted for 5-10 min before it dissipated, after which nothing notable occurred for the remainder of the collections. Once the last sample had been collected at 50 min, the bulk bitumen was cooled and sealed. All of the collected samples were covered in aluminum foil and stored at 8°C.

Each individual sample was taken up using the standard SPME technique[33] and measured with GC-MS to determine the composition of its gaseous phase. The headspace samples were diluted 1:40 with air. This was done by piercing the septum covering the samples with a needle and glass syringe, taking in 0.5 mL of the headspace gas and

depositing it into a 20 mL flame dried scintillation vial though a valve cap. The samples were allowed to thermally equilibrate at 35°C with a water bath. The SPME fiber was inserted though the cap valve of the vial where the diluted headspace gas was allowed to adsorb onto the SPME fiber for 2 min at 35°C. GC-MS samples were run as detailed in the techniques section. Traditionally, GC-FID is used for the determination of petroleum samples. This detection method, however, was not available at the time this experiment was carried out.

Peaks were compared to those from a blank fiber to determine which peaks were caused by sample and which were noise from the fiber. Once those peaks had been eliminated, the remaining peaks were analyzed using their resulting mass spectra. These spectra were compared to the NIST 2017 Mass Spectral Library[34] to best determine possible structures for the compounds present. Compounds were selected based on their R.Match values, which is a measure of how closely the experimental data[ii] matches a mass spectrum from the database. A manual comparison between the database and the experimental data was carried out, by comparing relative peak intensities, the base peaks, and prominent peak fragments. Matches from the database were discounted if they possessed a peak fragment that was not present in the experimental data. This search was limited, however, as the Varian 3800 Gas Chomatograph coupled to a Varian 2000 Ion Trap Mass Spectrometer that was used for the experiment, was unable to detect any compound fragments below 50 atomic mass units (amu). This made the determination of chains of thee carbon atoms or smaller impossible, and thus many potential compounds may have been missed. Also, peaks were chosen based on their listed Retention Index

[ii] Any R.Match value above 800 is considered a probable match for the compound. Any value above 1000 implies that is it almost definitely that specific compound.

(RI) in the database. The RI had to be searched in increasing order, so any compounds that had smaller RIs than the previously determined compound were not identified. The fractional distillation samples were all analyzed using this method, with 10 samples run in total. All samples were clean, with no visible residue from the boiling AWB bitumen, including for the fractions that started to build smoke. All samples were analyzed with SPME and common compounds found in all of the runs were compiled in Table 2.

Short chain alkanes of six or less carbon atoms were the most common components distilled from the bitumen (noting again that compounds of less than 50 amu could not be detected in this experiment). Across all of the fractionated samples, a handful of components consistently appeared (Table 2). These components could be used as internal standards to help identify additional compounds, found in individual runs, from their retention times and fragmentation patterns. The compounds in Table 2 are those that were identified as being present thoughout all fractional trials (unless otherwise noted). These are important, as by following their GC retention times, they could be used as markers in the bitumen trials to help disqualify other compounds. For instance, if two compounds had been tentatively identified in a sample using the NIST 2017 Mass Spectral Library,[34] the retention indices (RI)[iii] of the compounds would be compared to make an educated guess as to which of the compounds would be more likely to be present. By comparing these retention indices to the retention indices of the compounds in Table 2, a potential compound could be disqualified if it eluted too quickly or slowly compared to the compounds in Table 2.

[iii] The retention index of a chemical compound is its retention time normalised to the retention times of adjacently eluting n-alkanes. This value is independent of the specific retention time of the compound, which varies with the individual chomatographic system. The retention index increases linearly, such that compounds with a higher retention index will take longer to elute than a compound with a lower retention index.

Table 2: Compounds and their retention times identified by GC-MS after fractional distillation of AWB bitumen

Determined Compound	Average Retention Time (min)	Base Peak (amu)	Average R.Match Value[†]
2,2-Dimethyl butane	1.4	57	820
2-Methyl pentane	1.7	71	853
Methyl cyclopentane	2.1	56	871
Methyl cyclohexane	3.2	55	858
Dimethyl disulfide[*]	3.6	94	912
p-Xylene[*]	5.3	91	865

*Compound is not present past 30 min of fractional distillation.

[†]Table entries are averaged as the R.Match value is specific to each individual mass spectrum.

The presence of dimethyl disulfide in some of the AWB bitumen fractions was unexpected. To confirm its presence, a simple distillation of 30 mL bitumen was conducted; this yielded ~7 mL of a colourless liquid which smelled strongly of sulfur. A procedure was adapted from the Canadian Conservation Institute Notes 17/5[35] to test for sulfur using lead acetate. One gram of lead acetate was added into a vial and dissolved in 10 mL water. To this, 2 mL of a 3% hydrogen peroxide solution was added. The resulting solution was heated with a blow torch until it reached about 60°C. A drop of the distilled colourless liquid was then added to the lead acetate solution. Upon addition, an immediate colour change to dark brown was observed before dissipating within 1-2 seconds. A few more drops of the colourless liquid were added and again yielded the same results. This confirmed the presence of sulfur within the bitumen sample.

The sulfur test and the compounds found in the SPME analysis of the gases evolved above boiling AWB bitumen (Table 2) are all consistent with its reported

composition in April 2019, the date that the sample was obtained.[36,37] The compounds listed in Table 2 are mostly short chain alkanes that might have come, at least primarily, from the diluent used in the preparation of AWB bitumen. The AWB dilbit averaged ~17.5% w/w of short chain alkanes on that date. This implies that the majority of the detected compounds came from the diluent used to reduce the viscosity of the bitumen. The short chain alkanes were observed, rather than heavier compounds, as they were more volatile and thus easier to detect with this method. On the same date, the AWB bitumen was reported to have a 3.8% w/w sulfur content.[36,37] Although the sulfur test conducted here was not useful for a quantitative determination, it did confirm the presence of sulfur in the AWB bitumen sample.

Experiment Two

A second set of samples were tested using SPME. The AWB bitumen samples used were those from Section 3; their ^{1}H NMR spectra are given in Figures 30-34. All of these samples were handled and tested using the same method as described above for the samples from the fractional distillation of bitumen. The sealed samples were compared to the open to air samples to try and determine if photo-oxidation utilized primarily atmospheric oxygen or if it occurred though contact with water.

In this experiment, the 10 samples (both open and sealed) were all found to contain the same or similar compounds as those listed in Table 2. These compounds were also present across the entire 3 h experimentation range for the samples, though not necessarily all of them were present in all runs. Also conspicuous were the presence of

isomeric and derivative compounds related to those in Table 2. For example, o-xylene and 2,2,3-trimethyl-butane were common compounds identified in this sample set; both are isomers of compounds found in Table 2. This implies that during the process of photo-oxidation, compound fragmentation and methyl shifts occurred, resulting in the formation of such isomeric compounds. These could not have been generated during the mass spectrometry analysis, as they would then have been observed in the fractional distillation samples as well. This adds legitimacy to the compounds in Table 2, as they have been detected in two quite different experiments. The open and sealed samples also displayed similar data, which shows the inherit sensitivity of the SPME technique. It was believed a priori that the majority of volatile compounds would have been lost during the photo-oxidation of the unsealed samples, as there was nothing protecting the headspace of the samples. For the samples that were unsealed for the duration of the experiment, no oxidative products were observed to be eluted until after the 60-min mark. This is consistent with the photo-oxidation rate of bitumen that was experimentally determined in Section 2. Notable compounds identified in these runs are listed below (Table 3). A compound was selected as notable if it was not detected in the fractional distillation sample (Table 2). Furthermore, the compound had to possess a carbonyl functional group or be a compound with a functional group not present within the fractional distillation sample.

Table 3: Partial list of potential products identified by GC-MS from the photo-oxidation of bitumen in the unsealed samples from Section 3

Sample Reaction Time (min)	Determined Compound	Retention Time (min)	Base Peak (amu)	R.Match Value
120	1-Pentanol	3.5	70	907
180	1-Pentanol	2.6	70	791
180	1-Octene	2.8	55/70*	796
180	3-Hexen-2-one	3.3	55/83*	903
180	4-(1,1-Dimethylethyl)-benzenepropanal	9.6	175	843

*Samples with two base peaks listed have two base peaks of roughly the same intensity in the mass spectrum. Though only one base peak should be selected, the relative intensities were so close together that a singular assignment for the base peak was not possible. This resulted in more compounds than normal being flagged in the NIST 2017 Mass Spectral Library.

There are a few things to note about the potential oxidative products identified in the unsealed samples, as listed in Table 3. First, due to the method of determination, along with its limitations, instances like the double appearance of 1-pentanol in Table 3 occur. 1-Pentanol was identified in both the 120- and 180-min samples but with different retention times. This implies that one of the two has been incorrectly assigned. While the samples are internally consistent, as judged by their increasing RI values, they are not consistent between runs due to limitations of the GC-MS used. The error is likely associated with the Varian 2000 Ion Trap Mass Spectrometer that was used for the experiment, as it was unable to detect any fragments below 50 atomic mass units. This led to trouble identifying potential matches with the NIST 2017 Mass Spectral Library since these important smaller fragments were not available for mass spectral matching purposes. As discussed above, it was also noticed that some of the compounds listed in

Table 3 were either isomers or rearranged forms of compounds found in Table 2, *p*- and *o*-xylene being such examples.

Another thing to note is that 1-octene was tentatively identified in the 180-min unsealed sample. In the fractionally distilled bitumen samples, with the exception of aromatic compounds such as xylene, there were very few unsaturated hydrocarbons absorbed from the gas phase. They were either not volatile enough to be absorbed onto the fibre, or they were not present in the fractionally distilled sample. Their presence in the photo-oxidized samples implies one of two things. First, it is possible that these compounds were present within the bitumen, but required an increase in energy (such as supplied by the sunlight) enough for them to become volatile and observed in the second set of experiments. This, however, is unlikely to have been the cause as the same compounds should have also been volatilized in the fractional distillation experiment when the bitumen was boiled. If these compounds were not present in the original bitumen samples, this implies that they were formed chemically in the presence of UV light. They may have been formed by reduction when another compound was oxidized, or they might have formed from hydrocarbon fragments produced during the formation of CO_2. This also implies that lower molecular weight volatiles also form but these cannot be detected due to the limitations of the method. The presence of such unsaturated hydrocarbons is important regardless, and must be noted. In addition, Table 3 includes a variety of oxidized compounds as expected.

The last thing to note is that some of the compounds in Tables 2 and 3 are found with roughly the same retention times but have been given different assignments; methyl cyclohexane in Table 2 and 3-hexen-2-one in Table 3 are good examples of this. This

again is due to the errors associated with the GC-MS method. As fragments below 50 mass units were not observable, it was sometimes difficult to make accurate compound identifications. The 3-hexen-2-one in Table 3 does share a base peak with the methyl cyclohexane in Table 2, and the two could, in fact, arise from the same compound. The presence of a peak at 83 mass units, in the mass spectrum of the latter, led to the idea that the sample could be a mixture of products having the same retention time. 3-Hexen-2-one was selected to be more likely due to the strong RI value assigned from the database.

The headspace analyses of the sealed samples did show a significantly wider range of compounds to be present, relative to the unsealed samples and to the bitumen control, as expected. What can be immediately seen by comparing the data in Tables 3 and 4 is an increase in the number of compounds that elute after 5 min in the latter. With the bitumen control, the last consistently observed compounds that eluted were xylene isomers at 5.3 min. The sealed samples had compounds eluting up to 8 min in the GC-MS and the unsealed samples took up to 10 min. In this experiment, which was run over a longer time period, larger mass compounds and/or more non-polar compounds were able to enter the gas phase to be absorbed by the fibre.

For the most part, compounds identified in the samples with the shorter reaction times are not present in those from the longer times, and vice versa. This is an indication that the compounds that are oxidized early are either fully reacting to CO_2 during that time, or that they are leeching out of the bitumen layer. The compounds that are present later indicate that it does take more exposure to UV light for higher mass compounds to react, which explains why they are not observed in the lower reaction time samples.

Table 4: Potential products identified by GC-MS from the photo-oxidation of bitumen in the sealed samples from Section 3

Sample Reaction Time (min)	Determined Compound	Retention Time (min)	Base Peak (amu)	R.Match Value
30	Isopropylcyclobutane	2.8	55/70	924
60	3,4-dimethyl-1-Pentene	2.6	70	734
60	3-Hexen-2-one	3.3	55	910
60	Z-3,4,4-Trimethyl-2-pentene	4.1	97	822
60	2-Ethyl-bicyclo[2.2.1]heptane,	6.0	67	795
60	1-ethyl-4-methyl-benzene	6.5	67	927
90	3-Buten-2-ol	1.5	57	762
90	2,5,5-Trimethyl-1-hexene	4.8	57	772
90	1-Ethyl-4-methyl-benzene	6.5	105	896
90	(Z)-3-Dodecene	8.0	55	870
120	3,5-Dimethyl-1-hexene	3.4	57	774
120	3,3-Dimethyl-1-hexene	3.5	69	765
120	6-Methyl-1-octene	4.3	97	767
120	Mesitylene	6.5	105	815
150	Isopropylcyclobutane	2.8	55	898
180	Isopropylcyclobutane	2.8	55	927
180	1-Decene	8.0	55	874

What is also evident from the GC-MS data, but not depicted in Table 4, are the large number of isomeric compounds that are detected. This indicates that rearrangements may be taking place in the presence of UV light, possibly as a pre-measure before

oxidation occurs. Table 5 provides an idea of how prevalent these rearrangement reactions are within one bitumen sample. It includes all of the possible matches identified for the sealed sample that was removed after 90 min in the sun and analyzed.

Table 5: Complete list of potential products identified by GC-MS from the photo-oxidation of bitumen in the sealed 90 min sample from Section 3

Determined Compound	Retention Time (min)	Base Peak (amu)	R.Match Value
2,2-Dimethyl-butane	1.6	57	902
3-Methyl-pentane	1.8	56	837
Cyclohexane	2.5	56	695
1,3-Dimethyl- cyclopentane	2.8	70	931
Heptane	2.9	71	861
Methyl- cyclohexane	3.3	55	897
1,2,4-Trimethyl-cyclopentane	3.5	70	906
1,2,3-Trimethyl-cyclopentane	3.6	55	885
Cis-1,3-dimethyl-cyclohexane	4.1	97	774
1,1-Dimethyl- cyclohexane	4.2	97	838
Octane	4.3	85	844
2,6-Dimethyl- heptane	4.7	71	824

The results of these experiments show that SPME analysis can be used to identify volatile compounds in bitumen samples when coupled with GC-MS. Some compounds were consistently found in the samples, whether the bitumen was boiled or photo-oxidized, so these compounds could be used as potential internal standards. In addition to

the standard compounds, there were other, new compounds formed in the photo-oxidized AWB bitumen samples, notably 1-pentanol, 3-hexen-2-one and 1-octene. There were, however, some issues with the experimental method. The first was that the Varian 2000 Ion Trap Mass Spectrometer was unable to detect any compound fragments below 50 amu, so lighter compounds could not be identified. There was also an issue with consistency between samples, as seen from the varying retention times sometimes observed for the same compound identified in different runs. While the samples are internally consistent for their respective trials, as judged by their increasing RI values, they are not consistent between runs due to limitations of the GC-MS used. It was also noted that isomerization and fragmentation must occur during the photo-oxidation process. Finally, it was shown that the SPME technique is sensitive, as it was able to detect potential oxidative products from the samples that were left unsealed to the atmosphere during the experiment. It was thought that these samples would not yield results as any volatile products would disperse before the analysis; this proved not to be the case. With refinement of the method, SPME analysis should be a valuable tool for the detection of volatile compounds within bitumen samples.

Section 5: Gas-cell oxidations

Experiment One

Gas cell oxidation experiments were conducted to try and determine the extent of the photo-oxidation that could occur with bitumen. A quartz gas cell was sealed on both ends with NaCl plates and rubber washers. The gas cell was purged with dry nitrogen for a period of 2 min to remove any CO_2 (the IR spectrum of a gas cell containing only hemin is shown in Figure 35 as an example of a blank control). The cell was unsealed, and 1 mL of a bitumen sample [AWB bitumen (Figures 36 and 37), AWB bitumen weathered[iv] for a period of two weeks (Figures 38 and 39), or AWB Bitumen + 1% w/w hemin (Figures 40 and 41)] was dispensed into the gas cell. The cell was immediately resealed with the two NaCl plates and rubber washers. The IR spectrum of the sample was recorded after the infrared spectrometer had been purged with dry nitrogen for a period of 5min (this dry nitrogen atmosphere was taken as the background). An IR spectrum of each bitumen sample was taken at 0 min as a control. The gas cell containing the sample was then placed in the midday sun for 3 h. The intensity of the sunlight was also recorded over the course of the experiment. After this time, the infrared spectrometer was again purged with dry nitrogen gas, and the IR spectrum of the photo-oxidized sample in the gas cell was measured.

[iv] Weathered bitumen was prepared by taking AWB bitumen and leaving it exposed to open circulating air for a period of 2 weeks, giving time for any volatiles to escape. This sample was left in a dark place for the duration of the two weeks to minimize any potential photo-oxidation.

For these samples, the peak of interest in the IR spectra is the CO_2 peak centred[28] at 2340 cm^{-1} which arises from the asymmetric stretching vibration of the molecule. CO_2 typically gives rise to a strong signal in the infrared spectrum, which implies that the presence of even a small amount of generated gas will be detectable in these experiments. Another advantage is that the asymmetric stretching vibration of CO_2 gives rise to a signal in a region of the IR spectrum that is generally unpopulated; this reduces the chances of overlaps and false positives if this peak is monitored.

In all thee samples, it was observed that the CO_2 peak arising from the gas above the sample increased significantly in size with time compared to that in the initial sample (0 min). This suggests that some of the hydrocarbons within the bitumen are being oxidized all the way to CO_2 with prolonged exposure to sunlight, instead of only forming partially oxidized compounds. In this experiment, only the gaseous phase within the cell is being sampled, not the bitumen layer itself. This means that any partially oxidized compounds being formed in the bitumen (ν(C=O) at 1700 cm^{-1}) will not be observed in the spectrum, unless they are highly volatile and formed in significant concentrations. This experiment is thus primarily focussed on whether any of the hydrocarbons in bitumen are fully oxidized to CO_2. Such oxidation has previously been described by Ward *et al.*[12,13], who found that bitumen is photo-oxidized to CO_2 during oil spills, thus changing the bitumen's chemical composition slightly.

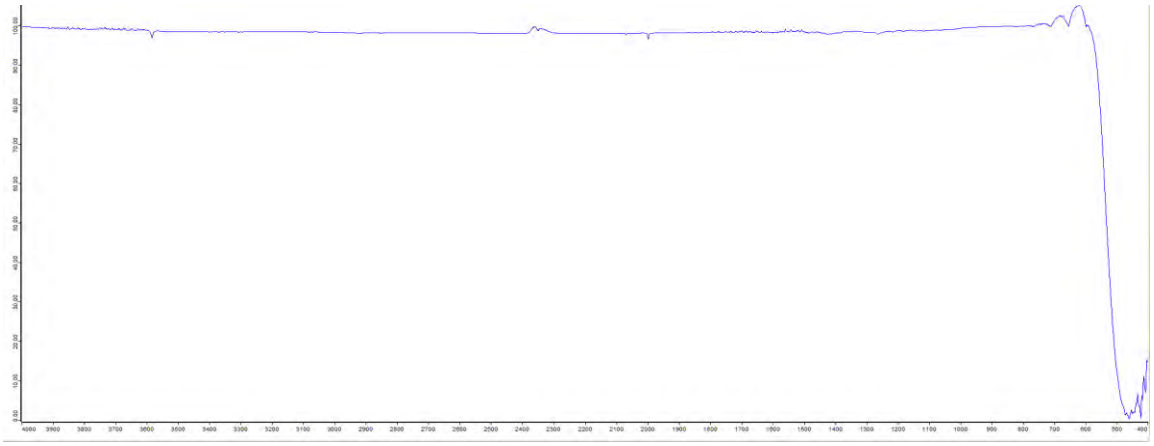

Figure 35: Infrared spectrum of a sample of hemin in a sealed quartz gas-cell after being exposed to sunlight for 3 h. The results show that neither hemin nor the presence of air within the gas cell has any effect on the spectrum recorded; in particular no peaks arising from the presence of atmospheric CO_2 are observed. The slight inverse peak in the CO_2 range is due to the purging of the infrared spectrometer with dry nitrogen gas.

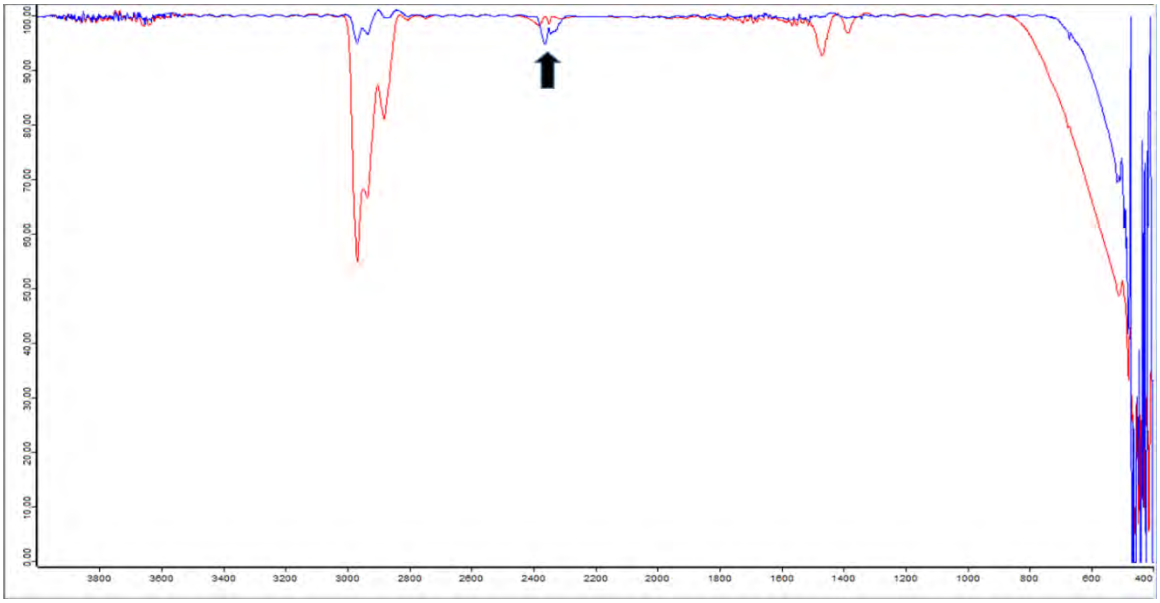

Figure 36A: Infrared spectra of the gases above a photo-oxidized sample of AWB bitumen run in a sealed quartz cell, before exposure to sunlight (red) and after being exposed to sunlight for 3 h (blue).

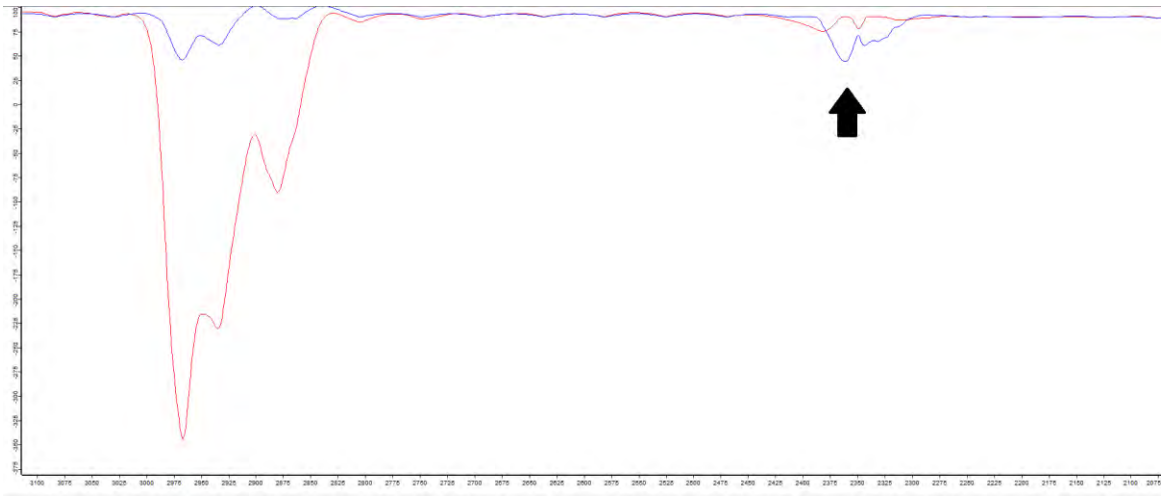

Figure 36B: Infrared spectra for the gases above a photo-oxidized sample of AWB Bitumen run in a sealed quartz cell focussed on the 2100-3100 cm^{-1} region, before exposure to sunlight (red) and after being exposed to sunlight for 3 h (blue).

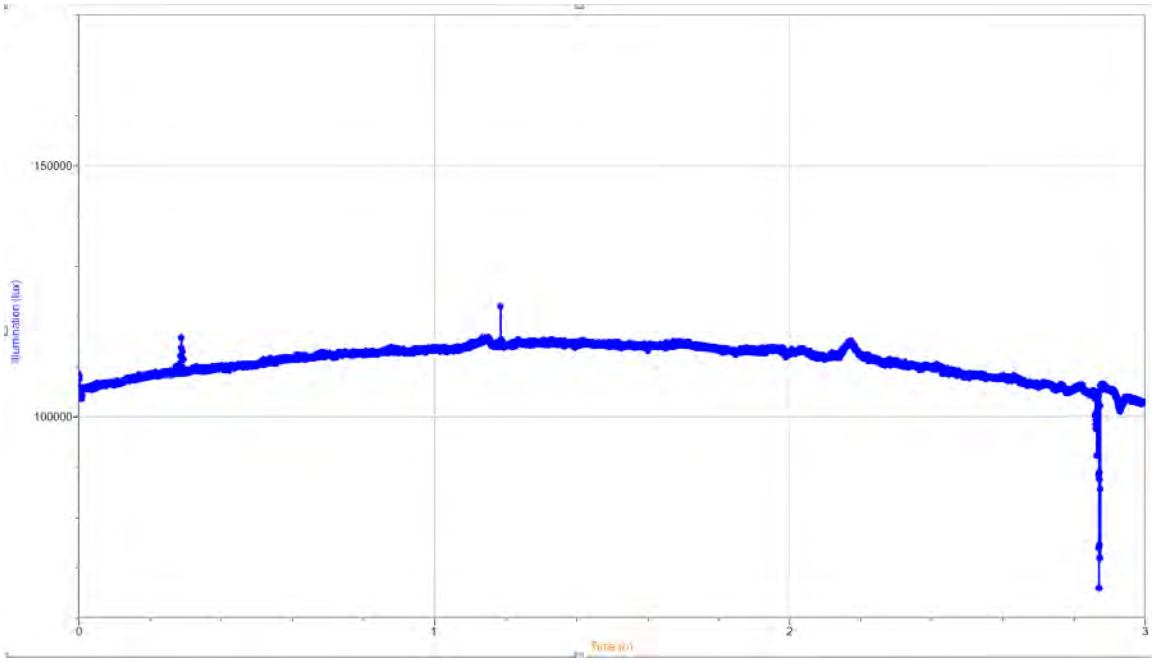

Figure 37: Measurement of the sun intensity (in Lux) recorded over the course of the gas cell experiment for the AWB bitumen sample.

From these figures, it is apparent that there is a striking reduction in the CH symmetric and antisymmetric stretching vibrations in the region of 2900 cm^{-1}, along with

that of the CH bending at 1500 cm^{-1}. This would indicate that volatile hydrocarbons are being oxidized to CO_2 over the 3-hour experiment. This is supported by the concomitant rise in the CO_2 peak in the 2300 cm^{-1} region. Another possible explanation for the dramatic drop observed in the CH peak intensity could be due to a possible leak in the gas cell, which would allow the volatile hydrocarbons to diffuse out. This would have to be accompanied by photo-oxidation of the sample, in order to explain the increased intensity of the CO_2 peak.

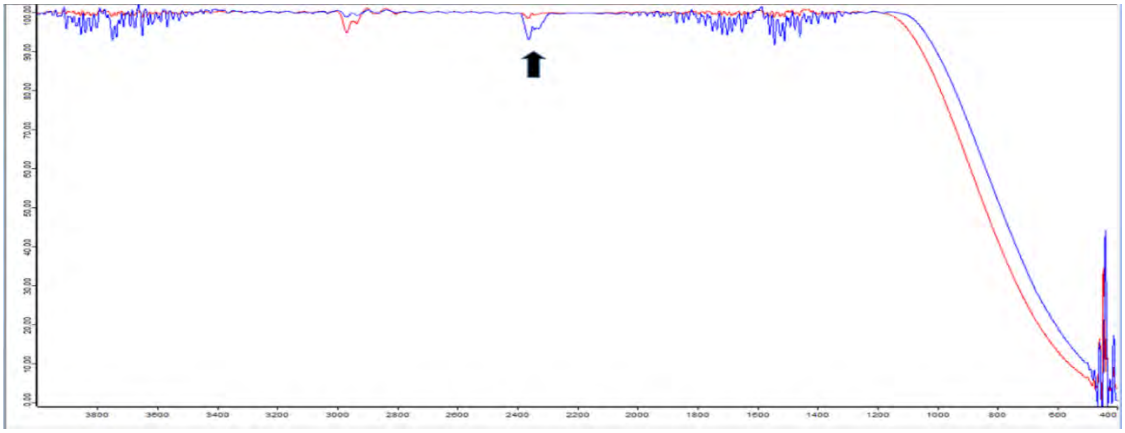

Figure 38A: Infrared spectra for the gases above a photo-oxidized sample of weathered AWB bitumen run in a sealed quartz cell, before exposure to sunlight (red) and after being exposed to sunlight for 3 h (blue).

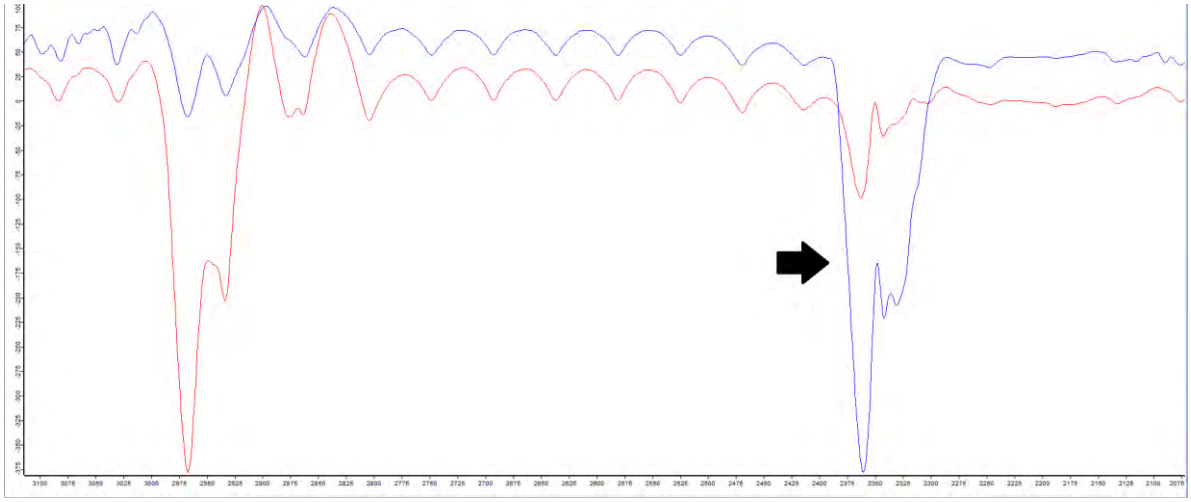

Figure 38B: Infrared spectra for the gases above a photo-oxidized sample of weathered AWB bitumen run in a sealed quartz cell focussed on the 2100-3100 cm^{-1} region, before exposure to sunlight (red), and after being exposed to sunlight for 3 h (blue).

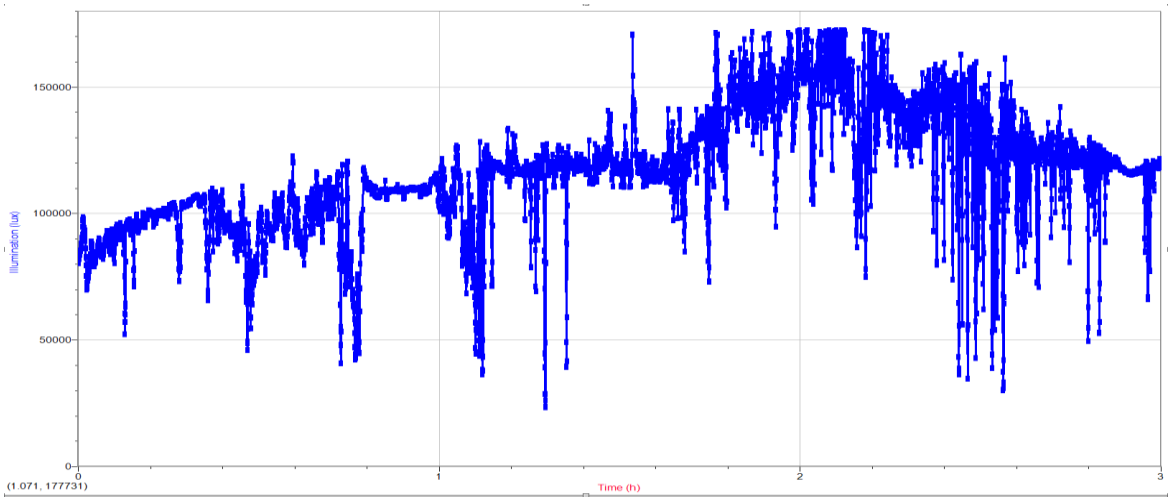

Figure 39: Measurement of the sun intensity (in Lux) recorded over the course of the gas cell experiment for the sample of weathered AWB bitumen.

From these figures, there is a slight reduction in the CH symmetric and antisymmetric stretching region at 2900 cm^{-1} after exposure of the sample to sunlight. These peaks are less intense than those in the spectra of the previous sample, which can be attributed to the fact this sample was weathered AWB bitumen. The process of weathering would have reduced the amount of volatile hydrocarbons within the sample,

which would have caused a reduction in the IR peak intensity in the CH stretching region. The reduction of the peaks in the CH stretching region was accompanied by an increase in the peak intensity in the CO_2 region. This suggests that there was also photo-oxidation to CO_2 over the course of this experiment.

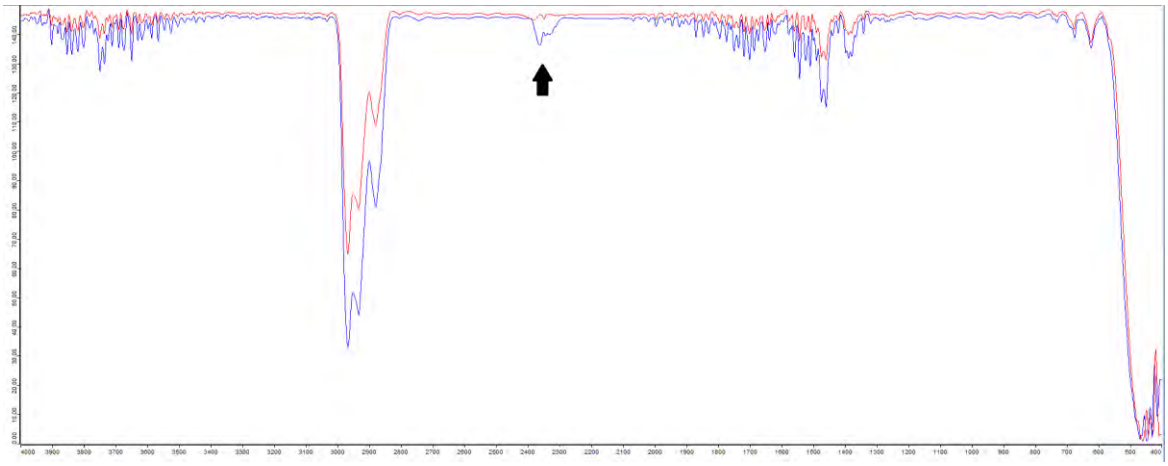

Figure 40A: Infrared spectra for the gases above a photo-oxidized sample of AWB bitumen mixed with 1% Hemin w/w run in a sealed quartz cell, before exposure to sunlight (red) and after being exposed to sunlight for 3 h (blue).

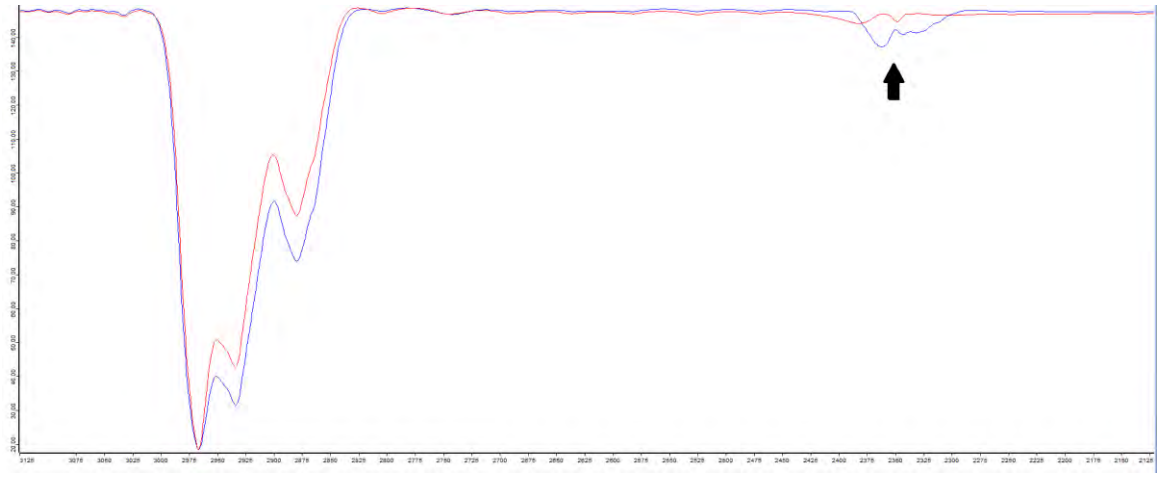

Figure 40B: Infrared spectra for the gases above a photo-oxidized sample of AWB bitumen mixed with ~1% Hemin w/w run in a sealed quartz cell focussed on the 2100-3100 cm^{-1} region, before exposure to sunlight (red) and after being exposed to sunlight for 3 h (blue).

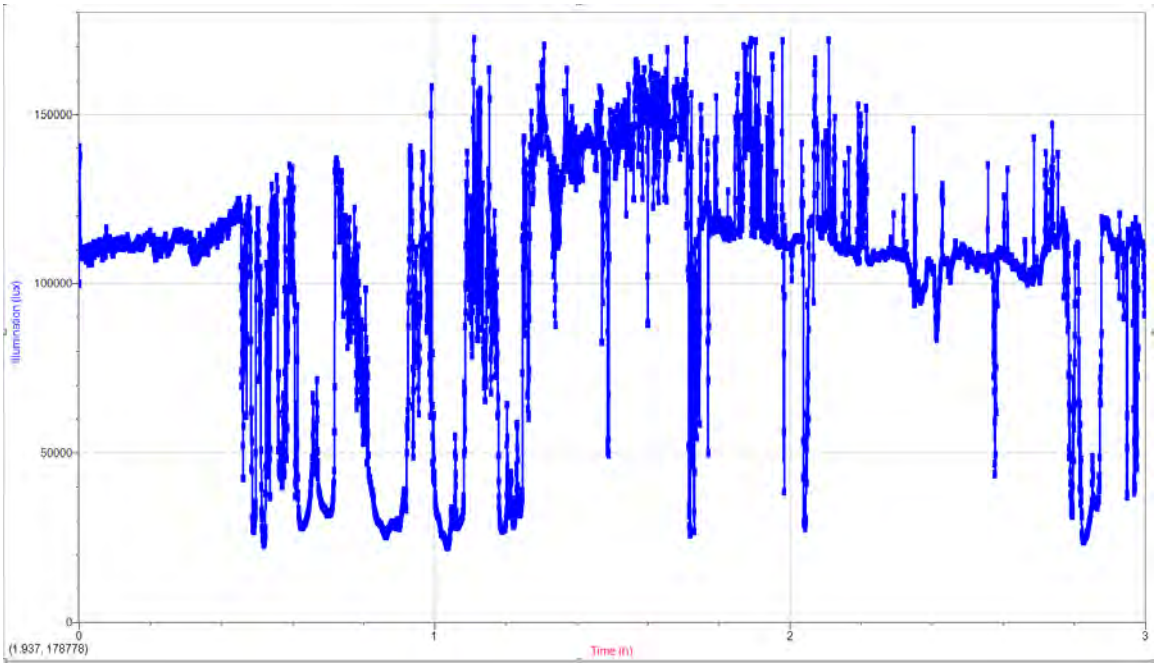

Figure 41: Measurement of the sun intensity (in Lux) recorded over the course of the gas cell experiment for the sample of AWB bitumen + ~1% Hemin w/w.

From these figures, it is unclear what is happening to the sample due to the presence of the added hemin. The CH stretching and bending regions of the IR spectrum grow in intensity after UV light exposure for 3 hs. This does not match the previous experiments which saw reduction of these peaks in the IR. Hemin itself has been shown not to react in the presence of UV light, so it is unlikely that it is decomposing to produce volatile hydrocarbons. There is a visible increase in the strength of the CO_2 vibration which does indicate that photo-oxidation has occurred. One possible explanation for this phenomenon could be that the presence of the hemin is causing the catalytic decomposition of non-volatile compounds in the bitumen, in the presence of UV light, forming more volatile hydrocarbon species.

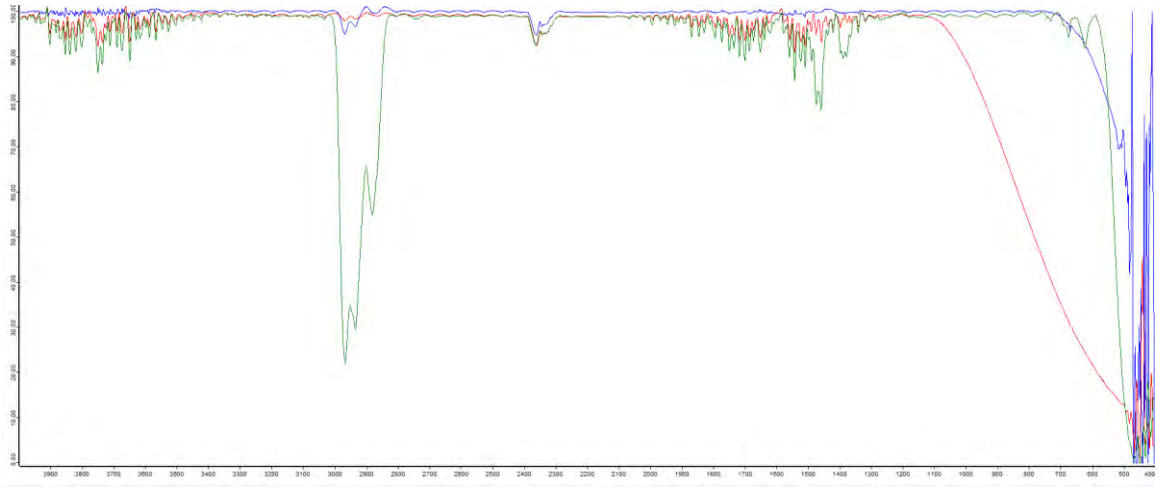

Figure 42: Infrared spectra for the gases above photo-oxidized samples of thee bitumen samples after 3 h of sun exposure, for scale comparison only: AWB bitumen (red), weathered AWB bitumen (blue), AWB bitumen + 1% w/w hemin (green).

The results from these trials make it quite clear that with exposure to UV light, hydrocarbons in bitumen are oxidized to CO_2. The oxygen required for this process to occur must come from the atmosphere. This conclusion has been drawn since the quartz gas-cell is a closed system, containing only atmospheric air and the dispensed bitumen. Once initially sealed, the IR spectrum was taken of the gaseous phase within cell before it was placed into direct sunlight. Since the CO_2 peak was observed to grow in intensity after 3 h of sunlight exposure, with the C-H stretching peaks also concomitantly decreasing (with the exception of the hemin sample), it is logical to conclude that hydrocarbons in the samples were converted to CO_2. For the hemin sample, it is possible that the same process did occur, but that it was also accompanied by the catalytic decomposition of non-volatile compounds from the bitumen in the presence of UV light into more volatile species. These volatile species should also ultimately be converted to CO_2 but possibly not as quickly, leading to their buildup.

The only form of oxygen present in the gas cell was O_2, which indicates that this oxidation likely occurs with atmospheric oxygen. Similar observations were made across all of the AWB, and weathered AWB bitumen samples, where changes in the IR spectra on exposure to sunlight suggested that volatile compounds from the bitumen were being photo-oxidized all the way to CO_2. The sample where 1% w/w of hemin was added to AWB bitumen did display an increase in CO_2 levels as well, however, it also displayed unforeseen increases in the intensities of all of the other hydrocarbon derived peaks in the IR spectrum.

Experiment Two

After learning that bitumen would oxidize in the presence of direct midday sunlight, the next step was to see if the reaction would still occur with indirect sunlight, i.e. on an overcast day. The same method as described above was followed. 1 mL of the AWB bitumen was deposited into the quartz gas-cell and it was sealed with the NaCl plates. The IR spectrum of the sample in the cell was measured at 0 min and it was then placed outside in view of the sky but on a day when there was complete cloud cover.

As can be seen from Figure 44, the intensity of the light was consistently around 20000 Lux for the first 1.5 h of the experiment. It then started to increase, and after 2.5 h the cloud cover had completely dissipated to reach the full intensity of the sun, over 100000 Lux. So, unfortunately, this sample was exposed to a mixture of cloud and sun, with about 1.5 h of total sun exposure by the end of the experiment.

The IR spectra in Figure 43, shows little to no increase in the amount of CO_2 within the gas-cell over the course of the experiment. There must not have been enough time for appreciable amounts of CO_2 form. All of the previous experiments with the gas-cell were given 3 h of full sunlight and the rate of oxidation over that period was not determined. It makes sense that cloud cover would absorb UV-light and reduce or even prevent photo-oxidation from occurring. However, it would have been expected that a noticeable reaction would occur in the final 2 h of the experiment when the sun was unobstructed. The CH stretching vibration at 2900 cm^{-1} and the CH bending vibration at 1500 and 1400 cm^{-1} in the IR spectra did show a slight increase in peak height over the course of 3 hours. This may have occurred because volatiles were being formed or off gassed from the bitumen, but without their oxidation to CO_2. On the overcast day there was either not enough energy or enough time to convert the volatile hydrocarbons to CO_2.

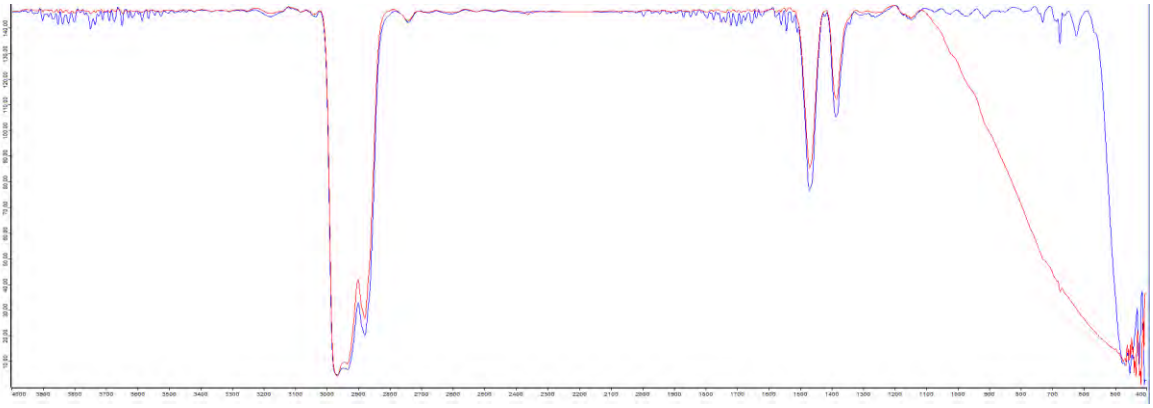

Figure 43: Infrared spectra for the gases above a photo-oxidized sample of AWB bitumen run in a sealed quartz cell on an overcast day, prior to exposure to "reduced" sunlight (red) and after being exposed to "reduced" sunlight for 4 h (blue).

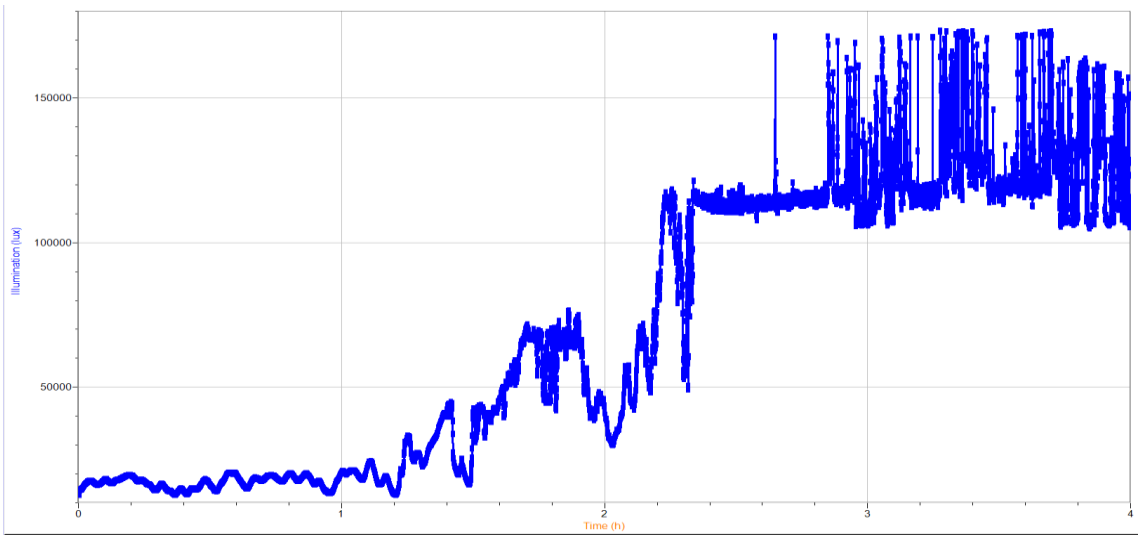

Figure 44: Measurement of the sun intensity (in Lux) recorded over the course of the gas cell experiment for the AWB bitumen sample run on an overcast day. The clouds cleared up 2.5 h into the experiment, leading to a significant increase in the recorded intensity. Experiment was set to run for 4 h to help maximize oxidation on an overcast day.

Experiment Thee

An experiment to try and determine the rate of CO_2 production was carried out using IR measurement of a bitumen sample in the quartz gas-cell. Following the same methods as described above, 1 mL of AWB bitumen was dispensed into the quartz gas cell which had been purged with dry nitrogen. The gas cell was immediately sealed with NaCl plates and an IR spectrum was recorded for time zero. The gas cell was placed into direct midday sunlight to allow photo-oxidation of the bitumen. The IR spectrum of the volatiles above the sample in the gas-cell was measured every 20 min over the course of 3 h (Figures 45 and 46). A control sample was run directly afterwards; in it the AWB bitumen was not exposed to light at all for the duration of the experiment (Figures 47 and

48). The intensity of the sunlight was not recorded as the instrument normally used for its measurement was unavailable.

Initially the IR spectrum shows there is only a bit of CO_2 present within the sample. It also shows a broad C=C peak in the 1640 cm^{-1} region arising from volatile species having isolated C=C bonds. As time passes, the concentration of CO_2 varies but rises overall. This is also accompanied by a reduction in the volatile C=C peak, which indicates that such species are being consumed. The volatile C=C peak is replaced by two resolved peaks at 1700 and 1600 cm^{-1} attributable to C=O and aromatic C=C vibrations, respectively. These are likely from species being released from the bitumen and/or forming in the gas phase as the first step of oxidation. As the concentration of C=O rises, it would be expected that the concentration of CO_2 would also rise, as the CO_2 is likely formed by further oxidation of these species. This turned out not to be the case, and the CO_2 concentration ultimately decreased, so it is possible that the gas cell was not fully air tight. Thus the CO_2 could diffuse out of the cell once its concentration had risen high enough.

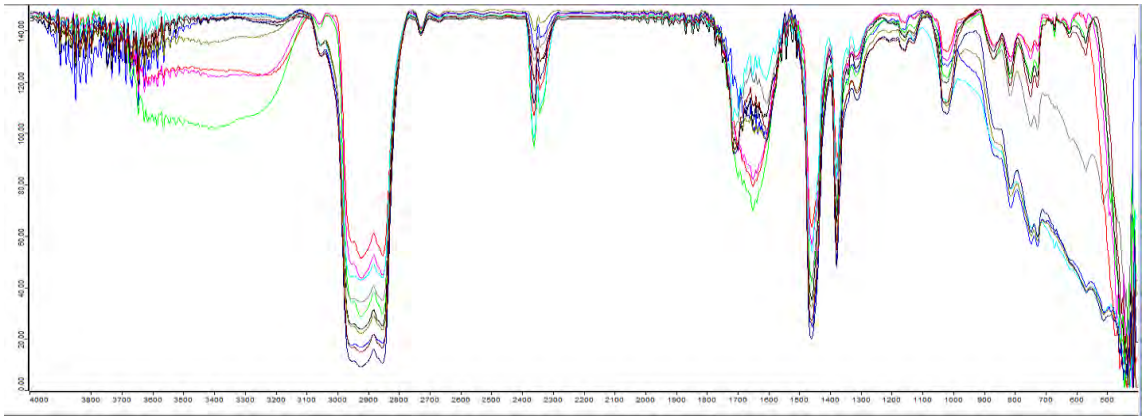

Figure 45: The same infrared spectra as shown in Figure 46 for the gases above a photo-oxidized sample of AWB bitumen deposited and run in the quartz gas cell over 3 hours (measurement taken every 20 min). Spectra have been overlaid to highlight differences in peak intensities. The large peak at ~3400 cm^{-1} is attributed to a volatile OH-containing species and/or water.

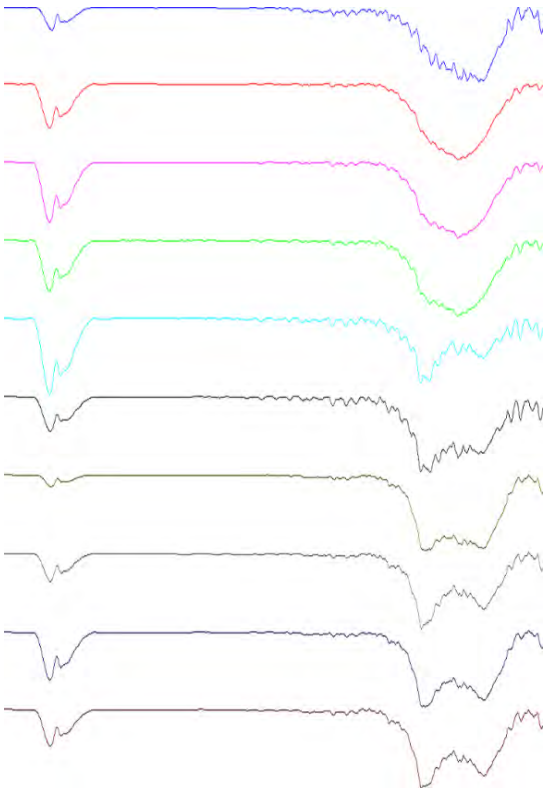

Figure 46: Infrared spectra for gases above the AWB bitumen sample photo-oxidized in a quartz cell with exposure to direct sunlight focussed on the 2500-1500 cm^{-1} region: bitumen control at time 0 min (top), and then increasing at 20-min intervals for each respective spectrum below it and ending at 180 min (bottom).

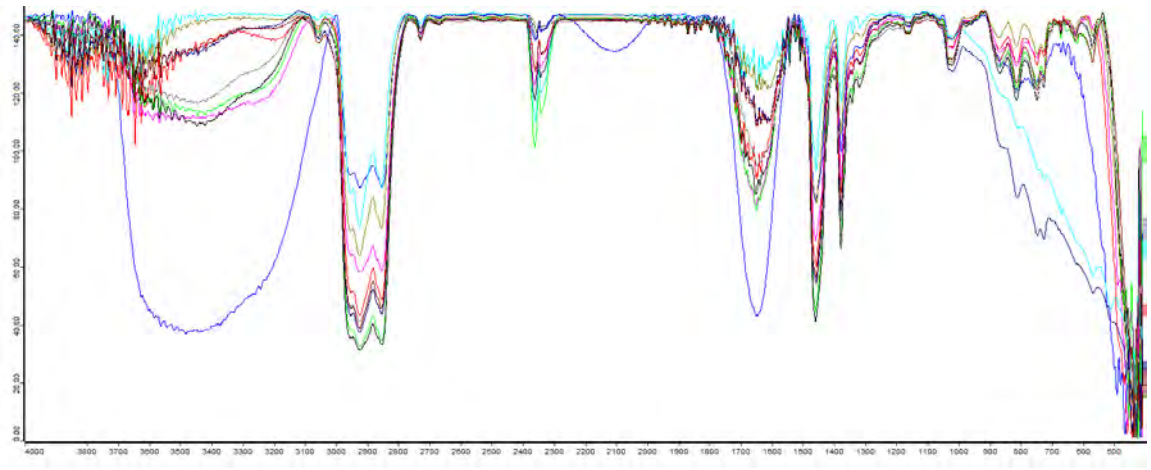

Figure 47: The same infrared spectra as shown in Figure 48 for the gases above a sample of AWB bitumen run in the quartz cell kept in darkness over 3 hours (measurement taken every 20 min). Spectra have been overlaid to highlight differences in peak intensities. The large peak at ~3400 cm^{-1} is attributed to a volatile OH-containing species and/or water.

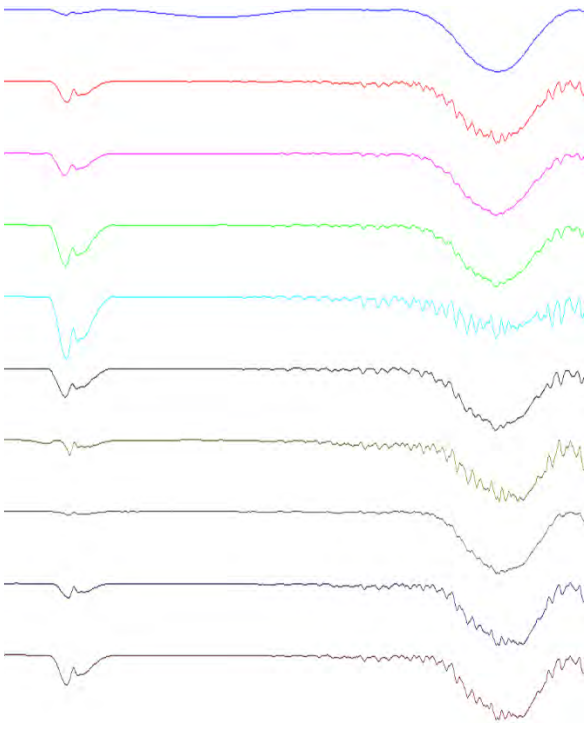

Figure 48: Infrared spectra for the gases above an AWB bitumen sample in a quartz gas cell kept in darkness focussed on the 2500-1500 cm^{-1} region: bitumen control at time 0 min (top), and then increasing at 20-min intervals for each respective spectrum below it and ending at 180 min (bottom).

The infrared spectra show that CO_2 is being formed in the dark sample, just as it was in the sun sample. This may be from off gassing from the bitumen sample. This immediately raises the question as to much of the CO_2 in the previous sample was from formation and how much was from off gassing? The amount of CO_2 in the dark sample is considerably less than that of the sun sample, judging from the peaks in their respective IR spectra, which at least indicates that there is CO_2 formation in the sun sample, as observed in previous evperiments. More interesting is the C=C stretch arising from isolated volatile molecules at the 1640 cm^{-1} region of the spectra. This peak does not change much over the entire time range which indicates that these species are not being oxidized in the complete darkness. This is similar to the results seen in Sections 1 and 2.

Figures 45-48 suggest that there is an increase in CO_2 with time for both the sample exposed to sunlight and for that left in the dark. The size of the CO_2 signal is maximal in the spectra collected at 80 min before decreasing in both samples. This implies that CO_2 is reaching its maximum concentration at 80 min within the sample before somehow dissipating. A possible explanation is that the CO_2 is leaking from the gas cell. Initially, the hydrocarbons that are most susceptible to forming CO_2 must react faster than the rate of diffusion out of the gas cell. This leads to a buildup of CO_2 within the cell. However, as these hydrocarbons are used up, the rate of formation decreases to below the diffusion rate. The CO_2 levels drop as there is not enough being produced to sustain the diffusion rate. This would also explain the disappearance of the volatile OH-containing species which initially give rise to the vibrations at 3400 cm^{-1}.

The C-H symmetric and antisymmetric stretching vibrations[27] in the region of 2900-3100 cm^{-1} and the isolated alkenyl C=C stretch at 1640 cm^{-1} are where the most

noticeable differences are observed between the spectra of the sunlight and dark samples. In both of the samples, the initial measurements show a large, broad peak at 1640 cm^{-1} (associated with isolated C=C stretches) which decreases as the experiment proceeds. For the samples exposed to UV light (Figures 45 and 46), this peak disappears and resolves into a peak at 1700 cm^{-1} (associated with C=O) and 1600 cm^{-1} (associated with aromatic C=C stretching) over the course of the 180 min, similar to the experiments in Section 2. This is particularly interesting as it demonstrates that the oxidative products are also volatile, which adds validity to the compounds found during the SPME experiments in Section 4. For the UV light sample (Figures 45 and 46) the disappearance of the 1640 cm^{-1} peak happens at the 60- to 80-min mark. For the dark sample (Figures 47 and 48), this peak decreases only very slowly and never completely disappears. Instead it is only reduced in intensity enough that the 1600 cm^{-1} peak becomes apparent. In the light sample, there must be a loss of the volatile C=C containing compounds as the experiment proceeds and these presumably contribute to both the C=O containing species being formed and also to the CO_2 being produced. The amounts of these species in the gas phase must also be bolstered from the same type of products being released from the bitumen phase as it is exposed to the sunlight. In the dark sample, all of these processes are slower both in the bitumen and in the gas phase.

For the C-H stretching in the 2900-3100 cm^{-1} region, there is an interesting trend observed in the spectra of the sunlight exposed sample; as the peak intensity at 1640 cm^{-1} decreases, the peak intensity in the C-H stretching region increases. It would appear that as the volatile alkenyl C=C compounds react, they are oxidized to saturated hydrocarbons (and CO_2), which increases the relative intensity of the C-H stretching peak.

Surprisingly, the same trend was observed for the sample kept in darkness, where the rate of oxidation must be much slower. In the spectra of the dark sample the C-H stretching vibrations are much less intense relative to those in the spectra of the light sample but they do also increase in intensity over time, For the dark sample, the volatile compounds will still escape into the gaseous phase but the rate of their oxidation will be very slow. This means that the peak at 1640 cm^{-1} should be present longer within the dark sample compared to the UV light exposed sample, and the C-H stretching vibrations will increase in intensity much more slowly, which is, in fact, what is observed experimentally.

The results of these experiments showed that CO_2 gas formed above samples of AWB bitumen over the relatively short period of 3 hours. The IR spectra of samples in the quartz gas cell revealed that the CH stretching vibration in the 2900 cm^{-1} region shank after exposure to UV light, which was accompanied with growth of the CO_2 peak at 2300 cm^{-1}. An increase in the intensity of the CO_2 peak was also observed in the IR spectrum of a hemin spiked bitumen sample, but this was accompanied by growth of the CH stretching peak. It could be that the hemin caused the catalytic decomposition of non-volatile compounds in the bitumen, in the presence of UV light, forming more volatile hydrocarbon species. For an experiment run on an overcast day, there was no observed photo-oxidation, even when the cloud cover dissipated halfway though the run. It is thought that there was not enough energy (or enough time) to convert the volatile hydrocarbons to CO_2.

The rate determination for the photo-oxidation of the bitumen in the gas cell showed that the CO_2 signal in the IR spectra reached its maximum at 80 min before decreasing in both samples. This implies that the CO_2 reached its maximum concentration

at 80 min before somehow dissipating. A possible explanation is that the CO_2 was slowly leaking from the gas cell. The dark sample also showed a growth in the CO_2 peak over time, which implies that there is potential off gassing of CO_2 from bitumen, perhaps due to slow oxidation. The amount of CO_2 formed in the dark sample was considerably less than that of the sun sample, indicating that more photo-oxidation did occur in the sun sample, as observed in previous evperiments. Further experimentation, with improvements to make the quartz gas cell air tight, should be conducted to test the validity of these results.

Section 6: Saturate, Aromatic, Resin and Asphaltene (SARA) testing – carried out at the Bedford Institute of Oceanography

Samples of bitumen of different types (1 mL) were deposited onto 10 mL of ultrapure water in a quartz cuvette. The types of bitumen used were: 5% hemin w/w mixed with AWB bitumen, unaltered AWB bitumen, "weathered" AWB bitumen, and Athabasca bitumen. Unless otherwise stated, the bitumen used was provided by the Bedford Institute of Oceanography (BIO). Weathered bitumen was made by taking AWB bitumen and leaving it exposed to open circulating air for a period of 2 weeks, giving it time for any volatiles to escape. This sample was left in a dark place for the duration of the weathering process to minimize any potential photo-oxidation.

Each type of bitumen sample was prepared in triplicate: one to be left in the dark and two to be exposed to sunlight for different lengths of time. The samples were sealed with rubber septa to prevent any foreign debris from entering the samples. One set of samples was placed into darkness for the duration of the experiment, one set were placed outside in a sunlight heavy location for a period of a month, and the last sample set was kept in darkness until the final day of the experiment when it was placed in bright sunlight for 3 h.

Table 6: Masses of the bitumen samples used for SARA analysis

Sample	Athabascan Bitumen†	AWB Bitumen	Weathered Bitumen	5% w/w Hemin Bitumen
Dark	0.07847 g	0.01132 g	0.01043 g	0.00996 g
Sun	0.07816 g	0.01041 g	0.00999 g	0.01076 g
Long-term	0.07914 g	0.01065 g	0.01098 g	0.01057 g

†Athabasca bitumen had a higher mass weighed out as it was the first prepared for SARA analysis. It was then determined there was not enough of the other samples to match this mass. Therefore, their amounts were reduced and normalized. This did not impact the results as the Athabasca bitumen sample was diluted to have same concentration as the other samples.

When the first phase of the experiment was complete, the samples were drained of water and brought to BIO for Saturate, Aromatic, Resin and Asphaltene (SARA) analysis. This method is used to separate and quantify the fractional components of heavy oil based on their polarity. In this process the bitumen sample is fractionated into the four named components (saturates, aromatics, resins and asphaltenes) of increasing polarity and then the relative amount of each fraction is determined. 75 mg is an optimal sample mass for SARA analysis. However, there was not enough of certain samples to use this large a mass. These samples were divided to give thee portions of similar weight (Table 6), which proved to be approximately 10 mg per portion. The samples were then diluted using DCM, where necessary, to make sure that they were all of similar concentrations.

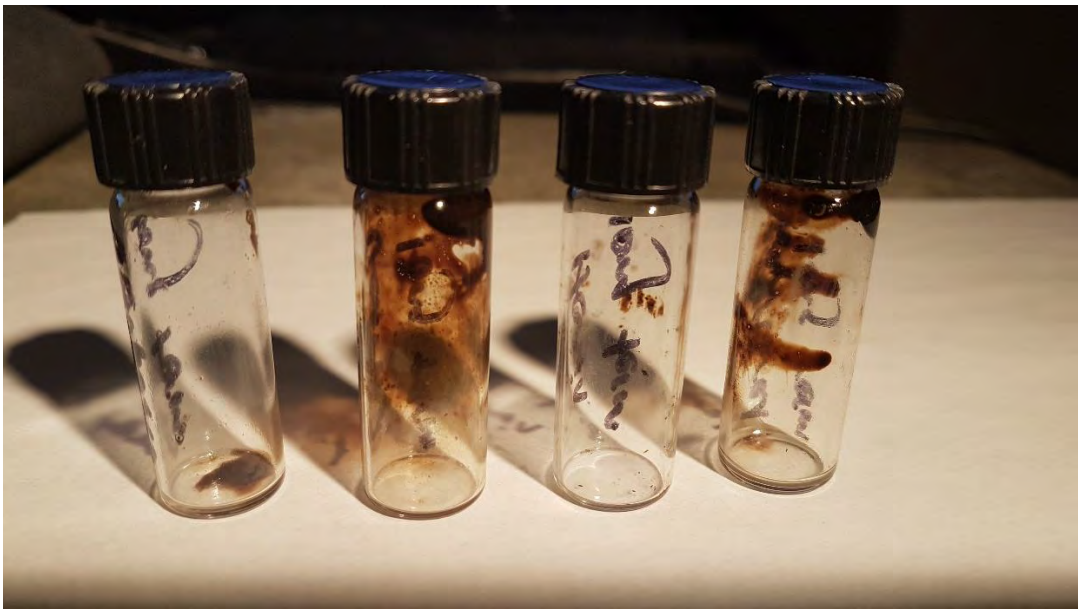

Figure 49: Post SARA long term samples. Left to right: Athabasca bitumen, AWB bitumen, 5% hemin and AWB bitumen, and weathered bitumen.

Tables 7-13 provide a percent composition for each of the individual component classifications of the bitumen samples. The saturate fraction consists of nonpolar materials including linear, branched, and cyclic saturated hydrocarbons (paraffins). Aromatics, which contain one or more aromatic rings, are slightly more polarizable. The remaining two fractions, resins and asphaltenes, have polar substituents. The distinction between the two is that asphaltenes are insoluble in an excess of heptane (or pentane) whereas resins are miscible with heptane (or pentane). A decrease in the amount of saturates or aromatics, with a corresponding increase in resins and/or asphaltenes, in a sample after exposure to sunlight is one indication that photo-oxidation has possibly occurred. For these experiments though, some samples have a relatively high standard deviation (included in the tables provided) that is unique for each trial. This is likely due, at least partially to the small sample masses employed. Any conclusions that are drawn

will have to be more qualitative than quantitative, unless the observed difference between the trials is significantly larger than their error range, as given by the standard deviations.

Figures 50-53 show the SARA data as a percentage of each fractional component within the different bitumen samples. Tables 7-13 show the same SARA data as Figures 50-56, each is paired with the graph of their respective data set below the table.

Table 7: SARA fractional composition of Athabasca Bitumen

Component	Average Athabasca Dark		Average Athabasca Sun		Average Athabasca Long-Term	
	Comp. %	Std. Dev. %	Comp. %	Std. Dev. %	Comp. %	Std. Dev. %
Saturates	10.68	0.57	11.93	0.20	10.71	0.31
Aromatics	46.38	0.31	48.18	1.11	21.76	0.24
Resins	42.33	1.23	39.34	1.17	66.64	0.62
Asphaltenes	0.61	0.53	0.56	0.29	0.89	0.12

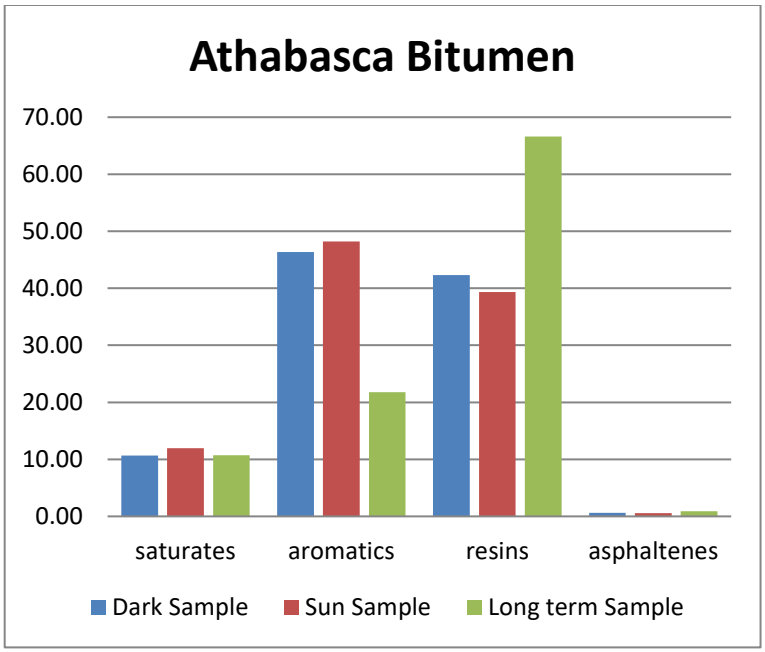

Figure 50: SARA fractional composition of the Athabasca bitumen samples divided according to light exposure (dark – blue, 3 h sun – red and long term – green).

The Athabasca Bitumen data in Table 7 shows that the saturate and the asphaltene fractions display only minor fluctuations across the thee trials, and nothing outside the range of their standard deviations. The dark and sun trials have almost identical compositions, so 3 h of sun exposure has not changed the sample composition significantly. However, there is a large decrease in the percent composition of the aromatic compounds, along with a proportional increase in the amount of resins, for the sample which had been subjected to long-term sun exposure. This is strong evidence that long-term exposure to sunlight can convert aromatic compounds into the more polar compounds that are found within the resin fraction.

Table 8: SARA fractional composition of AWB Bitumen

Component	Average Athabasca Dark		Average Athabasca Sun		Average Athabasca Long-Term	
	Comp. %	Std. Dev. %	Comp. %	Std. Dev. %	Comp. %	Std. Dev. %
Saturates	0.04	0.01	0.04	0.01	9.61	1.33
Aromatics	61.05	1.69	60.78	1.68	38.80	4.02
Resins	37.35	1.64	37.68	1.77	49.94	2.73
Asphaltenes	1.56	0.78	1.50	0.34	1.66	0.58

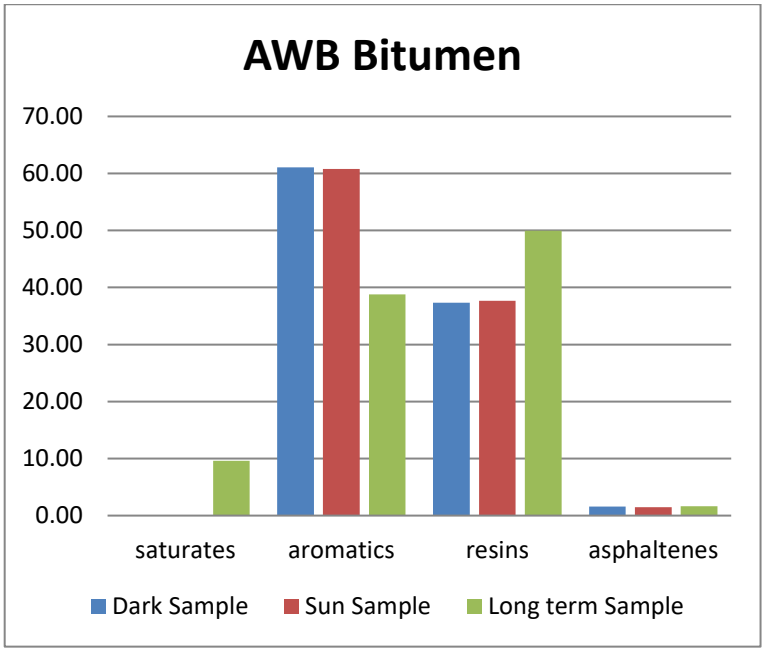

Figure 51: SARA fractional composition of the AWB bitumen samples divided according to light exposure (dark – blue, 3 h sun – red and long term – green).

The AWB bitumen data in Table 8 shows that significant changes have occurred in its composition after long-term exposure to sunlight. The 3-h exposure to sun does not yield any major changes in the fractional composition compared to that of the dark sample, but this is quite different for the month-long exposure. There is a decrease in the

amount of aromatic compounds, which is accompanied by increases to the saturates and resins respectfully, changes that are outside the error of the standard deviations. This is strong evidence that long-term exposure to sunlight can convert aromatic compounds to the more polar compounds that are found within resins, and also break the aromaticity of compounds to generate saturated hydrocarbons. The overall profile is very similar to that of the Athabasca bitumen, with the exception of the saturates level. While the saturates level in Athabasca bitumen remained constant at ~10% at all thee levels of sun exposure, the AWB bitumen saturates level increased from negligible amounts to ~10% only after a prolonged time in the sun.

Table 9: SARA fractional composition of Weathered Bitumen

Component	Average Athabasca Dark		Average Athabasca Sun		Average Athabasca Long-Term	
	Comp. %	Std. Dev. %	Comp. %	Std. Dev. %	Comp. %	Std. Dev. %
Saturates	11.67	1.4	11.19	1.42	11.06	1.70
Aromatics	50.40	2.28	42.57	2.73	28.78	1.51
Resins	36.05	0.59	43.67	3.02	58.88	3.38
Asphaltenes	1.88	0.71	2.57	0.95	1.27	0.79

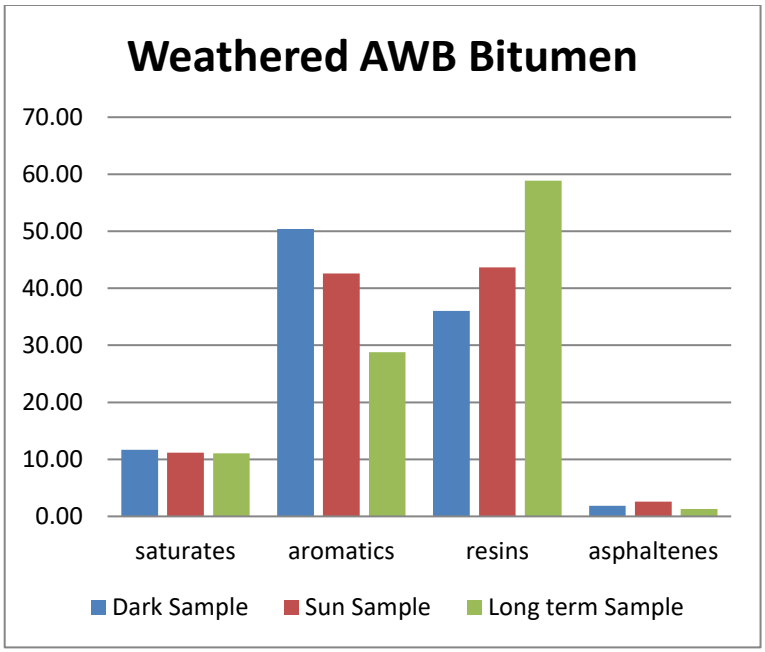

Figure 52: SARA fractional composition of the weathered AWB bitumen samples divided according to light exposure (dark – blue, 3 h sun – red and long term – green).

The weathered AWB bitumen data in Table 9 is somewhat different to the data of Tables 7 and 8. For this sample, the saturate and the asphaltene levels are relatively constant. What is apparent, however, is that even after only 3 h of exposure to sunlight, the aromatic compounds in the sample have decreased while the resins have increased (relative to the stability observed in the previous two samples). This trend continues to the long-term sunlight exposure, where the aromatics show a large overall decrease, while the resins show a large overall increase. This is a more rapid process than in the previous samples where no change was observed after 3 h in the sun. The overall result is similar to those exhibited by the Athabasca bitumen and the AWB bitumen, and is a strong indication that the aromatic components within bitumen are the likely sources of photo-oxidation. The weathered AWB bitumen shows a significant rise in the resin fraction, with a significant decrease in the amount of aromatics present over time, which

is consistent with the data in Tables 7 and 8. However, it appears to happen more quickly and to a somewhat greater extent than in these other samples.

Table 10: SARA fractional composition of the Hemin and bitumen mixture

Component	Average Athabasca Dark		Average Athabasca Sun		Average Athabasca Long-Term	
	Comp. %	Std. Dev. %	Comp. %	Std. Dev. %	Comp. %	Std. Dev. %
Saturates	11.5	2.6	9.2	0.6	9.1	0.4
Aromatics	34.0	6.1	43.4	0.9	41.3	2.8
Resins	47.4	4.4	45.0	0.4	43.4	2.4
Asphaltenes	7.1	2.3	2.4	0.7	6.2	1.3

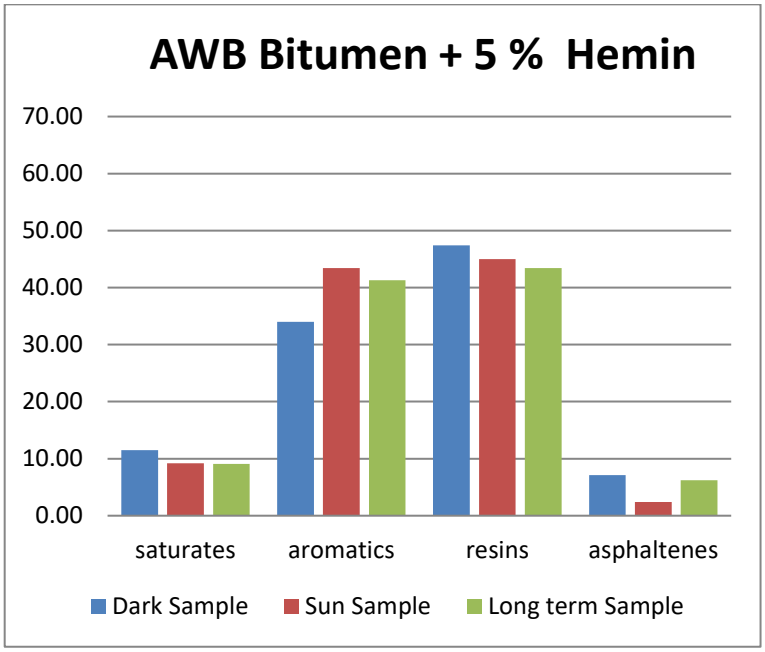

Figure 53: SARA fractional composition of the 5% w/w hemin and AWB bitumen samples divided according to light exposure (dark – blue, 3 h sun – red and long term – green).

The asphaltene level in all of the hemin spiked samples is higher than it is in the other samples, because of the porphyrin added to the sample. The added hemin fractionates out of the sample with the asphaltenes of the bitumen. The asphaltene level of the hemin 3 h sun sample is decreased but it is hard to determine if this is a real change, or just an experimental error, since it increases back to its initial level in the long-term sample. The 5% w/w hemin spiked bitumen data in Table 10 shows that all of the values for the hemin sample remain relatively constant over the entire experiment. Only the aromatic levels go up in a way that might be significant. This change occurs on exposure to 3 h of sunlight, and the level stabilizes again over a longer period of time. The saturate and resin fractions do appear to go down a bit to compensate for the observed increase in the resins. Overall, the hemin seems to be stabilizing the samples rather than promoting oxidation.

As can be seen from the values in Tables 7-9, there is an overall decrease in the amount of aromatic compounds present in a sample the longer it is exposed to UV light. For the Athabasca and AWB bitumen samples this does not occur after 3h but is only observed on long term sun exposure. The decrease in the aromatic fraction occurs more quickly in the weathered AWB bitumen (starting after only 3 h) but is observed in all but the hemin spiked sample. This likely indicates that photo-oxidation is occurring in these samples. Not only this, but the primarily compounds that photo-oxidation targets must be these aromatic compounds. This trend is not observed in the hemin spiked bitumen, Table 10, which indicates that the hemin could be interacting with the bitumen in a way that disrupts photo-oxidation instead of promoting it. Alternatively, the hemin could be converting compounds in the bitumen directly to CO_2 instead of forming intermediate

oxidative products. The fractional composition might then not change much and the process would comply with literary research[21-25]. At this point, either choice is pure speculation.

The following data (Tables 11-13 and Figures 54-56) are the same as that in Tables 7-10, except that it has been reorganized and regraphed to emphasize the relative differences between samples exposed to the different light levels.

Table 11: SARA of bitumen samples stored in darkness

Component	Athabascan Bitumen		AWB Bitumen		Weathered Bitumen		5% w/w Hemin Bitumen	
	Comp. %	Std. Dev. %	Comp. %	Std. Dev. %	Comp. %	Std. Dev. %	Comp. %	Std. Dev. %
Saturates	10.68	0.57	0.04	0.01	11.67	1.4	11.5	2.6
Aromatics	46.38	0.31	61.05	1.69	50.40	2.28	34.0	6.1
Resins	42.33	1.23	37.35	1.64	36.05	0.59	47.4	4.4
Asphaltenes	0.61	0.53	1.56	0.78	1.88	0.71	7.1	2.3

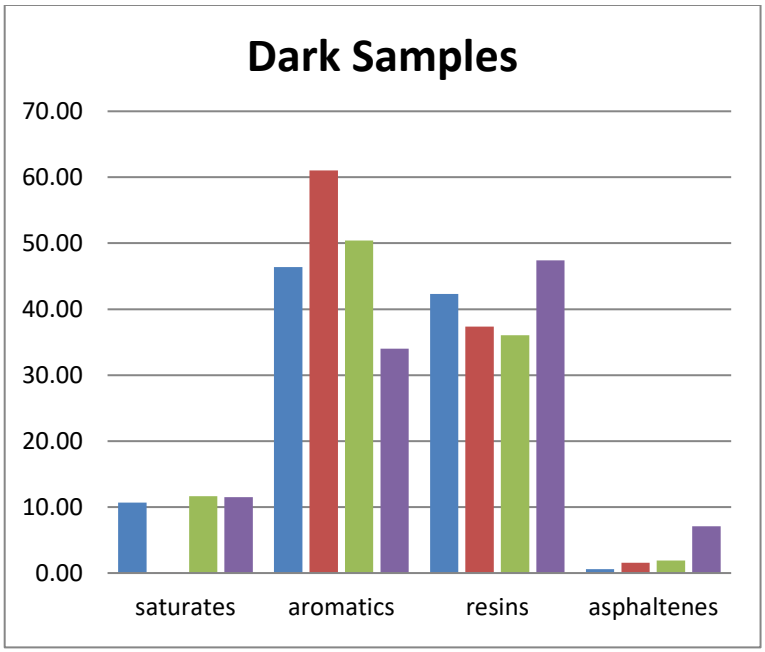

Figure 54: SARA fractional components of bitumen samples stored in darkness divided according to bitumen type (Athabasca – blue, AWB bitumen – red, weathered AWB bitumen – green and AWB bitumen + 5% hemin - purple).

The level of saturates in all of the dark samples (Figure 54) are relatively equal in percent composition for the different samples, with the exception of AWB bitumen where essentially none were found. It may be that the industrial solvents used to dilute this blend are aromatic in nature, and present in such high concentrations that they effectively mask the saturated compounds in the bitumen.

This idea may have some merit as the percentage of aromatics in AWB bitumen is significantly higher than that in any other of the samples. The aromatics of weathered AWB bitumen and Athabasca bitumen are relatively similar in level, which would make sense as they derive from the same initial source of bitumen. The hemin spiked sample, however, is much lower in aromatics. It is also relatively higher in the percentage of the resin fraction. This is the same type of change observed in all of the samples upon

exposure to prolonged periods of sunshine. It may be that the hemin spiked sample has already changed (before any measurements can be made) to be similar in composition to the unspiked samples of bitumen which have undergone long sun exposure. The samples that were not spiked with hemin have relatively similar values for resins and asphaltenes, while the hemin spiked sample has a greater amount of asphaltenes (and possibly resins) because the added porphyrin separates in those fractions.

Table 12: SARA of bitumen samples photo-oxidized for 3 hours

Component	Athabascan Bitumen		AWB Bitumen		Weathered Bitumen		5% w/w Hemin Bitumen	
	Comp. %	Std. Dev. %	Comp. %	Std. Dev. %	Comp. %	Std. Dev. %	Comp. %	Std. Dev. %
Saturates	11.93	0.20	0.04	0.01	11.19	1.42	9.2	0.6
Aromatics	48.18	1.11	60.78	1.68	42.57	2.73	43.4	0.9
Resins	39.34	1.17	37.68	1.77	43.67	3.02	45.0	0.4
Asphaltenes	0.56	0.29	1.50	0.34	2.57	0.95	2.4	0.7

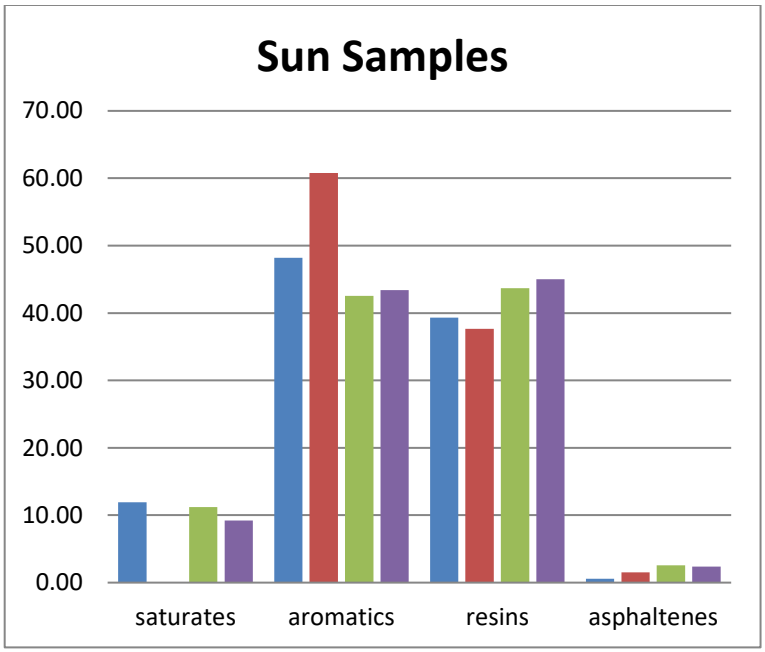

Figure 55: SARA fractional components of bitumen samples photo-oxidized for 3 hours divided according to bitumen type (Athabasca – blue, AWB bitumen – red, weathered AWB bitumen– green and AWB bitumen + 5% hemin - purple).

Just as in the previous figure, the saturates in the samples exposed to 3 hours of sunlight are all relatively equal in percent composition, with the exception of the AWB bitumen. This is likely due to the reason discussed above; the industrial solvents used to dilute the blend are more aromatic in nature, and present in such high concentrations, that they effectively mask any saturated compounds. Again, this idea is supported by the relatively higher percentage of aromatics in the AWB bitumen sample. It is significantly higher than that in any other of the samples, which are all relatively similar. The aromatic level of the hemin 3 h sun sample has risen compared to its level in the dark sample, for a reason that is not immediately obvious. All of the samples appear to have relatively similar values for resins and asphaltenes. The asphaltene percentage in the hemin sample has decreased to be more like the other samples, compared to Figure 54, though it is uncertain if this is a real change as it is not mathematically significant.

Table 13: SARA of bitumen samples photo-oxidized for one month

Component	Athabascan Bitumen		AWB Bitumen		Weathered Bitumen		5% w/w Hemin Bitumen	
	Comp. %	Std. Dev. %	Comp. %	Std. Dev. %	Comp. %	Std. Dev. %	Comp. %	Std. Dev. %
Saturates	10.71	0.31	9.61	1.33	11.06	1.70	9.1	0.4
Aromatics	21.76	0.24	38.80	4.02	28.78	1.51	41.3	2.8
Resins	66.64	0.62	49.94	2.73	58.88	3.38	43.4	2.4
Asphaltenes	0.89	0.12	1.66	0.58	1.27	0.79	6.2	1.3

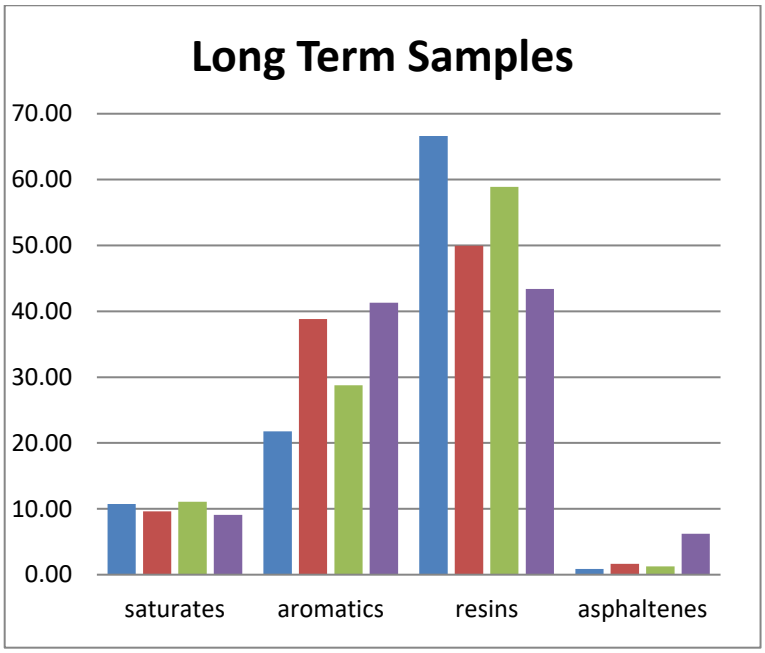

Figure 56: SARA fractional components of bitumen samples photo-oxidized over a month divided according to bitumen type (Athabasca – blue, AWB bitumen – red, weathered AWB bitumen – green and AWB bitumen + 5% hemin - purple).

The saturates composition for the weathered samples shown in Figure 56 are now all relatively equal. The AWB bitumen saturate level has risen by a significant amount,

while the amount of aromatics in that same sample has been considerably reduced. Again, this could be related to the solvents used in the preparation of AWB bitumen. For the aromatics, the Athabasca and the weathered samples have dropped to lower percentages than the other two. The AWB amount has also decreased by about the same amount as the other samples but it was higher to begin with and thus it remains higher. The hemin percentage is relatively unchanged compared to the data in Figures 54 and 55, so the hemin sample now has the largest fraction of aromatics of all of the samples. For the resins, the Athabasca and weathered samples have increased by a large margin, in direct contrast to the aromatic levels. The AWB sample has also increased by about the same amount, but since its initial level was lower, its final level is also a bit lower compared to the Athabasca and weathered samples. The hemin sample has hardly changed from its level in Figures 54 and 55. For the asphaltenes, the values are relatively stable in all 4 samples, being only relatively greater in the spiked sample because of the added hemin. The composition of the hemin sample has returned to match its original dark value in Figure 54. This suggests that the value observed for the 3-hour sample was an anomaly rather than a true experimental observation.

The results of these experiments showed that there was a fractional composition change within bitumen upon exposure to UV light. This occurred for a variety of different types of bitumen which were tested. With the exception of the hemin spiked sample, all of the samples showed the same general trend of losing aromatic compounds after exposure to UV light, accompanied by a related increase in their resin component. This trend was pronounced in all of the long-term samples but was apparent after 3 hours only in the sample of weathered bitumen. The results demonstrated that the SARA technique

can be used to quantify the products arising from photo-oxidation in bitumen samples. The primary consequence of photo-oxidation in bitumen, in terms of the SARA analysis, is the conversion of aromatic compounds to resins.

The hemin spiked sample had composition values for all of the fractions that remained relatively constant over the entire experiment. Only the aromatic level increased in a way that might have been significant. This change occurred on exposure to 3 hours of sunlight, and the level then stabilized again over a longer period of time. The saturate and resin fractions did appear to go down a bit to compensate for the observed increase in the resins. Overall, the hemin seems to be stabilizing the samples rather than promoting oxidation. A possible explanation for this is hemin could be interacting with the bitumen in a way that disrupts photo-oxidation instead of promoting it. Alternatively, the hemin could quickly be converting compounds in the bitumen directly to CO_2 instead of forming intermediate oxidative products. The fractional composition might then not change much over the course of the experiment and the process would comply with literary research.[21-25] At this point, either choice is pure speculation.

Conclusions

In these experiments, photo-oxidation was observed in bitumen samples with thee hours (or less) of exposure to light using IR, NMR, GC-MS, and SARA analysis. The results from the experiments in Section 1 revealed that bitumen samples underwent a chemical change in the presence of the UV radiation provided by a full spectrum grow light. The change was monitored by recording the differences observed in the IR spectra of dried bitumen samples deposited onto NaCl plates over time, specifically by determining the changes observed in the ν(C=O) peak at 1700 cm^{-1}. Bitumen samples that were left in the dark did not show any appreciable growth of this carbonyl peak, while its intensity steadily increased over time in the spectra of the samples exposed to the grow light. The IR spectra also revealed changes in the ν(C=C) region of the IR spectra in all samples. A peak at 1640 cm^{-1}, assigned to unconjugated alkenyl double bonds (likely to be in smaller more volatile compounds), disappeared over time from both the dark and light samples. This revealed a second ν(C=C) peak at 1600 cm^{-1} that was present in all samples. This peak was assigned to the C=C stretch in conjugated aromatic systems. Its intensity may have increased slowly over time on exposure to light, but not to the large extent observed for the ν(C=O) peak.

The trends were also observed again in the IR photo-oxidation experiments explored in Sections 2 and 3, where the bitumen samples were exposed to sunlight in addition to the grow light, with a dark control also included. There was an increase in the intensity of the carbonyl peak at 1700 cm^{-1} in the spectra of samples exposed to both types of UV light and similar changes to those observed in Section 1 were observed in the

C=C stretching region of these spectra as well. It was demonstrated in Section 2 that natural sunlight caused the same photo-oxidation processes that occurred with the growing light, except that it produced greater amounts of the oxidized products. Surprisingly, photo-oxidation occurred more slowly in the samples that were exposed to sunlight compared to the growing light. Perhaps, the full spectrum growing light had a higher percentage of UV light reaching the samples compared to the sun, as the growing light does not have the atmosphere to act as a UV filter. The results from Sections 1 and Section 2 also demonstrated that different bitumen types, Mesa and Athabasca, behaved similarly with exposure to UV light.

The results of Section 5 showed that the volatile compounds above bitumen in a quartz gas cell also underwent photo-oxidation, and that they were oxidized all the way to CO_2. In fact, the spectra obtained in all IR experiments, whether for dried bitumen (Sections 1 to 3) or for the gases above bitumen samples (Section 5), were very similar. This suggests that potentially volatile compounds within the bitumen are lost to the atmosphere above it over time (in the light or dark) and that no matter which phase they are in, they can be oxidized by UV light to give the same type of products. The C-H stretching vibration in the 2900 cm^{-1} region of the IR shank after exposure to UV light, and this was accompanied with growth of the carbonyl peak at 1700 cm^{-1} and the CO_2 peak at 2300 cm^{-1} (a CO_2 peak was observed in all of the IR experiments but only in the gas cell runs was the spectrometer purged so that the presence of CO_2 could be assigned solely to its generation in the sample). Further experimentation, particularly with improvements to make the quartz gas cell air tight, should be conducte to obtain more quanititative data, and to make the CO_2 determination unambiguous.

The increased photo-oxidation of bitumen in sunlight was also reflected by the results in Section 3, from the bitumen on water NMR experiments, which were also coupled with IR measurements. In the ^{1}H NMR spectra a signal assigned to photo-oxidation products was observed at ~4.6 ppm for bitumen samples exposed to a growing light, but a significantly larger peak was present in the spectra of bitumen samples exposed to sunlight. This signal was attributed to the presence of alcohols, phenols, and aromatic ethers in the bitumen. These are the sort of volatile species that could give rise to the peaks of interest being monitored in the IR experiments.

The results of Section 3 revealed other interesting properties of bitumen when exposed to water. Samples that were not photo-oxidized (dark samples) would become "gel-like", while those that were photo-oxidized formed smaller droplets of bitumen that dispersed thoughout the water when agitated. The bitumen on water experiments did not give quantifiable evidence of compounds leeching into the aqueous layer using the chosen methods. However, LC-MS did show that some compounds were eluted just after the solvent peak in the photo-oxidized samples but not from those left in the dark. These peaks appeared before the 5-min mark, indicating that they arose from polar compounds, which again is evidence that photo-oxidation occurred on exposure to light.

Samples that were exposed to large amounts of sunlight or exposed to it for long periods of time would show dramatic changes, as seen from the ~4.6 ppm signal found in the NMR data. There were also fractional composition changes in the SARA samples (Section 6) where the percentage of resins within bitumen, the polar compounds, increased after long term exposure to sunlight compared to the samples that were left in darkness. One of the most interesting changes observed was the formation of a film,

which was observed to form on the water surface in the bitumen on water experiments when the samples were exposed to sunlight. The film separated from the non-polar bitumen indicating that it must be more polar in nature. This was confirmed by the spectroscopic data, as the film samples did have much larger signal strengths in the 1700 cm^{-1} carbonyl region of the IR spectra, and in the ~4.6 ppm region of the NMR spectra. It is believed that this film was too polar to remain mixed with the non-polar bitumen, thus separating from it. However, the film must also have been too non-polar to enter the aqueous layer, which is why it remained on the surface of the water and recollected on it after being dispersed by agitation. The nature of the compounds being formed would also explain the increase in the level of resins observed in the later SARA analyses.

The results from Section 4 showed that SPME analysis can be used to identify volatile compounds in bitumen samples when coupled with GC-MS detection. Some compounds were consistently found in the samples, whether the bitumen was boiled or photo-oxidized, so these compounds could be used as potential internal standards. Some caution must be taken when interpreting the results of the SPME experiments. First, AWB bitumen was used in these experiments; AWB is a commercial dilbit blend already containing volatile solvents which could be detected using this method. Second, the samples used in the photo-oxidation portion of this experiment were subjected to different levels of sunlight exposure and thus had randomly different levels of photo-oxidized products in them. However, these same types of volatile compounds were observed in the ^{1}H NMR experiments and in the functional group analyses of the IR spectra of the NaCl plate experiments of Section 2 and the quartz gas cell experiments of Section 5. From the C-H stretching vibrations in the 2900 cm^{-1} region, and the peak at

1640 cm^{-1}, which has been attributed to the presence of C=C alkenyl-containing groups, these must be smaller (potentially volatile) organic compounds, such as those consistently found by SPME. In addition, according to the SPME results, there were other, new compounds formed in the photo-oxidized bitumen samples, including 1-pentanol, 3-hexen-2-one and 1-octene. SPME analysis did detect the presence of dimethyl sulfide in the boiled AWB bitumen, a fact later confirmed from its product specifications which showed it to contain approximately 4% sulfur. The SPME results also suggest that isomerization, fragmentation, and methyl shift all occur to components of the bitumen during the process of photo-oxidation. Overall, the results of Section 4 revealed the SPME technique to be sensitive, as it was able to detect oxidative products in all bitumen samples, although refinement of the method is still required.

The results of the SARA experiments detailed in Section 6 showed that there was a fractional composition change in bitumen upon its exposure to UV light. This occurred for a variety of different types of bitumen which were tested. With the exception of the hemin spiked sample, all of the samples showed the same general trend of losing aromatic compounds after exposure to UV light, accompanied by a related increase in their resin component. This follows the observed trends in the IR experiments, where the peak at 1640 cm^{-1} in the IR was reduced (volatile alkenyl products) and the carbonyl peak at 1700 cm^{-1} increased, as resins are classified as containing oxidized compounds. The formation of more resins in the bitumen samples with longer exposure to UV light also explains why the integrated peak ratio did not significantly change in the experiments carried out in Section 2; growth of the ν(C=C) peak for conjugated aromatics occurred in conjunction with the increased intensity of the ν(C=O) peak so the ratio observed

remained relatively constant. The SARA data also compliments the NMR data from Section 3, where there was an increase of the observed signal in the NMR spectra of light exposed samples at ~4.6 ppm attributed to alcohols, phenols, and aromatic ethers in the bitumen. The primary consequence of photo-oxidation in bitumen, in terms of the SARA analysis, is the conversion of aromatic compounds to resins. Somewhat surprisingly, the SARA samples did not usually show such changes until they had been exposed to prolonged periods of sunlight, while the other experiments showed such changes occurring more quickly, generally in less than 3 hours.

The results from all the hemin experiments across all sections, revealed that the hemin spiked samples did not follow the same trends observed for the unspiked samples. There was no statistically significant change for the IR peak ratios in the NaCl plate experiments in Section 2. The gas cell experiments in Section 5 did not reveal an increase in the intensity of the CO_2 peak at 2300 cm^{-1} or in the volatile oxidative products monitored using the ν(C=O) peak at 1700 cm^{-1}, for any of the hemin spiked samples. The SARA experiments in Section 6 also did not show any increase in the oxidative products for the hemin spikes samples. For the SARA data, the hemin samples were the only samples not to show an increase in resin composition after long term photo-oxidation. Instead of photo-oxidation occurring, what was observed was stabilization of the bitumen, so that its composition did not change much over time with its exposure to sunlight. A possible explanation for this is that hemin could be interacting with the bitumen in a way that disrupts photo-oxidation instead of promoting it. Alternatively, it is possible the hemin could quickly be converting compounds in the bitumen directly to CO_2, instead of forming intermediate oxidative products. Either interpretation is pure

speculation at this point. More experiments, especially with the quartz gas cell, are required to determine if photo-oxidation to CO_2 is occurring with hemin spiked bitumen, or if hemin is instead inhibiting the photo-oxidation of bitumen.

Section 7: Experimental

Chemicals

All materials, unless otherwise stated, were obtained from commercial suppliers and were used as received, without further purification.

AWB bitumen – supplied by the Bedford Institute of Oceanography (BIO)

Athabasca bitumen – supplied by BIO

Mesa bitumen – in house

Hemin

Solvents: n-hexanes, dichloromethane, chloroform, acetone, heptane, toluene

Deuterated solvents (D: ≥99%): deuterated dichloromethane (CD_2Cl_2), deuterated chloroform ($CDCl_3$), deuterated benzene (C_6D_6) – purchased from Cambridge Isotope Laboratories, Inc.

Dry nitrogen and helium

Spectroscopic and Characterization Techniques

The HPLC experiments were carried out on an Agilent 1100 LC-DAD instrument equipped with an autosampler, binary pump, vacuum degasser, thermostatted column, and diode array detector. The column used was a ZDRBAX Eclipse XDB-C18 column,

Rapid resolution 4.6x75 mm, 3.5 microns. All data was collected and processed using the software HP Chem Station.

The infrared spectra of all NaCl plate and quartz gas cell samples were obtained using a Bruker Vertex 70 Infrared Spectrometer, at room temperature. The liquid and gel bitumen samples were collected by attenuated total reflection (ATR) using an adapter on a Bruker Alpha Spectrometer. Data processing was completed using the OPUS 6.0 software suite[26].

All NMR experiments were carried out at 298 K, unless otherwise stated, on a Bruker Ultrashield 300 MHz NMR spectrometer with a 7.05 Tesla magnet. The samples were prepared by dissolving a small amount of the compound into an aliquot of the deuterated solvent. The ^{1}H NMR (300 MHz) spectra were internally referenced to trace amount of non-deuterated solvent, which were referenced relative to TMS (δ = 0 ppm).[38] The deuterated solvent was used as an internal reference for $^{13}C\{^{1}H\}$ NMR (75 MHz), and referenced relative to TMS (δ = 0 ppm).[38] The data was processed using Bruker TOPSIN 3.6.1.[39]

The UV-vis measurements were obtained on a Varian Cary 50 Bio UV-Visible Spectrophotometer and data processing was completed using Cary WinUV. All absorptions were collected as dilute dichloromethane solutions using a quartz cuvette with a 1 cm path length.

GC-MS analysis of all volatile compounds was conducted on a Varian 3800 Gas Chomatograph coupled to a Varian 2000 Ion Trap Mass Spectrometer. A VF-5MS capillary column (Varian, CP8944, 30m x 0.25 mm, 0.25 μm) was utilized to separate the

samples. The oven temperature was initially set at 35°C, held for 2 min, increased to 260°C at 15°C/min, and finally held for 2 min. Helium (99.9%) was used as the carrier gas and set at a constant flow rate of 1 mL/min. The fibers were manually injected and desorbed in the injection port at 260°C for 3 min. The transfer line and ion source were maintained at 250 °C. The fiber utilized was a SPME fiber assembly made of Divinylbenzene/Carboxen/Polydimethylsiloxane (DVB/CAR/PDMS) and purchased from Sigma, Canada.

SARA Analysis of total oil using Iatroscan is based on a technique utilizing thin-layer chomatography (TLC).[40] The TLC/FID analyzer (Iatroscan) consists of two separated instrumental units, the quartz silica-coated rods, which constitute the TLC component, and the FID scanner unit. The quartz rods have a diameter of 0.9 mm, a length of 152 mm (a useful length of 12 cm), and are coated with a thin layer (75 μm) of a mixture of soft glass powder and the absorbent, either silica gel (Chomarod SIII) or alumina (Chomarod A). The FID scanner unit consists of a hydrogen flame jet and an ion collector. Samples are applied to the chomarods using the auto-spotter. After spotting, the chomarods must be developed to separate the four components of the oil (alkanes, aromatics, resins, asphaltenes). This is done by placing the rods in solvents and allowing those solvents to move up the rods. Following the sample application and solvent development, a frame with a set of ten rods is transferred to the FID unit, where the rods are scanned and burned. The ions that are released as combustion products are captured by the collector electrode; the resulting signal is amplified in a manner similar to that in gas chomatography. After analysis is complete, each sample is manually integrated for the alkane, aromatic, resin and asphaltene peaks.

References

[1] Mehotra, A. *JCPT* **1992**, *31* (09).
[2] Borton, D.; Pinkston, D.; Hurt, M.; Tan, X.; Azyat, K.; Scherer, A.; Tykwinski, R.; Gray, M.; Qian, K.; Kenttämaa, H. *Energy & Fuels* **2010**, *24* (10), 5548-5559.
[3] Mullins, O. The Modified Yen Model†. *Energy & Fuels* **2010**, *24* (4), 2179-2207.
[4] U.S. Department of the Interior. *Heavy Oil and Natural Bitumen Resources in Geological Basins of the World*; U.S. Geological Survey: Reston, Virginia, **2007**.
[5] Fractal Systems, Inc. *Understanding the Value Proposition of the JetShear™ Technology Platform*; Fractal Systems, Inc.: Sherbrooke, Quebec, **2016**.
[6] McKee, R.; North, C.; Podhasky, P.; Charlap, J.; Kuhl, A. *Int. J. Toxicol.* **2013**, *33* (1_suppl), 168S-180S.
[7] Jahan, N.; Fawcett, J.; King, T.; McPherson, A.; Robertson, K.; Werner-Zwanziger, U.; Clyburne, J. *J. mar. sci.* **2015**, *3* (4), 1244-1259.
[8] Brient, J.A.; Wessner P.J.; Doyle M.N. Naphthenic acids. *Kirk-Othmer Encyclopedia of Chemical Technology*, 4; John Wiley & Sons: New York, **1995**; *16*, 1017-1029.
[9] Cyr, T. D.; Strausz, O. P. *J. Chem. Soc*., Chem. Commun. **1983**, 1028– 1083.
[10] Cyr, T. D.; Strausz, O. P. *Org. Geochem*. **1984**, *7* (2), 127– 140.
[11] Strausz, O. P. Bitumen and Heavy Oil Chemistry. In *AOSTRA Technical Handbook on Oil Sands, Bitumen and Heavy Oils*; Hepler, L. G.; His, C., Eds.; Alberta Oil Sands Technology and Research Authority: Edmonton, **1989**.
[12] Ward, C.; Sharpless, C.; Valentine, D.; French-McCay, D.; Aeppli, C.; White, H.; Rodgers, R.; Gosselin, K.; Nelson, R.; Reddy, C. *Environ. Sci. Technol.* **2018**, *52* (4), 1797-1805.
[13] Ward, C.; Armstrong, C.; Conmy, R.; French-McCay, D.; Reddy, C. *Environ. Sci. Technol. Lett.* **2018**, *5* (5), 226-231.
[14] FATE OF OIL AND WEATHERING. http://www.oilspillprevention.org/~/media/Oil-Spill-Prevention/spillprevention/r-and-d/dispersants/3-fate-of-oil-and-weathering.pdf (accessed Mar 9, 2020).
[15] Weathering. https://www.itopf.org/knowledge-resources/documents-guides/fate-of-oil-spills/weathering/ (accessed Mar 9, 2020).
[16] Borrego, A.; Blanco, C.; Prado, J.; Díaz, C.; Guillén, M. 1H NMR And FTIR Spectroscopic Studies Of Bitumen And Shale Oil From Selected Spanish Oil Shales. *Energy & Fuels* **1996**, *10* (1), 77-84.
[17] Quirke, J.; Cuesta, L.; Yost, R.; Johnson, J.; Britton, E. *Org. Geochem.* **1989**, *14* (1), 43-50.
[18] Wolff, G.; Chicarelli, M.; Shaw, G.; Evershed, R.; Quirke, J.; Maxwell, J. *Tetrahedro*n **1984**, *40* (19), 3777-3786.
[19] Eckardt, C.; Carter, J.; Maxwell, J. *Energy & Fuels* **1990**, *4* (6), 741-747.
[20] Barona-Castaño, J.; Carmona-Vargas, C.; Brocksom, T.; de Oliveira, K. *Molecules* **2016**, *21* (3), 310.
[21] Carvalho, C.M.B.; Brocksom, T.J.; de Oliveira, K.T. *Chem. Soc. Rev.* **2013**, *42*, 3302–3317.
[22] Betoni Momo, P.; Pavani, C.; Baptista, M.S.; Brocksom, T.J.; de Oliveira, K.T. *Eur. J. Org. Chem.* **2014**, 4536–4547.
[23] Carvalho, C.M.B.; Fujita, M.A.; Brocksom, T.J.; de Oliveira, K.T. *Tetrahedron* **2013**, *69*, 9986–9993.
[24] Cossy, J.; Belotti, D. *Tetrahedron Lett.* **2001**, *42*, 4329–4331.
[25] El-Sabagh, S.; Faramawi, S.; Harb, F.; Farouk, M. *Egypt. J. Pet.* **2017**, *26* (1), 135-143.
[26] *OPUS*, version 6.0; Software For Infrared Spectroscopy Collection And Processing; Bruker: Billerica, MA.
[27] Coates, J. Interpretation Of Infrared Spectra, A Practical Approach. *Encyclopedia of Analytical Chemistry* **2006**.
[28] Carbon dioxide. https://webbook.nist.gov/cgi/cbook.cgi?ID=C124389&Type=IR-SPEC&Index=1 (accessed Mar 23, 2020).
[29] Afonso, S.; Enríquez de Salamanca, R.; Batlle, A. *BJMBR.* **1999**, *32* (3), 255-266.
[30] Takamura, A.; Watanabe, K.; Akutsu, T.; Ozawa, T. *Sci. Rep.* **2018**, 8 (1).
[31] Dutta Majumdar, R. A Nuclear Magnetic Resonance Spectroscopic Investigation Of The Molecular Structure And Aggregation Behavior Of Asphaltenes. Ph.D., University of Lethbridge, **2015**.
[32] Majid, A.; Pihillagawa, I. *Fuel* **2014**, 1-7.
[33] Kataoka, H. *J. Liq.* **2017**, 1-37.

[34] NIST 2017 Mass Spectral Library; National Institute of Standards and Technology Mass Spectrometry Data Center, **2017**.
[35] Institute, C. How to Test For Sulfur in Materials Using Lead Acetate Test Paper – Canadian Conservation Institute (CCI) Notes 17/5 - Canada.ca. https://www.canada.ca/en/conservation-institute/services/conservation-preservation-publications/canadian-conservation-institute-notes/test-sulfur-acetate-paper.html (accessed Jul 10, 2019).
[36] Access Western Blend Analysis - CrudeMonitor.ca. https://www.crudemonitor.ca/crudes/index.php?acr=AWB (accessed Mar 20, 2020).
[37] POLARIS Applied Sciences, Inc. *A Comparison of the Properties of Diluted Bitumen Crudes With Other Oils*; POLARIS Applied Sciences, Inc.: Vancouver, **2013**.
[38] Fulmer, G. R.; Miller, A. J. M.; Sherden, N. H.; Gottlieb, H. E.; Nudelman, A.; Stoltz, B. M.; Bercaw, J. E.; Goldberg, K. I. *Organometallics* **2010**, *29* (9), 2176–2179.
[39] *Topspin*, version 3.6.1; Software Nuclear Magnetic Resonance Collection And Processing; Bruker: Billerica, MA.
[40] Napolitano, G.E.; Richmond, J.E.; Stewart, A.J. *Soil Sediment Contam.***1998**, *7* (6), 709-724.

Table of Contents

List of Figures

List of Schemes

List of Tables

Table of Symbols and Abbreviations

°	degrees
°C	degrees Celsius
δ	chemical shift
+ve	positive
−ve	negative
Å	Angstrom
aq	*aqueous*
Ar	Aryl
ATR	Attenuated Total Reflection
aux.	auxiliary
avg.	average
br	broad (NMR & IR spectroscopy)
ca.	approximately
calcd.	calculated
CDC	carbodicarbene
cm^{-1}	wavenumber
COSY	correlation spectroscopy
CSD	Cambridge Structural Database
D	doublet (NMR spectroscopy)
DCM	Dichloromethane
dd	doublet of doublets (NMR spectroscopy)
ddtt	doublet of doublets of triplets of triplets (NMR spectroscopy)
dec.	decomposition
DIPEA	*N,N*-diisopropylethylamine
Dipp	2,6-diisopropylphenyl
DMA	*N,N*-dimethylacetamide
e.g.	for example
esd	experimental standard deviation
ESI	electrospray ionization
Et	ethyl
eq.	equivalents
g	gram
HMBC	heteronuclear multiple-bond correlation
HOMO	highest occupied molecular orbital
HRMS	high-resolution mass-spectrometry
h	hours
HSQC	heteronuclear single-quantum correlation
Hz	Hertz
IMes	1,3-Dimesitylimidazol-2-ylidene
in situ	in the reaction medium
in vacuo	under vacuum
*i*Pr	isopropyl
IR	infrared
J	coupling

K	degrees Kelvin
LUMO	lowest unoccupied molecular orbital
m-	*meta*-
m	medium (IR spectroscopy)
m	multiplet (NMR spectroscopy)
Me	methyl
Mes	mesityl; 2,4,6-trimethylphenyl
mg	miligram
mL	millilitre
mmol	milimole
Mp	melting point
NHC	*N*-heterocyclic carbene
NMR	nuclear magnetic resonance
Nu	nucleophile
o-	*ortho*-
OTf	triflate; trifluoromethanesulfonate
p-	*para*-
Ph	phenyl
PI	phosgene iminium
ppm	parts per million
q	quartet (NMR spectroscopy)
qt	quartet of triplets (NMR spectroscopy)
RT	room temperature
s	singlet (NMR spectroscopy)
s	strong (IR spectroscopy)
SiPr	1,3-*Bis*(2,6-diisopropylphenyl)imidazolidin-2-ylidene
t	triplet (NMR spectroscopy)
*t*Bu	*tert*-butyl
td	triplet of doublets (NMR spectroscopy)
^{Ter}Ph	terphenyl; 2,6-di(phenyl)phenyl
THF	tetrahydrofuran
TMS	trimethylsilyl
vs	very strong (IR spectroscopy)
w	weak (IR spectroscopy)
xs.	excess

Chapter 1

1.1 Introduction to Carbocations

Carbon, one of the most prevalent atoms for the building of molecules, is a relatively simple atom compared to others on the period table. Carbon is found in the second row of the periodic table, which means it does not have a large electron shell. Instead, the four valence electrons that it has, making it tetravalent, allow for the formation of four bonds. From valence theory, carbon wants four bonds and four bonds only, any more or less is unfavourable. A carbocation is generally formed from a sp^2 hybridized carbon that has the *p*-orbital electron removed. This removal of the *p*-electron will create a formal positive charge on the carbon atom, with the sp^2 hybridized orbitals arranged in trigonal planar geometry. This has been traditionally referred to as a carbenium cation (Figure 1).

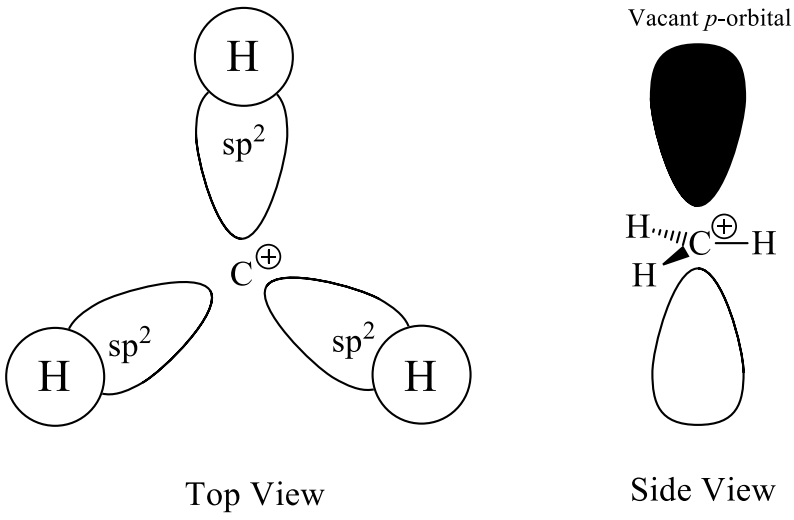

Figure 1: Structure of a carbocation.

Carbocations have had different names through the decades, from the time of their discovery, such as carbonium salts[i] or carbonyl salts,[ii] both of which are sometimes still used today. It was Baeyer, however, in 1902 who recognized the properties of these compounds and was allowed to name them. From then on, the term carbonium ion (or the interchangeably used term carbocation) was used to refer to a trivalent sp^2 hybridized carbon ion. This terminology continued for 70 years until the experiments of Olah[1] (which will be discussed later) forced a change. His synthetic experiments led to the identification of a pentavalent carbocation centre which did not fit the criteria of the definitions at the time. Olah suggested a change in terminology such that the term *carbonium ion* would refer to the pentavalent carbocation, while the term for trivalent sp^2 hybridized carbon ions would be replaced with *carbenium cations*. These two terms would be used to refer to these specific cations, but could be used interchangeably with the term *carbocation* which encompasses both terms in a more general definition. This terminology has remained in place to this day.

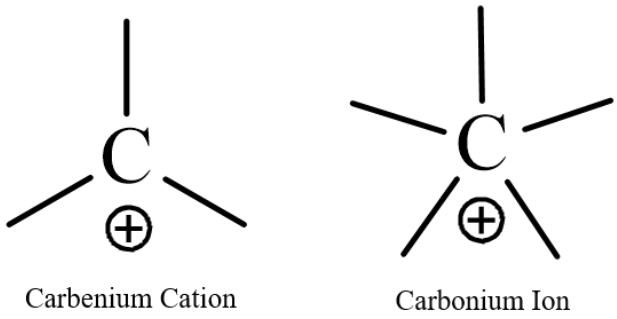

Figure 2: Carbocations: carbenium (left) and carbonium (right) ions.

[i] The term suggested by Baeyer.
[ii] The term suggested by Gomberg.

The study of carbenium cations, also more commonly referred to as carbocations, provides insight into chemical systems. From acting as intermediates in S_N1 reactions, to the salt-like properties that a carbocation possesses in isolatable form,[2] carbenium cations offer unique avenues for chemical reactions. They have applications in organic and organometallics syntheses, and are used to prepare conducting polymers and other synthetic materials. A specific type of carbenium cation, one that will be studied in this work, is the cyclopropenium cation, and by extension, its isomeric structure, the propargyl cation.

1.2 Historical Perspective

The discovery of the carbocation dates back to the turn of the 20th century, from independent observations by J. F. Norris,[3] and F. Kehrmann and F. Wentzel,[4] who were studying M. Gomberg's[5] description of the triphenylmethyl radical. Norris, with his discovery of triphenylcarbinol in concentrated sulfuric acid, and Kehrmann and Wentzel, with their discovery of triphenylmethyl chloride in concentrated sulfuric acid, are credited with the preparation of the first carbocations.[1] Though Norris, and Kehrmann and Wentzel are both credited with the first discovery of carbenium cations, they themselves did not recognize their accomplishments. It was not until a year later in 1902 that Adolf Baeyer realized the salt-like characteristics of the compounds.[1] It was this recognition that sparked the beginning of carbocation chemistry, and ensured a period of great activity in the field.

A number of important characterizations occurred between 1907 and 1930, which established, confirmed, and refined measurements for the ionic nature of the carbocation

species. At the same time, Hans Meerwein was studying the work of Georg Wagner on the ring rearrangements of terpenes.[6] From 1910 to 1925, Meerwein was able to demonstrate that carbon cation intermediates were a fundamental step in Wagner's reactions.[7] It was these rearrangements, which proceeded through carbocation intermediates, that have been designated as the Wagner-Meerwein Rearrangements.[6,7] The results of this early work paved the way to what has been called the "golden age of mechanistic organic chemistry".

The aforementioned "golden age", that lasted from the 1950s to the mid-1970s, was centred on the understanding of reaction pathways, and the identification and characterization of carbocation intermediates. This was possible only after the development of the new and more powerful characterization techniques, Nuclear Magnetic Resonance (NMR) and Infrared (IR) spectroscopies. These techniques help to identify the functional groups and chemical environments of molecules.

An in-depth look at the advancements made in the field of chemistry during this period is beyond the scope of this review, but a few of the important highlights are worth noting. In 1963 E. J. Corey and J. Casanova outlined a series of investigations of the carbocation.[8,9] These investigations provided insight on mechanistic pathways involving the carbocation, and caused some debate at the time. The studies of Roberts and Mazur identified stable carbocation intermediates as well as reversible reactions using carbocations.[10] Gleicher and Schleyer contributed much to the field of carbocations through their investigations of bridgehead ions,[11] which included extensive computational calculations.[12,13]

Finally, in the golden age of carbocations, one researcher contributed an incredible amount to the field and subsequently was awarded a Nobel Prize in 1994 for his work:

George A. Olah. Olah performed numerous studies on carbocations which still resonate today. He recognized the Lewis acidity of these compounds and their affinity to react in the presence any nucleophile. Olah was also able to demonstrate that Lewis acids could be used, not only to generate carbocations, but also to observe them. He was able to stabilize and isolate simple cations and then store them long enough for NMR studies.[14,15] The Nobel Foundation stated "Olah gave the cations of carbon a longer life", since he had extended the life of carbocations by up to a trillion-times.[1]

Olah's ability to create carbenium cations that could exist long enough for extensive analysis opened the way for what is now known as the modern age of carbocation investigation. This period extends from approximately the mid-1970s to the present, and it has allowed major steps forward to be taken in the field, especially with more refinement in characterization techniques such as NMR and X-ray crystallography. One such advancement is seen in the work of Martin Saunder *et al.*, who developed and applied a method of isotopic perturbation of equilibrium, which was observable via ^{13}C NMR spectroscopy.[16] This technique provides an unambiguous answer as to whether or not a system with two limiting structures is in equilibrium or delocalized. Care must be taken in its interpretation, however, as the perturbation of the equilibrium constant can be affected by the greater bond strength of C-D vs C-H, changes in hyperconjugative effects of C-D vs C-H bonds, or changes in basicity. This experimental technique[iii] provides insight into the underlying chemistry for individual chemical systems. It does not provide a generalized answer regarding the stability of carbocations, but instead is a way to distinguish between

[iii] The effect works when there is an isotopic substitution of an otherwise symmetrical system. This increases the stability of one of the equilibrating structures over the other. Deuterium substitution and observation of ^{13}C NMR signals is by far the most commonly used perturbation, but other isotopes are also able to give measurable effects.

possible factors acting within a chemical system. This is evident when comparing the research of Saunders *et al*.[16] with that of McMurry *et al*.[17] The Saunders group was able to demonstrate that the 2-deuterio-2-bicyclo[2.1.1]hexy1 cation exists in equilibrium instead of being delocalized (Figure 3). The McMurry group determined the exact opposite to be true for their system of an *in*-bicyclo[4.4.4]-l-tetradecyl cation.[17] Isotopic perturbation of the equilibrium was used to determine that the McMurry system was delocalized instead of being in equilibrium (Figure 4).

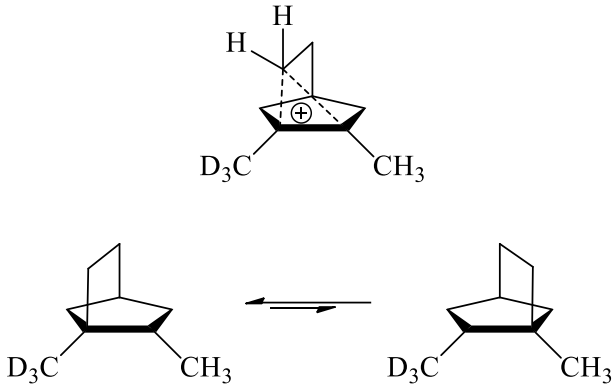

Figure 3: Isotopic perturbation of the equilibrium for 2-Deuterio-2-bicyclo[2.1.1]hexy1 cation.[18]

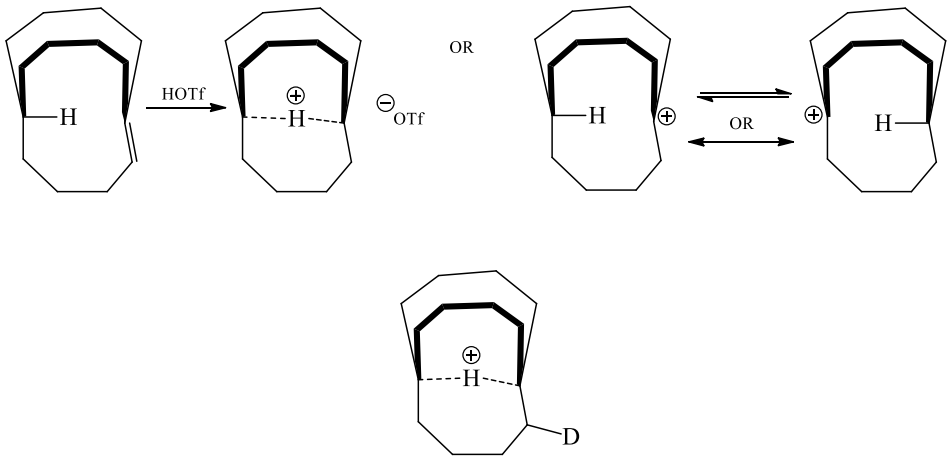

Figure 4: Isotopic perturbation of equilibrium for the *in*-Bicycle[4.4.4]-l-tetradecyl cation.[18] The Saunder's Technique shows a normal isotope shift of 0.8 ppm, rather than the much larger (>10 ppm) shift expected for an equilibrating cation.

The term "isotopic perturbation of equilibrium" does have some controversy around its use. Balzer and Berger [19] argue that the term "isotopic perturbation of resonance"[iv] is being used to explain, and detract from, normal intrinsic isotopic effects. They question whether it is justified to state that one mesomeric form or another is favoured by isotopic substitution. They conclude that "the observed signal displacements can be understood as normal intrinsic isotope effects in cations which are difficult to compare with neutral compounds owing to their unusual chemical shift".[19] They recommend that the aforementioned term(s) should no longer be used in the literature. There are, however, a few issues with the method described by Balzer and Berger.[19] They chose to examine the Δ isotope effect for three structurally similar, symmetrical molecules in order to gauge the isotopic effect difference as substitution moved away from the carbocation charge (Figure 5). Balzer and Berger observed interesting polarization, where the increased substitution in structure **3** created the opposite polarization compared to structure **1**. With these data, they have to correct the intrinsic isotope effects using values for a neutral system. Instead of making comparisons with non-cationic versions of their carbocations, they chose to measure substituted benzene rings, structures **4-6**, with the same R-groups as **1-3**. These not only have different intrinsic isotope effects compared to the neutral versions of **1-3**, but also introduce changes in basicity, resonance, and hyperconjugation not present within the original systems, which further influences the measurements. Another issue (already discussed with the results of Saunders and McMurry) is that different chemical systems present unique perturbations of equilibrium. As Balzer and Berger increased the substitution of the carbocation, they produced the unexpected result of changing the

[iv] The authors explain that the terms "isotopic perturbation of equilibrium or conformation, isotopic perturbation of resonance, and perturbation of hyperconjugation" are all synonymous.

polarity in **3** with respect to **1**. These issues still seem to be reflected in the literature as well, as the use of the terms "perturbation of equilibrium" and its synonyms, has not been abandoned, and they are still being used today.

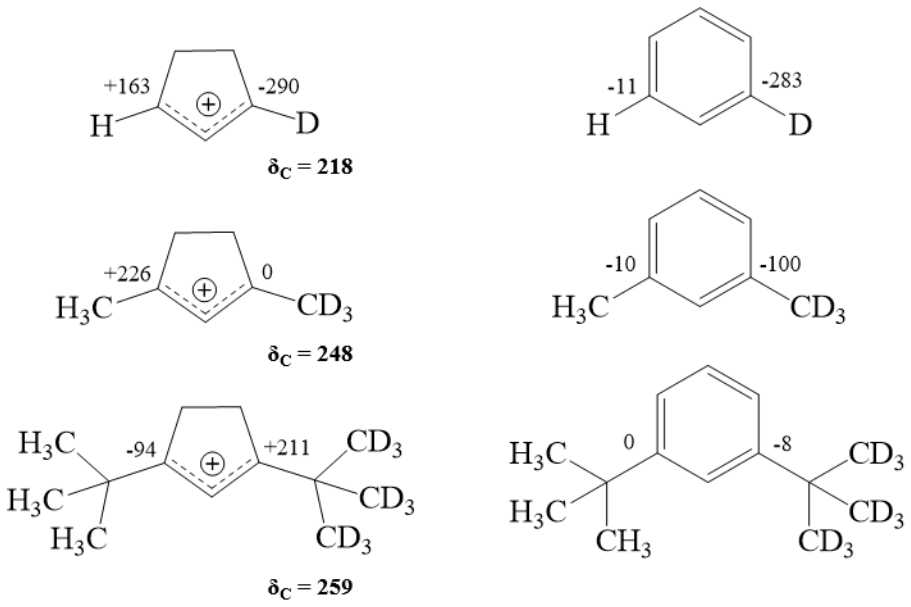

Figure 5: Measurement of closely related carbocation isotopic effects (left) and those in the related neutral compounds (right), adapted from Balzer and Berger. [19]

During the modern period of carbocation discovery, George Olah performed a number of notable experiments on his quest for stable, non-classical carbocations.[v] Olah, in his work on C-H and C-C bond activation, was able to synthesize a carbonium ion under superacid conditions.[20] The implications of this are far reaching. Instead of the normal carbenium cations, R_3C^+, which had been studied up to this point, Olah synthesized a stable new carbocation in the form of R_5C^+. As Olah was able to stabilize these carbonium ions,

[v] A carbocation is denoted by a single electron deficient carbon atom that bears a formal positive charge. A non-classical carbocation is therefore a formal positive charge that is delocalized across multiple carbon atoms.

intensive IR, NMR, and spectroscopic studies could be performed. This also led to extensive work in a new aspect of chemistry at the time, the study of super electrophiles.

While Olah was able to help shape our understanding of the carbocation, there was some controversy in his pursuit: had he prepared a classical or non-classical carbocation? Both George Olah and Saul Winstein were supporters of the existence of non-classical carbocations while others, such as Herbert Brown, thought that non-classical carbocations were not possible. This debate arose from what is now known as one of the most famous examinations of a non-classical carbocation, published by Winstein and Trifan in 1949. These authors reported the synthesis of the bicyclo[2.2.1]-2-hexyl carbonium ion (also known as the norbornyl cation).[21] This debate did not end until 1983 when Olah conclusively proved the existence of non-classical carbocations by studying the 2-norbornyl cation.[22] Through an X-ray photoelectron spectroscopic study, Olah was able to observe a 3-centre 2-electron bond, also known as a hyper-coordinate bond. Since this can only be a marker for a non-classical carbocation, Olah was able to prove its existence, thus ending the controversy over the existence of such carbocations.

1.3 Phosgene Iminium Salts

The use of phosgene iminium salts has become a popular method for generating stable carbocations. Phosgene iminium (PI) salts (Scheme 1) are convenient electrophiles for the addition of a one-carbon unit, at its highest oxidation level, to a variety of substrates.[23-26] The PI salt dichloromethylene dimethyliminium chloride[23-26] is the most commonly used reagent that falls within this classification. There are many methods for

the preparation of dichloromethylene dimethyliminium chloride; all of these involve the chlorination of thiocarbonyl compounds, with the most commonly used being the exhaustive chlorination of thiuram disulfide (Scheme 1).[23,24,26-29]

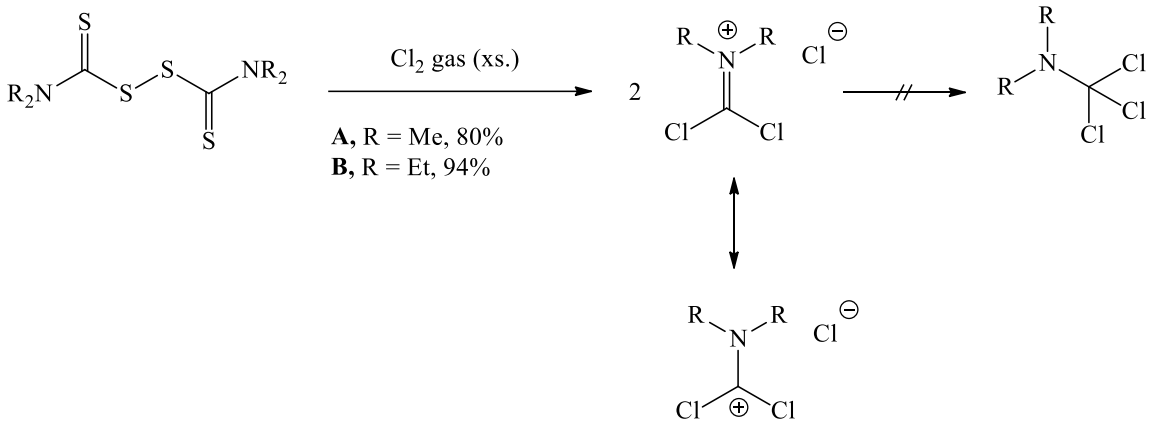

Scheme 1: Synthesis of PI salts,[23,24,26-29] via exhaustive chlorination of thiuram disulfide.

The PI salts shown in Scheme 1 have been known since 1959,[26,27] however, this class of compound was almost forgotten until Viehe *et al*. began their systematic investigations in 1971.[26,30] Due to the numerous contributions made by Viehe and his group, dichloromethylene dimethyliminium chloride (Scheme 1, R = Me) is now commonly referred to as *Viehe's Salt.*[23-26] Although the salt has been known for over 50 years, the structure of Viehe's Salt has remained speculative until recently.[26,35] It was generally accepted that Viehe's Salt exists as the ionic structure depicted in route **A** of Scheme 1, due to its low solubility in non-polar solvents[23-26,30]. The ionic nature of Viehe's Salt has only recently been separately confirmed by Land,[26] and Regnier *et al.*[31] through X-ray crystallographic determination of its structure, though the anion was determined to be HCl_2^- and not Cl^-.

Viehe's Salt is commercially available, highlighting its utility as a powerful synthon. It has been extensively studied;[23-26] several review articles have previously been published and therefore these will not be reproduced here. Additionally, there is no reported spectroscopic evidence to support the existence of the covalently bonded structure, the rearrangement isomer shown in Scheme 1.

1.4 Reactions of Halopropenium Salts

Through various reactions of Viehe's salt, it is possible to prepare halopropenium salts, where the C_3 fragment is a good starting point for ligand design (Scheme 2).[32,33] It is unsaturated and the delocalized positive charge, in the form a of a carbocation, can be used to stabilize charged species, but it can also form a rigid backbone. The electrophilic C3 framework is a potentially useful precursor because it can undergo addition reactions. In this work, the preparation of 1,3-dichloro-1,3-*bis*(dimethylamino)propenium hydrogendichloride was carried out using known literature methods,[30, 34] primarily following the synthesis described by Land.[26] The preparation of the halopropenium salt A was further improved by Land [35] after the completion of his thesis work. The halopropenium salt A was reported by Land[26,35] to be unstable under atmospheric conditions; decomposing rapidly with exposure to oxygen and/or water. In order to prevent this, an anion metathesis reaction was performed with potassium hexafluorophosphate (Scheme 2), which yielded salt B, that was determined to be air and water stable.[26,35]

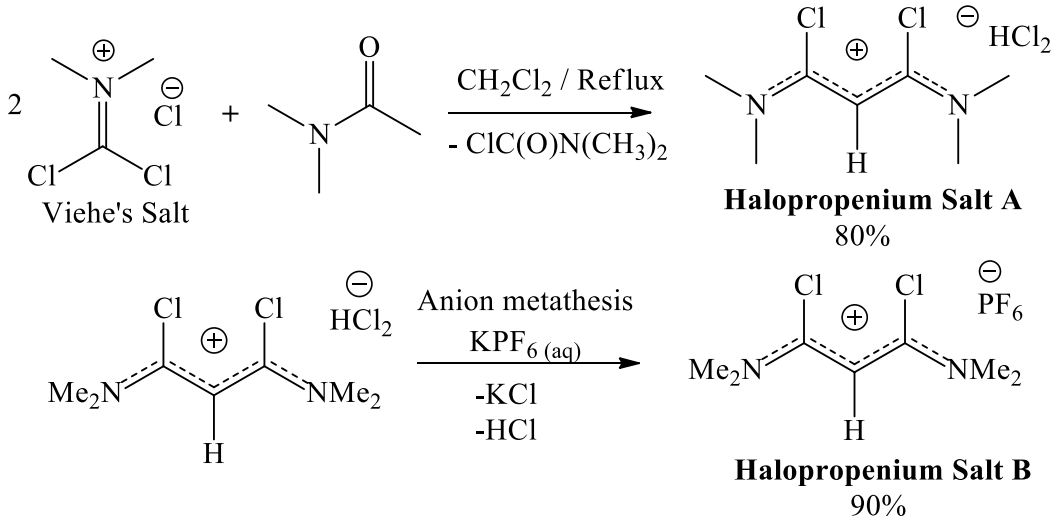

Scheme 2: Synthesis of the chloropropenium salts A and B[26,32,33,35] from the phosgene iminium salt, Viehe's Salt.

The generation of the halopropenium salts creates a versatile starting material for different organic reactions. Both Regnier *et al.*,[31] and Furstner *et al.* [36] have synthesized halopropenium salts and performed organic reactions with them. Regnier *et al.*[31] used them to generate imidazolium salts, which then can be used to form N-heterocyclic carbenes. In contrast, Furstner *et al.*[36] used the halopropenium salts to generate allenes. Land[26,35] and Viehe[30] have shown that halopropenium salts can be used to generate propargyl carbocations.

1.5 N-Heterocyclic Carbenes

A carbene is defined as a neutral compound containing a divalent carbon atom, with a six-electron valence shell.[37] This deficient electron shell creates high reactivity, and instability within the structure. Typically, carbenes can be classified as being in either the singlet or triplet state. For a singlet carbene, the electrons on the divalent carbon atom are

spin-paired in the ground state, usually in a sp^2 hybrid orbital. A triplet carbene is formed when the electrons are unpaired in the ground state, with one of the electrons in a higher energy orbital. Typically for a carbene, the triplet ground state is favoured over the singlet ground state.

Carbenes generally exist on a short time-scale, although stable carbenes can be formed; these exist as the free-carbenes and are generally N-heterocyclic carbenes (NHCs). Many NHCs contain imidazole-based rings with bulky side groups coordinated to the nitrogen atoms of the ring to provide stabilization. In their reactions, NHCs are often converted to salts where the positive charge is delocalized over a portion of the central carbene ring. In the case of the imidazole-based carbenes an imidazolium carbocation is formed.

NHCs are a class of stable singlet carbenes with a neutral divalent carbon atom directly attached to at least one nitrogen atom within a heterocyclic scaffold.[38,39] The presence of the nitrogen atom allows for the donation of π-electrons into the empty *p*-orbital of the carbene carbon.[37] The stability of a NHC is further increased due to the cyclic structure, as this forces the carbene carbon into a bent, sp^2-like arrangement.[37]

There are innumerable tetravalent carbon compounds, in which all four valence electrons of each carbon are engaged in bonding. Compounds in which a carbon has only two electrons involved in bonding, while two nonbonding electrons remain at the carbon atom, are far less common. These divalent carbon derivatives comprise carbon monoxide, isocyanides, and carbenes. While examples of the two former types of complexes have been known for more than a century, carbenes were initially only observed when stabilized in metal complexes.[40-43] Wanzlick and Schikora proposed the synthesis for imidazolidin-

2-ylidene in 1960. This was to be done by the α-elimination of chloroform from an imidazoline derivative, but only the dimeric enetetramine[vi] was isolated.[40,44] It was not until 1988 that Bertrand was able to synthesize a stable carbene, [*bis*-(diisopropylamino)phosphino](trimethylsilyl)carbene.[40,45] This compound was stabilized by the phosphorus and silicon substituents next to the central carbon atom. Following this, 1,3-*bis*(adamantyl)imidazol-2-ylidene was isolated in 1991 by Arduengo *et al*.[40,46] The presence of the bulky substituents adjacent to the carbene carbon created an additional stabilization effect for the carbene. Dimerization of the compound was sterically less favourable, a problem that had been observed with the structure of Wanzlick.[37,40,44] The carbene isolated by Arduengo *et al*.[40,46] was the first NHC that was stable enough to be produced and sold as a reagent, and their study sparked research on these compounds which has not abated in over three decades.

1.6 Imidodiphosphinate Ligands

Though many persistent carbenes exist as in the form of imidazole-based carbenes, there has been little evidence for the formation of carbon analogues of NHCs, where the carbene carbon is not adjacent to electron donating nitrogen groups.[47,48] These carbenes are known to exist in the triplet state,[49,50] and have been shown to have short half-lives, on the order of 40 minutes. A persistent carbo-carbene analogue, might be captured, using a method similar to that described by Bertrand *et al.*[45,51] for the phosphinocarbenes. One

[vi] In a dimeric enetetramine the carbenic carbon double bonds to another carbenic carbon.

possible way to capture a carbon analogue of an NHC could be through the use of an imidodiphosphinate ligand.

Several classes of phosphorus-nitrogen compounds can both interact with metals and be used in inorganic catalyst synthesis. In these classes of phosphorus-nitrogen bonded compounds both atoms hold an oxidation state of three and exhibit Lewis base donor abilities.[52] Imidodiphosphinate ligands (also known as PNP ligands[52]) consist of a framework of one nitrogen atom bonded to two dialkyl phosphorus (III) groups. These phosphorus (III) atoms are typically bonded to two R-group substituents on each side of the symmetric ligand.[52] The PNP ligand itself has been shown to adopt two tautomers (Figure 6). The first form has a proton bonded to the nitrogen, and the other form has the proton bonded to one of the phosphorus atoms of the ligand. The tautomer that predominates depends on the R-group substituents of the PNP ligand, and on the reaction conditions.[52,53] PNP ligands are able to coordinate in a number of ways, monodentate (through either nitrogen or phosphorus), bidentate, or ambidentate. The Lewis acidity is different across the ligand, where the nitrogen atom generally behaves as a hard Lewis base, while the phosphorus atoms behave as soft Lewis bases. The most likely site of reaction in the PNP ligand are the phosphorus atoms, as they are able to act as π^* acceptors.[52,54] The nitrogen atom is less likely to be the site of reaction as it is a poor π^* acceptor and thus has little potential to accept electron density via back-donation.[52] This ability of the PNP ligands to accept back donation is relevant when considering carbocations and propargylenes, as PNP ligands may be able to capture and stabilize such species. Due to the reactivity of the compounds presented in Sections 1.3-1.5, PNP ligands

might be able to reversibly coordinate such molecules. Doing so could result in the generation of carbodicarbenes or propargyl carbocations.

Bis(diphenylphosphino)amine is the most commonly used form of the PNP ligand, however, the isopropyl analogue, *bis*(diisopropylphosphino)amine, is also used,[52] and both have been utilized in this work. The phenyl and diisopropyl PNP ligands are both synthesized in the same manner, from the addition of the respective substituted chloro-phosphine to *bis*(trimethylsilyl)amine. The synthesis of the phenyl substituted PNP ligand is attributed to H. Nöth and E. Fluck,[55] while the diisopropyl substituted PNP ligand is attributed to Ritch *et al.*[56] The solid-state structures of both of these compounds are known,[55,57] and are found in the Cambridge Structural Database (CSD).[58]

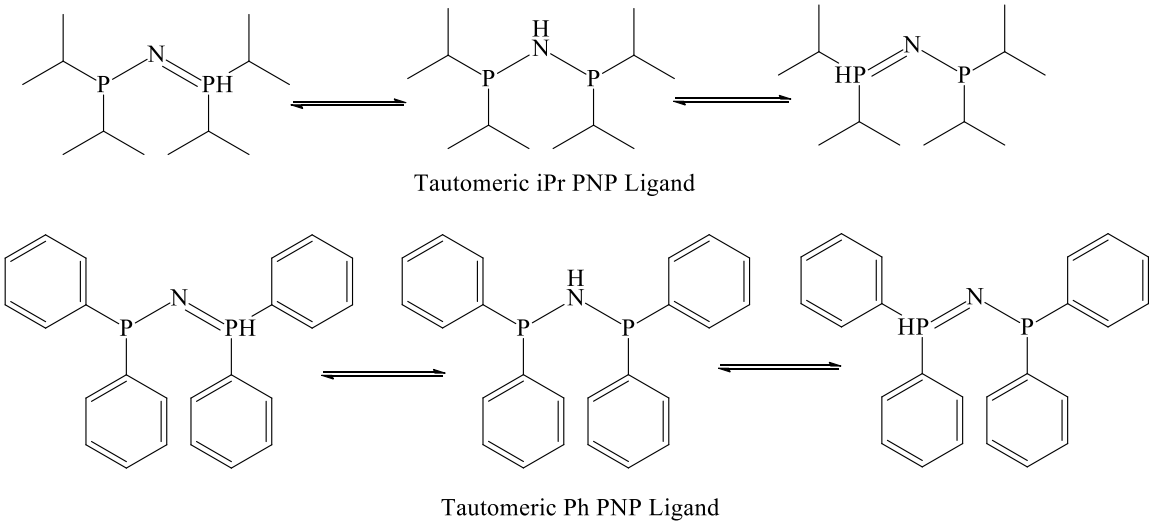

Figure 6: Tautomeric structures of the diisopropyl and diphenyl PNP ligands.

1.7 Carbodicarbenes/Bent Allenes

Allenes[59] have been a fascination for chemists, both experimentally and theoretically, for decades.[60] Allenes are compounds with the general formula $R_2C=C=CR_2$ in which the two π-bonds on the central carbon atom are orthogonal to each other giving a C-C-C angle of 180°,[60] and where the R_2C groups in the general formula $R_2C=C=CR_2$ are N-heterocyclic carbenes. Not only are allenes generally formed from NHCs, but they themselves can be thought of as carbenes. Instead of having a central C=C=C group, allenes can be thought of as carbodicarbenes instead, where the lone pairs of the NHCs form a coordinated covalent bond, as shown in Figure 7. Allenes are of interest in the field of chemistry as their reactivity and selectivity can be tuned via electronic and steric effects by changing the substituents on the NHC.[61] Bent allenes are systems with a nonlinear C=C=C framework, and are characterized by π-bonds that are no longer completely orthogonal.[60,62,63] G. Bertrand[63] has suggested that the weakening of the π-bonds leads to a bending of the C=C=C framework in allenes. This effect can be regulated on the basis of the electron-withdrawing and electron-donating characteristics of the substituents bound to the allene.[60,63,64] Allenes and bent allenes normally exist with relatively linear structures, with the C=C=C angles ranging from ∼100° to 170°.[62] Although there is controversy in assigning allenic character to some of these systems,[65] the current understanding is that allenes with zwitterionic character are still classified as allenes.[66] In rare examples, severe bending within the allene π-system causes extreme electronic disturbances. This results in the central carbon atom no longer being *sp* hybridized as is found in a typical all-carbon allene. Instead, it attains a unique configuration with two lone pairs of electrons on the central carbon, and two NHC ligands acting as donor groups.[60,64] As has been described by

G. Frenking, after extensive study of the electronic systems of bent allenes, they can be drawn as divalent carbon (C(0)) systems (L→ C ←L) with a novel bonding environment for carbon (Figure 7).

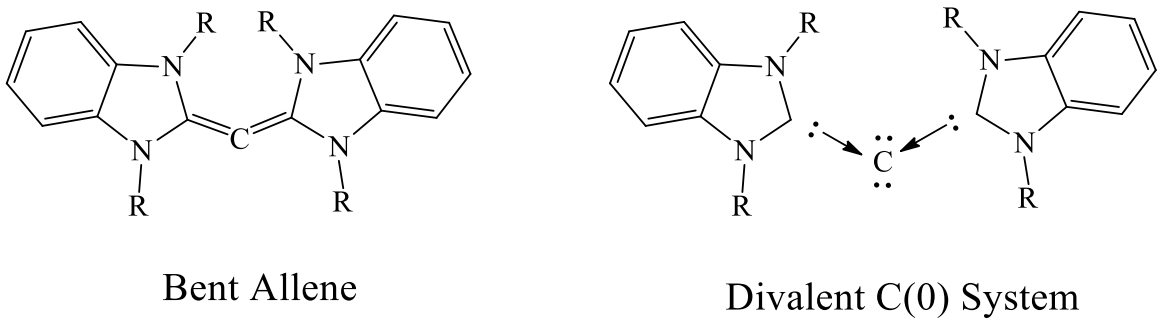

Figure 7: Possible structures of bent allenes.

These divalent C(0) systems are defined by three criteria.[60,67] The first is that the central carbon atom accepts electrons from electron-donating groups. The second is that there are two lone pairs on the central carbon atom occupying σ- and π- type orbitals, and the last is there is high nucleophilicity at the central carbon. These compounds are found to be different from carbenes, where the carbon atom has one σ-type lone-pair orbital and a formal oxidation state of two (divalent carbon (0)).

1.8 Propargylenes, C_3H_2 Isomers and their Structures

The structure of the simplest allene is one possible form of the propargylene molecule, C_3H_2. This molecule (**^{3}1,** Figure 8) has not yet been isolated, and its characterization and properties remain unknown. However, high level computational chemistry does provide predictions of its geometry, electronic structure, and relative stability. The molecule was discovered by Skell and Klebe[68,72] and predicted to exist in a

triplet ground state (^{3}**1** in Figure 8) due to molecular orbital considerations.[69,72] High level computational calculations support the idea that propargylene exists in a triplet ground state,[vii] though both its exact geometry and electronic structure are still debated.[70,72]

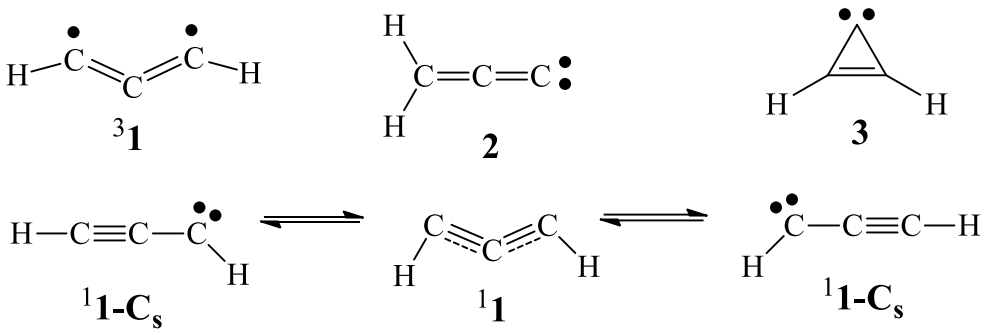

Figure 8: Structures of relevant C_3H_2 isomers;[72] all molecules are in the triplet state as determined by high level computational calculations.[68-70,72]

It was originally thought that triplet propargylene favoured the structure ^{1}**1-C$_s$**, having both electrons localized on one sp^2 hybridized carbon atom, similar to other carbenes.[70] This structure was thought to provide increased stabilization over that of ^{3}**1**, where there are unpaired electrons on two different carbon atoms. Continued investigations into the structure of ^{1}**1-C$_s$** did not yield any further insight; this was due to the fact that there was very high spin contamination of the Unrestricted Hartree-Fock (UHF) calculations, combined with the fact that the structure was not at minimum energy at higher levels of theory.[70] These results led R. Herges and A. Mebel[70] to apply the quadratic configuration interaction (QCI) method and the multireference configuration interaction

[vii] This is traditionally a contradiction, as it is uncommon that the triplet state is lower in energy than the singlet state. Since the triplet state is the lowest in energy for these molecules, it is the ground state for the molecule.

(MRCI) method to their calculations. They reached the conclusion that propargylene (^{3}**1**) predominantly exists as a quasilinear C_2 diradical species.

Though this structure is predominant, natural resonance theory suggests the ^{1}**1-C$_s$** structure is still a significant contributor and must not be discounted from the stable state of the molecule.[71] Even though propargylene has a triplet ground state, with a considerable singlet-triplet energy gap of ~58 kJ/mol,[70] the singlet species (structure ^{1}**1**) should not be neglected.[72] A method similar to that used to investigate the triplet energy surface was utilized to study singlet propargylene (structure ^{1}**1**). The structure was predicted to have C_{2v} symmetry and consist of a transition state that is frozen between the two ^{1}**1-C$_s$** structures, with localized lone pairs and an energy barrier between ^{1}**1** and ^{1}**1-C$_s$** of ~9 kJ/mol.[70]

The computational investigations of propargylene revealed that it has two isomers which were identified as having local-minima on the C_3H_2 potential energy surface (PES),[73] vinylidenecarbene (structure **2**), and cyclopropenylidene (structure **3**). Both of these isomers exist in singlet ground states, unlike propargylene which has a triplet ground state, with C_{2v} symmetry.[73,74] Calculations performed by DeFrees predicted that **3** is the global minimum on the C_3H_2 PES,[73] while Osborn *et al*. calculated ^{3}**1** and **2** to be ~51 kJ/mol and ~59 kJ/mol higher in energy than structure **3**, respectively.[75] This shows that structure **3** is the global minimum for C_3H_2 structures, with the singlet state being lower in energy than the triplet state. This implies that all C_3H_2 isomers can autoisomerize to structure **3**, provided there is sufficient activation energy available.

1.9 Propargyl Carbocation Reactivity

Though the propargylene structure is similar to that of a propargyl carbocation, they are not the same compound. This is because the propargylenes described by Skell and Klebe[68,72] are radical species, while the propargyl carbocation is a cationic species. Not only this, but a propargyl carbocation can also be thought of as an allene. This is because a propargyl carbocation can exist in the form $C3{\equiv}C2\text{-}C1^{+}(R)_2$ (the predominant structure),[76] or $C3^{+}{=}C2{=}C1(R)_2$ (the subsidiary structure)[76] through resonance (Refer to Figures 9 and 10 in this Chapter, and Scheme 11 in Chapter 4). This can be seen from the dissociation channels resolved by Fischer[77] for a propargyl radical species (Figure 9). This also helps to support the work of Skell and Klebe[68,72] for the stable structures of the C_3H_2 isomers (Figure 8). The structure of a propargyl carbocation is shown in Figure 10, where it is believed that the C1 and C3 carbons are the best sites for nucleophilic attack to take place. This is supported by the work of Fischer,[77] as the propargyl radical cation shows rearrangement to the 1-propene-1-yl-3-ylidene structure, which has a lone pair of electrons on the C3 carbon. Though a radical species is different from a carbocation and more reactive, it does provide insight on how a carbocation might resonate or even potentially rearrange. The work of Fischer[77] also shows that an allyl radical is able to take the form of either a propargyl complex or an allene complex after elimination of H. This would imply that a propargyl complex could be converted to an allene complex, as mentioned earlier. Rearrangement would be due to resonance in a carbocation, instead of due to loss of H such as occurs in allyl radical species.

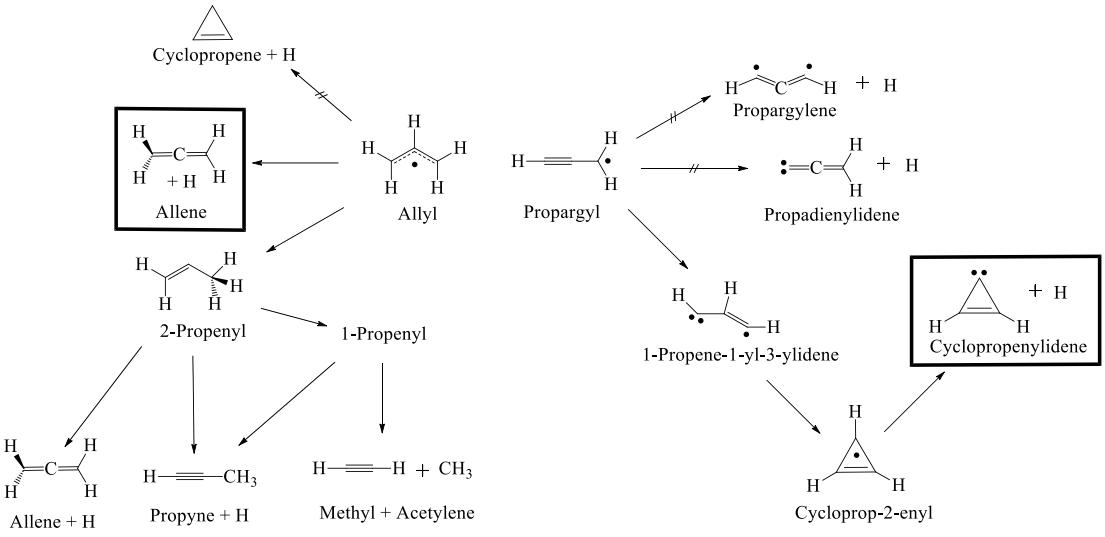

Figure 9: Summary of the most important unimolecular dissociation channels for allyl and propargyl at energies corresponding to UV excitation. Boxes drawn around lowest energy molecules for allyl and propargyl routes. Adapted from the work of Fischer.[77]

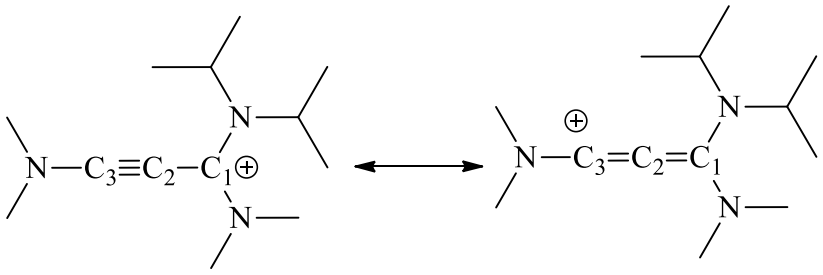

Propargyl Carbocation

Figure 10: Structural example of a propargyl carbocation. Only the two resonance structures discussed above are depicted here.

1.10 Cyclization of Propargyl Carbocations

Two cyclization reactions of note are available for propargyl carbocations, the Huisgen cycloaddition[78,79] and the Diels-Alder reaction.[80] Both of these reactions are well documented in the literature and their mechanisms are well understood. In the case of the Huisgen cycloaddition, an azide (usually organic) in the presence of an alkyne reacts, to form a 5-membered ring, with the first and third nitrogen atoms in the azide (see Figure 11). By definition, this reaction is concerted, with the necessary bonds breaking and then forming in a single step.

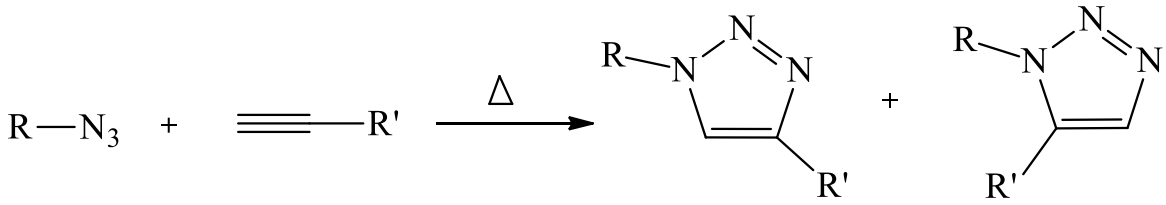

Figure 11: Reaction equation for the Huisgen cycloaddition.

Unfortunately, the thermal Huisgen 1,3-dipolar cycloaddition of alkynes to azides usually requires elevated temperatures and often produces mixtures of the two regio-isomers when using asymmetric alkynes. To circumvent this, it was discovered[78,81] that the use of copper or ruthenium catalysts allows for regioselectivity of the cycloaddition (Figure 12). The Cu reaction, although no longer concerted, has several advantages over the Huisgen cycloaddition; it is fast, requires low temperatures, and forms the product in high yields. This form of copper catalyzed cycloaddition is thus recognized as a different reaction from the Huisgen cycloaddition, as it is no longer concerted. Instead, it is classified as a Copper(I)-catalyzed azide-alkyne cycloaddition (CuAAC), or more commonly

referred to as "Click Chemistry".[viii] The copper-catalyzed reactions can be carried out in aqueous conditions, at room temperature, and give the 1,4-disubstituted regio-isomers specifically; the ruthenium-catalyzed reaction gives the opposite regioselectivity with the formation of 1,5-disubstituted triazoles. The CuAAC and RuAAC reactions satisfy all of the requirements to be considered as true click reactions.

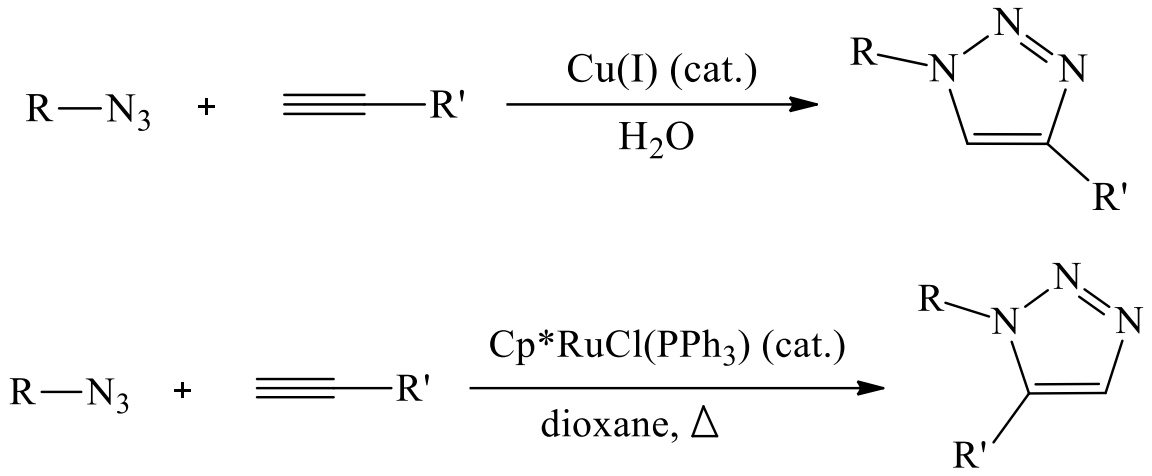

Figure 12: Azide-alkyne cycloaddition regioselectivity resulting from the addition of a catalyst, top Cu(I) and bottom Cp*RuCl(PPh_3).

Another issue with the Huisgen reaction is that it requires a terminal alkyne to proceed. There are examples of reactions carried out with substrates that contain both a terminal and non-terminal alkyne showing that only the terminal alkyne reacts, with no isomerization detected.[79] This issue can be overcome, however, by the use of an appropriate catalyst. The use of ruthenium catalysts[ix] has been documented to allow cycloaddition reactions on non-terminal alkynes.[79]

[viii] RuAAC in the case of a ruthenium catalyst.
[ix] The catalyst is usually added in the form of Cp*RuCl(COD) or Cp*RuCl$(L)_2$ (where L is any ligand). Copper catalysts, in the form of SiO_2-NHC-Cu(I), have also been demonstrated to work.

Through the use of a propargyl carbocation, it is believed that azide cycloaddition could occur without the introduction of a catalyst. Having a carbocation adjacent to the alkyne should create electron delocalization which may be enough to overcome the energies required for a Huisgen cycloaddition. In this case, the reaction may not be true "click" chemistry, as it will still proceed through the Huisgen cycloaddition. It will be similar to "click" chemistry in that it will be a fast reaction, carried out at low temperature, and giving a high yield. In this case, as it is believed that the mechanism will have to proceed through a concerted reaction, it will still fulfill the definition of a Huisgen cycloaddition. However, it will have to be determined if the reaction is stereoselective under these conditions. If it is, it will have become a true click reaction. Another possibility is that instead of undergoing a concerted reaction, the nucleophilic azide will attack the propargyl carbocation, which will then undergo an autocyclization to form the triazole ring. This, however, is unlikely as organic azides that cyclize tend to form cyclic amines, with N_2 being produced as a by-product.[82]

The other type of cycloaddition reaction that can be carried out on a propargyl carbocation is the Diels-Alder reaction (Figure 14), which is relatively straight-forward compared to the Huisgen cycloaddition. This reaction entails the [4+2]-cycloaddition of a conjugated diene to a dienophile (an alkene or alkyne[x]). This is an electrocyclic reaction that involves the 4 π-electrons of the diene and 2 π-electrons of the alkyne. The driving force of the reaction is the formation of new σ-bonds, which are energetically more stable than the π-bonds they replace.[80,83]

[x] The term alkyne will be used in the remainder of this section, but do note that alkenes are also utilized in this type of reaction.

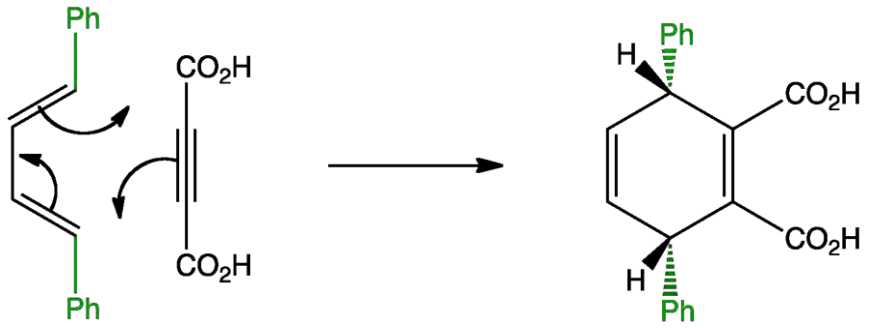

Figure 13: The mechanism of a Diel-Alder reaction illustrated using an alkyne substrate.

Overlap between the highest occupied molecular orbital (HOMO) of the diene and the lowest unoccupied molecular orbital (LUMO) of the alkyne is thermally allowed in the Diels-Alder reaction, provided that the orbitals are of similar energy (see Figure 14). The reaction is facilitated by electron-withdrawing groups on the alkyne, since this will lower the energy of the LUMO, while the diene component should be as electron-rich as possible.[80,83]

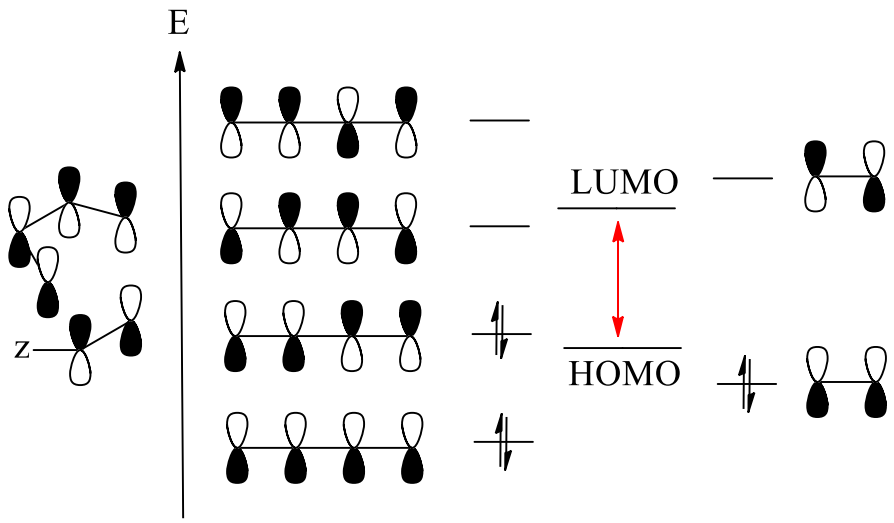

Figure 14: Molecular Orbital diagram for a Diels-Alder reaction.

In the recent literature it has been shown that Diel-Alder reactions are possible with non-terminal alkynes, both with and without the use of a catalyst.[84,85] Diels-Alder reactions, or any of the other reactions discussed in this section, should be possible with the compounds of interest in this thesis, the propargyl carbocations. Coordination reactions can occur at the alkyne site of propargyl cations with both electron donating and electron accepting materials. For electron donating ligands, common choices, such as cyclopentadienyl (Cp) or pentamethylcyclopentadienyl (Cp*), are able to donate electron density in a manner similar to that of a carbene. However, instead of a single carbon on the ligand being the site of bond formation to the π-system of the alkyne, all five (η^5) of the Cp or Cp* carbon π-electrons are able to coordinate to the propargyl cation due to the delocalized charge of the ligands.

Two different scenarios must be considered; in the first, the Cp or Cp* ligands are subject to potential ring slippage.[86] The ring anion is potentially able to coordinate to an electron acceptor, with the number of electrons equal to η^x, where x is the number of carbon atoms with π-electrons coordinating to the acceptor.[xi] Ring slippage occurs when there are fewer coordinating π-electrons than the maximum number of carbon atoms in the ring. In the second scenario, the Cp or Cp* ligand undergoes an anion metathesis, rather than coordinating to the propargyl cation, replacing the anion in the propargyl carbocation salt. This reaction is only possible if cyclopentadienide is added instead of the freshly deprotonated ligand.

[xi] The number of carbon π-electrons that coordinates to a site cannot exceed the number of carbon atoms in the ring with the delocalized electron charge.

These scenarios show that the reaction of a propargyl carbocation with electron donating ligands, such as Cp or Cp*, could result in either a Diels-Alder or an anion metathesis reaction. A Diels-Alder reaction is possible, as the electron donating ligand would be able to add across the unsaturated CC triple bond, resulting in a cycloaddition. For the metathesis reaction to occur, the Cp/Cp* would have to have a greater affinity for the compound than the original anion has. The Cp/Cp* would also have to remain negatively charged, otherwise it would disrupt the ionic system of the propargyl carbocation.

1.11 Reactions of Propargyl Carbocations and NHCs.

With the generation of a propargyl carbocation from an NHC, as described by Barry *et al*.,[87] and from halopropenium salts, as described by Land,[26,35] it is surprising that a direct reaction between a propargyl carbocation and a carbene has not yet been reported. The carbene is a strong nucleophile due to the presence of two unshared valence electrons on the carbenic carbon. The expectation was that a nucleophilic attack would occur at the C3 carbon of the alkyne in the propargyl cation. The reaction should happen almost instantly due to the nearly non-existent activation energy required for a carbene.[88] In this reaction the C3 carbon would accept the valence electron pair from the carbene, which would destabilize it and force π-electrons to break into the (R)-C3≡C2-C1^{+}-(R')(R") backbone. This would then rearrange to an (R)(R^{+})-C3=C2=C1-(R')(R") structure where the new R^{4} substituent[xii] has formed a carbocation (Figure 15). There is experimental evidence to show

[xii] The R^{4} substituent is from the carbene addition.

that carbene and carbon radicals do form such carbocationic structures following their reaction.[89-91] As discussed earlier, the combination of a bent allene and a carbocation could undergo further auto-isomerization, as calculated by Osborn, to give a cyclic structure provided there is sufficient activation energy.[75]

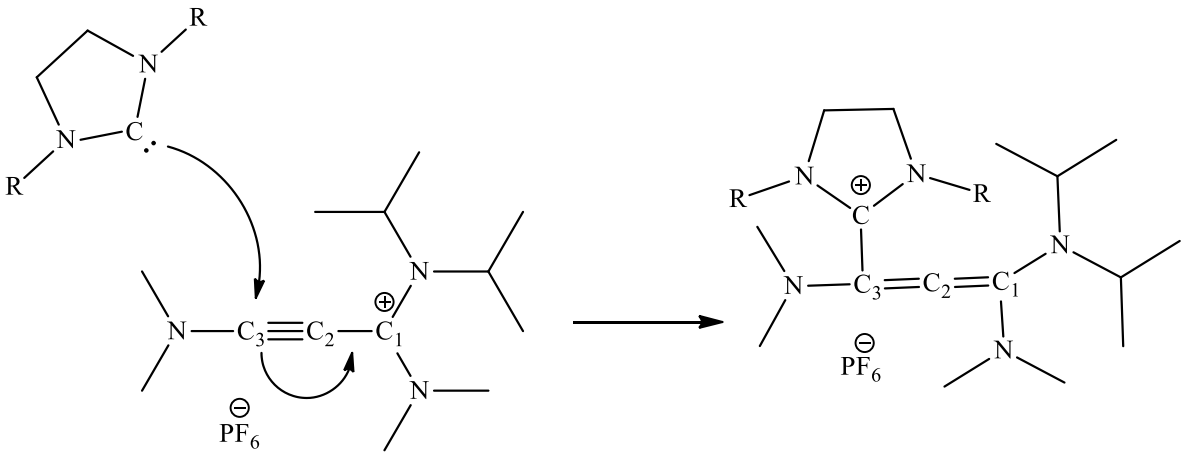

Figure 15: Generation of an allene from an NHC and a propargyl carbocation.

None of these reactions have been documented in the literature to date. This lack of groundwork can be attributed to the fact that propargyl cations have not been studied extensively. Only a handful of papers document the synthesis of reactive propargyl complexes, including those by the groups of Bertrand,[92] Masuda,[93] and Clyburne.[26,35,87]

With the propargyl cation being so electron rich at the site of the alkyne, this substituent can readily undergo electrophilic addition in the presence of available nucleophiles. This leads to a wide range of possible chemical reactions including cyclization, addition, reduction, or coordination. As discussed by Barry *et al*.,[87] a propargyl carbocation can be reduced to a cumulene after reaction with potassium graphite (KC_8).[87]

This reaction disrupts the ionic salt-like properties of the carbocation, and produces a neutral compound. The product can exist in one of three potential forms: as a neutral open-shell biradical (singlet or triplet) or as a neutral closed-shell singlet cumulene.[87,94] Of these three potential forms, the closed-shell singlet structure possesses the lowest energy, which makes it the most favoured, and thus the most likely to form.

In this work I have expanded on the results of Barry *et al.*[87] and of Land.[26,35] I have made propargyl cations. I have reacted them with a variety of nucleophiles to determine the site of coordination. I have successfully carried out cyclization reactions. I have also prepared a number of new PNP complexes and also a variety of *m*-terphenyl iminium salts. All of the products have been studied by a combination of spectroscopic techniques and X-ray crystallography.

Chapter 2

2.1 Synthesis and Reactivity of PNP Compounds

Phosphorus-nitrogen-phosphorus (PNP) pincer ligands are compounds that have undergone a great deal of research devoted to their capture of other molecules.[95-98,102,103] Though they are usually used as chelating agents to bind to metals, they can also be used to capture main group elements. From this, it was believed that a PNP ligand might bind to and stabilize an aryl carbene generated *in situ* with the ligand. PNP ligands have been synthesized in the same manner since the 1970s,[99] via reaction of a phosphoranimine with a halogenated phosphine.[96] Once synthesized, the PNP ligands used in this section exist as tautomeric complexes with the Lewis acidic proton shifting between the P and N positions. This effect primarily exists when the PNP ligand is dissolved in solution, however, Elder *et al*.[100] have shown that tautomers can also exist in the solid state in some coordinated PNPs. The solid-state structures[55,57] of the free ligands generally show that these structures exist with a protonated nitrogen atom. The acidic proton is a good leaving group, creating a delocalized electron pair across the PNP bonds. This electron density can be used to capture materials with a new PNP complex being formed.

In this work, the generation of an aryl carbene from 9-diazofluorene was attempted. It was believed that reaction of 9-diazofluorene with a phosphorus-nitrogen-phosphorus (PNP) ligand would result in the removal of the diazo group from the fluorene to produce the 9-fluorenylidene complex shown in Figure 16. This would be an aryl carbene as it would not be stabilized by adjacent nitrogen atoms, instead it would be stabilized by resonance of the delocalized electron density. It was also believed that the presence of the

PNP ligand would act as further stabilization for this aryl carbene. The generation of such a compound was of interest as a potential entry point into allene chemistry, or for the generation of a new type of propargyl carbocation by reaction with an acetylene.

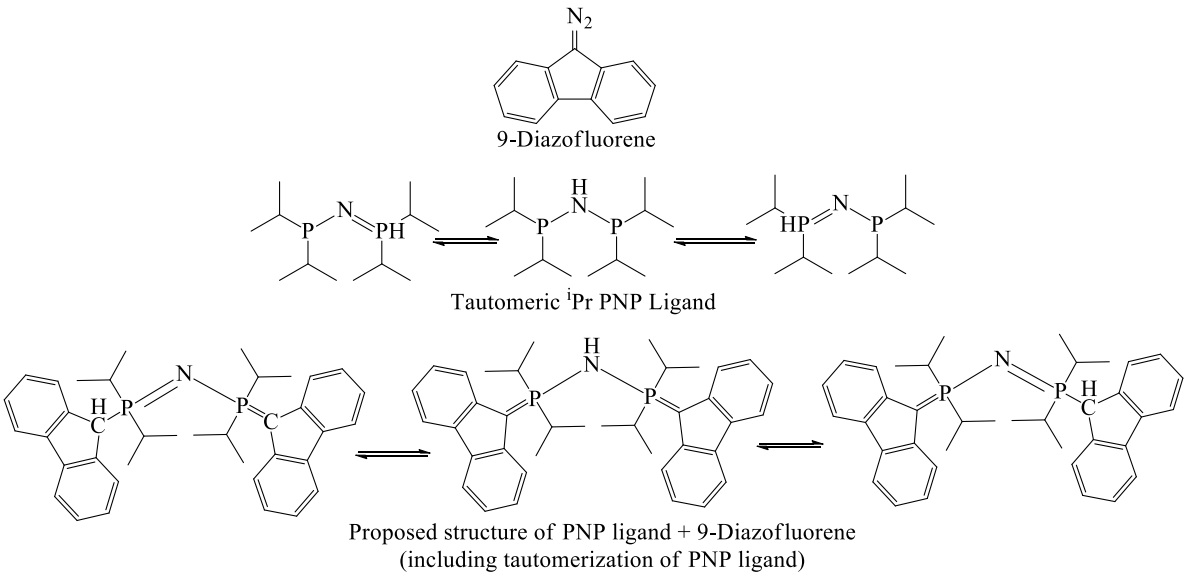

Figure 16: Structure of 9-diazofluorene (top), the diisopropyl PNP ligand, including its tautomeric forms (middle), and the proposed structure after capture of 9-fluorenylidene (bottom).

9-Fluorenylidene had the further advantage of being a flat molecule, which would minimize steric hindrance. 9-Fluorenylidene is also unusual in that it exists in a triplet ground state.[101] It was believed that reacting 9-diazofluorene with a PNP ligand would result in the release of nitrogen gas. The carbene formed would be stabilized by the PNP ligand, which could then be removed in a later step. This reaction was also done to further expand the research being carried out using PNP ligands in our group (Riley *et al.*[102, 103]).

9-diazofluorene was synthesized in house, using known literature methods, and purified by crystallization.[104,105] A small amount of this material was dissolved in DCM.

To this solution, one of two different PNP ligands [xiii] was added, either *bis*(diisopropylphosphino)amine or *bis*(diphenylphosphino)amine. In each case, 0.5 equivalents of the respective PNP ligand was added to the solution of 9-diazofluorene. This molar ratio was used as it was thought that a phosphorus atom would be the site of reaction for the PNP ligand and thus each molecule of the PNP ligand would be able to capture two molecules of carbene. The solutions were allowed to stir for 15 h, after which they were left to slowly evaporate. This process did not produce crystals, so the solutions were redissolved in DCM and layered with hexanes for solvent diffusion. Yellow crystals were isolated from each flask, the structures of which were determined by X-ray crystallography. The resulting structures showed that the reactions had not produced new carbenes. Nitrogen was not removed from the 9-diazofluorene and instead it had been coordinated directly to the PNP ligands. The structures of the crystals were determined to be *N*-((2-(9H-fluoren-9-ylidene)hydrazinyl) diisopropylphosphoranylidene)-*N*'-(9H-fluoren-9-ylidene)-P,P-diisopropyl-phosphinohydrazonic amide, **1a**, and *N*-((2-(9H-fluoren-9-ylidene)hydrazinyl)-diphenylphosphoranylidene)-*N*'-(9H-fluoren-9-ylidene)-P,P-diphenylphosphinohydrazonic amide, **1b**, from the reactions of the iso-propyl and phenyl PNP ligands, respectively. A third structure was later determined from a crystal in the sample of **1a**, and it had salt-like characteristics. This structure proved to be (2-(9H-fluoren-9-ylidene)hydrazinyl)(((2-(9H-fluoren-9-ylidene)hydrazinyl)diisopropyl-phosphoranylidene)amino)diisopropyl-phosphonium chloride, **2a**.

[xiii] PNP ligands were made in house following the methods outlined in Section 1.6

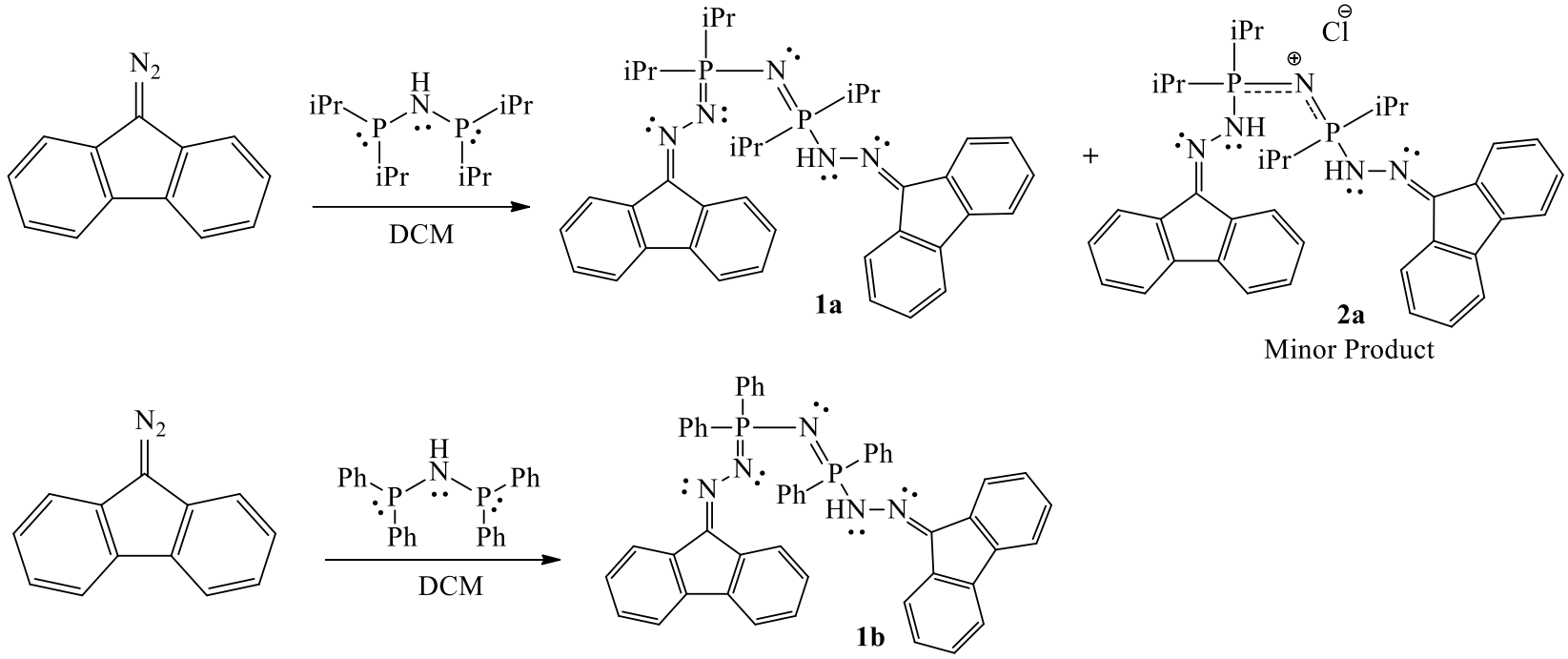

Scheme 3: Reaction conditions that led to the isolation of compounds **1a** (top, left), **2a** (top, right), and **1b** (bottom) from the reaction of 9-diazofluorene with PNP ligands.

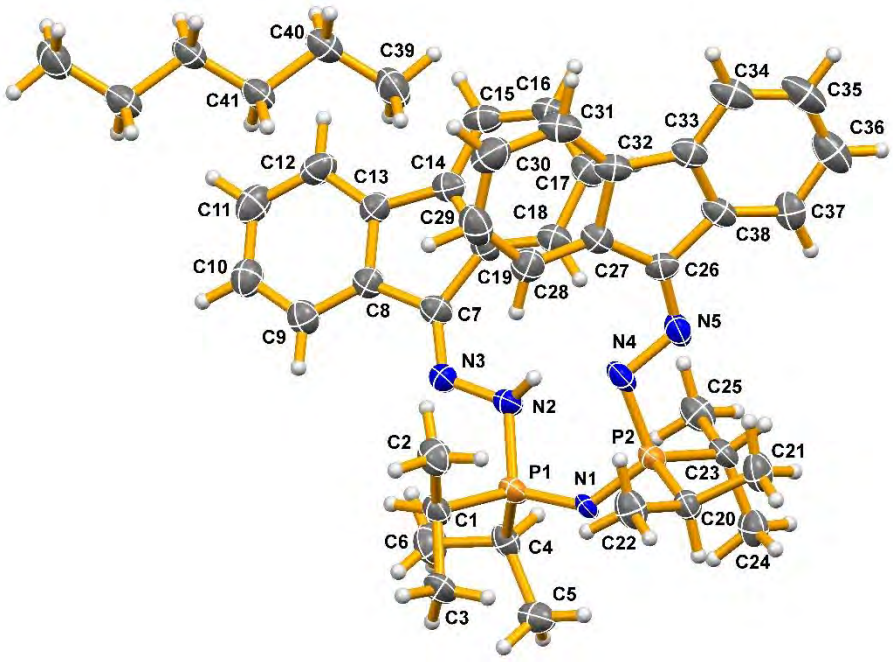

Figure 17: Solid state structure of **1a.** The structure is solvated with one molecule of hexane for every two molecules of compound. Only the unique non-hydrogen atoms have been labelled. Thermal ellipsoids are drawn at the 50% probability level. All crystal structure diagrams have been prepared using Mercury 2020 software.[106]

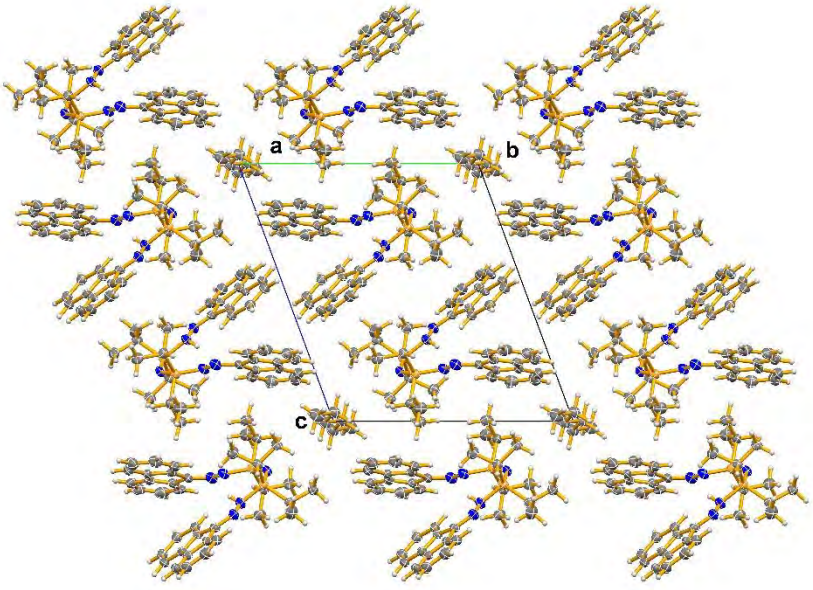

Figure 18: Solid state packing diagram of **1a** viewed down the *X*-axis. Thermal ellipsoids are drawn at the 50% probability level.

From Figures 17 and 18, it can be seen that compound **1a** contains two 9-diazofluorene molecules, each coordinated to one of the phosphorus atoms of the PNP ligand. This means that the tautomeric proton that shifted between the phosphorus and nitrogen atoms of the PNP ligand has been removed and a proton is now bound to one of the diazo groups in one single 9-diazofluorene group. This means that in order to satisfy Lewis theory, the nitrogen atom of the PNP ligand would have to double bond with a phosphorus atom, and that same λ^3-phosphorus will have to become a λ^5-phosphorus, as the compound **1a** is neutral. Unless compound **1a** is tautomeric, with the proton on a single diazofluorene being able to shift to the other, it does not appear that there is a resonance form for the structure, without the introduction of a zwitterion.

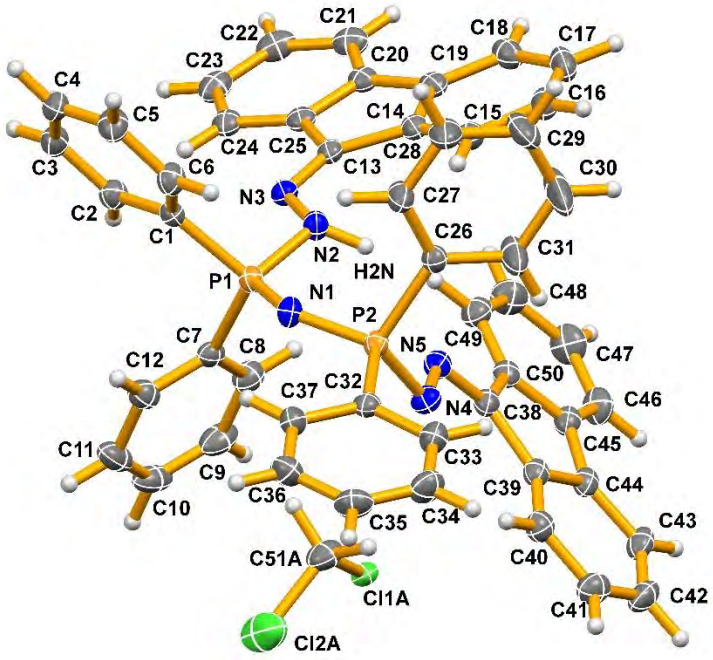

Figure 19: Solid state structure of **1b**. Minor components of the solvent disorder have been removed. The structure is solvated with one molecule of dichloromethane per molecule of compound. The hydrogen atoms have not been labelled. Thermal ellipsoids are drawn at the 50% probability level.

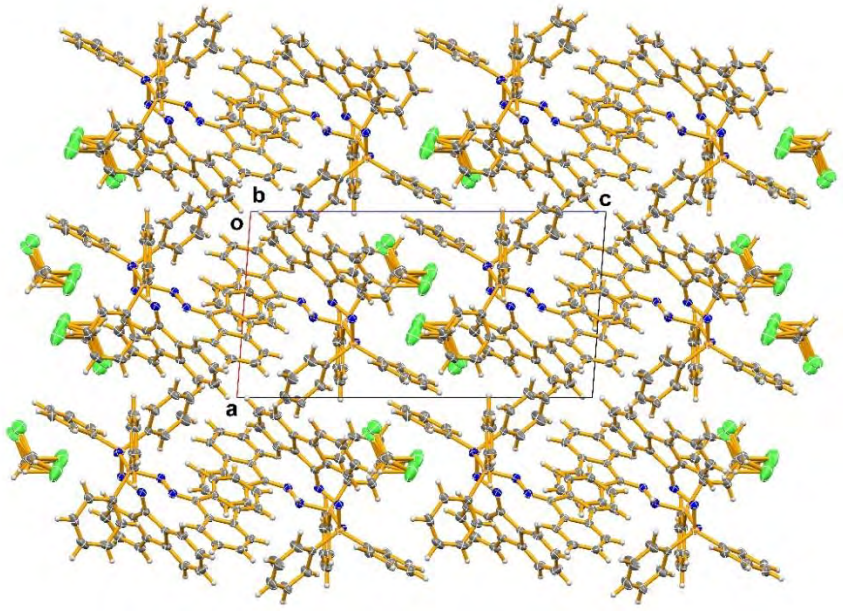

Figure 20: Solid state packing diagram of **1b** viewed down the *Y*-axis. Thermal ellipsoids are drawn at the 50% probability level.

From Figures 19 and 20, it can be seen that compound **1b** also contains two 9-diazofluorene molecules each coordinated to one of the phosphorus atoms of the PNP ligand, just as found in compound **1a**. This means that the tautomeric proton that shifted between the phosphorus and nitrogen atoms of the PNP ligand has been replaced by one bound to one of the diazo groups in a single 9-diazofluorene. Just like **1a**, in order to satisfy Lewis theory, the nitrogen atom of the PNP ligand would have to double bond with a phosphorus atom, and that same λ^3-phosphorus will have to become a λ^5-phosphorus, as the compound **1b** is neutral. Just like **1a**, it is unlikely that there is a resonance form for **1b**.

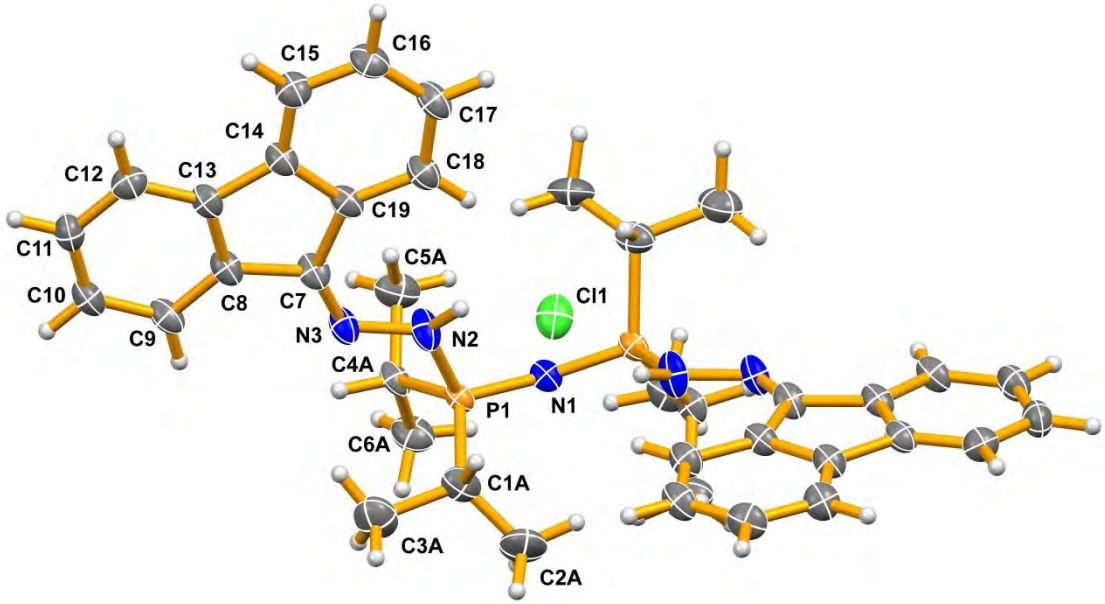

Figure 21: Solid state structure of **2a**. Minor components of the disordered cation have been removed. Only the unique non-hydrogen atoms have been labelled. Thermal ellipsoids are drawn at the 50% probability level.

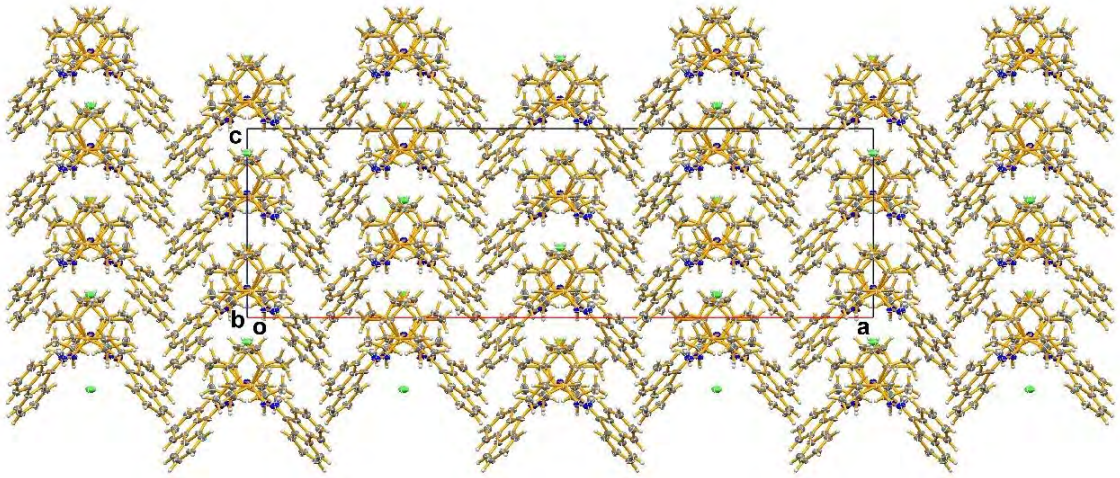

Figure 22: Solid state packing diagram of **2a** viewed down the *Y*-axis. Thermal ellipsoids are drawn at the 50% probability level.

From Figures 21 and 22, it can be seen that compound **2a** also contains two 9-diazofluorene molecules each coordinated to one of the phosphorus atoms of the PNP

ligand. However, unlike the previous compounds, **2a** has both of the diazofluorene groups protonated, giving a mono-Cl salt as the isolated product. One of the protons is likely from the tautomeric hydrogen, now bound to a diazo group, as in compounds **1a** and **1b**. The second proton could be from any source; since **2a** has a chloride anion, it is possible that it comes from the DCM solvent. Unlike compounds **1a** and **1b**, in order to satisfy Lewis theory, the nitrogen atom of the PNP ligand would have to double bond with a phosphorus atom, and that same phosphorus will have to become a λ^5-phosphorus. The other phosphorus, however, will have to be λ^4 with a formal positive charge to pair with the negative anion. This charge, however, can be delocalized across the PNP bonds, giving them a bond order of 1.5, as depicted in Scheme 3.

As can be observed in the crystal structures of compounds **1a** (Figures 17 and 18) and **1b** (Figures 19 and 20), they both share many similar characteristics. They are both triclinic crystal systems along with being monoprotonated on a single nitrogen of one of the azo groups. In both structures, this proton exhibits hydrogen bonding to the nitrogen of the adjacent azo group in the same molecule (Table 4). There is, however, a difference in the fine points of the crystal structures between the two compounds. Though there are no significant differences in the common bond lengths of the compounds, the same cannot be said for the bond angles. Specifically, there is a large difference between the ∠N1P2N4 angles. The angle of the ∠N1P2N4 bond for compound **1a** is 109.4(2)º while the angle for compound **1b** is 122.14(8)º, a difference of 13º. It is likely that this difference is a result of the steric hindrance of the diisopropyl groups in compound **1a**, since only this one angle is involved. The phenyl groups of compound **1b** create less hindrance, being flat and thus able to pack more efficiently.

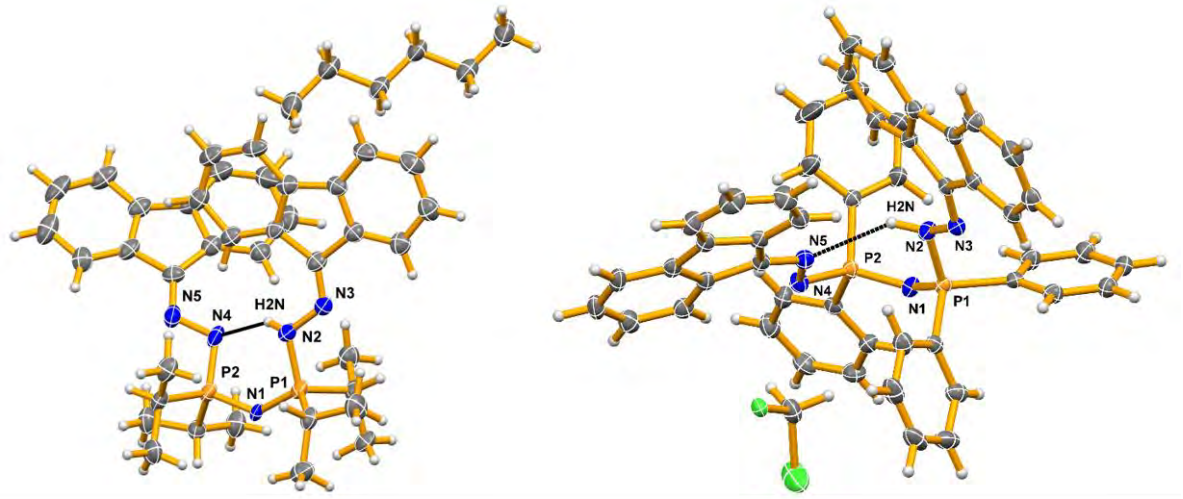

Compound **1a** Compound **1b**

Figure 23: Comparison of the N-H…N hydrogen bonding between compounds **1a** and **1b** (see Table 4 for values). Only the atoms involved in the hydrogen bonds and the PNP backbone atoms have been labelled. Thermal ellipsoids are drawn at the 50% probability level.

It should be noted that although the proton is on N2 for both **1a** and **1b** in the solid-state, the structures are likely tautomeric in solution, with the proton able to add onto any of the non-carbon atoms. Compounds **1a** and **1b** pack differently even though they have relatively similar structures. From the solid-state packing diagrams of **1a** and **1b** (Figures 18 and 20, respectively) it can be seen that both of the compounds are solvated, **1a** with hexanes, and **1b** with DCM. Though Figure 18 appears to show potential stacking interactions between the 9-diazofluorene groups, none actually exist. Instead the molecules are arranged to create channels running parallel to the *X*-axis which allows the solvating hexane to enter. **1b**, however, does have stacking interactions between the 9-diazofluorene groups (Figure 24), even though the compound is solvated with DCM. This is likely due to the flat phenyl substituents of **1b** having a greater ease of packing compared to the

diisopropyl groups of **1a**, which are bulky and more sterically hindered. **1b** has stacking interactions from the center of gravity of the 5-membered ring (C13, C14, C19, C20, C25) of one 9-diazofluorene group to the center of gravity of the 5- and a 6-membered ring (C20 to C25) of another 9-diazofluorene, generated by symmetry (1-*x*, 1-*y*, -*z*) equal to 3.6330(12) Å and 3.5021(12) Å, respectively. **1b** also has stacking interactions for the center of gravity of one of the 6-membered rings (C14 to C19) of the 9-diazofluorene towards the center of gravity of a 6-membered ring (C20 to C25) of another 9-diazofluorene (same symmetry as above) equal to 3.7439(12) Å. The minimum distance in **1b** is 3.5021(12) Å, which is a relatively close contact. The stacking interactions of **1b** only occur with the protonated 9-diazofluorene groups. The non-protonated 9-diazofluorenes does not show contacts that were close enough to be considered stacking interactions.

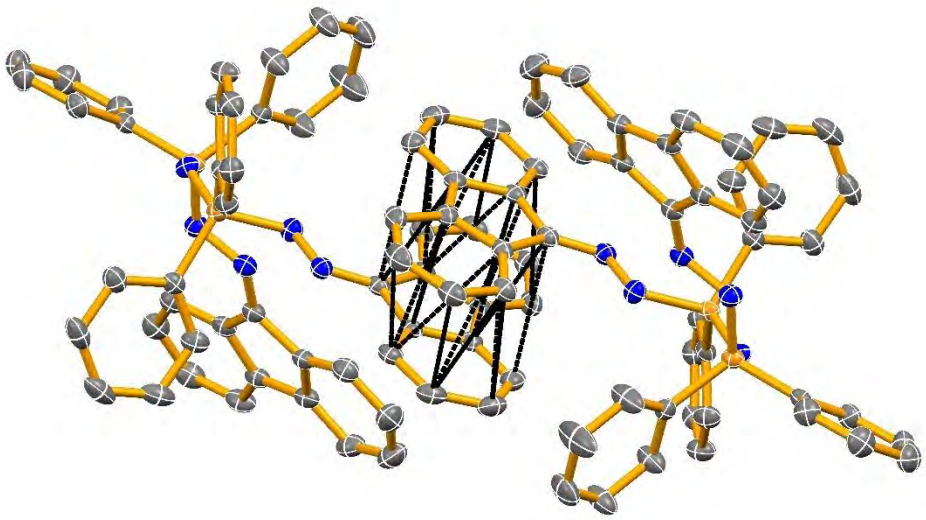

Figure 24: Stacking interactions of 9-diazofluorene groups in compound **1b**. Hydrogen atoms have been removed for clarity. Thermal ellipsoids are drawn at the 50% probability level.

With the exception of the angle ∠N1P2N4, compounds **1a** and **1b** have no significant differences between the bond lengths and bond angles in the common parts of their structures. It is interesting that there is a slight difference in the C=N double bond length of the two 9-diazofluoroene groups in both compounds **1a** and **1b**; the 9-diazofluorene group that is monoprotonated has a C=N bond length of 1.280(6) Å in compound **1a,** and 1.286(2) Å in compound **1b**. The non-protonated side has a bond length of 1.320(6) Å in compound **1a**, and 1.312(2) Å in compound **1b**. The C=N double bond in 9-diazofluorene has an average bond length of 1.319(5) Å[xiv] as reported by Kawano *et al.*[107] This implies that there is a slight reduction in the bond length of the C=N double bond due to the monoprotonation of the 9-diazofluorene. Not only this, but the reaction of 9-diazofluorene with the PNP ligands disrupts the N=N double bond of the diazo groups, forming single bonds instead, as can be seen in the structures in Scheme 3. This means that the average linear ∠NNC bond angle of 179.4(4)°[xv] reported by Kawano *et al.*[107] changes to typical sp^2 hybridized angles of 115.5(4)° and 114.3(2)° for compounds **1a** and **1b**, respectively, at the unprotonated 9-diazofluorene. The ∠NNC bond angles are 118.3(4)° and 117.9(2)° at the protonated 9-diazofluorene for compounds **1a** and **1b**, respectively. This shows the new geometry of the NNC region once reaction occurs with the PNP ligands. The NNC region in 9-diazofluorene, as reported by Kawano *et al.,*[107] exists as a linear zwitterion (a positive λ^4-nitrogen and a negative λ^2-nitrogen), but when it is reacted, each of the nitrogen atoms become λ^3-nitrogens, with a single bond between them instead

[xiv] Average calculated value from the N=C bond length for two molecules in the asymmetric unit of diazofluorene.
[xv] Average calculated value from the ∠NNC bond angle for two molecules in the asymmetric unit of diazofluorene.

of a double bond. This change in configuration is evident in the Lewis structure (Scheme 3).

There is also one notable difference in the respective bond lengths and angles between compounds **1a** and **1b**, and their unreacted PNP starting materials. The diisopropyl PNP compound has an average P-N bond length of 1.705(16) Å[xvi] and the average ∠PNP bond angle is 121.2(4)º,[xvii] as reported by Dickie *et al*.[57] The P2-N1 bond length is 1.606(4) Å on the non-protonated side, while the P1=N1 bond length is 1.551(4) Å on the protonated side, for compound **1a**. The ∠PNP bond angle for compound **1a** is 134.7(2)°. For the phenyl PNP compound, the average P-N bond length is 1.692(16) Å and the ∠PNP bond angle is 118.92(8)º, as reported by Nöth and Fluck.[55] The P2-N1 bond length is 1.605(2) Å on the non-protonated side, while the P1=N1 bond length is 1.565(2) Å on the protonated side, for compound **1b**. The ∠PNP bond angle for compound **1b** is 133.4(1)°. This shows that reaction of the PNP ligands with 9-diazofluorene shortens both the N1-P1 bond length and increases the ∠PNP bond angle (~14º) for both compounds **1a** and **1b**. What are of particular interest, however, are the P2-N1 and P2=N4 bond lengths on the non-protonated side for the neutral compounds **1a** and **1b**. From the Lewis structures of the compounds, and from Allen *et al*.,[108] the P1-N1 bond should be a double bond, the P2-N1 bond should be a single bond, and the P2-N4 bond should be a double bond, in both compounds **1a** and **1b**. The experimental bond lengths reveal that compound **1a** has P2-N1 and P2=N4 bond lengths of 1.606(4) Å (a P≃N bond order of 1.5[55]) and 1.649(4) Å (a single bond[55]),

[xvi] Value was calculated from averaging the four P-N bonds present across the two molecules in the asymmetric unit.
[xvii] Value was calculated from averaging the two ∠PNP bonds angles present across the two molecules in the asymmetric unit.

respectively. The experimental bond lengths reveal that compound **1b** has P2-N1 and P2=N4 bond lengths of 1.6054(15) Å (a P≃N bond order of 1.5[55]) and 1.6267(15) Å (a single bond[55]), respectively. It is particularly interesting to speculate why the P2=N4 bond is longer and the P2-N1 bond is shorter than predicted by Lewis theory. It was initially believed that this was due to either the change in electronics of a λ^5-phosphorus, compared to the previous λ^3-phosphorus, or the presence of a zwitterion between P2 and N4, but these are both unlikely. A more plausible explanation would be due to the presence of hydrogen bonding at the H2(N2) proton to the N4 atom in both compounds **1a** and **1b**. The hydrogen bonding directed to the N4 site may be taking electron density away from the P2=N4 double bond, which would create a bond lengthening from the expected value. This withdrawing of electron density would also create an electron deficiency at the P2 atom, which would then withdraw electron density from the N1 atom, creating a shorter single bond than expected, as the hydrogen bonding is located at the same site for both compounds **1a** and **1b**. This, however, is not a complete answer. Although a hydrogen bond does have some covalent bonding character,[109] it is largely electrostatic in nature, which cannot be electron withdrawing. It is possible as well that the geometry of the compounds is influencing the hydrogen bonding, and not that other way around. This phenomenon is observed in both compounds **1a** and **1b** but not in the diprotonated compounds **2a** and **2b** (see below). This explanation also allows for Lewis theory to be satisfied without invoking charge separated Lewis structures. That being said, the phenyl compounds seem to behave more as expected with respect to the Lewis structures drawn, while the diisopropyl compounds behave slightly differently.

From the crystal structures of **1a**, **1b**, and **2a** it was believed that these compounds had the potential to coordinate with a metal center. This assumption was based on the fact that the PNP ligand formed a small pocket, with the fluorene molecules surrounding it, in all three structures. The electron density of the fluorene molecules would be able to help coordinate and stabilize a metal centre if it were to be inserted into the pocket of the PNP ligand. A common metal salt, nickel (II) chloride hexahydrate, was selected in an attempt to add a metal centre to these compounds. A relatively polar solvent(s) was required to dissolve the metal salt, but it also had to be able to dissolve compounds **1a**, **1b**, and **2a**.

For the first synthetic attempt, compound **1b** was chosen as it did not appear to have formed any co-products in the original reaction (as found in the X-ray crystallographic determination). Compound **1b** was dissolved in acetonitrile and to the solution one equivalent of nickel chloride hexahydrate was added. The solution was allowed to stir for 24 h before being decanted and allowed to crystallize by slow evaporation. After 24 h crystals had begun to grow from the solution. The structure of one of these crystals was determined by X-ray crystallography to be (2-(9H-fluoren-9-ylidene)hydrazinyl)(((2-(9H-fluoren-9-ylidene)hydrazinyl)diphenylphosphoranylidene)amino)diphenyl phosphonium chloride, **2b**, analogous to the iso-propyl product **2a**.

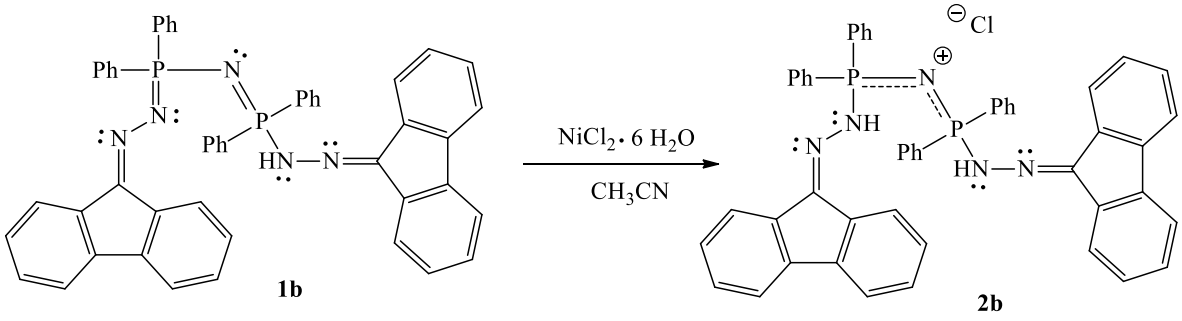

Scheme 4: Reaction conditions that led to the isolation of compound **2b**.

Although the reaction with compound **1b** was unsuccessful, and no metal center was inserted into the product, there was an unintended effect which led to the isolation of compound **2b**. In hindsight using atomic nickel might have provided more fruitful results for the intended reaction. However, the use of nickel chloride hexahydrate did result in the protonation of the second N_2 group in the molecule. This in turn created a cation on the respective phosphorus molecule in the PNP ligand, with a chloride from the nickel salt able to act as the charge balancing anion. An interesting effect of the protonation and new ionic properties of compound **2b**, is the intermolecular hydrogen bonding from the N-H hydrogens to the chloride anion. This is the same as in compound **2a**, the diisopropyl derivative, which shares a similar structure, while it differs from the intramolecular hydrogen bonding observed in **1a** and **1b**.

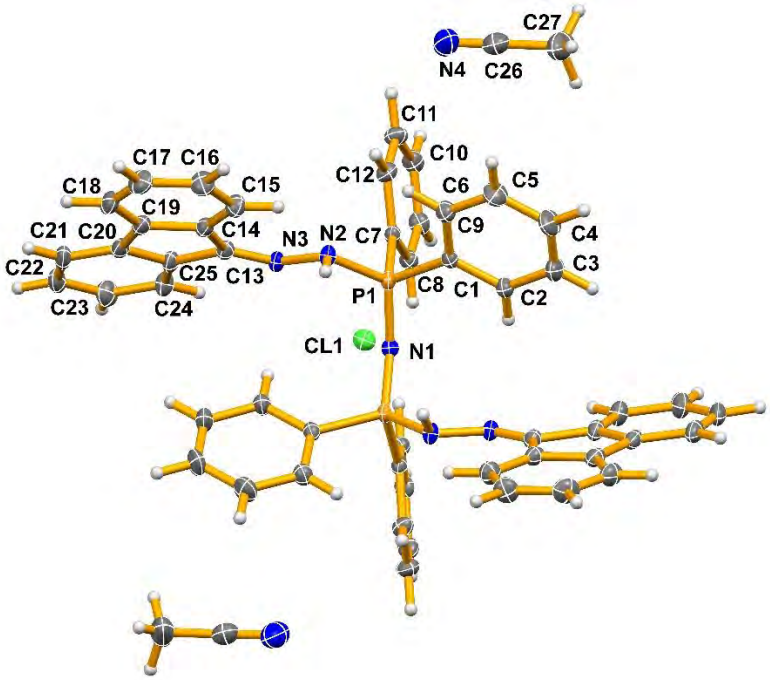

Figure 25: Solid state structure of **2b**. The structure is solvated with two molecules of acetonitrile per molecule of compound. Only the unique non-hydrogen atoms have been labelled, Thermal ellipsoids are drawn at the 50% probability level.

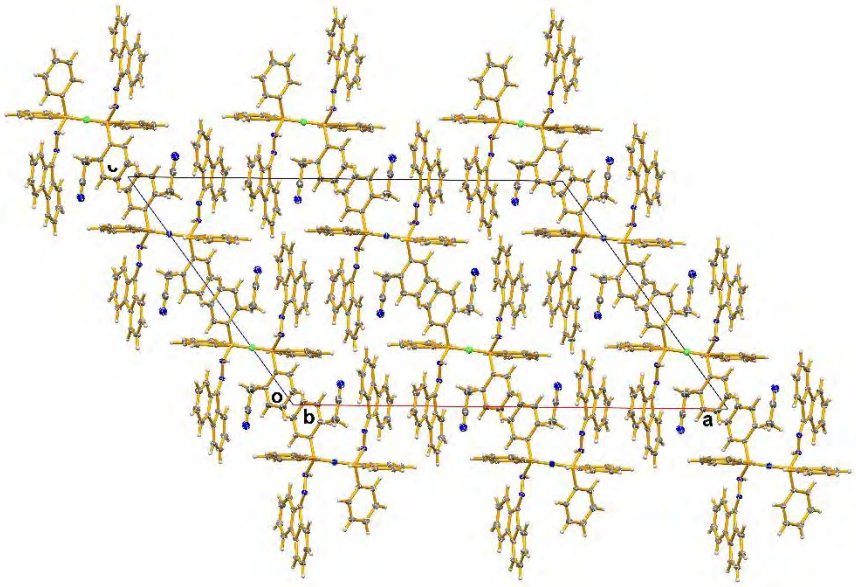

Figure 26: Solid state packing diagram of **2b** viewed down the *Y*-axis. Thermal ellipsoids are drawn at the 50% probability level.

Compounds **2a** and **2b** are very similar to each other from a structural point of view, although they are vastly different in their crystal structures. Compound **2a** crystallizes in an orthorhombic crystal system while **2b** is monoclinic. Though they both are diprotonated, with one proton on each azo group, the packing of the crystals is very different. Compound **2a** packs in well-organized columns where the 9-diazofluorene groups are "shingled" over each other in an alternating pattern. There is also a void, which the chloride anion is able to fill, around the diisopropyl groups. That being said, **2a** is also disordered in the isopropyl groups of the cation. This disorder is likely due to thermal motion which creates even more steric hindrance than would otherwise occur. Compound **2b**, however, is similar in its packing structure to that of **1b**, where the molecules are arranged such that there are stacking interactions between the 9-diazofluorene groups. **2b** also has stacking interactions from the center of gravity of one 9-diazofluorene to the center of gravity of another symmetry related 9-diazofluorene group (3/2-*x*, 1/2-*y*, 1-*z*). **2b** has a number of reasonably

close stacking interactions between the rings of the two interacting groups. The shortest is from the center of gravity of the 9-membered ring (C13 to C20 plus C25)[xviii] of one 9-diazofluorene towards the center of gravity of the same 9-membered ring[xix] (C13 to C20 plus C25) on the other 9-diazofluorene. The minimum distance in **2b** is 3.5972(10) Å, which is similar to that observed in **1b**.

The fact that only the phenyl substituted compounds have close stacking interactions implies that the diisopropyl group of compounds **1a** and **2a** have steric hindrances which prevent stacking interactions from occurring between their 9-diazofluorene groups.

Though compounds **2a** and **2b** do possess related bond lengths that are not significantly different from each other, some of their bond angles are different, specifically the N1-P1-N2, the P1-N1-P1#,[xx] and the P1-N2-N3 angles. It is important to note that both compounds are symmetrical molecules, with 2-fold rotation axis through the central nitrogen atom, and thus have the same bond lengths and angles on both sides. P1# refers to the atom generated from P1 by this 2-fold rotation of the molecule. The angle ∠N1-P1-N2, which is where the PNP ligand bonds to the 9-diazofluorene, for compound **2a** is 110.3(2)º while the same angle for compound **2b** is 119.1(1)º. The angle ∠P1-N1-P1# for compound **2a** is 159.3(4)º while the angle for compound **2b** is 139.1(1)º. The angle ∠P1-N2-N3 for compound **2a** is 116.8(3)º while the angle for compound **2b** is 109.8(1)º. This

[xviii] 9-membered ring of 9-diazofluorene is equal to the combined 5- + 6-membered rings (phenyl).
[xix] 13-membered ring of 9-diazofluorene is equal to the entire fluorene group.
[xx] To generate P1# in compound **2a**, the symmetry required is (-*x*, -*y*+1, +*z*). In compound **2b** the symmetry required is (-*x*+1, +*y*, -*z*+1/2).

means that the differences in the ∠N1-P1-N2, ∠P1-N1-P1#, and ∠P1-N2-N3 angles are ~9º, ~20º, and ~7º, respectively.

These differences in the bond angles for the PNP ligand where it bonds to the azo groups help to show the differences in the solid-state structures between the diisopropyl and diphenyl substituted compounds. The phenyl substituted compound, **2b**, has shallower ∠P1-N1-P1# and ∠P1-N2-N3 angles, which implies less steric stress across the bonds compared to those in compound **2a**, though the ∠N1-P1-N2 angle is more obtuse in **2b** than **2a** (119.08(5)° and 110.3(2)°, respectively). This would imply that the PNP bonds to the azo group are under more stress in **2a** than **2b**, as the expected bond angle for this hybridization should be 120° (trigonal bipyramidal). Since the angle in **2a** is significantly less than the expected 120° compared to **2b**, this would imply that that the diisopropyl groups of compound **2a** are creating increased steric hindrance compared to the phenyl substituents and causing a shallower ∠N1-P1-N2 angle than expected for **2a**.

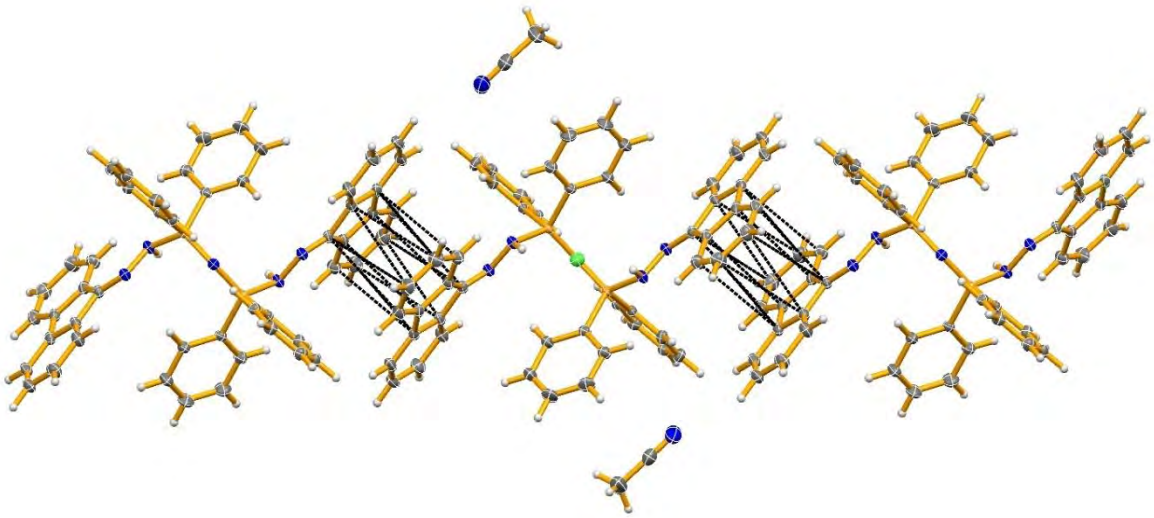

Figure 27: Ring stacking interactions of the 9-diazofluorene groups in compound **2b.**

Compounds **2a** and **2b** also both have hydrogen bonding (Table 4) like the mono-protonated structures **1a** and **1b**. Here however, the two equivalent hydrogen bonding interactions are not directed to the adjacent intramolecular azo group. Instead, in compounds **2a** and **2b**, the hydrogen bond acceptor is the chloride anion. Both of the azo groups are protonated in these compounds, with both of the H(N) hydrogens in one cation forming interactions with the same chloride anion (Figure 28).

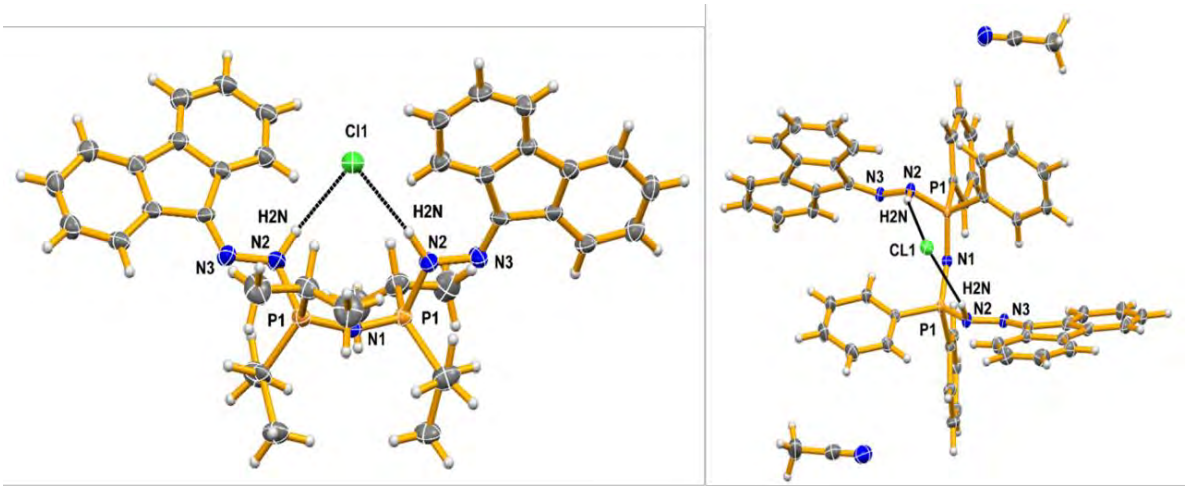

Compound **2a** Compound **2b**

Figure 28: Comparison of the hydrogen bonding in compounds **2a** and **2b** (see Table 4 for values). Only the atoms involved in the hydrogen bonds and the PNP backbone atoms have been labelled. Thermal ellipsoids are drawn at the 50% probability level.

As seen with compounds **1a** and **1b**, the protonated 9-diazofluorene groups of compounds **2a** and **2b** show a shortening of the C=N bond length, to 1.289(6) Å, and 1.286(2) Å, respectively, from the average bond length of 1.319(5) Å reported by Kawano *et al.*[107] This implies that there is a slight reduction in the length of the C=N double bond due to the protonation of the 9-diazofluorene nitrogen atom. The C=N bond lengths in

compounds **2a** and **2b** are also the same as those of the protonated 9-diazofluorene groups in the compounds **1a** and **1b**, which further shows that the proton influences this bond length. This also implies that the ionic nature of the diprotonated system has no influence on the C=N bond length compared to those found in the neutral compounds **1a** and **1b**. Not only this, but the reaction of 9-diazofluorene with the PNP ligands causes the ∠NNC bond angle to change from the average linear ∠NNC bond angle of 179.4(4)º[xxi] reported by Kawano *et al.*[107] to 119.4(4)º for compound **2a** and 118.3(1)º for compound **2b**. This shows that, like the monoprotonated compounds which have identical bond angles, the ∠NNC bond angles for compounds **2a** and **2b** are also the same. Not only this, but the ∠NNC bond angles of compounds **2a** and **2b** are also similar to those on the monoprotonated side of compounds **1a** and **1b**.

There is, however, a difference in the bond lengths and angles between compounds **2a** and **2b**, and their respective unreacted PNP precursors. The diisopropyl PNP ligand has an average P-N bond length of 1.705(16) Å[xxii] and the average ∠PNP bond angle is 121.2(4)º,[xxiii] as reported by Dickie *et al*.[57] The P≃N bond length is 1.556(2) Å across both N1-P1 and N1-P1# in compound **2a**, which implies a delocalized double bond for both. The ∠PNP bond angle for compound **2a** is 159.3(4)°, which is significantly more linear than that in the unreacted PNP compound. For the phenyl PNP ligand, the average P-N bond length is 1.692(2) Å[xxiv] and the ∠PNP bond angle is 118.9(1)º, as reported by Nöth

[xxi] Average calculated value from the N=C bond length for two molecules in the asymmetric unit.
[xxii] Value was calculated from averaging the four P-N bonds present across the two molecules in the asymmetric unit.
[xxiii] Value was calculated from averaging the two ∠PNP bonds angles present across the two molecules in the asymmetric unit.
[xxiv] Value was calculated from averaging the two P-N bonds in the asymmetric unit.

and Fluck.[55] The P≃N bond length is 1.578(1) Å across both N1-P1 and N1-P1# for compound **2b**, which implies that they are delocalized double bonds. The ∠PNP angle for compound **2b** is 139.1(1)°. This is a significant change in the ∠PNP angle compared to that in the phenyl PNP starting material.[55] This is a slightly larger change in the ∠PNP bond angle compared to that in compound **1b**, which is likely due to the different hybridization at the central nitrogen of compound **2b**. Since compound **1b** is unsymmetrical with the protonation, there are steric effects present with could also create a more acute angle compared to the symmetrical compound **2b**. This shows that reaction of the PNP ligands with 9-diazofluorene shortens both of the N1-P1# bond lengths for compounds **2a** and **2b**, and increases the ∠PNP bond angle by ~38º for compound **2a** and ~20° for compound **2b**. The observed phenomenon of hydrogen bonding electron withdrawal in compounds **1a** and **1b** is not observed in compounds **2a** and **2b**, as both the 9-diazofluorene groups are protonated and the hydrogen bonding is directed to the chloride anion rather than to a nitrogen atom in the same molecule.

At the same time that compound **2b** was being synthesized, another experiment was carried out, with the same goal of adding a metal center to one of the PNP ligand complexes. Instead of trying to add a nickel metal centre, the second reaction involved the addition of zinc to compound **1b**. At the time no zinc salts were available, and thus a different source of zinc was utilized. The chosen source of zinc was diethyl zinc. As per the reaction used to prepare **2b**, compound **1b** was dissolved in acetonitrile. The flask for the solution was placed under vacuum, so as to not incite an unintended reaction with the diethyl zinc.[xxv] A vacuum was chosen, over a dry nitrogen atmosphere, as gas would be

[xxv] It is important to note that for safety, diethyl zinc should NOT be added to acetonitrile.

generated during this reaction and the use Schlenk techniques would have been necessary with a nitrogen atmosphere.[xxvi] One equivalent of diethyl zinc in hexanes was added, and the reaction was allowed to stir for 24 h. Once complete, the solution was exposed to the atmosphere and allowed to crystallize by slow evaporation. Crystals grew after 24 h. The structure of the crystals was determined by X-ray crystallography to be *N*-((2-(9H-fluoren-9-ylidene) hydrazinyl) diphenylphosphoranylidene)-*P,P*-diphenylphosphinic amide, **3**.

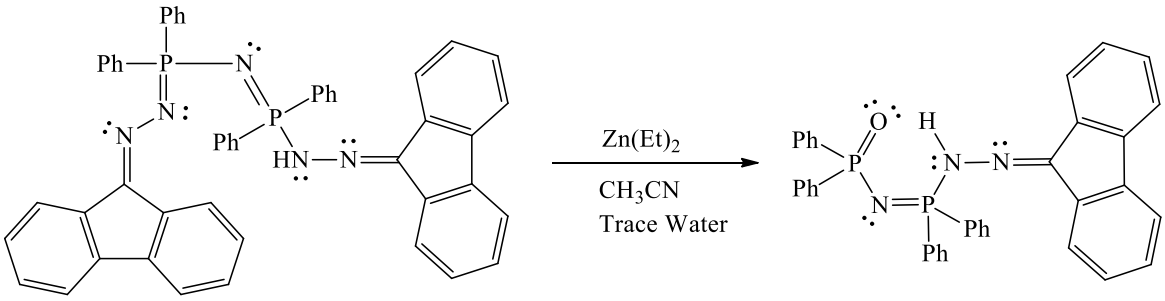

1b **3**

Scheme 5: Reaction conditions that led to the isolation of compound **3**.

Compound **3** seems to result from cleavage at one of the diazo nitrogen-phosphorus bonds in compound **1b**. A trace amount of water, likely from wet acetonitrile, has then reacted with the now exposed phosphorus of the PNP ligand. This results in the hydrolysis of the phosphorus while the second attached 9-diazofluorene group is maintained. In the solid state, the PNP ligand participates in a *pseudo* six-member ring, due to the hydrogen bonding present between the oxygen and N(H) hydrogen atom (Figure 31).

[xxvi] Dry nitrogen should have been used, as the reaction was not kept as dry as was necessary with vacuum, and it is also possible that the diethyl zinc was completely pulled from the reaction by the vacuum.

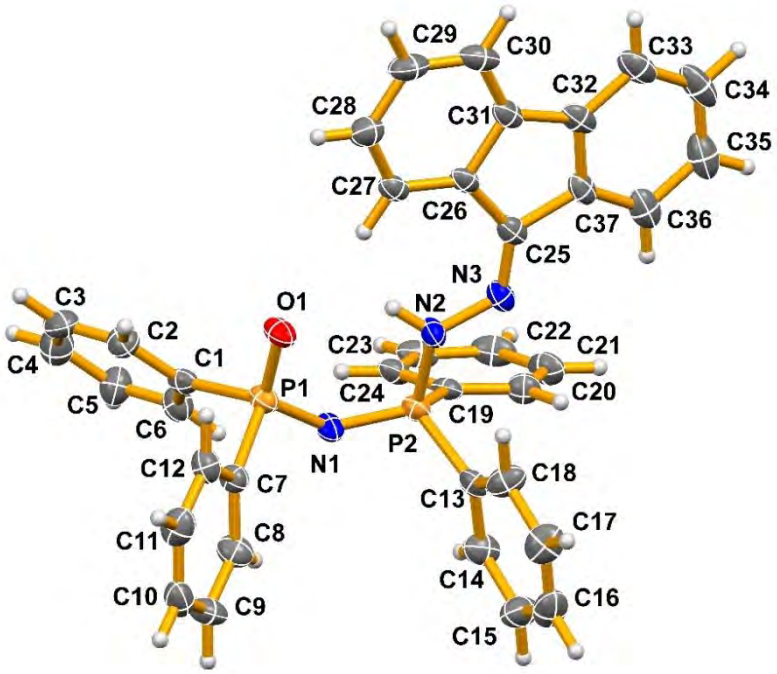

Figure 29: Solid state structure of **3**. Only the non-hydrogen atoms have been labelled. Thermal ellipsoids are drawn at the 50% probability level.

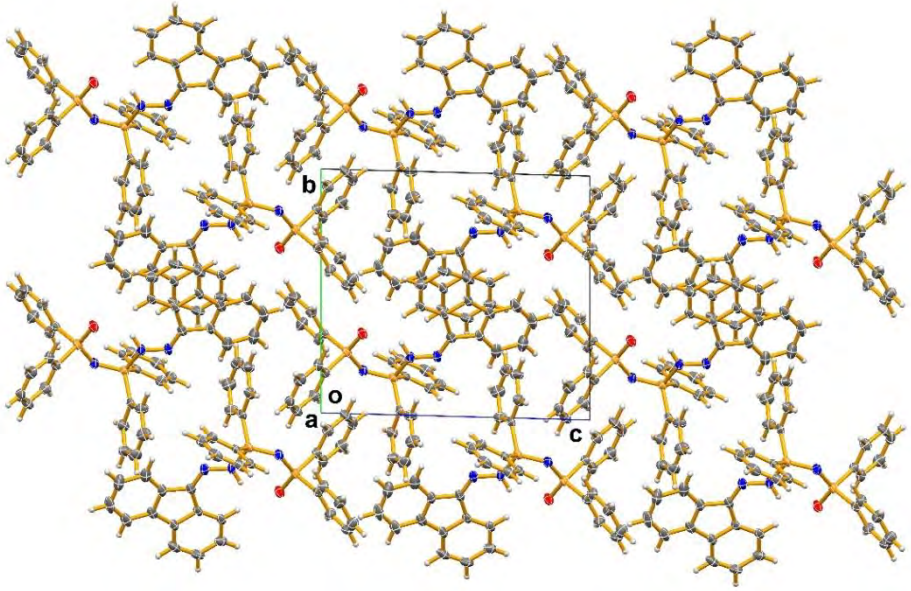

Figure 30: Solid state packing diagram of **3** viewed down the *X*-axis. Thermal ellipsoids are drawn at the 50% probability level.

Compound **3** is unlike any of the previous compounds mentioned, as it has fragmented at one of the 9-diazofluorene phosphorus bonds. Instead of having two coordinated 9-diazofluorene groups, there is instead only one, with the other phosphorus center forming a P=O group after hydrolysis. It is unlikely that compound **3** was formed from a PNP ligand that was mono-coordinated to 9-diazofluorene, as compound **3** was synthesized from a crystalline sample of compound **1b**. Compound **3** also does not show any significant changes in bond lengths or bond angles in comparison to the analogous bonds and angles in the related half of its closest derivative, compound **1b**.

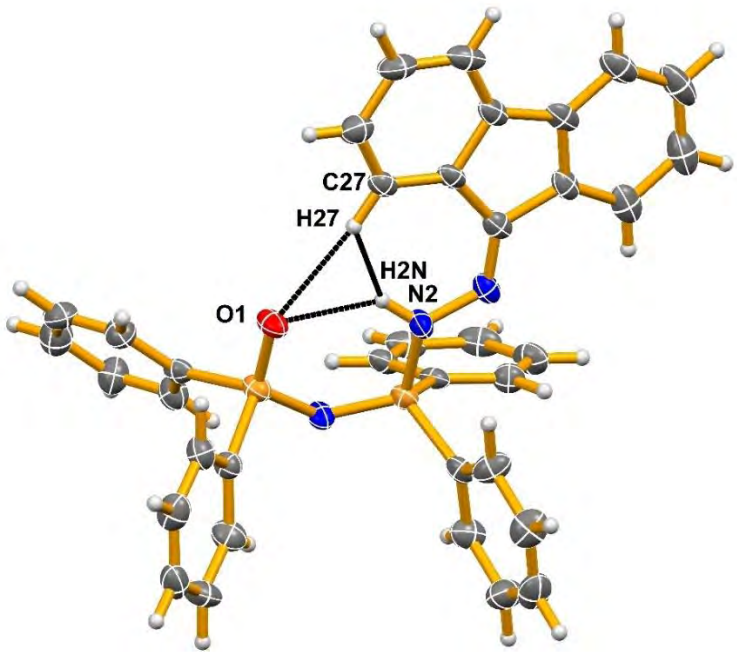

Figure 31: N-H hydrogen bonding in compound **3** (Table 4). The interactions N2-H2N…H27-C27 (1.95 Å and 141°) and C27-H27…O1 (2.42 Å and 171°) form in addition to the primary N-H…O hydrogen bond. Only the atoms involved in the hydrogen bonds have been labelled. Thermal ellipsoids are drawn at the 50% probability level.

The new structures reported in this section do not appear to have related compounds deposited in the CSD.[58] The structures of the starting phenyl[55] and diisopropyl[57] PNP compounds are reported in the CSD, as is that of 9-diazofluorene.[104,105] Even though the individual structures are well documented, there are no examples of a PNP compound coordinated with 9-diazofluorene, or bound to any diazo-containing group. There is one example of 9-diazofluorene forming a phosphorus complex, that reaction having been carried out with triphenylphosphine by Bethell *et al.*[110] (Figure 32). Comparing the structure of Bethell *et al.* to all previous compounds, there are minor changes in the P=N, N-N, and N=C_i bond lengths. The Bethell *et al.* structure has the shortest P=N bond length of all the structures; at 1.619(3) Å it is only just short enough to be considered a P=N double bond.[108] The non-protonated sides of **1a** and **1b** are depicted in their Lewis structure as having P=N double bonds (Scheme 3), though as theorized earlier, there may be additional forces creating a lengthening of the P=N double bonds (to 1.649(4) Å and 1.627(2) Å for **1a** and **1b** respectively). For the protonated sides/structures, the shortest P-N single bond is 1.664(4) Å in **2a**, highlighting the difference in the P-N bond lengths. The N-N and N=C_1 bond lengths in the Bethell *et al.* structure have no significant differences compared to the previously mentioned structures. The bond angles in the Bethell *et al.* compound are also very similar to the non-protonated values for **1a** and **1b**; where the ∠N2N3C_i angle is 116.06(2)º and the ∠PNN is angle 108.90º[xxvii] for the Bethell *et al.* structure. For the non-protonated side of **1a** and **1b**, the ∠NNC are similar but less obtuse compared to the angle in that of Bethell *et al*., which is to be expected due to their similarity. The protonated side of **1a** and **1b** are also not significantly different, but it should be noted that unlike the non-

[xxvii] The bond angle was calculated using Mercury Software (see reference 91), and an ESD was not included in the calculation.

protonated side, the angles for **1a** and **1b** are more obtuse compared to those in the Bethell *et al*. complex (Table 3). The ∠PNN bond angles, however, do show significant differences between that of Bethell *et al*. and the compounds of this chapter. **1a** has the closest bond angle to that of Bethell *et al*. at 109.6(3)º for the non-protonated side, while **1b** is 112.5(1)º for the non-protonated side. The less obtuse angle of Bethell *et al*. is likely due to a lack of steric hindrance, as the molecule is so small. The compounds in this chapter are significantly bulkier in comparison, which may act to create more obtuse ∠PNN angles compared to that in the structure in Bethell *et al*. Compound **3** is much different from compounds **1a**, **1b**, **2a**, and **2b** which is to be expected as it has a significantly different structure. **3** does not share similarities to any structures documented within the CSD, with the exception of that of Bethell *et al*.[110]

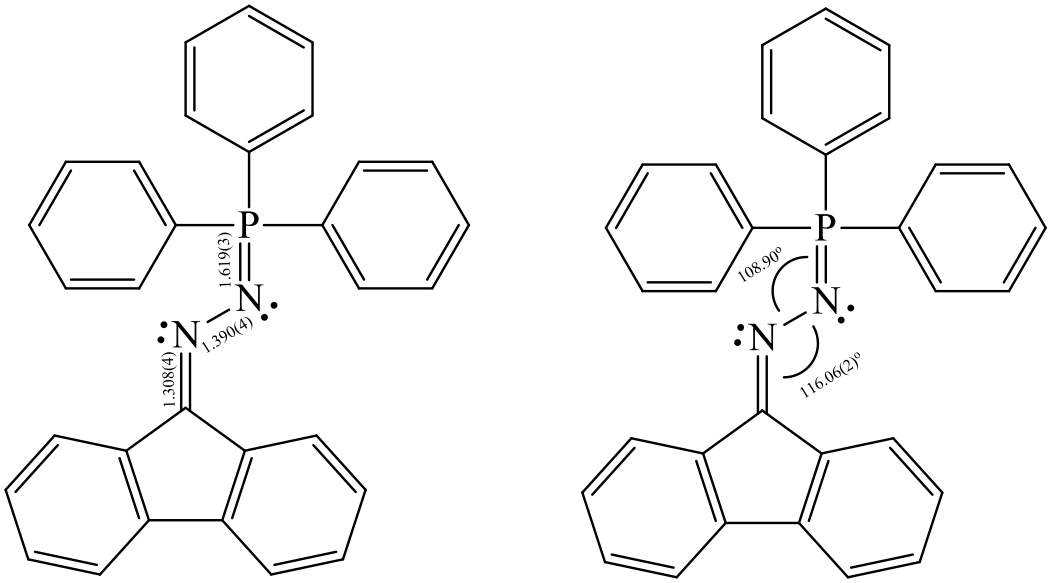

Figure 32: Structure of 9-fluorenone triphenylphosphazine as reported by Bethell *et al*.[110] Important bond lengths (Å, left) and angles (°, right) have been included.

In summary, the addition of 9-diazofluorene to PNP ligands in attempts to generate and capture 9-fluorenylidene, were unsuccessful. The generation of the aryl carbene, 9-fluorenylidene, should have been attempted through the method of Wang *et al.,*[111] in which the 9-diazofluorene would be exposed to ultraviolet light. Once isolated, it could then have been reacted with a PNP ligand to capture the carbene.

Although the experiments in this chapter did not produce the expected results, the results that were obtained are no less interesting. The extended structures of compounds **1a**, **1b**, **2a**, and **2b**, along with that of the hydrolysis product **3**, have not been observed before. These compounds could potentially be used for metal capture, as the crystal structures reveal a "bowl-like" cavity within some of the molecules, while others possess stacking of the 9-diazofluorene groups. Additionally, if a deprotonation reaction could be carried out at the H-N=N sites, then delocalization of electrons might occur across the entire structure. These aspects unfortunately could not be explored in depth in the available time frame. Continuation of this line of research could yield interesting results.

Table 1: Crystal Data and Structure Refinement Details for Compounds in Chapter 2

Identification code	**1a**	**1b**	**2a**	**2b**	**3**
Empirical formula	$C_{41}H_{52}N_5P_2$	$C_{51}H_{39}Cl_2N_5P_2$	$C_{38}H_{46}ClN_5P_2$	$C_{54}H_{44}ClN_7P_2$	$C_{37}H_{29}N_3OP_2$
Formula weight	676.81	854.71	670.19	888.35	593.57
Crystal system	Triclinic	Triclinic	Orthorhombic	Monoclinic	Triclinic
Space group	*P-1*	*P-1*	*Fdd2*	*C*2/*c*	*P-1*
a (Å)	9.675(3)	10.4341(10)	44.675(8)	31.166(3)	8.812(3)
b (Å)	13.444(5)	11.7915(12)	12.046(2)	9.0650(10)	12.958(5)
c (Å)	15.414(5)	18.6856(18)	13.484(2)	20.185(2)	13.777(5)
α (°)	69.680(4)	96.9450(10)	90	90	87.987(5)
β (°)	86.860(4)	91.3780(10)	90	126.5420(10)	79.194(5)
γ (°)	88.453(4)	111.0640(10)	90	90	71.304(5)
Volume ($Å^3$)	1877.2(11)	2123.9(4)	7256(2)	45810.6(9)	1463.1(9)
Z	2	2	8	4	2
Density (calc. g/cm^3)	1.197	1.336	1.227	1.288	1.347
Absorption coefficient (mm^{-1})	0.151	0.272	0.227	0.199	0.185
F(000)	726	888	2848	1856	620
Crystal size (mm^3)	0.320 x 0.070 x 0.040	0.400 x 0.300 x 0.100	0.300 x 0.175 x 0.175	0.475 x 0.300 x 0.	0.450 x 0.250 x 0.075
2θ range for data collection (°)	1.410 to 23.967	1.101 to 28.885	1.823 to 27.151	1.627 to 28.951	1.505 to 25.372
Index ranges	$-11 \leq h \leq 11$	$-14 \leq h \leq 14$	$-56 \leq h \leq 57$	$-40 \leq h \leq 40$	$-10 \leq h \leq 10$

	$-15 \leq k \leq 15$ $-17 \leq l \leq 17$	$-15 \leq k \leq 15$ $-24 \leq l \leq 24$	$-15 \leq k \leq 15$ $-17 \leq l \leq 17$	$-12 \leq k \leq 12$ $-26 \leq l \leq 27$	$-15 \leq k \leq 15$ $-6 \leq l \leq 16$
Reflections collected	16666	25945	20166	27173	5322
Independent reflections	5850	10242	4020	5740	5322
R_{int}	0.1367	0.0300	0.0936	0.0300	?
Data/restraints/parameters	5850 / 366 / 446	10242 / 46 / 602	4020 / 369 / 274	5740 / 1 / 294	5322 / 1 / 393
Goodness-of-fit on F^2	0.937	1.016	1.062	1.029	1.021
Final R indexes ($I > 2\sigma(I)$)	$R_1 = 0.0678$, $wR_2 = 0.1225$	$R_1 = 0.0430$, $wR_2 = 0.0953$	$R_1 = 0.0541$, $wR_2 = 0.0940$	$R_1 = 0.0363$, $wR_2 = 0.0895$	$R_1 = 0.0804$, $wR_2 = 0.1914$
Final R indexes (all data)	$R_1 = 0.1831$, $wR_2 = 0.1617$	$R_1 = 0.0666$, $wR_2 = 0.1066$	$R_1 = 0.0820$, $wR_2 = 0.1030$	$R_1 = 0.0475$, $wR_2 = 0.0963$	$R_1 = 0.1497$, $wR_2 = 0.2258$
Largest diff. peak and hole ($e.Å^{-3}$)	0.290/-0.356	0.493/-0.424	0.234/-0.221	0.435/-0.343	0.480/-0.440

Table 2: Important Bond Lengths (Å) in the Compounds of Chapter 2

Identification code	N1-P1	N1-P2	P1-N2	P2-N4	N2-N3	N4-N5	N3-C_i	N5-C_i
1a	1.551(4)	1.606(4)	1.682(4)	1.649(4)	1.370(5)	1.368(5)	1.280(6)	1.320(6)
1b	1.5646(15)	1.6054(15)	1.67228(16)	1.6267(15)	1.395(2)	1.372(2)	1.286(2)	1.312(2)
2a	1.5557(15)	1.5557(15)	1.664(4)	1.664(4)	1.381(5)	1.381(5)	1.289(6)	1.289(6)
2b	1.5785(6)	1.5785(6)	1.6749(11)	1.6749(11)	1.4043(15)	1.4043(15)	1.2862(17)	1.2862(17)
3	1.599(5)	1.563(5)	1.670(5)	P1O1 = 1.493(4)	1.375(6)	N/A	1.291(7)	N/A

Table 3: Important Bond Angles (°) in the Compounds of Chapter 2

Identification code	N1P1N2	N1P2N4	P1N2N3	P2N4N5	P1N1P2	N2N3C_i	N4N5C_i
1a	109.9(2)	109.4(2)	117.0(3)	109.6(3)	134.7(2)	118.3(4)	115.5(4)
1b	111.00(8)	122.14(8)	113.86(12)	112.51(11)	133.38(10)	117.8(14)	114.27(15)
2a	110.3(2)	110.3(2)	116.8(3)	116.8(3)	159.3(4)	119.4(4)	119.4(4)
2b	119.08(5)	119.08(5)	109.83(8)	109.83(8)	139.06(11)	118.27(11)	118.27(11)
3	N1P1O1 = 117.6(2)	110.0(2)	N/A	116.7(4)	130.5(3)	119.6(5)	N/A

Table 4: Hydrogen Bonding (Å and °) in the Compounds of Chapter 2

Identification code	D(D-H)	D(H…A)	D(D…A)	<(DHA)
1a N2-H2N···N5	0.91(2)	2.39(2)	3.154(2)	142.3(18)
1b N2-H2N···N4	0.89(5)	2.16(5)	2.954(6)	148(4)
2a N2-H2N···Cl1	0.91(6)	2.30(6)	3.147(5)	154(5)
2b N2-H2N···Cl1	0.872(14)	2.417(14)	3.1968(12)	149.1(15)
3 N2-H2N···O1	0.89(2)	2.12(4)	2.852(6)	139(5)

Chapter 3

3.1 Approach to Generate a Bent Allene

In his MSc thesis, Land[26,35] reported the synthesis of 1,3-*bis*(dimethylamino)-1,3-*bis*(2,6-diphenylphenolato) propenium chloride from the 1,3-dichloropropenium salt, however, Land did not explore its reactivity. Though the synthesis is relatively simple and proceeds in good yield,[26,35] the product, 1,3-*bis*(dimethylamino)-1,3-*bis*(2,6-diphenylphenolato) propenium chloride, was highly insoluble, only dissolving in chloroform. This would be an issue in the subsequent utilization of this compound, such as in its possible reactions to form a bent allene.

The diphenylphenolato compound has delocalized double bonds over the propenium backbone (Scheme 6). Removing the proton on the C2 carbon of the propenium backbone would prevent this electron delocalization by forcing the C2 carbon to make two double bonds, one to C1 and one to C3. This structure would be an allene, and due to the sterics of the terphenyl groups, it was believed that the allene would also be bent. The terphenyl groups were chosen as they have been widely used to form "bowl-shaped" pockets in other complexes. In the 1,3-*bis*(dimethylamino)-1,3-*bis*(2,6-diphenylphenolato) propenium chloride crystal structure reported by Land,[26,35] this pocket was observed to be ~4 Å wide. Such a pocket, in combination with the allene, might be sufficient to react with and bind a metal atom. In order to generate the bent allene, an anion metathesis would be required in order to first increase the solubility of the phenolato complex, as literature reports suggested allene generation requires the use of solvents such as THF, benzene, or toluene.[64,112-116]

Following a method reported by Land[26] the 1,3-dichloropropenium salt was reacted with 2,6-diphenylphenol and diisopropylethylamine (Scheme 6). After the reaction, ammonium salts were removed *via* an *aqueous* wash and an orange oil was obtained. The oil was dried under reduced pressure which yielded a pink powder. The powder was washed with 3 x 5 mL acetone which turned the powder white. The characterization data for the product matched that provided by Land,[26] confirming the structure to be 1,3-*bis*(dimethylamino)-1,3-*bis*(2,6-diphenylphenolato) propenium chloride (**4a** in Scheme 7).

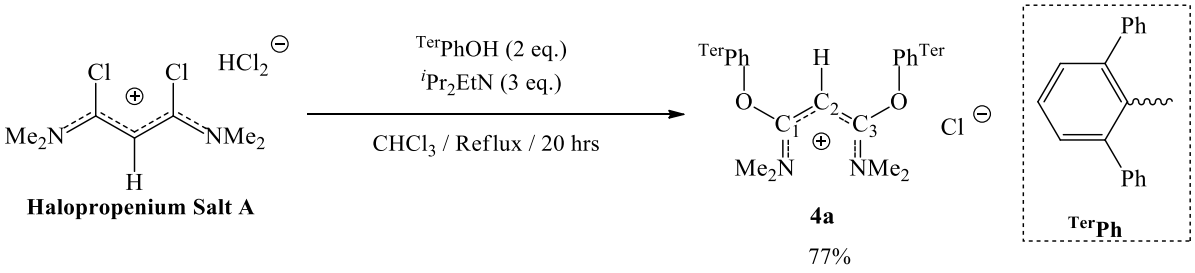

Scheme 6: Reaction conditions that led to the isolation of compound **4a**. The structure of the *m*-terphenyl substituent is also shown.

The investigation of **4a** was not pursued by Land[26] as it was determined that this ionic material was insoluble in most organic solvents. Chloroform was the only exception found, which was not suitable for his purposes.[26,35] It was decided that an anion metathesis might tune the physical properties of **4a** such that it could be made more soluble. A metathesis with the BPh_4 anion was tried as the steric hindrance of the anion would make it more weakly coordinating compared to the chloride anion, while the phenyl group could provide π-stacking potential to make any products more likely to crystallize. **4a** was dissolved in chloroform and reacted with excess sodium tetraphenylborate. The suspension was gravity filtered and the resulting solution slowly evaporated to give hexagonal shaped crystals in good yield. Using X-ray crystallography, the crystals were determined to be 1,3-

bis(dimethylamino)-1,3-*bis*(2,6-diphenylphenolato) propenium tetraphenylborate (**4b** in Scheme 7).

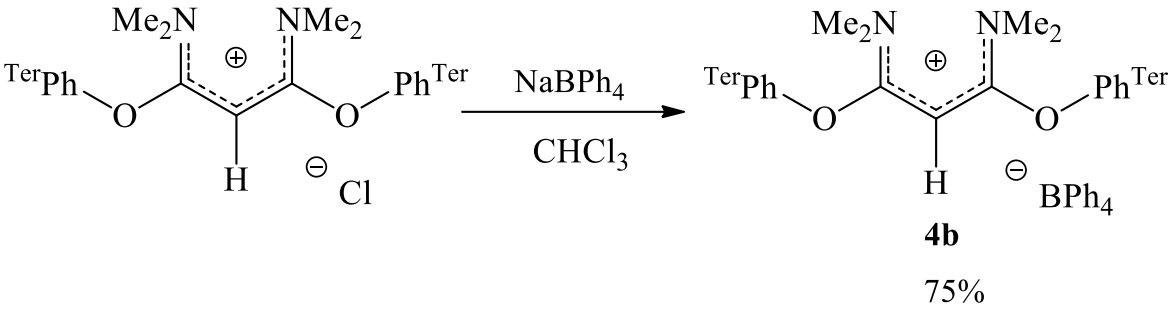

Scheme 7: Reaction conditions that led to the isolation of compound **4b**.

The characterization data of **4b**[xxviii] was nearly identical to that of **4a** with the exception of new BPh_4 signals in the ^1H NMR and ^{13}C NMR spectra (see the experimental section). The crystal structure of **4b$_1$** is orthorhombic with only a single cation/anion pair in the asymmetric unit. The crystal is also solvated with one molecule of chloroform in the asymmetric unit. The solvent is disordered, likely because of thermal motion even at 125 K, but the cation/anion pairs are much more ordered. The bond length between C1-C2 is 1.387(2) Å, and between C2-C3 is 1.390(2) Å which are both short for single bonds, as reported by Allen *et al.*[108] This does show that they have double bond character, further emphasizing the delocalization of electrons across the backbone of the molecule. The bond angle ∠C1C2C3 along the cation backbone is 127.89(17)°.

[xxviii] In this work, the compound **4b** has been isolated in multiple unique crystal forms. Due to this, compound **4b** has been given additional numbering in order to help differentiate between the multiple unique structures to be presented. The first of the crystal structures for **4b** to be discussed will be that of **4b$_1$**.

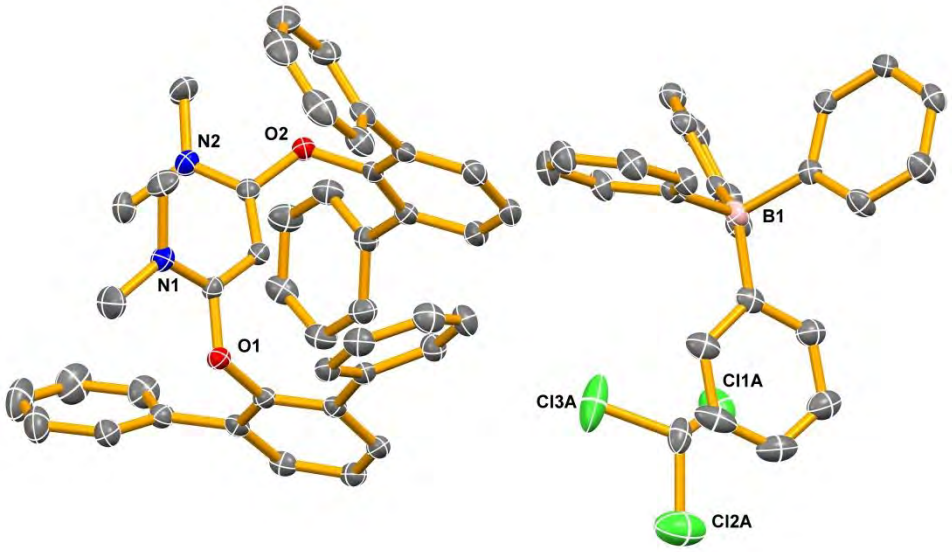

Figure 33: Solid state structure of 1,3-*bis*(dimethylamino)-1,3-*bis*(2,6-diphenylphenolato) propenium tetraphenylborate, **4b$_1$**. Crystal solvated with one molecule of chloroform per cation/anion pair (disorder has been removed). Hydrogen atoms are not shown and only some of the atoms have been labelled to improve the clarity. Thermal ellipsoids are drawn at the 50% probability level.

The packing diagram of **4b$_1$** forms a vertical wave pattern when viewed down the *Y*-axis. *m*-Terphenyl groups appear to be what compose the basic wave pattern, which encapsulates the propenium backbone structure from another cation. It also appears that the tetraphenylborate anion aligns with the terphenyl groups in the pattern. This pattern appears to leave small channels that run parallel to the *Y*-axis, which the chloroform solvent is able to occupy.

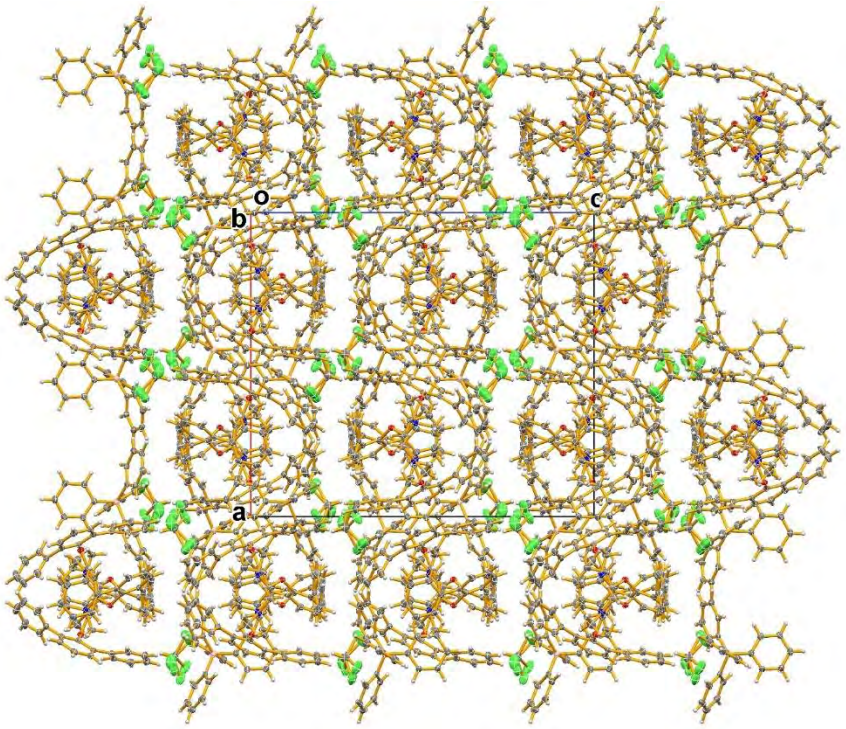

Figure 34: Solid state packing diagram of **4b**$_1$ viewed down the *Y*-axis. The crystal is solvated with chloroform. Thermal ellipsoids are drawn at the 50% probability level.

The solubility of **4b** was tested and it was determined to be soluble in THF, toluene, and benzene. This was of importance as these solvents allowed the chemistry of this compound to be investigated. In particular, if the central hydrogen (on C2) could be removed by deprotonation, then it was believed that the structure would form a C1=C2=C3 allene. In this case, a bent allene, also known as a carbodicarbene, would be the likely product (Scheme 8) as per the work of multiple authors (Dyker *et al.,*[64] Frenking *et al*.,[112] Goldfogel *et al*.,[113] Roberts *et al.,*[114] Schwesinger,[115] and Saalfrank *et al.*[116]).

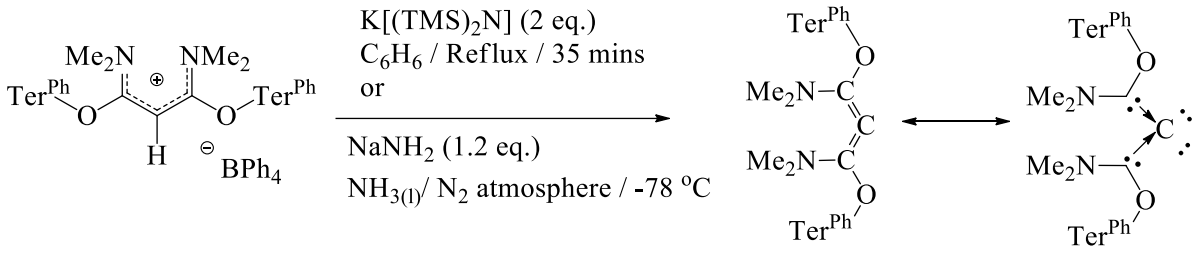

Scheme 8: Potential syntheses from **4b** to generate a bent allene (and its resonance form - highlighting that it is an example of a carbodicarbene). Three potential reaction methods are given.

Following known literature methods[64,112-116] additional reactions were performed starting from **4b,** in attempts to generate a bent allene/carbodicarbene. All reaction attempts, however, were unsuccessful and only the starting material **4b** was ever isolated from the experiments. This, however, does not mean that interesting results for **4b** were not observed. In each of the experiments, **4b** was crystallized under different conditions, which produced a unique crystal structure for each form of compound **4b**. The reaction methods used to prepare all of the derivatives of **4b** are shown in Scheme 9. As each of the structures are the same as **4b**, from this point onwards, there will be additional numbering and **4b** shall be referred to as **4b1** in order to differentiate between the compounds.

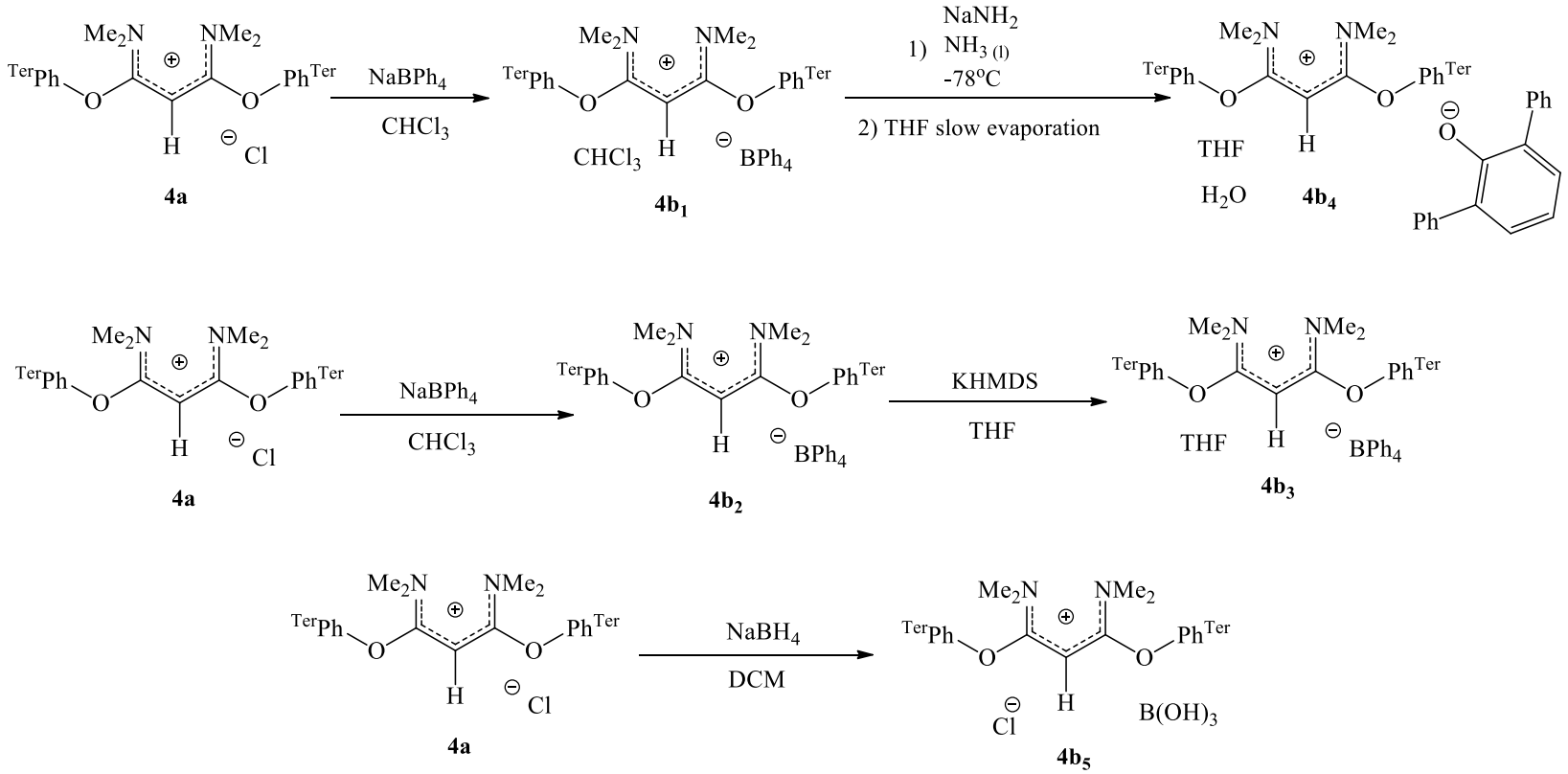

Scheme 9: Reaction conditions that led to the isolation of the derivatives of 4b prepared in this work. Structures are shown as their respective formula units as determined using X-ray crystallography.

The next structure determined, denoted as **4b$_2$**, was synthesized in an identical manner to **4b$_1$** (as shown above), though the reaction was scaled up by a factor of five. It is unknown why this produced a different crystal structure compared to **4b$_1$**, but a likely idea is that with more material, **4b$_2$** crystallized more slowly as there was more solvent to evaporate. This could have allowed it to pack and crystallize without incorporating chloroform into the structure. The compound **4b$_2$** has a single cation/anion pair in the asymmetric unit and is a monoclinic structure. Unlike the previous crystal **4b$_1$**, which was orthorhombic, **4b$_2$** does not have any solvent in the unit cell. The bond length C1-C2 is 1.385(3) Å, and C2-C3 is 1.388(3) Å. These show no significant differences from the bond lengths in the cation of **4b$_1$**. The bond angle ∠C1C2C3 is 128.35(19)°, which is an insignificant difference compared of that of **4b$_1$**.

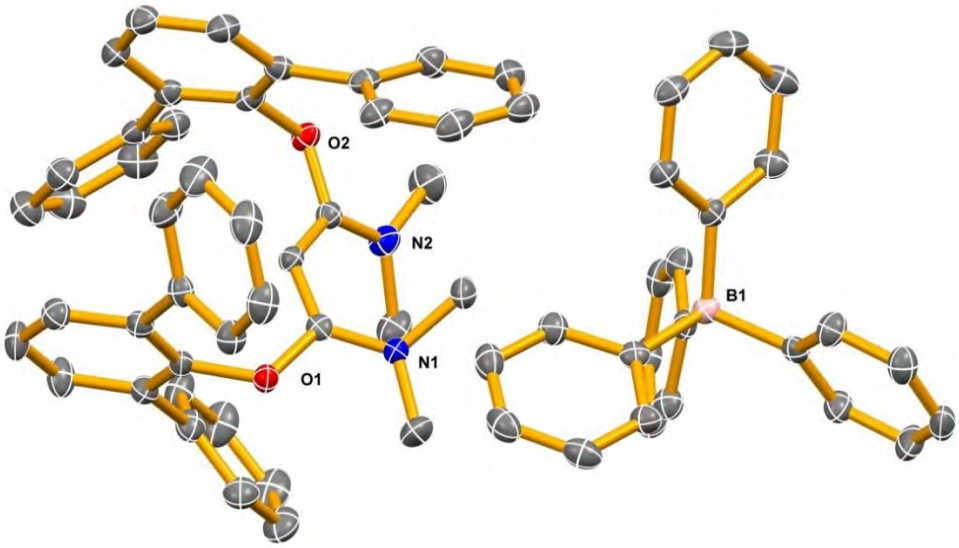

Figure 35: Solid state structure of 1,3-*bis*(dimethylamino)-1,3-*bis*(2,6-diphenylphenolato) propenium tetraphenylborate, **4b$_2$**. The crystal is not solvated. Hydrogen atoms are not shown and only some of the atoms have been labelled to improve the clarity. Thermal ellipsoids are drawn at the 50% probability level.

The packing diagram for **4b$_2$** forms a diagonal wave pattern when viewed down the *Y*-axis. The *m*-terphenyl groups compose the wave pattern, but unlike in **4b$_1$**, these groups do not appear to be encapsulating the propenium cations. Instead the tetraphenylborate anion is overlapping the propenium backbone parallel to the *Y*-axis, lying either on top or underneath the propenium backbone.

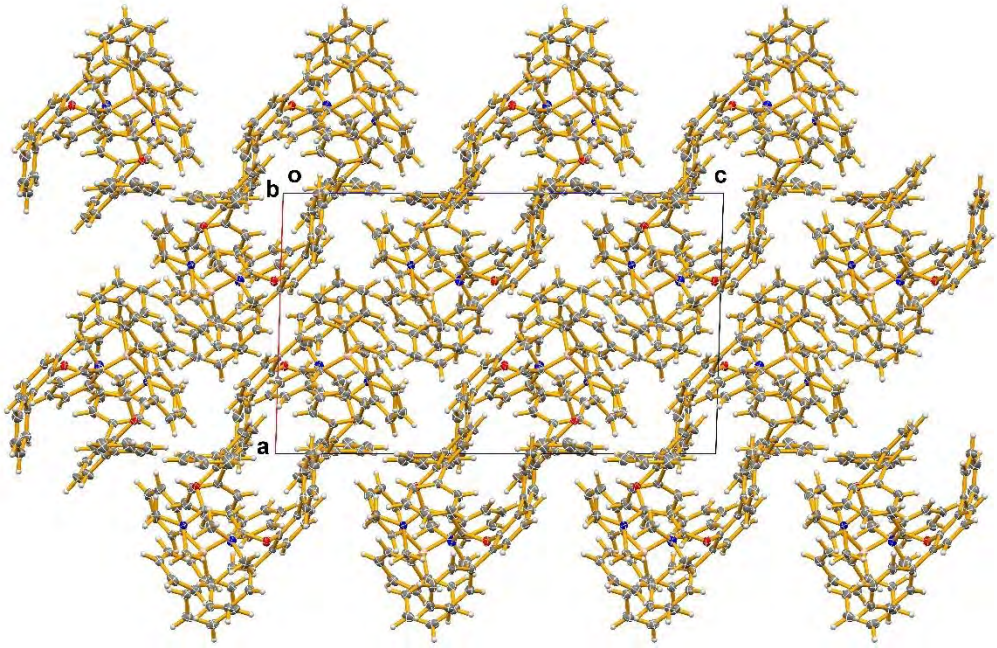

Figure 36: Solid state packing diagram of **4b$_2$** viewed down the *Y*-axis. The crystal is not solvated. Thermal ellipsoids are drawn at the 50% probability level.

The next structure determined, denoted as **4b$_3$**, was isolated after yet another attempt to generate a bent allene. Under a dry nitrogen atmosphere, **4b** was dissolved in THF with an excess of potassium *bis*(trimethylsilyl)amide (KHMDS) and the solution was left to stir for 24 h. It was then filtered through Celite and left to slowly evaporate in the dry nitrogen atmosphere. Crystals grew from the solution. The structure of **4b$_3$** has two

unique cation/anion pairs in the asymmetric unit and is also monoclinic. **4b$_3$** has two molecules of tetrahydrofuran within the asymmetric unit, which appear to have extensive thermal disorder. The propenium backbone of the first cation has bond lengths of C9-C10 = 1.385(2) Å, and C10-C11 = 1.396(2) Å. The ∠CCC angle is 126.02(13)°. For the second cation, the corresponding bond lengths are C52-C53 = 1.388(2) Å, and C53-C54 = 1.393(2) Å. The angle ∠CCC is 126.77(13)°.

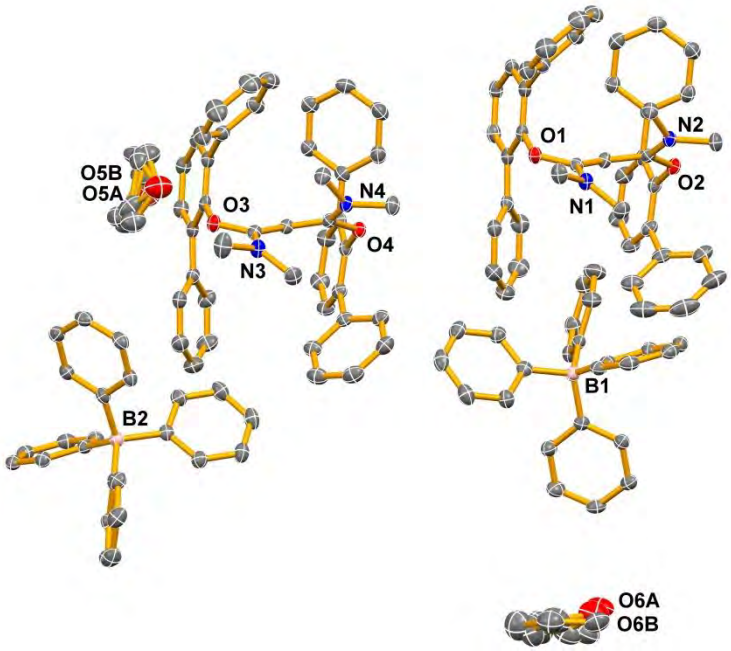

Figure 37: Solid state structure of 1,3-*bis*(dimethylamino)-1,3-*bis*(2,6-diphenylphenolato) propenium tetraphenylborate, **4b$_3$**. The crystal solvated with one molecule of tetrahydrofuran (disordered) for each cation/anion pair. Hydrogen atoms are not shown and only some of the atoms have been labelled to improve the clarity. Thermal ellipsoids are drawn at the 50% probability level.

The packing diagram of the molecules for **4b$_3$** does not form any discernable pattern when viewed down any axis. When viewed down the *X*-axis, the disordered tetrahydrofuran

groups appear to situate themselves adjacent to the boron in the anions. It appears as if it fits into a pocket formed in the structure between the propenium cation backbone and the tetrahedral orientation of the tetraphenylborate anion.

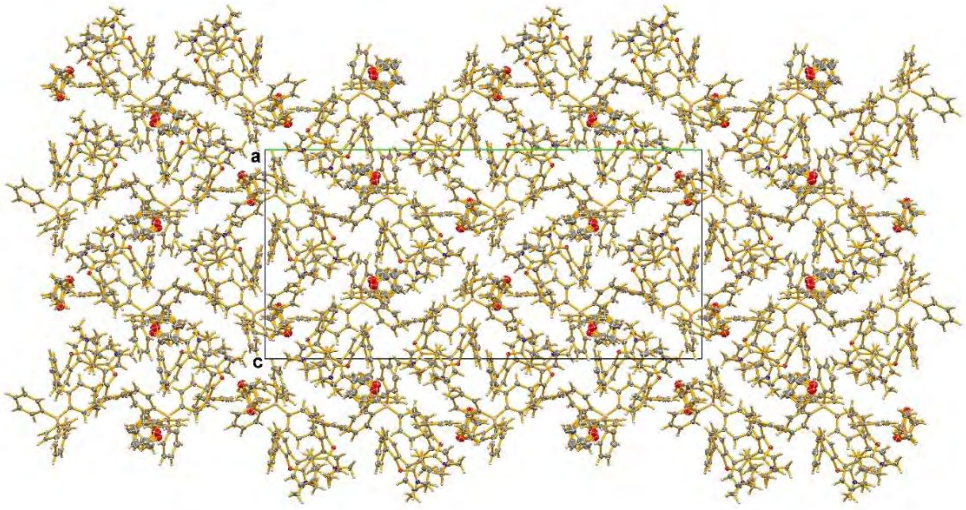

Figure 38: Solid state packing diagram of **4b$_3$** viewed down the *X*-axis. The crystal is solvated with tetrahydrofuran. Thermal ellipsoids are drawn at the 50% probability level.

The next structure determined, denoted as **4b$_4$**, was again isolated from an attempt to generate a bent allene. Under a nitrogen atmosphere, **4b** was deposited into a 3-neck flask with an excess of sodium amide. The flask was sealed, connected to a Schlenk apparatus, and a cold finger was added. All of the air was purged and replaced with $N_{2(g)}$ under constant flow. The flask was placed into an acetone/dry ice bath and ammonia was allowed to enter the Schlenk apparatus; the gas condensed into a liquid upon contact with the cold finger. Enough liquid ammonia was added such that the **4b**/sodium amide mixture was covered. This reaction was allowed to proceed for a few hours, in which time the white powder of **4b** had become yellow. Under a nitrogen atmosphere, the sample was dissolved in DCM. This resulted in a bright red solution being formed. It should be noted at this point

that the addition of DCM to the product was a mistake, as sodium amide is not compatible with halogenated solvents. This may have created unintended reactions, or even destroyed the bent allene, if one had been formed. The solution was left to slowly evaporate under a dry nitrogen atmosphere, which resulted in yellow crystals that were determined to be **4b$_4$**. The water and THF solvents found in the crystal were not present in the reaction mixture. However, while slowly evaporating, the solution was placed beside another sample, **4b$_3$**, that was also slowly evaporating. It is believed that THF and water vapour from **4b$_3$** diffused into **4b$_4$** on standing, leading to the observed crystal structure.

The structure of **4b$_4$** has one unique cation/anion pair in the asymmetric unit and has a triclinic unit cell. **4b$_3$** has one tetrahydrofuran and one water molecule present in the asymmetric unit as solvents, and a 2,6-diphenylphenolate anion. Since the 2,6-diphenylphenolate is the anion, it is likely from a molecule of **2b** that has fragmented in the presence of sodium amide, likely during the addition of the DCM. The tetrahydrofuran and the water molecules within the unit cell are disordered (the former highly so). The propenium backbone bond length C1-C2 is 1.394(2) Å, and C2-C3 is 1.381(2) Å. The bond angle between ∠CCC is 127.81(16)°. The bond lengths and angles for the propenium cation backbone in **4b$_4$** do not show any significant differences from those in the previous molecules.

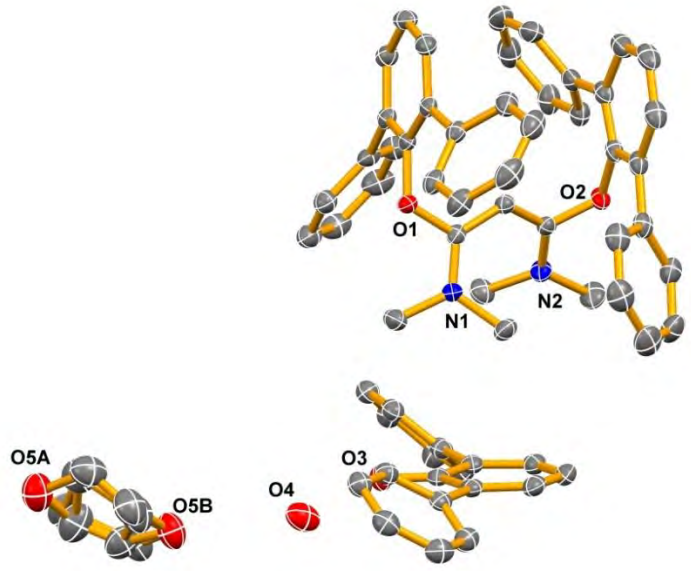

Figure 39: Solid state structure of 1,3-*bis*(dimethylamino)-1,3-*bis*(2,6-diphenylphenolato) propenium 2,6-diphenylphenolate, **4b**$_4$. The crystal is solvated with one molecule of tetrahydrofuran (disordered) and one molecule of water for each cation/anion pair. Hydrogen atoms are not shown and only some of the atoms have been labelled to improve the clarity. Thermal ellipsoids are drawn at the 50% probability level.

The packing diagram of the molecules for **4b**$_4$ forms horizontal rows parallel to the *Z*-axis when viewed down the *X*-axis, with the disordered water, tetrahydrofuran, and 2,6-diphenylphenolate anions fitting into a channel made between these rows.

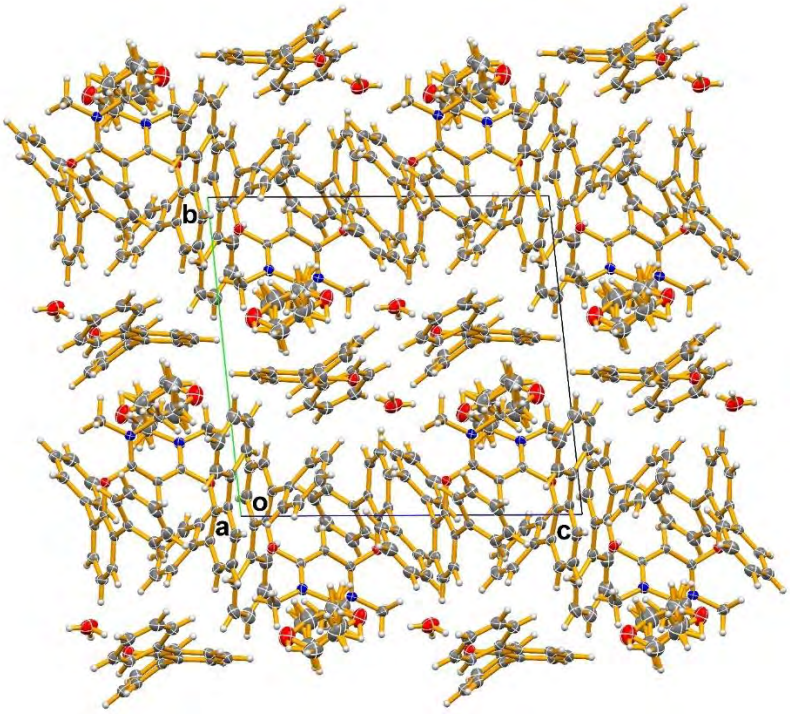

Figure 40: Solid state packing diagram of **4b$_4$** viewed down the *X*-axis. The crystal is solvated with tetrahydrofuran and water. Thermal ellipsoids are drawn at the 50% probability level.

The structure of **4b$_4$** has an extensive hydrogen bonding network (Figure 41, and Table 10). This extends through the water molecule, which interacts with the tetrahydrofuran and with two different 2,6-diphenylphenolate anions. The water was found to be in two different orientations, each with a different hydrogen bonding pattern. One of the hydrogen atoms in the water molecule is fully occupied, while the other is only 50% occupied; that hydrogen is divided between two sites, which are geometrically opposite to each other. This can be seen in Figure 41, where the water molecule has H1O, which is the 100% occupied hydrogen, while the H2O and H3O hydrogen atoms are each present only 50% of the time. It is not the hydronium ion it appears to be, but instead it is the described neutral water molecule.

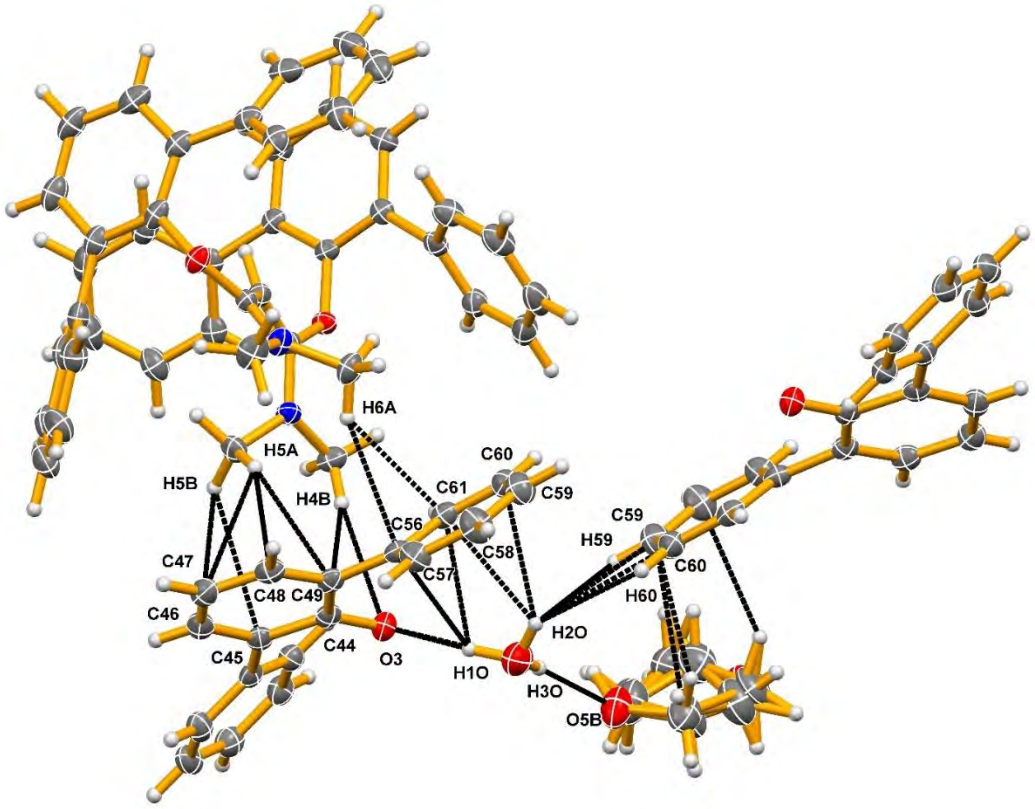

Figure 41: Solid state structure of 1,3-*bis*(dimethylamino)-1,3-*bis*(2,6-diphenylphenolato) propenium, **4b**$_4$. The crystal is solvated with tetrahydrofuran and water. Intermolecular hydrogen bonding within the structure is shown. Thermal ellipsoids are drawn at the 50% probability level.

The next structure determined, denoted as **4b**$_5$, was recovered from an attempted anion metathesis. **4b** was dissolved in DCM and an excess of sodium borohydride was added to the solution. The sample was left to stir for 5 h, before being filtered through Celite. The resulting solution was left to slowly evaporate, which did not yield crystals. This material was redissolved in DCM and layered with hexane for solvent diffusion. Colourless crystals grew within 15 h, the structure of which was determined to be **4b**$_5$. The structure of **4b**$_5$ has one unique cation/anion pair in the asymmetric unit and also has a triclinic unit cell. Though the cation of **4b**$_5$ is no different from the rest of the **4b** series,

there is a chloride anion, instead of the expected BPh_4, and neutral boric acid solvates the structure. The boric acid likely resulted from the hydrolysis of the sodium borohydride, as this reaction was not performed under a N_2 atmosphere. The propenium backbone of the cation has bond lengths C1-C2 = 1.3909(19) Å and C2-C3 = 1.393(2) Å, while the bond angle ∠CCC is 129.02(13)°.

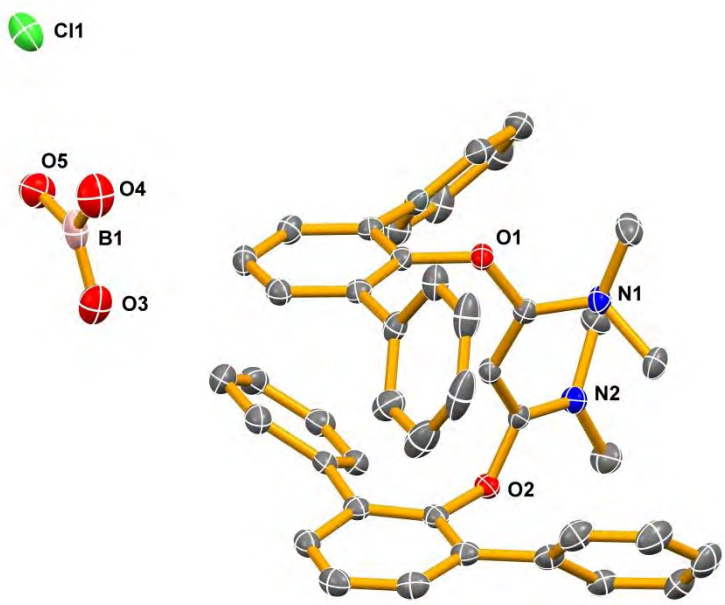

Figure 42: Solid state structure of 1,3-*bis*(dimethylamino)-1,3-*bis*(2,6-diphenylphenolato) propenium chloride boric acid solvate, **4b$_5$**. Hydrogen atoms are not shown and only some of the atoms have been labelled to improve the clarity. Thermal ellipsoids are drawn at the 50% probability level.

The packing diagram for **4b$_5$** forms a wave patterned channel that runs horizontally when viewed down the *X*-axis. This channel provides enough space for the chloride and boric acid to situate within the structure. The chloride and boric acid are oriented such that two boric acid molecules are between two chloride anions. Intermolecular forces result

from this orientation, as the boric acid molecules have hydrogens directed towards both oxygen atoms and chloride anions (Figure 44).

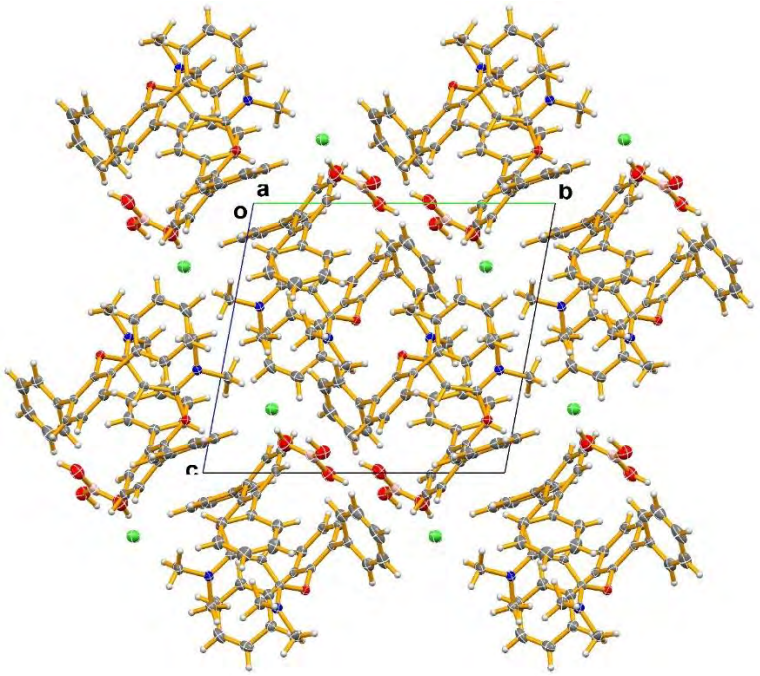

Figure 43: Solid state packing diagram of **4b$_5$** viewed down the *X*-axis. The crystal is solvated with boric acid. Thermal ellipsoids are drawn at the 50% probability level.

Unlike **4b$_4$** which had hydrogen bonding between water and the phenyl rings of the anion, **4b$_5$** has hydrogen bonding to more traditional acceptors (Cl and O atoms of the anion and solvate respectively). As mentioned earlier, the hydrogen bonding results in the orientation of two boric acid molecules between two chloride anions. Two boric acid molecules hydrogen bond (O-H···O) to each other in a stacked orientation, while each also forms two O-H···Cl hydrogen bonds with chloride anions. The cations also form weaker C-H···O hydrogen bonds with oxygen atoms of the boric acid resulting in large dimers comprised of two cations, two anions and two boric acid molecules being the main structural unit.

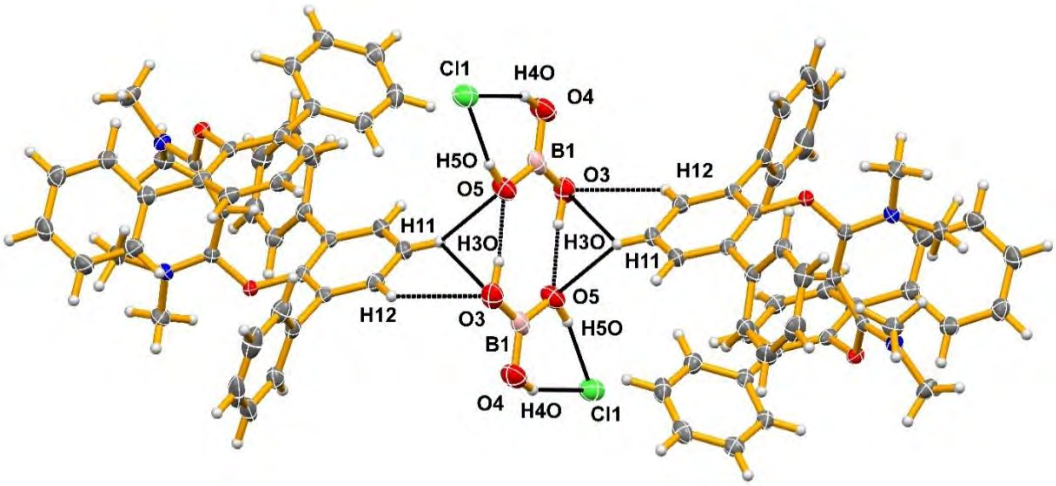

Figure 44: Solid state structure of 1,3-*bis*(dimethylamino)-1,3-*bis*(2,6-diphenylphenolato) propenium chloride boric acid solvate, **4b**$_5$ drawn to show the large dimeric structural unit held together by hydrogen bonding interactions. Thermal ellipsoids are drawn at the 50% probability level.

3.2 Comparison of the Planes in the 4b Compounds

As the cations of the **4b** compounds are all structurally identical, despite the attempts to generate a bent allene, typical comparisons are not that useful. Instead, specific discussion of the conformations of the cations must be made in order to properly compare the crystal structures of the **4b** series (Figure 45).

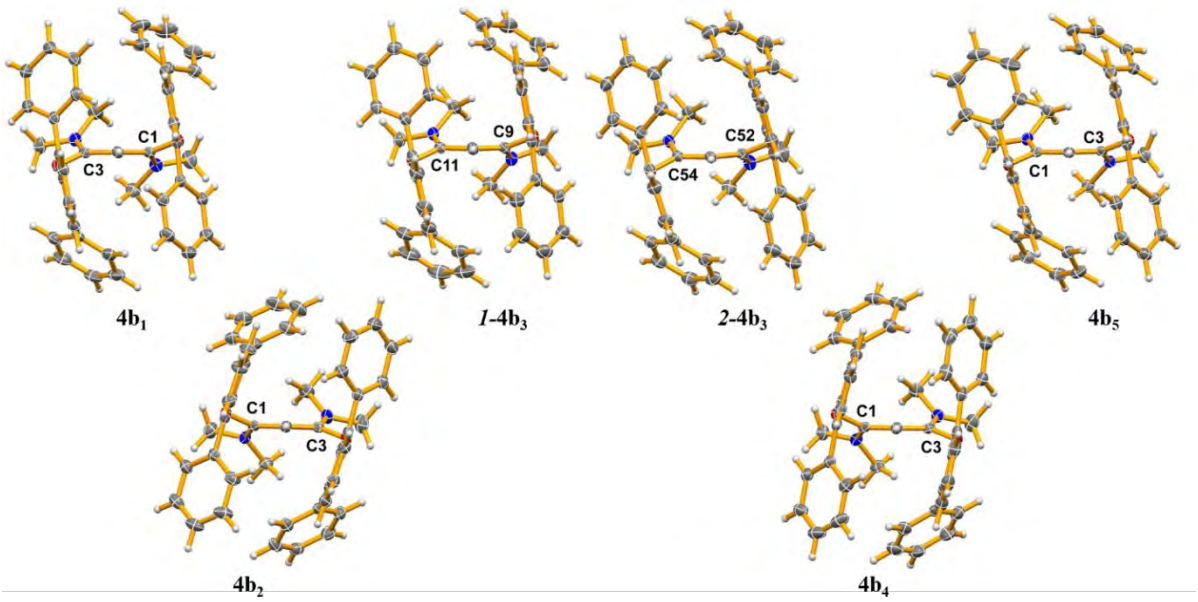

Figure 45: Comparison of **4b** compounds, viewed in the same plane. The cation backbone was oriented horizontally with the central hydrogen atom pointing out of the plane of the view. The cations were then rotated in the plane of the page until they all had similar orientations, regardless of the cation numbering.

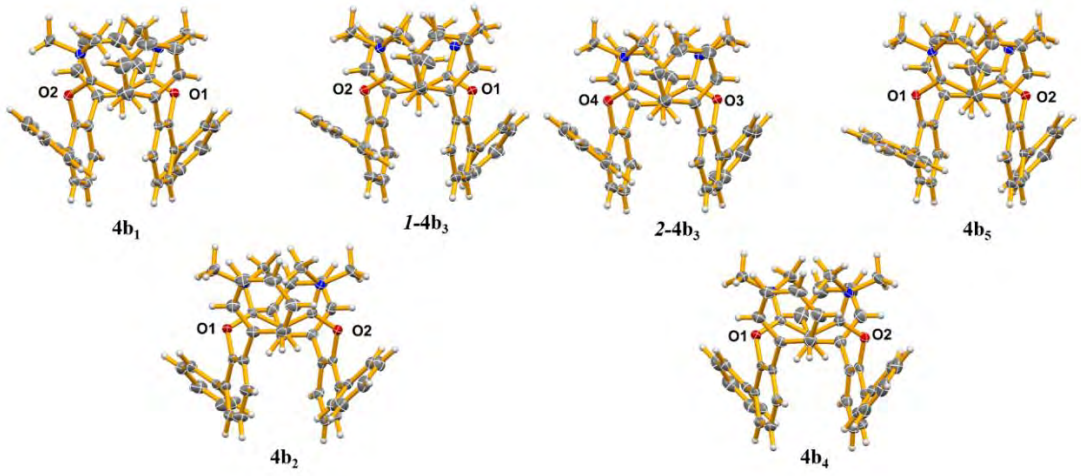

Figure 46: Comparison of **4b** compounds, rotated by 90º in the *x* direction from the original view.

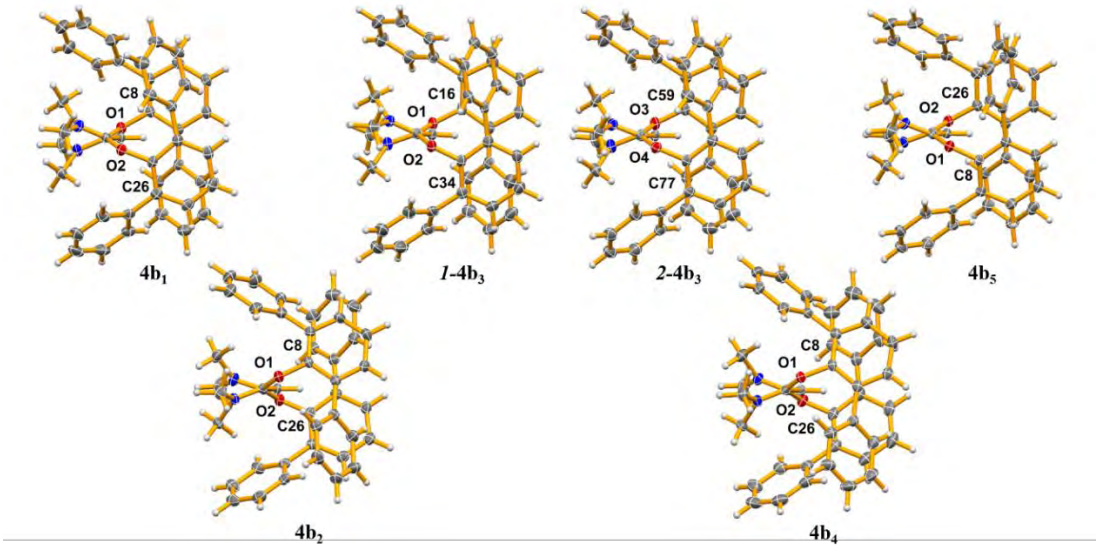

Figure 47: Comparison of **4b** compounds, rotated by 90º in the *y* direction from the original view.

In Figure 45, minor differences can be observed between the structures of the cations. The reasons that these differences occur, however, have to be examined individually to determine if they are due to effects from solvent and/or the anion, or if they are just a result of the crystal packing. These will be discussed subsequently. More importantly, it is immediately observed that **4b2** and **4b4** slant towards to the right, compared to the other structures which slant towards the left in the view shown. This also gives **4b2** and **4b4** the same orientation of the dimethyl amine and terphenyl groups, as would be expected. This is interesting, however, as **4b2** and **4b4** have different anions and solvents within the crystal unit cell; **4b2** has a tetraphenylborate anion and does not have any solvent, while **4b4** has disordered water, tetrahydrofuran, and 2,6-diphenylphenolate anions within the structure. There is also extensive hydrogen bonding in **4b4** that does not appear to affect the cation structure compared to that of **4b2**. In the previous Chapter, the

effects of hydrogen bonding were enough to influence to geometry of the compounds to create noticeable structural differences; it is interesting that this effect does not appear to have changed the geometry in **4b4**.

The other cations which slant towards to the left, **4b1**, ***1*-4b3**, ***2*-4b3**,[xxix] and **4b5**, all share similar differences to the basic structure of **4b2**, and **4b4**. **4b5** like **4b4** exhibits extensive hydrogen bonding, however, it has a conformation more akin to **4b1**, ***1*-4b3**, and ***2*-4b3**. From Figure 45, it can be seen that there is the same orientation of the dimethyl amine and terphenyl groups for **4b1**, **4b3**, and **4b5**. **4b1**, and **4b3**, are both solvated (with DCM and THF, respectively) and both have a tetraphenylborate anion. **4b5**, however, has a chloride anion while being solvated with boric acid. Despite this, it still shares the same conformation as **4b1**, and **4b3**.

In Figures 46 and 47, the same trend that is seen in Figure 45, is present with the **4b** compounds: **4b2**, and **4b4** are similar to each other but different from **4b1**, **4b3**, and **4b5** which are similar to each other. Specifically, in Figure 46, **4b2**, and **4b4** have the same rotation of the oxygen groups, where the left oxygen atom is out of the plane and the right oxygen atom is into the plane as drawn. This is also true for the left and right nitrogen atoms, respectively, in Figure 46 for **4b2**, and **4b4**. For **4b1**, **4b3**, and **4b5**, the opposite is observed in Figure 46. In Figure 47, a similar difference is seen in the orientation of the oxygen and nitrogen atoms. For **4b2** and **4b4**, O1[xxx] is out of the plane while O2 is behind the plane. For **4b1**, **4b3**, and **4b5**, the opposite is observed, with O2 out of the plane and O1 is behind the plane.

[xxix]Compound **4b3** has two molecules in the asymmetric unit. Unless there is a need to specifically distinguish between them, as denoted above, **4b3** will be used in reference to the compound.
[xxx] Numbering is as depicted in Figure 46, although the numbering is not consistent for all compounds.

Table 5: Torsion Angles (º) of the **4b** Compound Series

	N1C1C2C3	C1C2C3N2	O1C1C2C3	C1C2C3O2
4b$_1$	-27.3(3)	-29.1(3)	157.75(17)	153.57(17)
4b$_2$‡	26.5(4)	24.3(4)	-157.28(19)	-159.8(2)
***1*-4b$_3$**	-26.9(2)	-27.5(2)	157.00(14)	155.15(14)
***2*-4b$_3$**	-27.1(3)	-26.6(3)	156.28(14)	156.59(14)
4b$_4$‡	29.6(3)	24.5(3)	-153.75(16)	-159.04(16)
4b$_5$	-26.0(2)	-26.3(2)	157.55(13)	158.44(13)

Though the atoms in the compounds may be numbered differently, the signs of the reported torsion angles are independent of the numbering. The sign of the angles indicates direction of rotation between the external bonds of the torsion.

‡ A cation related by an inversion center to the cation type used for **4b$_1$**, **4b$_3$** and **4b$_5$**, was used for the torsion angles in **4b$_2$** and **4b$_4$**. Though the absolute values are not different, note that the signs for the values of these compounds are opposite to those of **4b$_1$**, **4b$_3$** and **4b$_5$**. This has not been changed in the table to coincide with the discussion below.

As can be observed in Table 5, the torsion angles of the **4b** series of compounds reveal the same trend identified in Figures 45, 46, and 47; the compounds can be divided into two distinct groups, **4b$_2$**, and **4b$_4$** form one, while **4b$_1$**, **4b$_3$**, and **4b$_5$** form another. This idea, however, became more suspect upon examination of the torsion angles, as it was noticed that although the signs were different, the magnitudes of the torsions were always very similar. This raised the question to whether or not an inversion center was present in the unit cell for the compounds **4b$_2$** and **4b$_4$**. If this were true it would mean that inverted molecules of **4b$_2$**, and **4b$_4$** were selected for refinement (relative to the other compounds) which would produce the exact same values for the torsion angles, but with the opposite

signs. This was determined to be the case, as shown in Figure 48, where the triclinic unit cell of **4b$_4$** contains only two cation/anion pairs. The asymmetric unit contains one cation with a second generated by inversion. These two cations have torsion angles with the same magnitudes but with opposite signs.

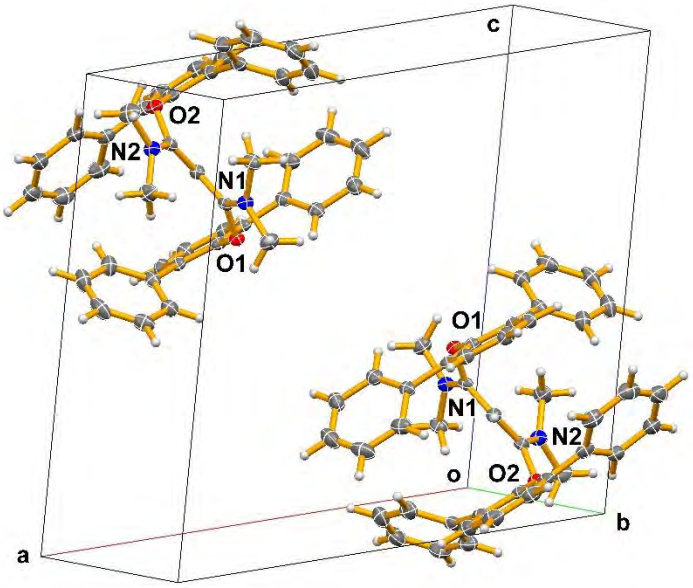

Figure 48: The triclinic unit cell of **4b$_4$** showing only the cations. The unique cation is shown as well as a second cation generated by inversion across the center at (½, ½, ½). THF solvent, water, and the anions have all been removed.

With the correct choice of the cation, relative to the inversion center, all of the structures will have the same signs of for the torsion angles. There is no further correction needed for compounds **4b$_2$** and **4b$_4$**, as the inversion center would only change the sign of the torsion angles in the cations; the absolute values of the angles will be the same. The structures share the same torsion angles, but the difference in the sign indicates that the angle of rotation is in the opposite direction.

Structure **4b$_4$** is particularly interesting (Table 5), as the difference between the torsion angles N1C1C2C3 and C1C2C3N2 is ~5º, which is also true for the difference between the O1C1C2C3 and C1C2C3O2 angles. The other compounds only have a difference of ≤ 3º between the same pairs of torsion angles. It is unknown why **4b$_4$** alone has this large difference in its crystal structure. Possibly it is due to the large amount of hydrogen bonding within the structure, although, if this were true, one would expect **4b$_5$** to also show these same differences.

Since no major differences were found in the conformations of the cations in the structures studied, a closer examination of the cation planes was next carried out. This was done to see if any minor differences in the conformations of the cations could be identified in these compounds.

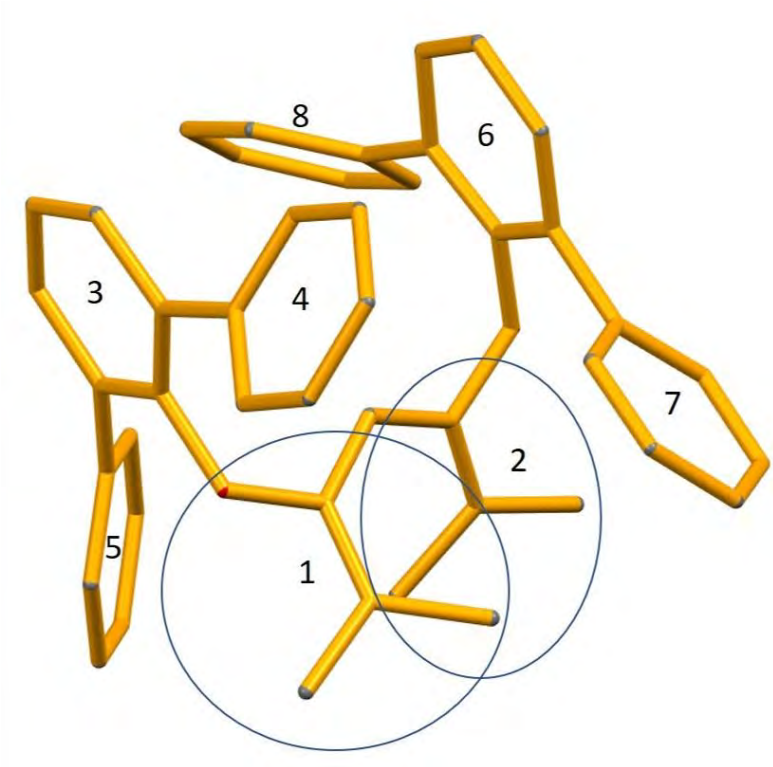

Figure 49: Defined planes of the **4b** cations.

In order to discuss the minor differences of the compounds in this Chapter, the same planes were defined for each of the cations in the compounds studied (Figure 49). Comparing the angles made between the defined planes in the individual cations can be used to find modest differences between the structures. Though the planes have been defined in Figure 48, there is no way to tell one side of the molecule from the other. This, however, does not matter when you compare planes across one side of the molecule to the other. The comparison of selected individual planes, for the cations only, is compiled in Table 6.

Table 6: Comparison of the Angles (º) Between Planes for **4b** Compounds

	4b1	**4b2**	***1*-4b3**	***2*-4b3**	**4b4**	**4b5**	**Δ max-min**
Plane 2 to 1	65.1	56.6	54.3	57.1	58.2	57.9	10.8
Plane 3 to 1	73.6	81.2	66.1	75.4	75.6	81.2	15.1
Plane 4 to 3	50.7	52.3	52.9	39.4	53.1	47.7	13.7
Plane 5 to 3	37.7	52.9	41.1	54.4	39.9	66.5	28.8
Plane 5 to 4	39.5	44.0	52.3	46.1	45.5	53.1	13.6
Plane 6 to 2	76.8	81.4	73.9	78.8	76.1	77.4	7.5
Plane 6 to 3	3.8	3.4	3.7	3.3	3.3	5.0	1.7
Plane 7 to 4	82.8	86.1	80.7	87.7	54.8	75.9	32.9
Plane 7 to 6	53.3	45.1	59.5	52.6	53.5	38.5	21
Plane 8 to 5	79.1	50.2	84.9	53.0	77.1	83.9	34.7
Plane 8 to 6	52.7	50.4	53.5	48.5	39.0	51.1	14.5
Plane 8 to 7	61.0	44.2	56.0	50.1	49.0	42.9	18.1

From these plane values, the compounds can be compared more quantitatively. Considering the 2 to 1 planes, the angle between the two halves of the cation backbone, there does not seem to be much difference between the plane angles for the **4b** compounds. The one exception, however, is that of **4b$_1$**, where there is a significant difference in this plane angle compared to those of the other compounds, which implies that **4b$_1$** is more opened compared to the other compounds.

Although the plane comparisons do show differences, the plane angles also reveal similarities, such as observed for the 6 to 3 plane angles. This angle relates the orientation of one central terphenyl ring to the orientation of the other terphenyl ring across the same molecule. All of the complexes share a relatively similar angle for these planes, with only a 1.7º difference between them. This small average value relating these two rings shows that the central terphenyl rings are almost parallel to each other in these complexes. It is important to note that although these rings are almost completely parallel there is no intramolecular stacking between the rings, as they are too far apart to have meaningful stacking interactions.

The next set of planes examined were the 5 to 4 and 8 to 7 planes, which both involve the angles between the planes of the phenyl rings on the same terphenyl group. As stated earlier, although there is no way to tell one side of the molecule from the other, it does not matter when you compare planes on one side of the molecule to those on the other. From the 5 to 4 and 8 to 7 planes, it can be seen that there is roughly that same variance between the max-min of the plane angles for each group, with values of 13.6º and 18.1º, respectively. This implies that the phenyl rings groups are twisted in significantly different orientations (but in much the same way) for each side of each of the **4b** cations. This could

be an effect of the individual packing arrangements of each compound, and helps to illustrate the subtle differences between the compounds.

Although the individual molecules of **4b$_3$** appear to be nearly identical in Figures 45-47, this is not necessarily the case when looking at the plane angles in Table 6. For example, in the 4 to 3 planes (which translates to the rotation of a phenyl group compared to the central ring of a terphenyl ligand) ***1*-4b$_3$** has an ~10º difference between the planes compared to ***2*-4b$_3$**. In fact, ***2*-4b$_3$**, when comparing the 4 to 3 planes, is significantly different from the other compounds. This is interesting as the molecules of **4b$_3$** crystallize together, so it would be expected that they would be more similar in geometry. Considering the 4 to 3 plane angles, ***1*-4b$_3$** is more similar to the other compounds than it is to ***2*-4b$_3$**, even though these molecules are a part of the same crystal unit cell. The most variability is seen in the angles that the outer phenyl rings create with respect to the central ring of the terphenyl group. The difference between the 5 to 3 plane and the 7 to 6 plane are 28.8º and 21.0º, respectively. These changes must allow the cation to pack as efficiently as possible in the different structures.

In summary, it is not clear why the **4b** compounds do not show any major conformational changes in the cations, as seen from Figure 45-48 and Table 5,[xxxi] however a few ideas can be proposed. First, it could be that the **4b** cations have achieved the ideal packing in the structures of all of these compounds. **4b$_1$**, and **4b$_3$**, are both solvated (with DCM, and THF respectively), while **4b$_2$** is free of any solvent, so this seems unlikely. It also does not explain why **4b$_4$** and **4b$_5$**, which both have hydrogen bonding, are also in the

[xxxi] After taking the inverted cations into account.

same configuration[xxxii] as the other **4b** compounds. It would be expected that **4b**$_4$ and **4b**$_5$ would pack differently than all of the other **4b** compounds because of the change in the anions and/or the increased intermolecular forces. However, this was not observed after analysis of the qualitative data and torsion angles. It appears that the **4b** cations pack in the "ideal" conformation regardless of additional intermolecular forces, solvent effects, and steric hindrances caused by the anions and solvents. It was expected that these forces would create noticeable differences within the solid-state structures, however this was not observed. This could potentially be examined in more detail with computational analysis, but that is beyond the scope of this thesis. Finally, and unfortunately, despite repeated attempts, the **4b** series of compounds never reacted to form a bent allene.

[xxxii] As seen from Figures 45-48 and the torsion angles in Table 5.

Table 7: Crystal Data and Structure Refinement Details of the **4b** Compounds

Identification code	**4b$_1$**	**4b$_2$**	**4b$_3$**	**4b$_4$**	**4b$_5$**
Empirical formula	$C_{68}H_{60}BCl_3N_2O_2$	$C_{67}H_{59}BN_2O_2$	$C_{142}H_{134}B_2N_4O_6$	$C_{65}H_{62}N_2O_5$	C_{43} $H_{42}BClN_2O_5$
Formula weight	1054.34	934.97	2014.14	951.16	713.04
Crystal system	Orthorhombic	Monoclinic	Monoclinic	Triclinic	Triclinic
Space group	*Pbca*	*P*2$_1$/*c*	*P2$_1$/n*	*P-1*	*P-1*
a (Å)	21.786(2)	13.2366(17)	13.4365(8)	13.3862(12)	12.3904(18)
b (Å)	21.155(2)	17.897(2)	41.888(3)	13.4836(12)	13.045(4)
c (Å)	24.595(3)	22.389(3)	20.6806(13)	14.7658(13)	13.2373(19)
α (°)	90	90	90	93.9410(10)	98.111(2)
β (°)	90	91.702(2)	103.7050(10)	104.7810(10)	116.5730(10)
γ (°)	90	90	90	96.1190(10)	93.041(2)
Volume (Å^3)	11336(2)	5301.5(12)	11308.3(12)	2549.5(4)	1878.0(6)
Z	8	4	4	2	2
Density (calculated g/cm^3)	1.236	1.171	1.183	1.239	1.261
Absorption coefficient (mm^{-1})	0.209	0.069	0.071	0.077	0.150
F(000)	4432	1984	4288	1012	752
Crystal size (mm^3)	0.425 x 0.325 x 0.300	0.300 x 0.200 x 0.150	0.500 x 0.350 x 0.300	0.430 x 0.310 x 0.260	0.400 x 0.300 x 0.300
2Θ range for data collection (°)	1.577 to 26.710	1.457 to 26.715	1.404 to 29.099	1.433 to 28.504	1.591 to 29.010
Index ranges	-27 ≤ h ≤ 27	-16 ≤ h ≤ 16	-18 ≤ h ≤ 18	-17 ≤ h ≤ 17	-16 ≤ h ≤ 16

	$-26 \leq k \leq 26$	$-22 \leq k \leq 22$	$-55 \leq k \leq 55$	$-18 \leq k \leq 17$	$-17 \leq k \leq 17$
	$-31 \leq l \leq 31$	$-28 \leq l \leq 28$	$-28 \leq l \leq 27$	$-19 \leq l \leq 19$	$-17 \leq l \leq 17$
Reflections collected	122412	58796	138430	31192	23105
Independent reflections	11985	11210	28338	12236	9131
R_{int}	0.0973	0.1111	0.0549	0.0475	0.0263
Data/restraints/parameters	11985 / 621 / 726	11210 / 0 / 653	28338 / 320 / 1487	12236 / 166 / 708	9131 / 0 / 485
Goodness-of-fit on F^2	0.998	0.995	1.010	1.002	1.034
Final R indexes ($I > 2\sigma(I)$)	R1 = 0.0444, wR2 = 0.0858	R1 = 0.0530, wR2 = 0.0961	R1 = 0.0499, wR2 = 0.0990	R1 = 0.0512, wR2 = 0.1039	R1 = 0.0424, wR2 = 0.0978
Final R indexes (all data)	R1 = 0.0909, wR2 = 0.1045	R1 = 0.1262, wR2 = 0.1213	R1 = 0.0944, wR2 = 0.1159	R1 = 0.1082, wR2 = 0.1246	R1 = 0.0644, wR2 = 0.1088
Largest diff. peak and hole ($e.Å^{-3}$)	0.288/-0.293	0.206/-0.205	0.305/-0.355	0.417/-0.230	0.381/-0.399

Table 8: Important Bond Lengths [Å] in the Compounds of Chapter 3

Identification code	C1-C2	C2-C3	C1-O1	C3-O2	O1-C_i	O2-C_i	C1-N1	C3-N2
4b$_1$	1.387(2)	1.390(2)	1.352(2)	1.352(2)	1.410(2)	1.407(2)	1.331(2)	1.323(2)
4b$_2$	1.385(3)	1.388(3)	1.362(2)	1.361(2)	1.412(2)	1.361(2)	1.326(2)	1.322(2)
***1*-4b$_3$**	1.385(2)	1.396(2)	1.3548(17)	1.3497(16)	1.4102(17)	1.4135(17)	1.3296(18)	1.3231(18)
***2*-4b$_3$**	1.388(2)	1.393(2)	1.3513(17)	1.3548(17)	1.4076(17)	1.4079(17)	1.3274(18)	1.3232(18)
4b$_4$	1.394(2)	1.381(2)	1.3527(18)	1.3545(19)	1.4154(19)	1.4109(19)	1.320(2)	1.330(2)
4b$_5$	1.3909(19)	1.393(2)	1.3563(16)	1.3470(16)	1.4102(16)	1.4101(16)	1.3269(18)	1.3290(18)

Table 9: Important Bond Angles [°] in the Compounds of Chapter 3

Identification code	C1C2C3	O1C1C2	C2C3O2	C1O1C_i	C3O2C_i	C2C1N1	C2C3N2
4b$_1$	127.89(17)	120.78(15)	120.98(16)	118.07(13)	119.12(13)	127.44(16)	127.38(17)
4b$_2$	128.35(19)	119.74(18)	119.88(18)	118.01(15)	118.82(15)	128.43(19)	128.2(2)
***1*-4b$_3$**	126.02(13)	121.09(13)	120.96(13)	118.15(11)	117.93(11)	126.46(13)	126.96(13)
***2*-4b$_3$**	126.77(13)	120.89(13)	120.83(13)	118.94(11)	118.42(11)	127.63(14)	127.61(13)
4b$_4$	127.81(16)	120.01(15)	120.45(15)	118.12(12)	118.82(12)	127.54(15)	127.99(16)
4b$_5$	129.02(13)	119.94(12)	119.66(12)	118.48(10)	118.56(11)	128.14(13)	127.89(13)

Table 10: Hydrogen Bonding [Å,°] in the Compounds of Chapter 3

Identification code	D(D-H)	D(H…A)	D(D…A)	<(DHA)
4b₄ O(4)-H(1O)···O(3)	0.946(16)	1.772(16)	2.7101(18)	171(2)
4b₄ O(4)-H(1O)···C(56)	0.946(16)	2.99(2)	3.511(2)	116.3(16)
4b₄ O(4)-H(1O)···C(61)	0.946(18)	2.81(2)	3.196(2)	106(2)
4b₄ O(4)-H(2O)···C(60)	0.894(18)	2.89(3)	3.638(2)	142(3)
4b₄ O(4)-H(2O)···C(61)	0.894(18)	2.72(3)	3.196(2)	114(3)
4b₄† O(4)-H(2O)···C(59)#	0.894(18)	2.96(3)	3.511(3)	121(3)
4b₄†O(4)-H(2O)···C(60)#	0.894(18)	3.01(2)	3.740(2)	140(3)
4b₄† O(4)-H(2O)···H(59)#	0.894(18)	2.34(4)	2.758(3)	108(3)
4b₄† O(4)-H(2O)···H(60)#	0.894(18)	2.44(2)	3.222(2)	146(3)
4b₄ O(4)-H(3O)···O(5Bb)	0.899(18)	2.23(2)	3.096(6)	161(4)
4b₅‡ O(3)-H(3O)···O(5)#	0.89(2)	1.90(2)	2.781(2)	170(2)
4b₅ O(4)-H(4O)···Cl(1)	0.93(3)	2.33(3)	3.2026(17)	157(2)
4b₅ O(5)-H(5O)···Cl(1)	0.91(3)	2.16(3)	3.0604(15)	168(2)

† The symmetry transformations used to generate equivalent atoms is -*x*,-*y*+1,-*z*+1
‡ The symmetry transformations used to generate equivalent atoms is -*x*+1,-*y*+1,-*z*

Chapter 4

4.1 Approach to Synthesize a Propargyl Carbocation - Introduction

Land[26,35] was the first to make the propargyl carbocation **5a** from the reaction of halopropenium salt B with diisopropylamine. Following the method of Land,[26] the halopropenium salt B was treated with diisopropylamine (Scheme 10). The reaction of the halopropenium salt A with an excess of diisopropylamine, instead of the addition of an auxiliary base, in chloroform had been performed by Land.[26] After the reaction, ammonium salts were removed *via* an *aqueous* wash and an orange oil was obtained. A dichloromethane solution of this oil was then stored at -15 ºC for 2 h resulting in the formation of pale-yellow crystals. Using X-ray analysis, the structure of these crystals was determined to be the propargyl carbocation (Scheme 10).

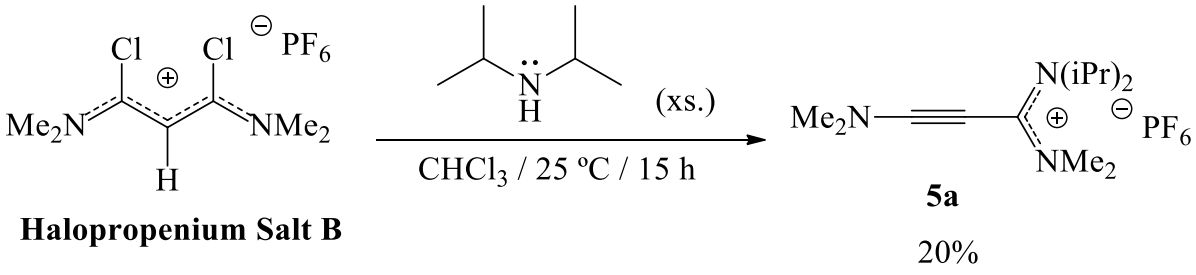

Halopropenium Salt B

5a

20%

Scheme 10: Synthesis of 1,3-*bis*(dimethylamino)-3-(diisopropylamino)propargyl hexafluoro- phosphate **5a**, method by Land.[26]

Land[26,35] used halopropenium salts to generate propargyl cation derivatives. One such complex that Land[26,35] generated was a propargyl containing a carbocation. The isolation of this carbocation suggested the potential of interesting chemistry, as the carbocation should be an activating source for any compounds that it is present in. Figure

50 includes a calculated electrostatic potential map and the HOMO for the propargyl carbocation synthesized by Land.[26,35] The models show that there is a higher than expected electron density across the C≡C bond, as indicated in Figure 50. This implies that the carbocation is creating a reactive site within the propargyl carbocation.

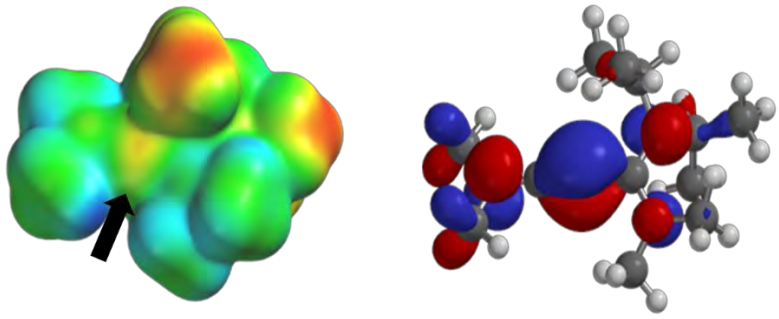

Figure 50: Electrostatic Potential Map (ESPM) and Highest Occupied Molecular Orbital (HOMO) for the propargyl carbocation. Calculated using Spartan 18 at the DFT B3LYP 631-G* level.[117]

A propargyl carbocation can be drawn in the form $C_3{\equiv}C_2\text{-}C_1^{+}(R)_2$ (the predominant structure[xxxiii]) or in the form $C_3^{+}{=}C_2{=}C_1(R)_2$ (the subsidiary structure) which are related through resonance. This was confirmed by the calculation of the electrostatic potential map of the propargyl carbocation shown above.[118] Based on the resonance structures drawn (Schemes 11) the C_1 and C_3 atoms of the propenium chain are the best sites for a nucleophilic attack to take place.

Due to the resonance forms of **5a** (Scheme 11), the site of nucleophilic attack on the cation (C_1 or C_3) is uncertain. The C_3 carbon is less sterically hindered compared to the

[xxxiii] This was based on the spectroscopic data, as ^{13}C NMR and IR demonstrate more alkyne-like qualities. Refer to the experimental section for details.

C_1 carbon, although the predominant resonance form of **5a** would suggest that C_1 is the more likely site of attack. The idea that **5a** reacts as the cumulene, forming a double bond between the C_3 and C_2 carbons, to give a carbocation with the charge at the C_1 position should also not be discounted. This resonance form is more likely to occur, rather than the C_2 carbon taking the electron density of the C_3 carbon and forming a zwitterion.

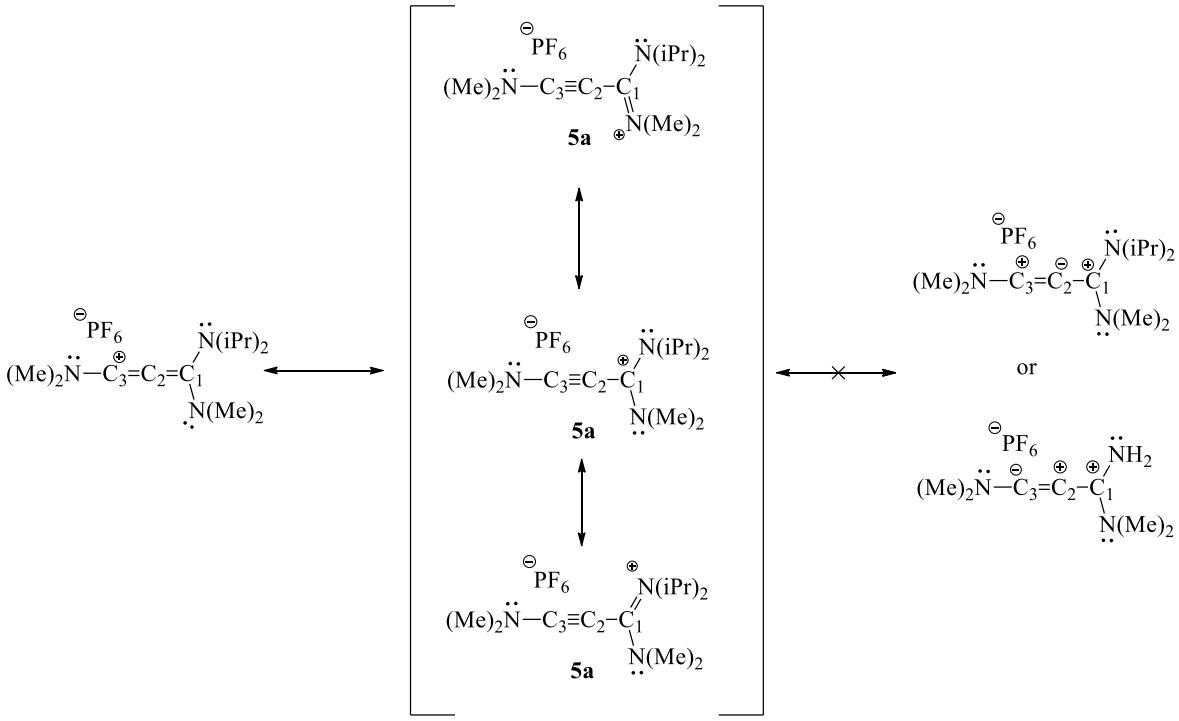

Scheme 11: Resonance structures of **5a**; showing the reactive site at C_3 in the cumulene (left), the reactive site at C_1 in the propargyl carbocation (middle), and zwitterion formation (right).

Not only had a propargyl carbocation been synthesized by Land,[26,35] but a related species had also been synthesized from a carbene through the work of Barry *et al*.[87] This suggested an alternative route for the formation of a propargyl carbocation, different from the halopropenium salts of Land.[26,35] Although the substituents of a carbene derived propargyl carbocation would likely be more sterically hindered than those of the

halopropenium derived cation, it was believed that the chemistry of the two carbocations would be similar.

4.2 Synthesizing a Propargyl Carbocation

As attempts to form a bent allene from **4b** were unsuccessful, a new tact was tried. Expanding on the reaction of Land,[26,35] the halopropenium salt A was prepared from Viehe's Salt. This propenium salt was then treated with a secondary amine. A reduction reaction of the propenium salt was observed, specifically by the generation of $HCl_{(g)}$, to form an alkyne structure (Scheme 10). In attempts to prepare the alkyne, several unintended products were also isolated. Orange rectangular prism crystals were grown, on only one occasion, of the product, *N*-(6-(dimethylamino)-2-methylcyclopenta[c]pyrrol-4(2H)-ylidene)-*N*-methylmethanaminium chloride, by slow evaporation of the solvent layer after the reaction of the halopropenium salt A with diisopropylamine.

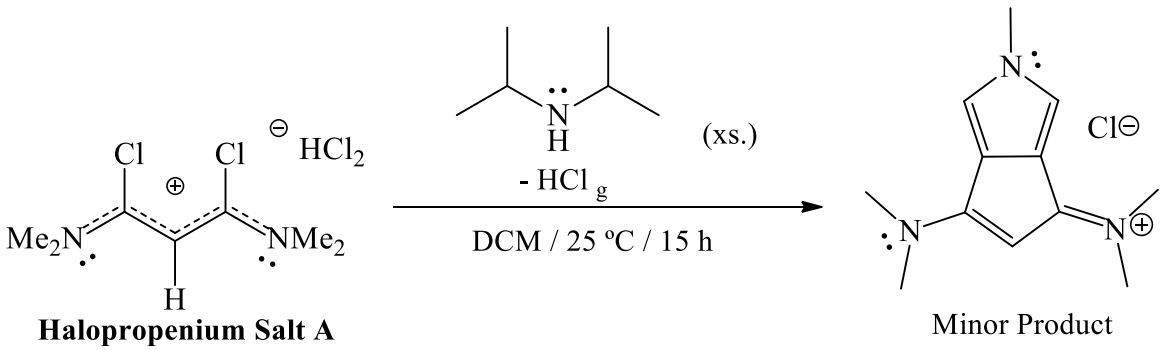

Scheme 12: Reaction conditions that led to the isolation of compound **UC1**.

As the compound in Scheme 12 was a minor product amongst several unintended compounds (mostly ammonium chloride salts), it will be denoted as **UC_1**.[xxxiv] Since the synthesis of UC_1 could not be reproduced, additional characterization, beyond X-ray crystallography, was not performed. The formation of **UC_1** is interesting, however, as it would have to have been formed from 2 eq. of halopropenium salt A, where one of the molecules was fragmented during the reaction. The central hydrogen of one of the halopropenium salt A molecules could bond with a chloride, likely from the cation, to form $HCl_{(g)}$, while the other chloride could react with a hydrogen from the fragmented molecule. The 1 and 3 carbons would then be able to react with what were likely the 1 and 2 position carbons from the fragmented propenium. The additional carbon atom in the cyclic structure could have come from one of the amino methyl groups that reacted intramolecularly with the fragmented propenium backbone. Figure 51 expresses the rough idea for the formation of **UC_1**, though it is not intended to be a mechanism for the formation of **UC_1**, just an example of what might have occurred.

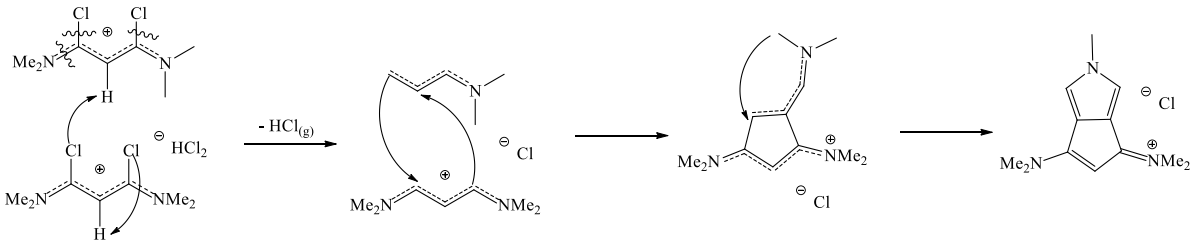

Figure 51: Rough visualization for the formation of UC_1 from 2 eq. of the halopropenium salt A. Formation of other compounds and the role of the diisopropylamine have not been included. This is not meant to be a mechanism, but rather is meant to provide an idea of how halopropenium salt A could form UC_1.

[xxxiv] This naming convention will be continued for all additional unintended compounds/minor products.

It is unlikely that the chloride anion participates in this reaction, as that would mean another chloride would have to establish itself as the anion to take its place. The intramolecular and intermolecular attacks would allow the resulting fragment to attack another fragmented propenium salt, resulting in carbon-carbon bond formation to generate a cyclopentene structure. From there, a methyl group of the dimethyl amine would be able to react intramolecularly to form the resulting pentalene structure.

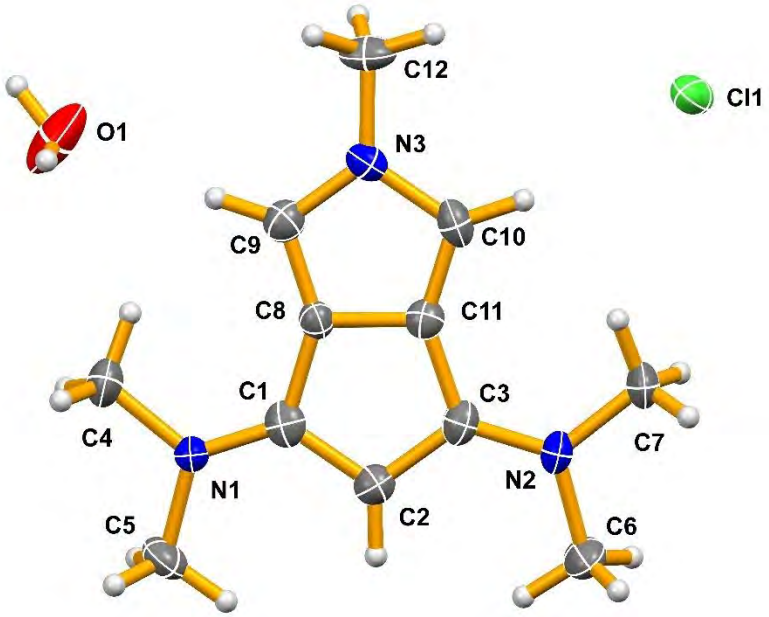

Figure 52: Solid state structure of *N*-(6-(dimethylamino)-2-methyl-1,3,3a,6a-tetrahydrocyclopenta[c]pyrrol-4(2H)-ylidene)-*N*-methylmethanaminium chloride monohydrate, **UC1**. Thermal ellipsoids are drawn at the 50% probability level.

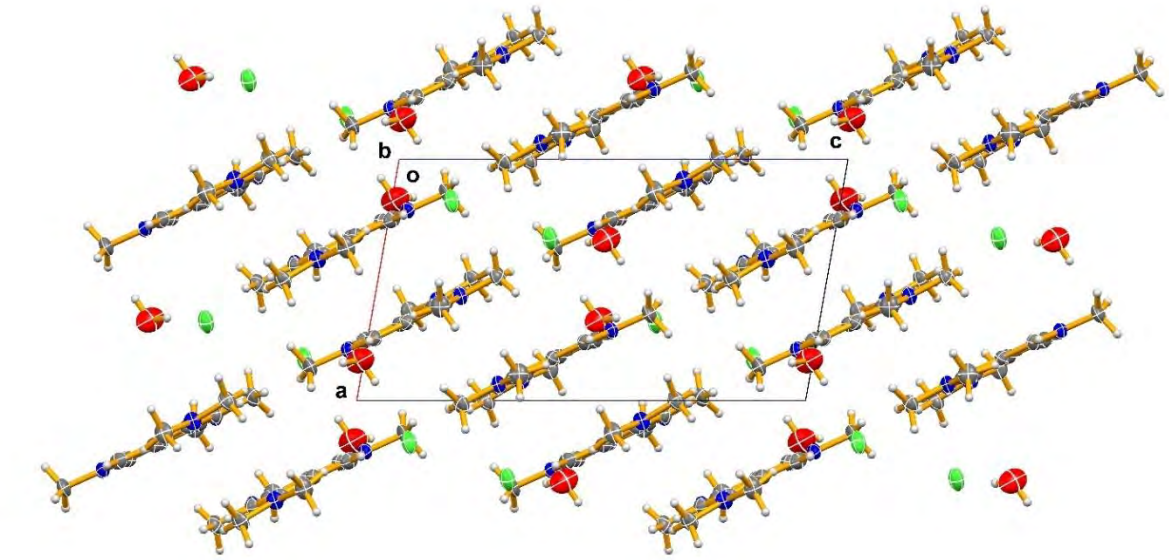

Figure 53: Solid state packing diagram of **UC1** viewed down the *Y*-axis. Thermal ellipsoids are drawn at the 50% probability level.

From the solid-state structure of **UC1** (Figures 52 and 53), the most striking visual characteristic is that the cation is flat. There appears to be little to no steric hindrance present for the dimethyl amino groups as well, as they are also in the same plane as the rest of **UC1**. There are, however, stacking interactions and hydrogen bonding present in **UC1**.

Compound **UC1**, in terms of stacking interactions, can be described as being composed of two 5-membered rings or one 8-membered ring, all of which can have stacking interactions with each other. The stacking interactions for the center of gravity of the 5-membered ring[xxxv] towards the center of gravity of the 5-(C8 to C11 plus N3), 5'-(C1 to C3 plus C8 and C10), and the 8-membered (C1 to C3, plus C8 to C11, plus N3) rings

[xxxv] The 5-membered ring is C1C2C3C11C8
The 5'-membered ring is C8C9N3C10C11
The 8-membered ring is combination of the 5- and 5'- membered rings

are equal to 3.782(3), 3.486(3), and 3.500(2) Å, respectively. The second molecule in the stacking interactions is generated by the symmetry operation 1-*x*,1-*y*,1-*z*.

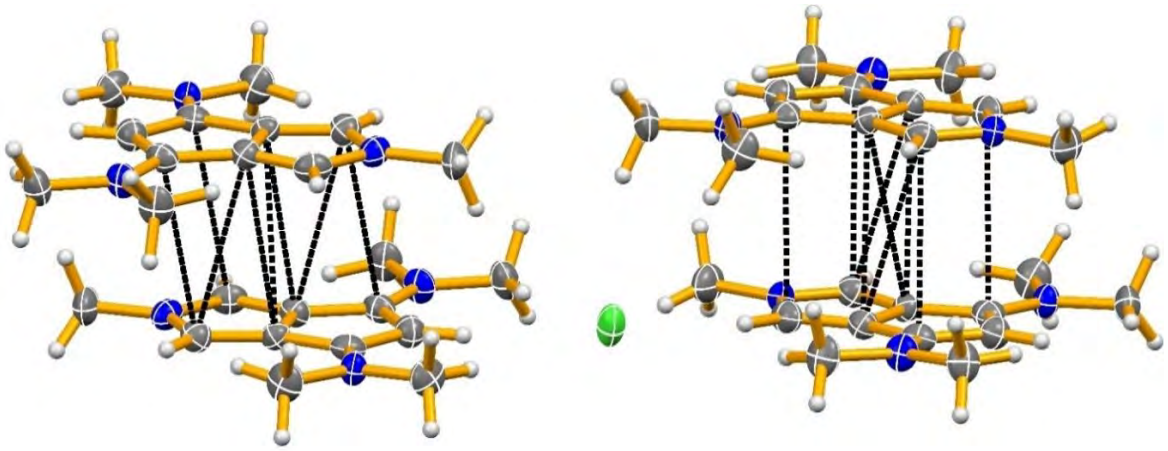

Figure 54: Stacking interactions of **UC1**.

As mentioned earlier, **UC1** is solvated with one molecule of water which participates in hydrogen bonding interactions within the crystal structure. This hydrogen bonding results in the form of a dimer where two molecules of water interact with two of the chloride anions (Figure 55). On the outside of the dimer C-H…O hydrogen bonds connect a neighbouring cation to each of the water molecules.

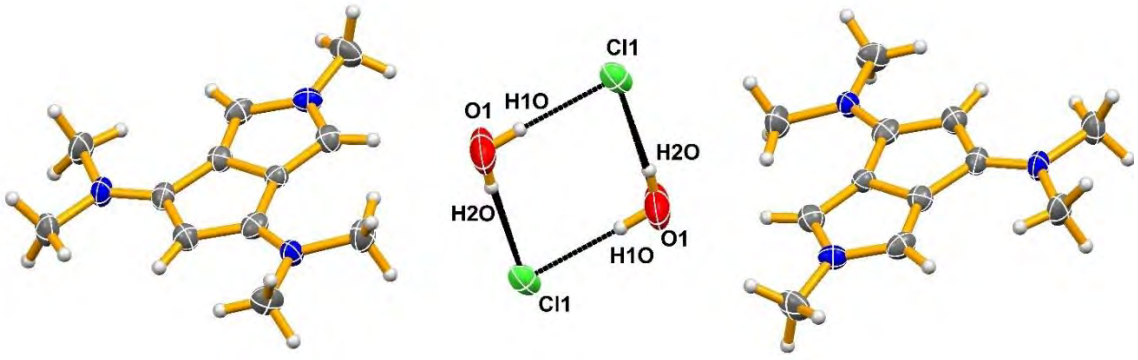

Figure 55: Hydrogen bonding of **UC1**.

Following the isolation of **UC1**, it was believed that the HCl_2 anion of halopropenium salt A was creating instability during the reaction used to prepare the alkynyl structure, discussed earlier and first presented by Land.[26,35] The HCl_2 anion caused this propenium salt to be sensitive to air and water, while the halopropenium salt B, a PF_6 salt (Scheme 2 in Chapter 1), did not have these sensitivities. It was thought that the synthesis of the alkynyl structure seen by Land[26] would be easier after an anion metathesis of salt A, instead of proceeding with the HCl_2 salt. This idea, however, was muddled by attempting to perform the synthesis *in situ* and in concert with the metathesis, without purification steps in-between them. Since the metathesis for the halopropenium salt A to the halopropenium salt B was nearly instantaneous, it was believed that the metathesis of the halopropenium salt A to a BPh_4 salt would also be instantaneous, and thus addition of a secondary amine would produce the desired reaction and product. Once the metathesis was thought to be complete, after roughly 24 h, excess diisopropylamine was added to the solution. The resulting mixture was allowed to stir for 15 h, after which the sample was treated with an aqueous wash. Colourless rectangular prism crystals were grown via solvent diffusion of a DCM/hexane solution. The crystals, however, were not the desired product. Instead of generating the alkynyl structure, X-ray crystallography showed the product to be 6-(dimethylamino)-4-(dimethyliminio)-2,2-diphenyl-4H-1,3,2-dioxaborinin-2-uide, **UC2** (Scheme 13).

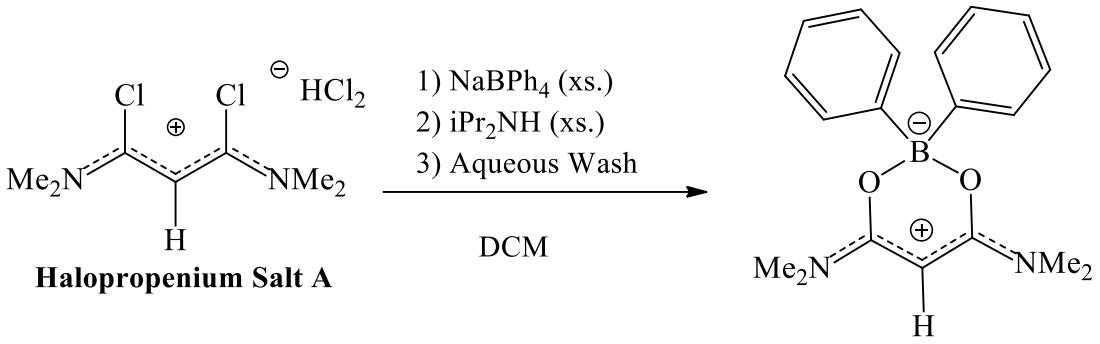

Scheme 13: Reaction conditions that led to the isolation of compound **UC2**.

The halopropenium salt A was hydrolyzed, resulting in a replacement of the chlorines with oxygen atoms. This intermediate then reacted with the BPh_4 anion to produce the structure **UC2**. This may have occurred during the aqueous wash step, which would imply that the metathesis proceeded but the elimination reaction of the chlorine atoms to generate an alkyne did not proceed. This theory, however, seems unlikely as the work of Land[26,35] suggests that the alkynyl structure should have formed. It is more likely that there was a trace of water in the synthesis mixture that allowed the hydrolysis of the BPh_4 anion. Since there was only a short amount of time allotted between steps 1 and 2 in Scheme 11, it is likely that the metathesis did not occur. Instead the addition of the basic amine with trace water in the system caused the hydrolysis of the sodium tetraphenylborate and formation of **UC2**. Interestingly, there is no separate anion in the compound **UC2** , instead the structure forms a zwitterion, as shown in Scheme 13.

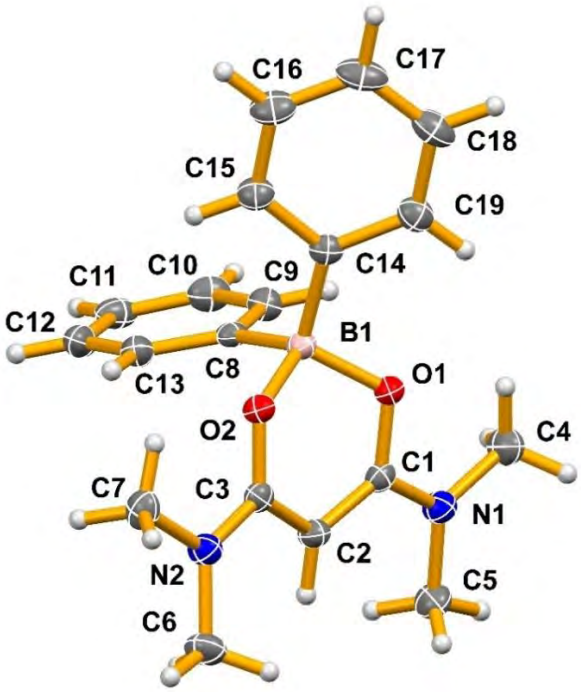

Figure 56: Solid state structure of 6-(dimethylamino)-4-(dimethyliminio)-2,2-diphenyl-4H-1,3,2-dioxaborinin-2-uide, **UC₂**. Thermal ellipsoids are drawn at the 50% probability level.

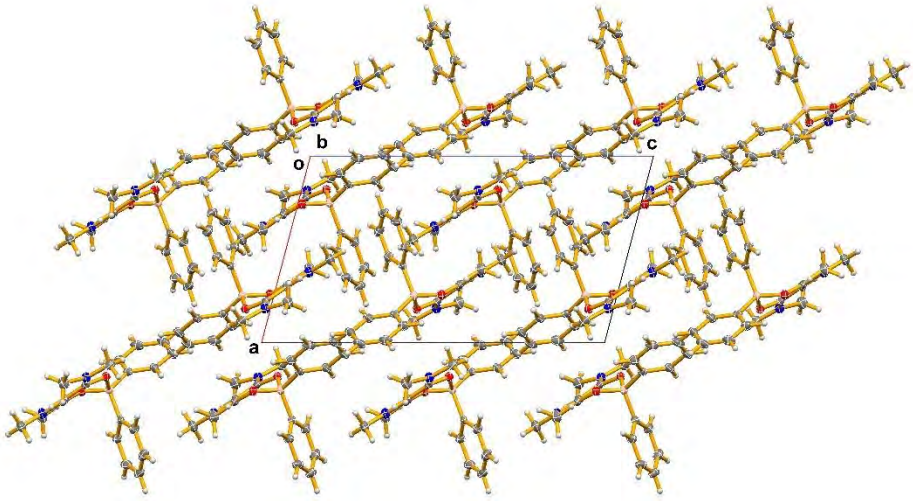

Figure 57: Solid state packing diagram of **UC₂** viewed down the *Y*-axis. Thermal ellipsoids are drawn at the 50% probability level.

From the solid-state structure of **UC₂**, it can be observed that, with the exception of one phenyl group, the compound is relatively flat, similar to the cation in **UC₁**. Unlike **UC₁**, however, **UC₂** does not have any close stacking interactions or solvent mediated hydrogen bonding. There is some order to the solid-state packing when viewed down the *Y*-axis (Figure 57), where the molecules of **UC₂** are arranged in even rows, with the orthogonal phenyl groups intersecting adjacent rows. Each intersecting phenyl group appears to act as an "end-cap", where two molecules of **UC₂** lie between two of the phenyl groups.

4.3 Synthesis of a Propargyl Carbocation from Propenium Salt

Land isolated the propargyl salt **5a** in only a low yield (20%). Improvements to the synthetic method were necessary in order to make this compound a viable starting point for further experimentation. In this work, the 1,3-dichloropropenium salt **B** was dissolved in DCM and reacted with an excess (4 eq) of diisopropylamine for 8 h (Scheme 14). Ammonium salts were removed *via* an *aqueous* wash, resulting in a viscous orange oil. The oil was dried *in vacuo* for 4-5 h which resulted in a bright orange solid. Yellow/orange crystals were grown by dissolving a small amount of this material in 3 mL of DCM, layering it with 5 mL of hexane, and storing at -15°C for 24 h. The crystals were washed with ethanol to remove any contaminating oil.

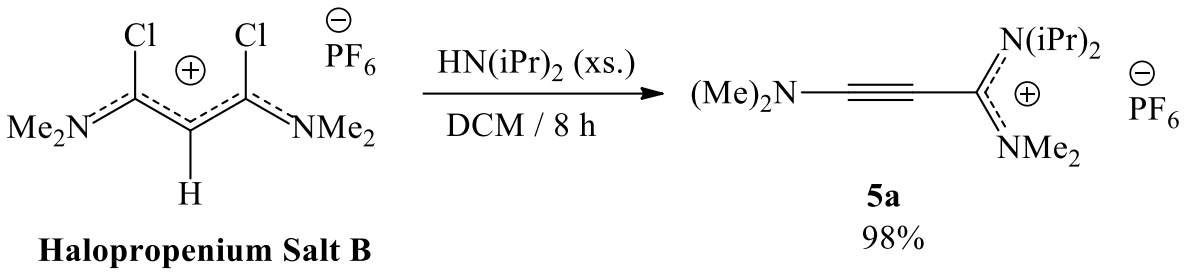

Halopropenium Salt B

5a
98%

Scheme 14: Improved synthesis of **5a**.

It was noticed that on rare occasions compound **5a** would not solidify while drying *in vacuo*. This, in turn, would result in the material not crystallizing by the solvent diffusion method using DCM and hexanes. This problem was circumvented by drying the solution *in vacuo* as much as possible, so that as little solution as possible remained. To this concentrated solution, 100 mL of ethanol would then be added, and it would then be stored at -15°C. Crystals would form after 1 hour, though the yield was reduced to ~75%.

The ^{1}H NMR spectrum of the ynamine amidinium salt **5a** matched that reported by Land,[26] and no additions to the analysis in his dissertation have been included here.[26] The ^{13}C NMR spectrum of **5a** also matched that determined by Land.[26] The signal of the C1 carbocation appeared further upfield than had been anticipated; the chemical shifts of carbocations in the work of Olah *et al.*[119] suggested that the signal of the analogous carbon atom should be downfield around, or in excess of, 200 ppm. For example, Olah *et al.*[119] determined that the stable compounds containing the carbocations, 2-methylpropan-2-ylium, 2-methylbutan-2-ylium, 3-methylpentan-3-ylium, and 2,3-dimethylbutan-2-ylium, have chemical shifts of 335.2 ppm, 335.4 ppm, 336.4 ppm, and 197.8 ppm, respectively, for the carbonium carbon atom in their ^{13}C NMR spectra. This difference, between the spectra of the stable carbocations of Olah *et al.*[119] and **5a**, is possibly due to the lone pairs on the nitrogen atoms in the latter being able to help shield the carbocation and thus push

the signal more upfield. This idea was not touched on by Land[26] in his discussion. Land[26] discussed the cumulene character of **5a**, similar to the compounds of Barry *et al*.,[87] and these arguments will not be restated here.

In the IR spectrum of **5a**, the characterization data matched that determined by Land,[26] and no additions to the analysis in his dissertation have been made.[26] Finally, the mass of the cation was confirmed using HRMS and it matched that determined by Land.[26] X-ray crystallography confirmed that the structure obtained was the same as that reported by Land.[26]

A single crystal of 1,3-*bis*(dimethylamino)-3-(diisopropylamino)propargyl hexafluorophosphate, **5a**, isolated from the solvent diffusion of DCM and hexanes, was used in another X-ray diffraction study. Although the compound itself was the same as that reported by Land,[26] the crystal structure was different. Both crystal types and structures have been shown to be reproducibly formed. The structure of the crystal first reported by Land[26,35] was orthorhombic[xxxvi] **(5a-o)** with one cation/anion pair in the asymmetric unit. In it, both the cation and anion are very disordered. The new structure of a **5a** polymorph reported here is monoclinic (**5a-m**) with four cation/anion pairs in the asymmetric unit. In it, the anions have extensive thermal motion, but the cations are much more ordered in comparison to that in the structure of Land. It is unknown why this compound crystallizes in two different forms, **5a-o** and **5a-m**. It would make sense that this would be due to the packing efficiency of the compounds, where **5a-o** slowly grows leading to an efficiently packed asymmetric unit, while **5a-m** grows rapidly and thus packs in an irregular way. This

[xxxvi] Crystal grown by Land was from DCM/Hexane layering at -15ºC

would explain why **5a-o** has only a single cation/anion pair in the asymmetric unit, while **5a-m** has four cation/anion pairs in the asymmetric unit. This, however, does not appear to be the case as **5a-o** grows more rapidly than **5a-m**, where Land reports 2 h for **5a-o**, while **5a-m** takes 24 h.[xxxvii] This idea is supported by the fact that the **5a-m** conformation is still acquired under the revised ethanol method described above, which grows crystals in ~1 hour. It does not make sense that the same conformation is obtained from both slow and rapid crystal growth, if it is purely a matter of packing efficiency. This implies that there is another factor influencing whether the **5a-o** or **5a-m** conformation is formed, although it is unknown what this may be. It still makes sense that the rate of crystallization must be an important contributing factor.

When examining the bond lengths in the **5a-o** and **5a-m** cations, there does not appear to be any significant difference between the cation reported by Land, and the four cations present in **5a-m**, as can be seen from the values in Table 13. All of the **5a** cations have "short" C1C2 bonds, 1.392(8) Å for **5a-o**, and an average of 1.401(7) Å for the **5a-m** cations. From the Lewis structure of **5a**, it would be expected that the C1C2 bond would be single, however, it appears that the bond length is more similar to that of a 1.5 order bond.[108] This is likely due to electron delocalization, to form the proposed allene structure shown in Scheme 11. It would also be expected that the C2C3 bond would be lengthened from the expected triple bond value. This, however, is not observed as the C2C3 bond length for **5a-o** is 1.199(7) Å, and the averaged[xxxviii] bond length of **5a-m** is 1.209(7) Å. This implies that **5a** is primarily in the propargyl carbocation form, and that the C1C2 bond

[xxxvii] With **5a-m**, the compound is grown more slowly over 24 hrs, though the precise time required is unknown, though the time required is greater than four hours.

[xxxviii] Average is based on all of the molecules in the asymmetric unit.

shortening must be from electron delocalization/electron withdrawal due to the presence of the carbocation, as described in Scheme 11. These bond lengths also demonstrate that there is not a significant difference between the **5a-o** and **5a-m** structures, besides the observed difference in the contents of the asymmetric unit.

When comparing the ∠CCC angles for **5a-o** and **5a-m**, the angles are 170.7(7)° and averaged to be 169.1(6)°, respectively. This, again, is not a significant difference between the different forms of **5a**. This, however, does raise the further question of why the **5a-o** structure of Land was repeatedly obtained, while the **5a-m** structure of this thesis was also repeatedly obtained, though there is no significant difference between the two except for their packing in the solid state.

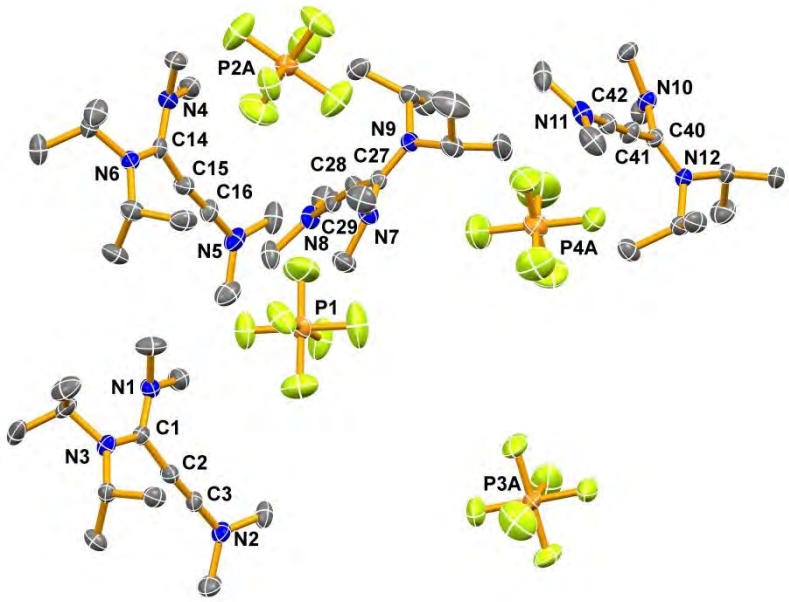

Figure 58: Solid state structure of 1,3-*bis*(dimethylamino)-3-(diisopropylamino)propargyl hexafluorophosphate, **5a-m**. Diagram is of the four unique cation/anion pairs in the asymmetric unit cell. Minor components of the disorder have been removed and hydrogen atoms are not shown. Thermal ellipsoids are drawn at the 50% probability level.

The packing diagram for **5a-m** forms a vertical "zig-zag" pattern when viewed down the *Z*-axis. This pattern creates vertical channels in which the hexafluorophosphate anions reside. Not only this, but the anions also appear to be stacked in their own channels that run parallel to the *X*-axis.

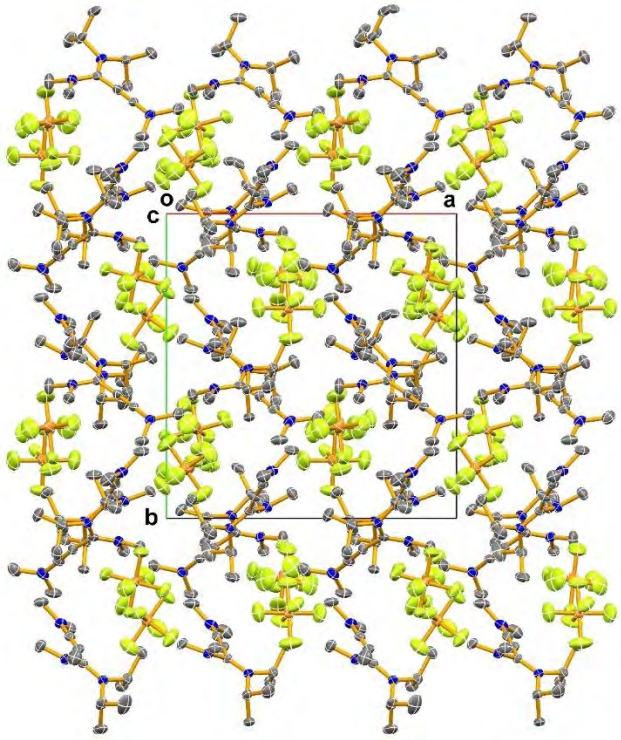

Figure 59: Solid state packing diagram of **5a-m** viewed down the *Z*-axis. Thermal ellipsoids are drawn at the 50% probability level. Hydrogen atoms have been removed for clarity.

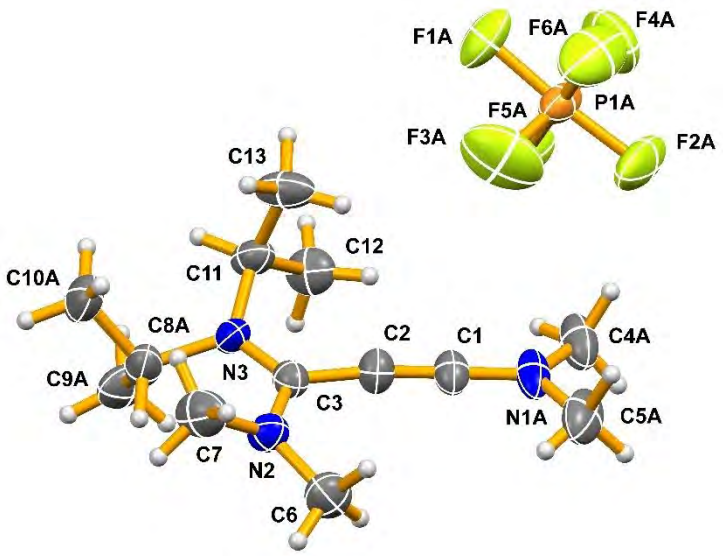

Diagram 1: Solid state structure of **5a-o**, reported by Land[26,35]. Diagram is of the one unique cation/anion pair in the asymmetric unit cell. Minor components of the disorder for both the cation and anion have been removed. Thermal ellipsoids are drawn at the 50% probability level.

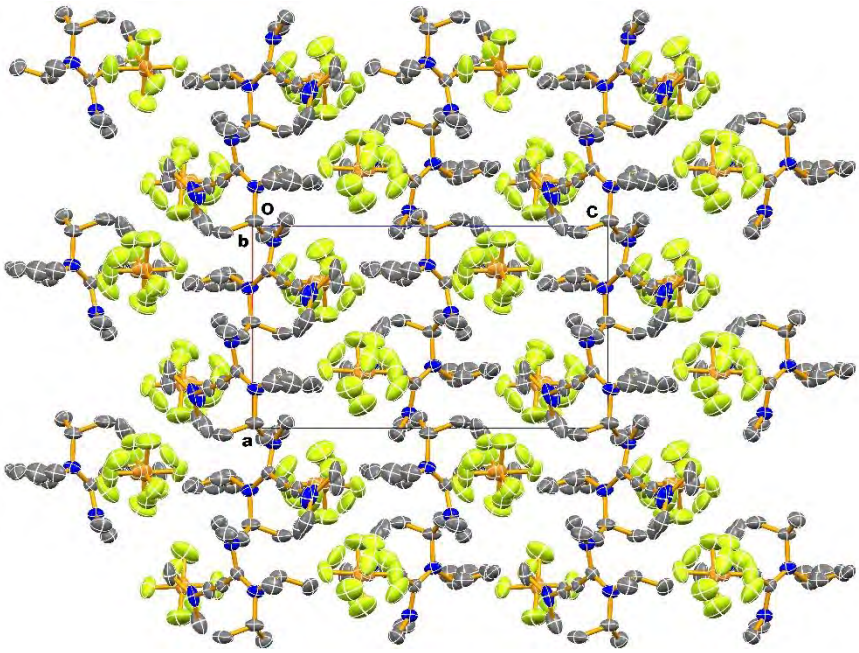

Diagram 2: Solid state packing diagram of **5a-o** reported by Land,[26,35] viewed down the *Y*-axis. Thermal ellipsoids are drawn at the 50% probability level. Hydrogen atoms have been removed for clarity.

From the packing diagram of **5a-o** reported by Land[26,35] (Diagram 2), there is a similar pattern when compared to the packing diagram of **5a-m** (Figure 59). Instead of the vertical "zig-zag" pattern when viewed down the *Z*-axis for **5a-m**, the molecules of the cation form a more linear structure in **5a-o**. The vertical channels for the hexafluorophosphate anion that are present in the packing diagram of **5a-m**, which run parallel to the *X*-axis, are also present for **5a-o**. The cations forming a more linear vertical structure in **5a-o** is likely the result of the more efficient packing when compared to **5a-m**. If the earlier proposed idea that **5a-o** packs in a more regular arrangement because the structure grows more slowly is true, then this would explain the more linear packing. The packing of **5a-o** appears to be more efficient than the "zig-zag" pattern of **5a-m**, which likely results from the need to accommodate the four cation/anion pairs in the asymmetric unit.

An anion metathesis reaction was carried out on compound **5a** to determine if the reactivity of the propargyl cation would increase with a less coordinating anion. To do this, sodium tetraphenylborate was chosen as the anion due to its large size and volume; it was believed that this steric hindrance would help to increase the reactivity of the new salt. The anion being less strongly coordinated than that in compound **5a** would result in the carbocation being more deshielded, in comparison to the hexafluorophosphate salt.

Compound **5a** was dissolved in DCM, and an excess of sodium tetraphenylborate was added. The solution was allowed to stir for 15 h, before it was filtered through Celite. The resulting solution was left to slowly evaporate, which produced colourless, cube-shaped crystals. These were examined by X-ray crystallography and the structure was

determined to be 1,3-*bis*(dimethylamino)-3-(diisopropylamino)propargyl tetraphenyl borate, **5b**.

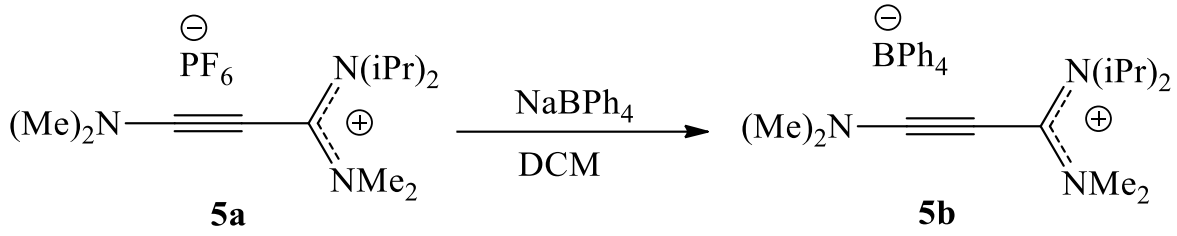

5a **5b**

Scheme 15: Synthesis of **5b**.

The compound **5b** was synthesized in ~80% yield. Although the yield is quite acceptable, the purification of the crystals was difficult, requiring many washes with solvent in order to free it from an oily coating. The crystals of compound **5b** were not as fine as those of **5a**. It was noticed that the crystals of compound **5b** would become dry and powdery with prolonged exposure to the atmosphere. The crystals were not desolvating in this case, as there is no solvent within the unit cell of compound **5b**. The reason for this effect remains unknown, however, it was not present with compound **5a**.

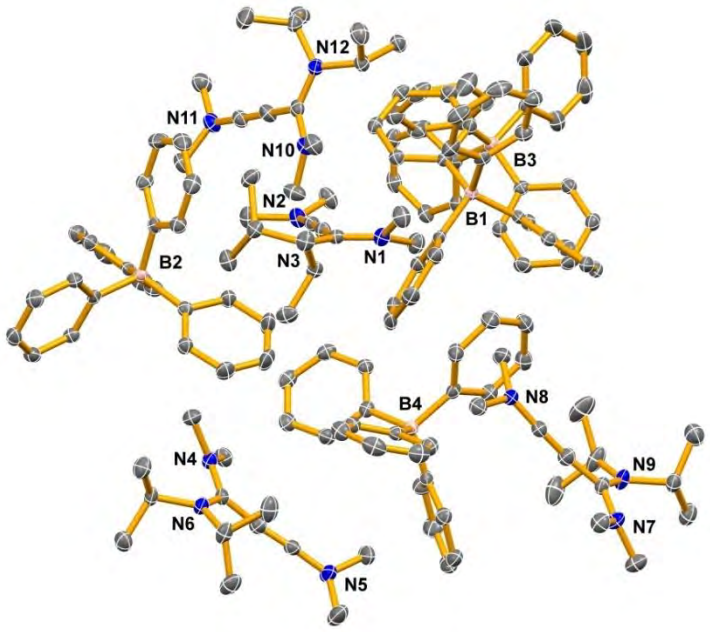

Figure 60: Solid state structure of 1,3-*bis*(dimethylamino)-3-(diisopropylamino)propargyl tetraphenylborate, **5b**. Diagram is of the four unique cation/anion pairs in the asymmetric unit. Hydrogen atoms are not shown and not all atoms have been labelled. Thermal ellipsoids are drawn at the 50% probability level.

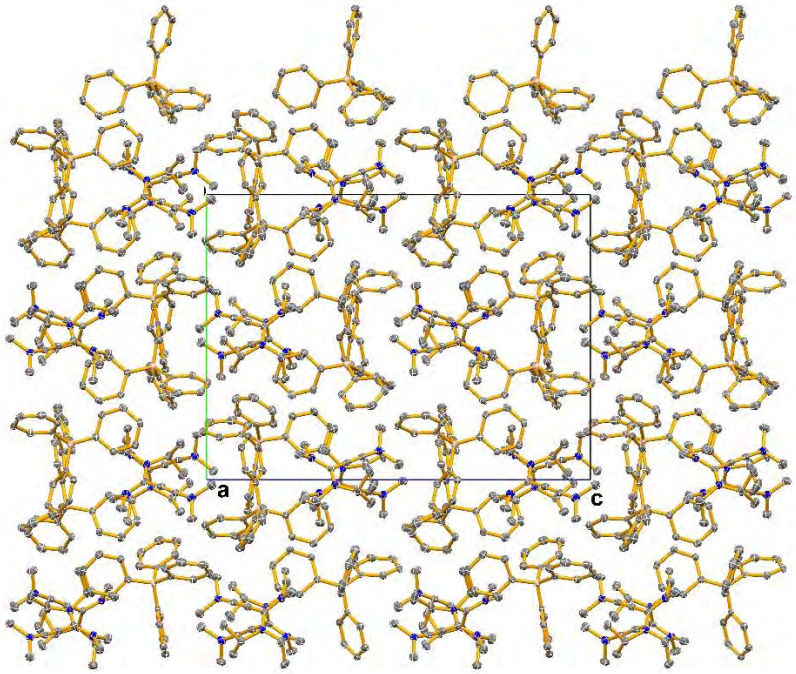

Figure 61: Solid state packing diagram of **5b** viewed down the *X*-axis. Thermal ellipsoids are drawn at the 50% probability level. Hydrogen atoms have been removed for clarity.

Compound **5b** has four cation/anion pairs in the asymmetric unit, just like that of **5a-m**. It should be noted that there is no disorder in the structure of **5b**, which is more similar to **5a-m** rather than to **5a-o** which is heavily disordered. This suggests that these compounds cannot pack themselves in an efficient arrangement. They need four different cation and anion pairs in a quite random arrangement, before they have a unit that can be built up to give the crystal. Typically, it would be expected that there would only be one cation/anion pair in the asymmetric unit to build a good crystal, which is seen in **5a-o**. When comparing the cations of **5b** to those of **5a-m**, there is no significant difference in the bond lengths. The averaged C1C2 bond length for **5b** is 1.404(4) Å, compared to the averaged value of 1.401(7) Å for **5a-m**. The averaged C2C3 bond length for **5b** is 1.206(4) Å, compared to the averaged value of 1.209(7) Å for **5a-m**. This shows that **5b** has the same delocalization across the C1C2 bond as found in **5a-m** and **5a-o**, without any significant difference from the observed values. The average ∠C1C2C3 angle for **5b** is 174.0(4)°, compared to the ∠C1C2C3 angle of 170.7(7)° and averaged value of 169.1(6)° for **5a-o** and **5a-m**, respectively. **5b** does appear to have a somewhat larger ∠C1C2C3 angle in comparison to the previous structures. The ∠C1C2C3 angle of **5b** itself differs by ~7° across the four molecules in the asymmetric unit, from 170.1(3)° to 177.4(3)°, so the averaged value is not fully representative of the individual cations in **5b**. The difference in the values of the ∠C1C2C3 angles in **5b** (Table 13), is most likely due to a combination of packing effects and steric hindrance.

Though the specific cause of the packing differences between **5a-o** and **5a-m**, along with **5b**, is unknown, it is likely related to the rate of growth of the crystals. **5a-o** grows more slowly, resulting in a low yield but a more efficient packing for the crystal structure.

This is in contrast to **5a-m** and **5b**, which essentially fall out of solution with high yield in crystalline form, but in a more random arrangement of four cation/anion pairs for the asymmetric unit. Though there is a difference in conformation, **5a-o** and **5a-m** are essentially identical with respect to the bond lengths and angles. Even the packing diagrams are relatively similar, with both forming a vertical structure for the cations and vertical channels for the anions. **5b** is the most different between the compounds, which is likely do to the size and steric hindrance of the tetraphenylborate anions.

4.4 Synthesis of a Propargyl Carbocation from a Carbene

Although compound **5a** was able to provide useful insights into the chemistry of the propargyl carbocation (Chapter 5), it is important not to base conclusions on the results of a single compound. It is for this reason, that the decision to synthesize a new propargyl carbocation was made. Deriving from the work of Barry *et al*.,[87] a propargyl carbocation was synthesized from the reaction of an alkyne and a carbene. It was proposed that a carbene (IMes) would be mixed with a halogenated acetylene, which would create a CC bond at the site of the carbenic carbon atom. CC bond formation would leave this carbon atom electron deficient, forming a carbocation which would be stabilized by resonance with the adjacent nitrogen atoms. The positive formal charge of the compound would be balanced by the negatively charged halogen anion. A propargyl carbocation would be formed, theoretically in a single step.

To do this, IMes was suspended in 5 mL of hexanes. To this suspension an excess of (bromoethynyl)benzene was added. Immediately upon the addition the sample became

bright pink in color. To ensure that the reaction had gone to completion, it was left to stir for 12 h. However, this was much longer than necessary, and no more than an hour should actually have been required. It should be noted that in subsequent attempts to synthesize this compound, long stirring times led to a reduction in the pink coloration. No impurities were noticed spectroscopically when this did occur, however crystallization of the product became more challenging. It should also be noted that IMes is not soluble in hexanes, which is why the reaction was carried out in suspension. Attempts to generate this carbocation from solvents in which IMes is soluble (such as toluene or THF) led to products that were less pure and significantly more difficult to crystallize. Even after purification and subsequent reaction, these compounds would still have solvent trapped in their crystals, as was shown by spectroscopy and X-ray crystallography. This solvent trapping phenomenon was not observed when hexanes were used to suspend the reaction mixture. Once the reaction was complete, the solution was filtered through fritted glass and washed with 5 x 5 mL hexanes. The sample was dried *in vacuo* for 4 h. The sample was dissolved in DCM and layered with hexanes, before being placed at -15°C. Crystals had grown after 48 h. The structure of the crystals was confirmed to be 1,3-dimesityl-2-(phenylethynyl)-1H-imidazol-3-ium bromide, **6a**, by X-ray crystallography.

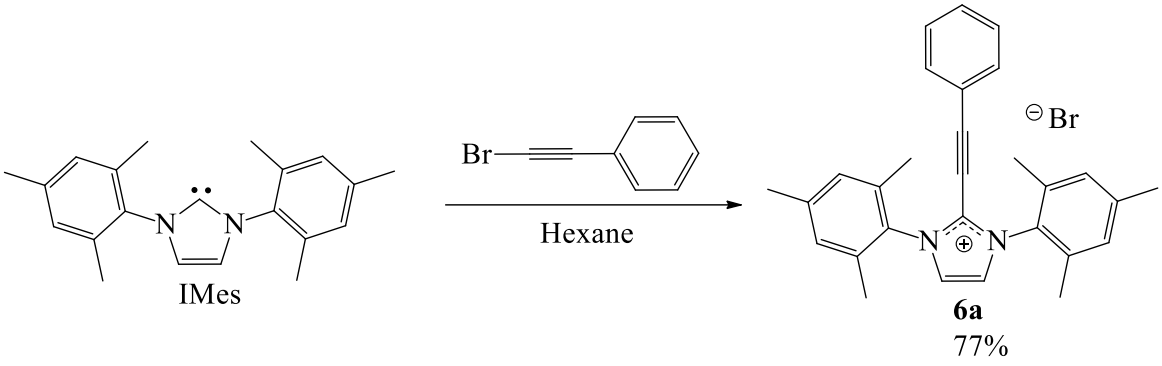

Scheme 16: Synthesis of **6a**. The reaction is analogous to the reaction described by Barry *et al*.[87]

Although the structure of compound **6a** was confirmed by X-ray crystallography, it could not be as easily purified by crystallization as compound **5a** had been. Unlike compound **5a** which was crystallized in high yields, compound **6a** could not be. Instead reactions with compound **6a** were primarily performed utilizing it as a powder. It is unclear why compound **6a** was so difficult to crystallize; usually the compound would oil out before solidifying. A property that compound **6a** did share with compound **5a** was that they were both stable/unreactive in an open atmosphere. Both compounds could be exposed to atmospheric conditions for over 30 days without visible degradation. Compound **6a** also did not show any evidence of reaction when exposed to water. These properties mean that compound **6a** is potentially bottleable, but in powdered form. The powdered form of compound **6a** was more than suitable to continue experimentation, as spectroscopy showed that its purity was high. The first reactions performed with compound **6a** were simple anion metathesis reactions. These reactions were primarily performed to obtain a crystalline sample of compounds **6a** for X-ray analysis. Though a crystal of the bromide salt had already been grown, the crystal quality was not good; therefore, obtaining a better crystalline sample with only a change of anion was attempted.

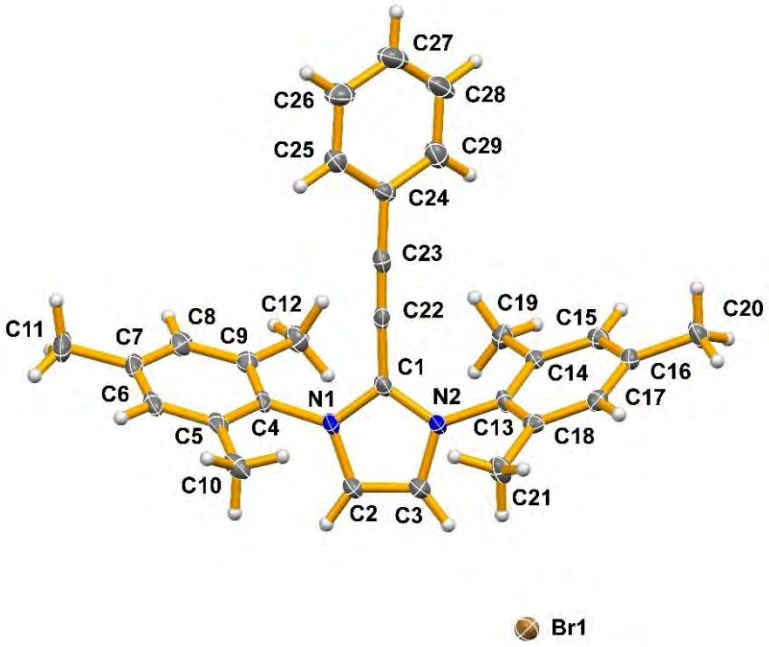

Figure 62: Solid state structure of 1,3-dimesityl-2-(phenylethynyl)-1H-imidazol-3-ium bromide, **6a**. Only the non-hydrogen atoms have been labelled. Solvent was removed from the crystal structure during refinement using the Squeeze routine in the program Platon.[120] Thermal ellipsoids are drawn at the 50% probability level. Solvent has been removed, as the molecules could not be identified.

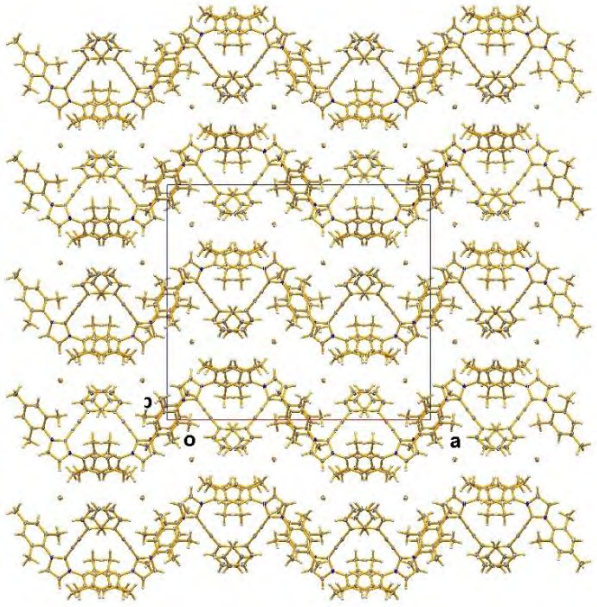

Figure 63: Solid state packing diagram of **6a** viewed down the *Y*-axis. Thermal ellipsoids are drawn at the 50% probability level.

Obtaining the crystal structure of **6a** provided some challenges in modelling the crystal disorder. It was determined that there was solvent within the crystal structure, however, the solvent could not be modelled properly. The routine Squeeze, in the program Platon,[120] had to be implemented in order to remove the electron density of the solvent from the model of **6a**. The potential solvent accessible volume in one-unit cell was calculated to be four voids of 203 $Å^3$ each, which was 16% of the total cell volume. After 7 cycles of refinement, 233 electrons had been removed from the unit cell (58 electrons per void). Even though the likely solvents were known (dichloromethane and hexanes), no model could be found which would account for both the number of electrons and the position of the top Fourier peaks in the final residual density map prior to SQUEEZE being applied. It is likely that the solvent moves relatively freely in the structure making it difficult to identify.

When comparing the observed bond lengths and angles for the solid-state structure of **6a** (Figure 62) to the predicted values based on the Lewis structure drawn in Scheme 16, there are no noticeable differences. The CC triple bond is linear, with a bond length of 1.188(5) Å, a ∠C1C2C3 angle of 177.5(4)°, and an ∠N1C1N2 angle of 107.5(3)º. The lack of a hydrogen atom at the C_1 location and the presence of the bromide anion prove that a carbocation has been formed from the reaction of IMes with (bromoethynyl)benzene, as suggested it would be, by the work of Barry *et al.*[87] As would be expected, the structure in the CSD[58] that best matches **6a** is that of the SiPr bromide salt described by Barry *et al.*[87] (Figure 64). When compared, the SiPr bromide complex has a CC triple bond with a length of 1.203(4) Å, a ∠C1C2C3 angle of 167.3(3)° and an ∠N1C1N2 angle of 113.1(3)º. This indicates that **6a** has a slightly shorter C≡C bond length (although this difference is likely

not significant). The ∠C1C2C3 angle is also much more linear than that in the SiPr cation of Barry *et al.*[87] The most likely explanation for this increase in linearity is the replacement of the sterically demanding diisopropyl groups of the SiPr by methyl groups on IMes in compound **6a**. The isopropyl groups are much larger and bulkier in comparison to the methyl groups of **6a**, which forces the CC triple bond to bend in accommodation. Barry *et al.* [87] do state that this non-linear arrangement is likely a crystal-packing effect due to a shallow potential for angle bending, which they were able to confirm by synthesizing a number of other monocationic compounds with structures similar to that shown in Figure 64. These new complexes reported by Barry *et al.* [87] had bond angles of 180°, which implies that there are similar crystal-packing effects occurring in **6a**.

From the ∠N1C1N2 angle, there is a slightly significant difference between **6a** and the structure of Barry *et al.,* [87] where the angle in **6a** is more acute than that of Barry *et al.*[87] This suggests that **6a** has less electron density around the carbocation, which would allow for a shallower angle. The difference between the ∠N1C1N2 angle for **6a** and that of Barry *et al.* [87] is greater than the difference between IMes and SiPr, which have ∠N1C1N2 angles of 101.4(2)°[121] and 104.98(11)°,[122] respectively.

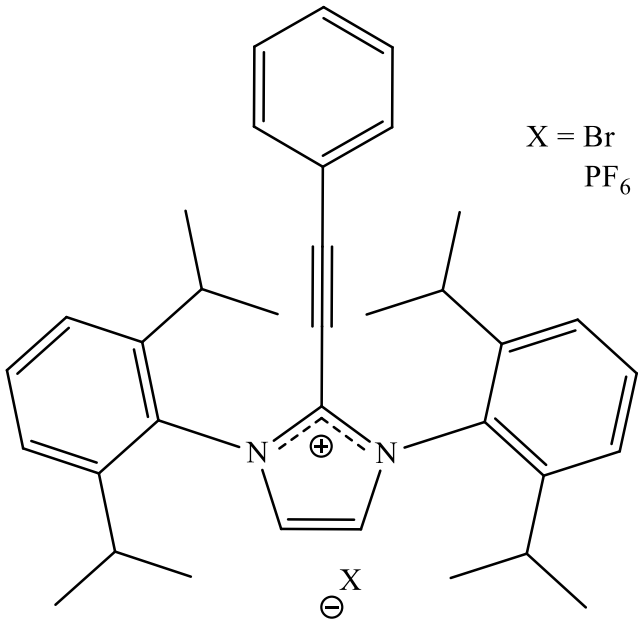

Figure 64: Lewis **s**tructures of the SiPr propargyl carbocation salts reported by Barry *et al.* [87]

The metathesis reaction performed on compound **6a** used potassium hexafluorophosphate. This metathesis was performed in a similar manner to that used to prepare the halopropenium salt **B**. Compound **6a** was dissolved in DCM. To the sample, an equal amount by volume of saturated aqueous potassium hexafluorophosphate was added. The sample was vigorously agitated for several minutes. Once complete the organic layer and aqueous layer were separated. The aqueous layer was washed with more DCM to extract any sample that might have remained in it. The DCM layers were combined and dried *in vacuo*. The resulting solid material was dissolved in DCM and left to slowly evaporate, which resulted in crystals growing. The structure of the crystals was confirmed using X-ray crystallography to be 1,3-dimesityl-2-(phenylethynyl)-1H-imidazol-3-ium hexafluorophosphate, **6b**.

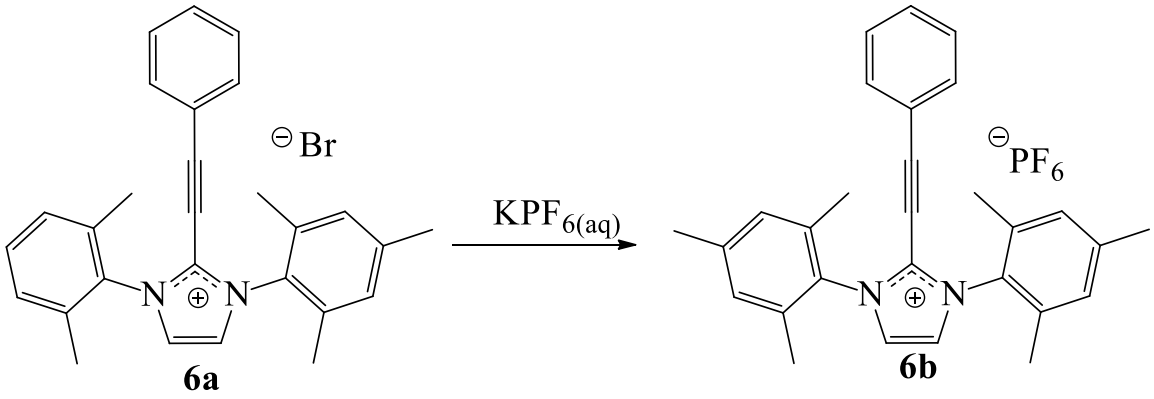

Scheme 17: Synthesis of **6b**.

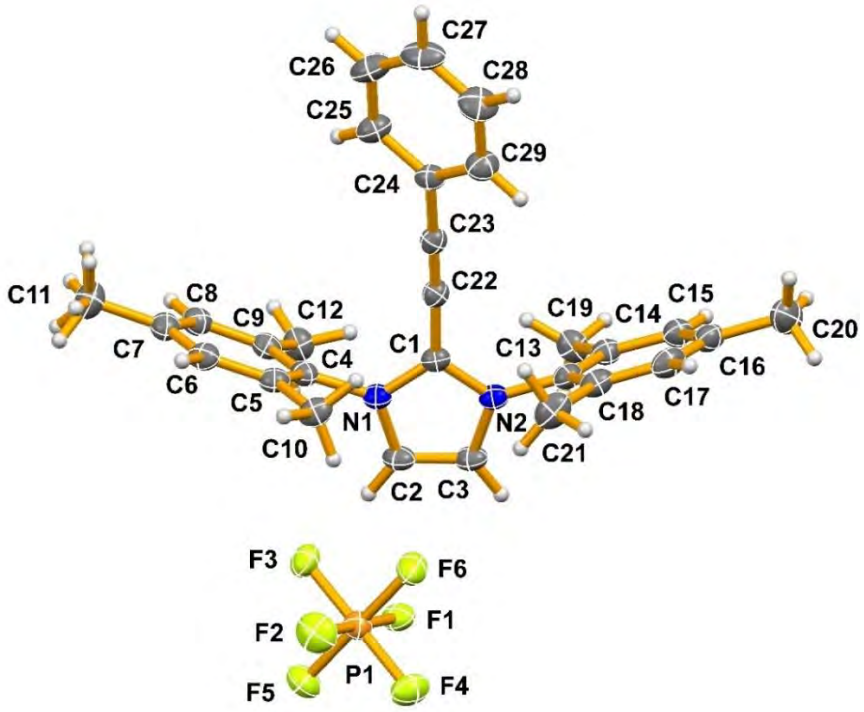

Figure 65: Solid state structure of 1,3-dimesityl-2-(phenylethynyl)-1H-imidazol-3-ium hexafluorophosphate, **6b**. Only the non-hydrogen atoms have been labelled. Thermal ellipsoids are drawn at the 50% probability level.

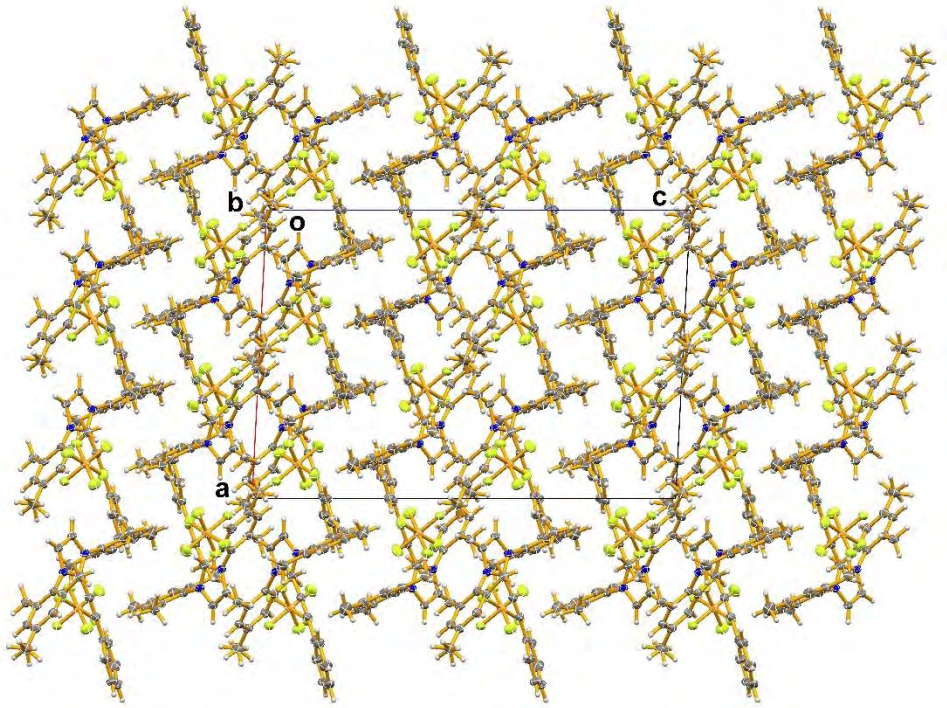

Figure 66: Solid state packing diagram of **6b** viewed down the *Y*-axis. Thermal ellipsoids are drawn at the 50% probability level.

The work of Barry *et al.* [87] also includes a SiPr structure with a hexafluorophosphate anion corresponding to that of **6b**. As in **6a**, the solid-state structure of **6b** (Figure 65) confirms the Lewis structure drawn in Scheme 17. The CC triple bond is linear, with a bond length of 1.190(2) Å and a ∠C1C2C3 angle of 175.72(17)°. This bond angle for **6b** is slightly less linear than that of **6a**, which is a significant difference according to the standard error at 99% confidence. This implies that the conformation of **6b** is changed slightly with the hexafluorophosphate anion compared to that with the bromide anion in **6a**. When compared, the SiPr hexafluorophosphate salt has a CC triple bond with a length of 1.100(3) Å and a symmetric ∠C1C2C3 angle of 180°. This indicates that **6b** has a longer C≡C bond length (which is a significant difference) but is also less linear compared to the SiPr hexafluorophosphate salt of Barry *et al.*[87] As stated above, it is likely that this

difference in the linearity of **6b** could be due to crystal-packing effects arising from a shallow potential for angle bending, as stated by Barry *et al.* [87]

The compounds synthesized in this chapter, show that it is possible to make propargyl carbocations by two different methods, those of Land[26,35] and Barry *et al.* [87] The cations, **5a**, **5b**, **6a**, and **6b** display similar characteristics to each other even though they are structurally different. Not only this, but they also display similarities to the literature structures described by Land[26,35] and Barry *et al.*[87] which is to be expected as the compounds **5** and **6** are based on their work, respectively. The interesting aspect, however, is that there are also cross similarities, where the structures derived from the work of Land[26,35] show aspects also present in the structure derived from Barry *et al.*[87] and vice versa. This also shows how little research there is in literature about the propargyl carbocation, as there are few examples with which to compare the structures of **5** and **6** to. To continue the work of determining the reactivity of the propargyl carbocations, reactions must be performed to explore the resonance theory described in Scheme 11, and to show that the carbocation is an activating source in this chemistry. It is also recommended that computational studies be performed in order to properly determine the electronics and potential mechanisms for the reactions of the propargyl carbocations.

Table 11: Crystal Data and Structure Refinement Details of the **UC** Compounds

Identification code	**UC_1**	**UC_2**
Empirical formula	$C_{12}H_{20}ClN_3O$	$C_{19}H_{23}BN_2O_2$
Formula weight	257.76	322.20
Crystal system	Monoclinic	Monoclinic
Space group	$P2_1/n$	$P2_1/c$
a (Å)	8.339(3)	9.6720(13)
b (Å)	10.638(3)	10.9149(14)
c (Å)	15.269(5)	17.178(2)
α (°)	90	90
β (°)	99.959(4)	104.6770(10)
γ (°)	90	90
Volume ($Å^3$)	1334.2(7)	1754.3(4)
Z	4	4
Density (calculated g/cm^3)	1.283	1.220
Absorption coefficient (mm^{-1})	0.276	0.078
F(000)	552	688
Crystal size (mm^3)	0.200 x 0.100 x 0.100	0.500 x 0.450 x 0.250
2Θ range for data collection (°)	2.345 to 25.881	2.177 to 28.986
Index ranges	$-10 \leq h \leq 10$	$-13 \leq h \leq 12$
	$-13 \leq k \leq 13$	$-14 \leq k \leq 14$

	$-18 \leq l \leq 18$	$-22 \leq l \leq 22$
Reflections collected	13657	20837
Independent reflections	2586	4391
R_{int}	0.1189	0.0238
Data/restraints/parameters	2586 / 122 / 165	4391 / 0 / 221
Goodness-of-fit on F^2	1.008	1.042
Final R indexes ($I > 2\sigma(I)$)	$R_1 = 0.0647$, $wR_2 = 0.1359$	$R_1 = 0.0428$, $wR_2 = 0.1103$
Final R indexes (all data)	$R_1 = 0.1364$, $wR_2 = 0.1661$	$R_1 = 0.0530$, $wR_2 = 0.1177$
Largest diff. peak and hole ($e.Å^{-3}$)	0.452/-0.263	0.424/-0.189

Table 12: Crystal Data and Structure Refinement Details of the Compounds in Section 4.2

Identification code	**5a-o**	**5a-m**	**5b**
Empirical formula	$C_{13}H_{26}F_6N_3P$	$C_{13}H_{26}F_6N_3P$	$C_{148}H_{184}B_4N_{12}$
Formula weight	369.34	369.34	2174.30
Crystal system	Orthorhombic	Monoclinic	Monoclinic
Space group	$P2_12_12_1$	$P2_1$	$P2_1$
a (Å)	8.778(2)	15.957(4)	15.764(3)
b (Å)	13.402(4)	15.377(3)	17.370(3)
c (Å)	15.423(4)	16.107(4)	23.413(4)
α (°)	90	90	90

β (°)	90	113.475(2)	91.255(2)
γ (°)	90	90	90
Volume (Å^3)	1814.4(9)	3625.2(14)	6409.7(18)
Z	4	8	2
Density (calculated g/cm^3)	1.352	1.353	1.127
Absorption coefficient (mm^{-1})	0.208	0.208	0.065
F(000)	776.0	1552	2352
Crystal size (mm^3)	0.354 × 0.165 × 0.131	0.500 x 0.400 x 0.350	0.230 x 0.190 x 0.180
2Θ range for data collection (°)	4.026 to 51.334	1.324 to 28.880	1.292 to 28.984
Index ranges	$-10 \leq h \leq 10$	$-21 \leq h \leq 20$	$-21 \leq h \leq 21$
	$-16 \leq k \leq 16$	$-20 \leq k \leq 20$	$-22 \leq k \leq 23$
	$-18 \leq l \leq 18$	$-21 \leq l \leq 21$	$-31 \leq l \leq 30$
Reflections collected	18667	43494	78595
Independent reflections	3447	17445	31062
R_{int}	0.0660	0.0352	0.0400
Data/restraints/parameters	3447/619/324	17445/1712/1083	31062 / 1 / 1509
Goodness-of-fit on F^2	1.057	1.034	1.009
Final R indexes ($I > 2\sigma(I)$)	R_1 = 0.0645, wR_2 = 0.1557	R_1 = 0.0539, wR_2 = 0.1254	R_1 = 0.0501, wR_2 = 0.1001
Final R indexes (all data)	R_1 = 0.0932, wR_2 = 0.1727	R_1 = 0.0739, wR_2 = 0.1384	R_1 = 0.0689, wR_2 = 0.1083
Largest diff. peak and hole (e.Å^{-3})	0.28/-0.33	0.322/-0.320	0.261/-0.187

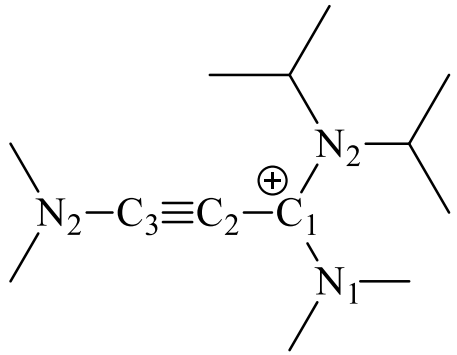

Diagram 3: Atomic labelling of important atoms within **5a**.

Table 13: Selected Solid-State Metrical Parameters for the Compounds Discussed in Section 4.2

Compound	C1−N1 / Å	C1−N3 / Å	C3−N2 / Å	C1−C2 / Å	C2−C3 / Å	∠C1C2C3 / °
5a-o	1.347(7)	1.341(7)	1.32(5)	1.392(8)	1.199(7)	170.7(7)
***1*-5a-m**	1.350(6)	1.334(6)	1.303(6)	1.399(6)	1.214(7)	169.4(5)
***2*-5a-m**	1.348(6)	1.343(6)	1.299(6)	1.406(7)	1.217(7)	169.4(5)
***3*-5a-m**	1.346(6)	1.339(6)	1.292(6)	1.403(7)	1.209(7)	168.8(6)
***4*-5a-m**	1.349(6)	1.349(6)	1.301(6)	1.398(7)	1.199(7)	168.8(6)
***1*-5b**	1.349(4)	1.349(3)	1.315(4)	1.407(4)	1.204(4)	177.4(3)
***2*-5b**	1.347(3)	1.348(3)	1.314(4)	1.403(4)	1.201(4)	170.1(3)
***3*-5b**	1.344(4)	1.349(4)	1.305(3)	1.402(4)	1.208(4)	173.5(3)
***4*-5b**	1.339(4)	1.354(4)	1.307(4)	1.407(4)	1.211(4)	175.0(3)

Table 14: Crystal Data and Structure Refinement Details for Compounds in Section 4.3

Identification code	**6a**	**6b**
Empirical formula	$C_{29}H_{29}BrN_2$ + [solvent]	$C_{29}H_{29}F_6N_2P$
Formula weight	485.45+ [solvent]	550.51
Crystal system	Orthorhombic	Monoclinic
Space group	*Pbcn*	*C2/c*
a (Å)	25.5521(17)	16.0791(5)
b (Å)	9.6175(6)	14.6534(5)
c (Å)	22.8339(15)	23.5604(8)
α (°)	90	90
β (°)	90	92.909(2)
γ (°)	90	90
Volume ($Å^3$)	5611.4(6)	5544.0(3)
Z	8	8
Density (calculated g/cm^3)	1.149	1.319
Absorption coefficient (mm^{-1})	1.481	1.420
F(000)	2016	2288
Crystal size (mm^3)	0.108 x 0.056 x 0.021	0.167 x 0.080 x 0.068
2Θ range for data collection (°)	1.954 to 25.349	3.757 to 74.494

Index ranges	$-30 \leq h \leq 30$	$-20 \leq h \leq 19$
	$-11 \leq k \leq 11$	$-18 \leq k \leq 18$
	$-27 \leq l \leq 27$	$-29 \leq l \leq 29$
Reflections collected	114605	105465
Independent reflections	5135	5660
R_{int}	0.1251	0.0358
Data/restraints/parameters	5135 / 0 / 295	5660 / 0 / 348
Goodness-of-fit on F^2	1.073	1.123
Final R indexes ($I > 2\sigma(I)$)	$R_1 = 0.0543$, $wR_2 = 0.1217$	$R_1 = 0.0392$, $wR_2 = 0.0964$
Final R indexes (all data)	$R_1 = 0.0709$, $wR_2 = 0.1289$	$R_1 = 0.0409$, $wR_2 = 0.0974$
Largest diff. peak and hole ($e.Å^{-3}$)	0.501/-0.723	0.315/-0.362

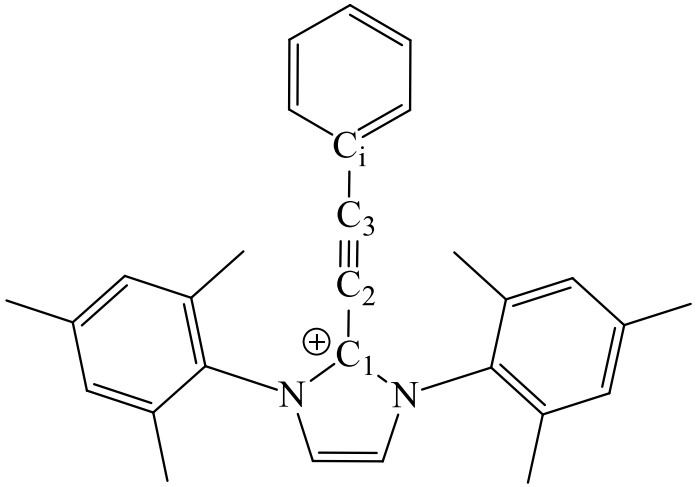

Diagram 4: Atomic labelling of important atoms within **6a**

Table 15: Important Bond Lengths (Å, °) in the Compounds of Section 4.3

Identification code	C1-C2	C2-C3	C3-C_i	∠C1C2C3	∠C2C3C_i	∠N1C1N2
6a	1.424(5)	1.188(5)	1.429(5)	177.5(4)	178.1(4)	107.5(3)
6b	1.415(2)	1.190(2)	1.435(2)	175.72(17)	178.78(17)	107.32(13)

Chapter 5

5.1 Reactions of Propargyl Carbocations

The propargyl carbocation has few references in the literature and even fewer report on its reactivity. Reactions of propargyl carbocations would be expected to proceed similarly to those of standard non-terminal alkynes, so reagents which target nucleophilic attacks across the CC triple bond should provide insight into their reactivity. From Scheme 11 in Chapter 4, it would be expected that nucleophilic attack would occur at the C3 carbon atom due to the possible resonance of the propargyl carbocation to the allene. Figure 67 shows the atom designations that have been used for the discussions in this chapter. Notable reactions that have been attempted are halogenations, reactions with a sterically bulky nucleophile, reactions with inorganic cyanide, and reactions with inorganic azide. Both of the propargyl cations synthesized and characterized in Chapter 4 have been studied. For the reaction with azide, it is rare to have inorganic azide react with a non-terminal alkyne under mild conditions and without the use of a catalyst. It was believed that the presence of the positive charge in our propargyl cations would be activating enough for the non-terminal alkynes to react with azide under such mild conditions. The presence of the carbocation should also promote all of the other proposed reactions.

There are a few notable examples of this type of reaction performed with related substrates that have been reported in the literature and the CSD,[58] including the work of Kantlehner *et al.*[123] and that by Golovanov *et al.*[124] Kantlehner *et al.*[123] reacted

$((CH_3)_2N)_3CC{\equiv}CC(N(CH_3)_2)_3$[xxxix] with benzoyl azide to produce a Huisgen cycloaddition across a non-terminal alkyne, at room temperature. While this reaction was not done with a propargyl carbocation, a carbocation complex with a triazole ring was generated. The second example is that of Golovanov *et al.*,[124] where a protonated triazole ring complex was synthesized from the reaction $PhC{\equiv}CC{=}CC(O)Ph$[xl] and potassium azide. Although, again, a carbocation was not formed the complex does have a cyclic ring adjacent to the protonated triazole ring.

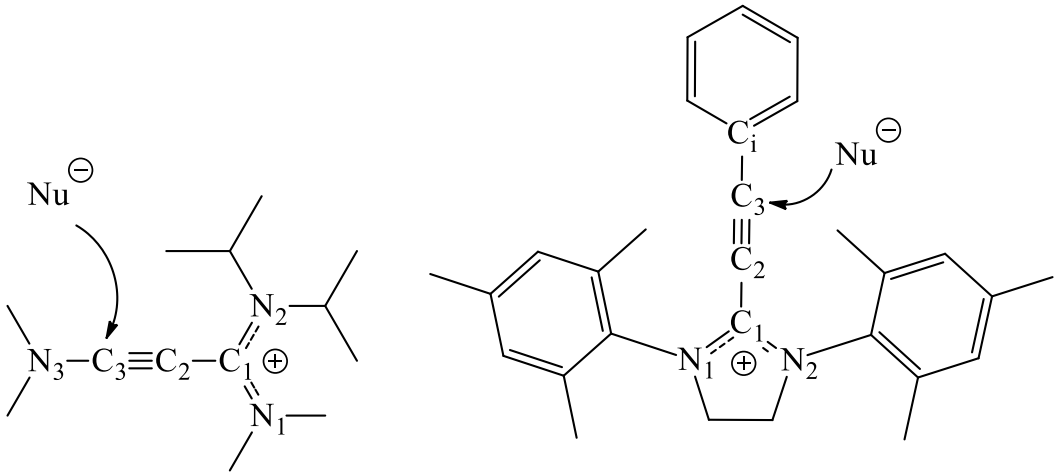

Figure 67: Atomic labelling of the structures in the Chapter 5 discussion.

It was important to test the reactivity of the propargyl carbocations that had been synthesized, including compound **5a**. To begin, a number of simple addition reactions were used to gauge its reactivity, rather than starting with more complicated procedures. The first reaction chosen was a simple halogenation across the carbon-carbon triple bond. This type of reaction has been well documented in the literature, and it should have been simple

[xxxix] IUPAC naming of this compound is N1,N1,N'1,N'1,N''1,N''1,N4,N4,N'4,N'4,N''4,N''4-dodecamethylbut-2-yne-1,1,1,4,4,4-hexaamine.
[xl] IUPAC naming of this compound is (E)-1,5-diphenylpent-2-en-4-yn-1-one.

to perform in order to determine the reactive site in compound **5a**. This reaction did produce a result, though it was not the one that was intended.

Compound **5a** was dissolved in DCM, and 0.5 eq. of I_2 was added. The solution was stirred for 15 h before crystallization was attempted by slow evaporation. Crystals did not form by this process, so the sample was redissolved in DCM and layered with hexane, to allow solvent diffusion. After 48 h needle-shaped crystals had formed. The solvent was decanted, and the crystals were washed with ethanol until the solution was colourless. The crystals were colourless but had dark spots splattered on the surface, likely from excess iodine. A yield was not determined for the crystals due to this iodine contamination which could not be removed. The crystals were examined by X-ray crystallography to determine the structure, which was found to be *N*-(1-(diisopropylamino)-3-(dimethylamino)-3-oxopropylidene)-N-methylmethanaminium hexafluorophosphate, **7**.

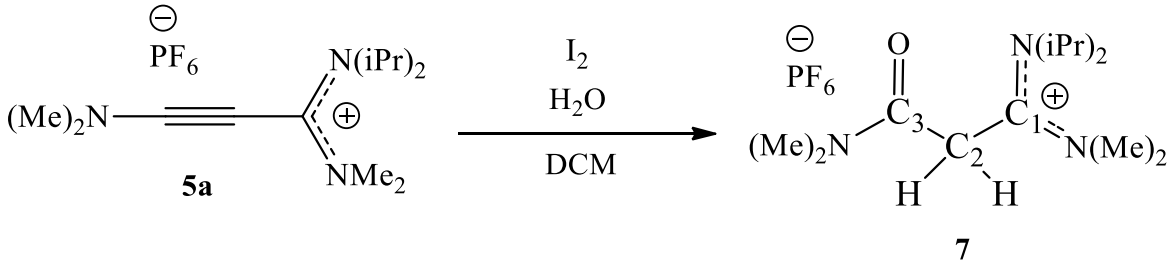

Scheme 18: Reaction conditions that led to the isolation of compound **7**.

X-ray crystallography was able to determine that the iodization of compound **5a** had been unsuccessful. However, the hydrolysis of compound **5a** was successful, with the site of reaction being on the C3 carbon as had been predicted a priori. The hydrolysis likely occurred because of the presence of a trace of water within the reaction system. It is also not known why the hydrolysis depicted in Scheme 19 occurred instead of the halogenation

reaction. It is important to note that compound **5a** does not react in the presence of water when it is in its crystalline form. It is possible that compound **5a** only reacts with water when it is dissolved in a solvent or if an activating agent, such as the iodine used in this case, is present but this has yet to be proven.

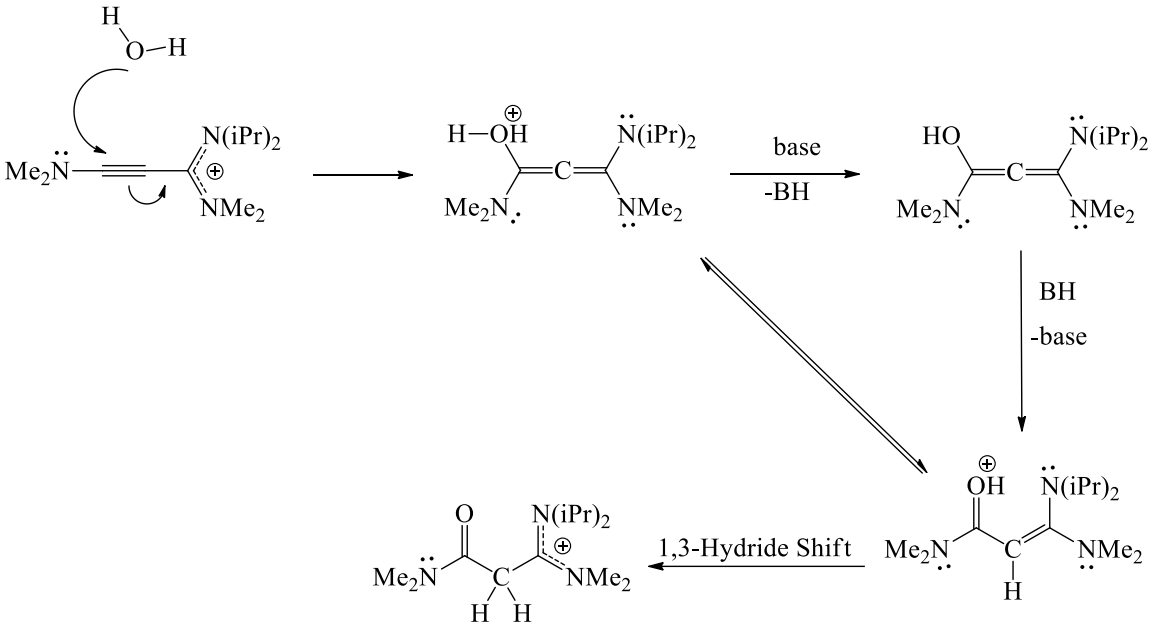

Scheme 19: Proposed mechanism for the formation of the cation in compound **7**.

What is important, in terms of the reaction of **5a** to give compound **7**, is that the site of reaction appears to be the C3 carbon atom and not C1. The carbocation on the C1 carbon does not seem to have been affected at all, as there is still an anion present in the product, in the form of hexafluorophosphate. The carbocation being unaffected implies one of two things for compound **5a**. The first is that there may be too much steric hindrance for the carbocation to react, thus leaving the only possible site of reaction as the C3 carbon. The second is that the resonance of compound **5a** as described in Scheme 11, Chapter 4, could result the formation of a cumulene, placing the formal charge on the C3 carbon. This would

allow compound **5a** to react at the C3 carbon, before reforming the carbocation at the C1 position in the final product.

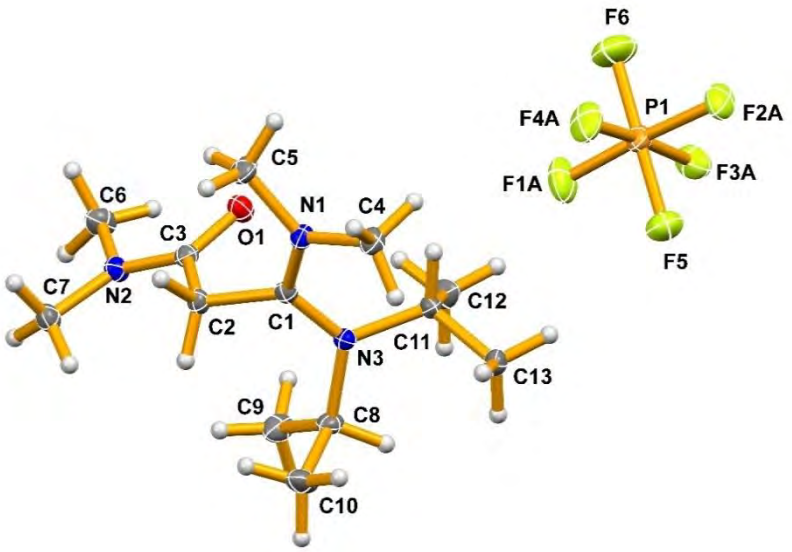

Figure 68: Solid state structure of *N*-(1-(diisopropylamino)-3-(dimethylamino)-3-oxopropylidene)-N-methylmethanaminium hexafluorophosphate, **7**. Diagram is of the one unique cation/anion pair in the asymmetric unit. Minor components of the anion disorder have been removed. Thermal ellipsoids are drawn at the 50% probability level. Hydrogen atoms have not been labelled.

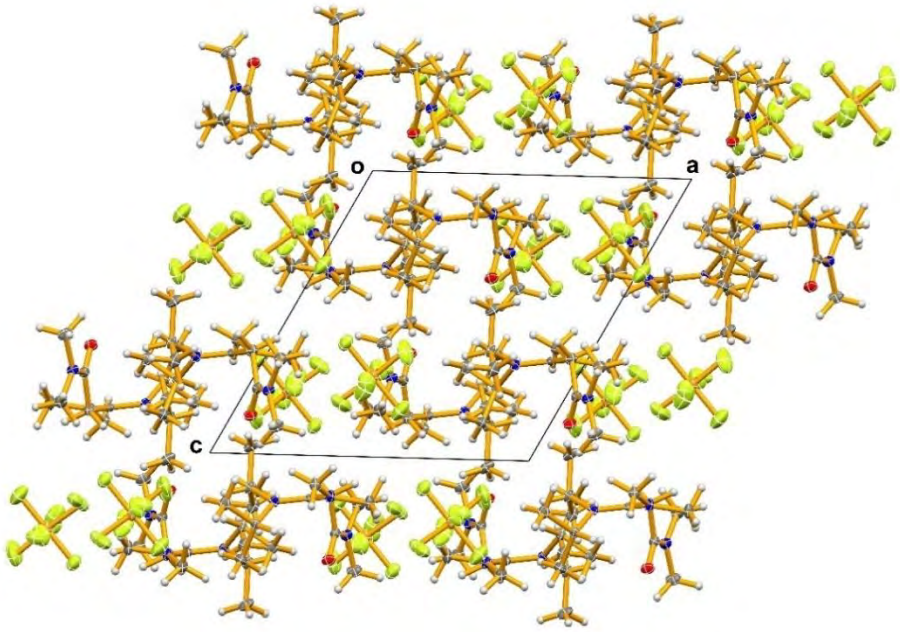

Figure 69: Solid state packing diagram of **7** viewed down the *Y*-axis. Thermal ellipsoids are drawn at the 50% probability level.

In the packing diagram of **7**, it appears that the cations are arranged such that the diisopropyl groups entangle with those of another cation of **7**. The CC triple bond has been disrupted in the reaction with the water; as the C2C3 bond length[xli] is now 1.5346(13) Å, significantly longer than the average C2C3 bond of 1.2097(7) Å in all of the **5a** molecules. The C3O1 bond length is as expected for an amide carbonyl at 1.234 Å.[108] Interestingly, the C1C2 bond has also been lengthened in **7** compared to that in **5a**. In compound **7**, the C1C2 bond length is 1.5122(13) Å, while this same bond length is averaged to be 1.4015(7) Å in **5a**. **5a** has a resonance structure that moves electron density from the alkyne into the C1C2 bond in order to form an allene (as depicted in Scheme 11, Chapter 4). This

[xli] See Figure 67 for an explanation of the atomic labelling used.

resonance shortens the bond from the expected single bond length. This is not possible in **7a** so the C1C2 bond is a pure single bond (and its length is as expected).

Land[26,35] also isolated compound **7** in his dissertation work, but in his structure the crystal system was triclinic, instead of the monoclinic system of **7**. The crystal structure of **7**, and the structure of Land[26,35] are essentially identical, with the exception of minor twisting, likely due to packing effects. The structure of Land[26,35] was isolated from a reaction involving his form of compound **5a** (**5a-o**), which potentially explains the different crystal systems. Additional characterization data for his compound **7** was not included in the work by Land.[26,35]

Although the propargyl carbocation did not react at first, a series of experiments eventually led to numerous new products. These new products were similar in structure to that of compound **7**, since the initial site of attack was always on the C3 carbon. Unlike compound **7**, these new compounds were not saturated, and thus retained a double bond between the C2 and C3 carbon atoms.

Compound **5a** was found to react with phenylacetylide to form compound **8**. At first phenylacetylene was used, but unexpectedly no reaction occurred. It was thought that maybe a catalyst would be necessary. The reaction was then repeated with the addition of n-butyl lithium, which was used to deprotonate the phenylacetylene and promote a nucleophilic attack on the cation. The addition of the n-butyl lithium to the reaction mixture did yield the desired product. It is likely that the phenylacetylene required deprotonation in order for the reaction to proceed. Although the product was formed, and its structure was confirmed using X-ray crystallography, the sample was impure and proved difficult to purify. A purer sample was synthesized by direct reaction of compound **5a** with lithium

phenylacetylide. This reaction proceeded with no trouble, unlike the previous attempt, which was likely due to phenylacetylide being a better nucleophile. It is possible that the presence of the lithium may help to facilitate the reaction as well, but this idea will have to be tested at a later time.

Compound **5a** was dissolved in THF, which resulted in a golden solution. To this solution 1.1 eq of lithium phenylacetylide was added. This addition immediately resulted in the formation of an orange/brown solution. This solution was allowed to stir for 12 h, and was then left to crystallize by slow evaporation. Crystals had grown after 24 h and their structure was determined using X-ray crystallography to be (E)-N-(1-(diisopropylamino)-3-(dimethylamino)-5-phenylpent-2-en-4-yn-1-ylidene)-N-methylmethanaminium hexafluorophosphate(V), **8**.

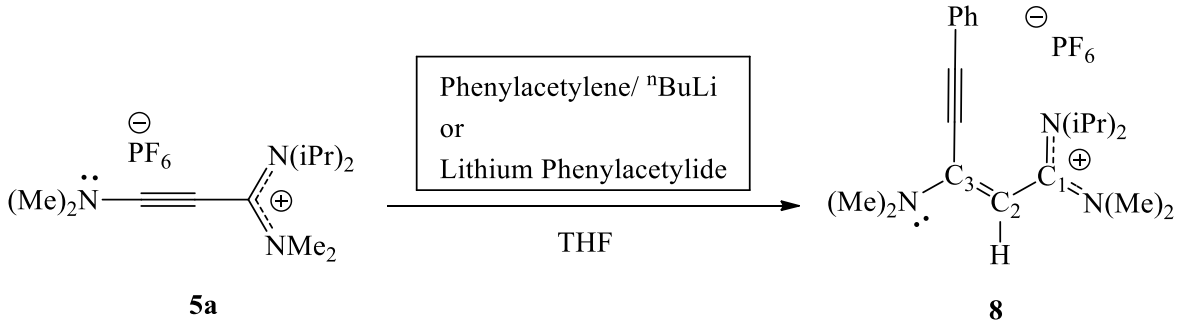

5a **8**

Scheme 20: Synthesis of **8**, via two methods.

Compound **8**, would have had to pick up a proton from solution, since there is a proton on the C2 carbon in the product. It is also interesting that compound **8** crystallizes in a cis rather than a trans configuration across the C2C3 double bond, since the former would be expected to be higher in energy. Across all of the crystal structures determined for compound **8**, the trans isomer was never observed.

Although the precise mechanism for this reaction has not been determined, it would be interesting to know. Since the trans isomer has not been observed, it implies that this reaction is stereoselective. This stereoselectivity could be specific to the reaction, or it could be due to the presence of the carbocation. If the products from this type of reaction, carried out with different nucleophiles, all displayed cis configurations, then it would confirm that the presence of the carbocation renders its reactions stereoselective.

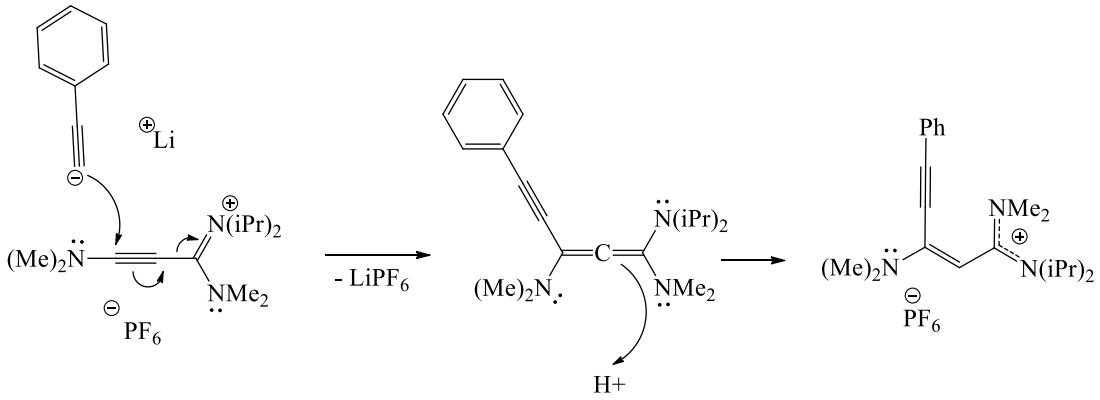

Scheme 21: Proposed mechanism for the formation of **8**.

Figure 70: Solid state structure of (E)-N-(1-(diisopropylamino)-3-(dimethylamino)-5-phenylpent-2-en-4-yn-1-ylidene)-N-methylmethanaminium hexafluorophosphate(V), **8**. Only the non-hydrogen atoms have been labelled. Thermal ellipsoids are drawn at the 50% probability level.

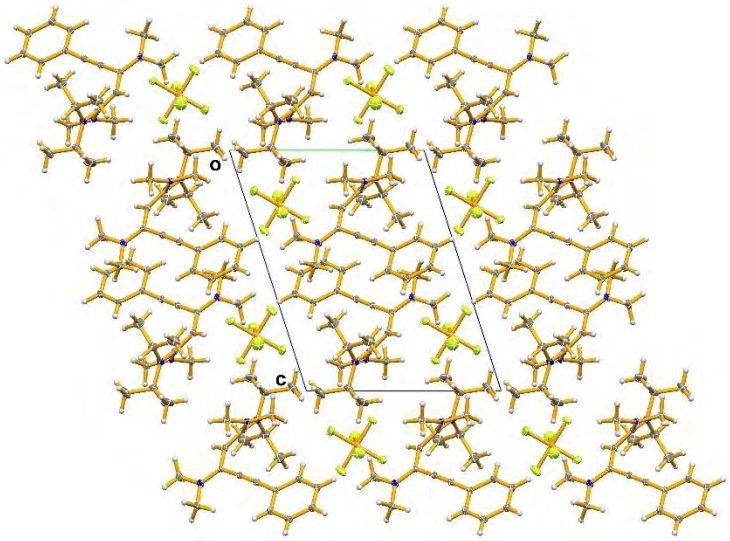

Figure 71: Solid state packing diagram of **8** viewed down the *X*-axis. Thermal ellipsoids are drawn at the 50% probability level.

From the packing diagram, it can be seen that **8** is arranged in double rows of cations, where the ethynylbenzene groups are all oriented in the same direction in the same row and in the opposite direction in the second row. This arrangement also allows for pseudo-channels within the structure where the diisopropyl substituents of the cations and the hexafluorophosphate anions are able to alternate. The C2C3 bond length is 1.3937(11) Å, typical of a CC double bond,[108] compared to the C2C3 single bond length of 1.5122(13) Å for **7**, and the averaged C2C3 triple bond length of 1.2097(7) Å for **5a**. The C1C2 bond length in **8** is 1.4274(11) Å, which is interesting as it had been expected to be a single bond. Instead, the C1C2 bond length in **8** is similar to the averaged bond length of **5a** at 1.4015(7) Å. This implies that **8** also has allenic properties due to resonance along the C1C2C3 bonds. This was unexpected as there is only a CC double bond present in **8**, which gives it less electron density to share compared to **5a**. A possible explanation can be found in the resonance forms shown Scheme 22.

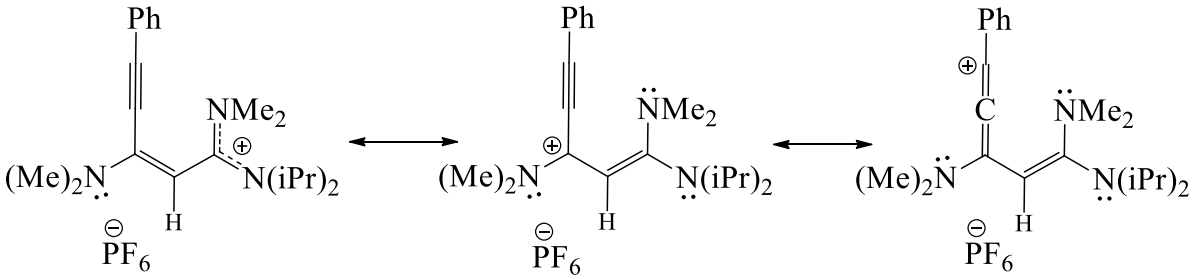

Scheme 22: Proposed resonance structures of compound **8**.

From the structures in Scheme 22, there could be extended resonance across the structure shifting the carbocation from the C1 carbon to the C3 carbon (see also Chapter 4, Scheme 11). This could then further resonate to give the right most structure in Scheme 22,

where an allene has been formed, similar to what occurs in **5a**. This can be substantiated from the bond lengths of **8**; if the CC triple bond length in the ethynylbenzene is more characteristic of a double bond rather than a triple bond, that would be strong evidence for the proposed resonance structures in Scheme 22. The C3C14 bond length is 1.4354(11) Å, which is again too short to be a single bond. The C14C15 bond, however, is firmly a triple bond with a length of 1.2061(11) Å. This means that the right most resonance structure of Scheme 22 is not a contributor. The shorter bond lengths along **8** does, however, suggest delocalized electron density, which would be required from the observed 1.5 bond orders in **8**. These 1.5 order bonds would be expected to generate 120º angles at the carbon atoms involved as they would have to be sp^2 hybridized. This is observed, as the ∠C1C2C3 angle is 121.93(7)º. The triple bond of the ethynylbenzene is also linear with a ∠C1C14C15 angle of 177.00(8)º and a ∠C14C15C16 angle of 177.80(9)º.

For compound **8**, a search of the CSD[58] was conducted to determine if there were any structures reported in literature that were similar to it. There were no examples within the CSD that were similar enough to **9** to warrant a comparison of the structures.

During one attempted synthesis of compound **8**, different crystals were obtained, and they proved to be another unexpected compound. The structure of the crystals was determined using X-ray crystallography and confirmed to be lithium *bis*(((Z)-3-(diisopropylamino)-1-(dimethylamino)-3-(dimethyliminio)prop-1-en-1-yl)oxy)*bis*((E)-N-(1-(diisopropylamino)-3-(dimethylamino)-5-phenylpent-2-en-4-yn-1-ylidene)-N-methyl methanaminium)hexafluoro phosphate(V) dihydrate, **UC3**.

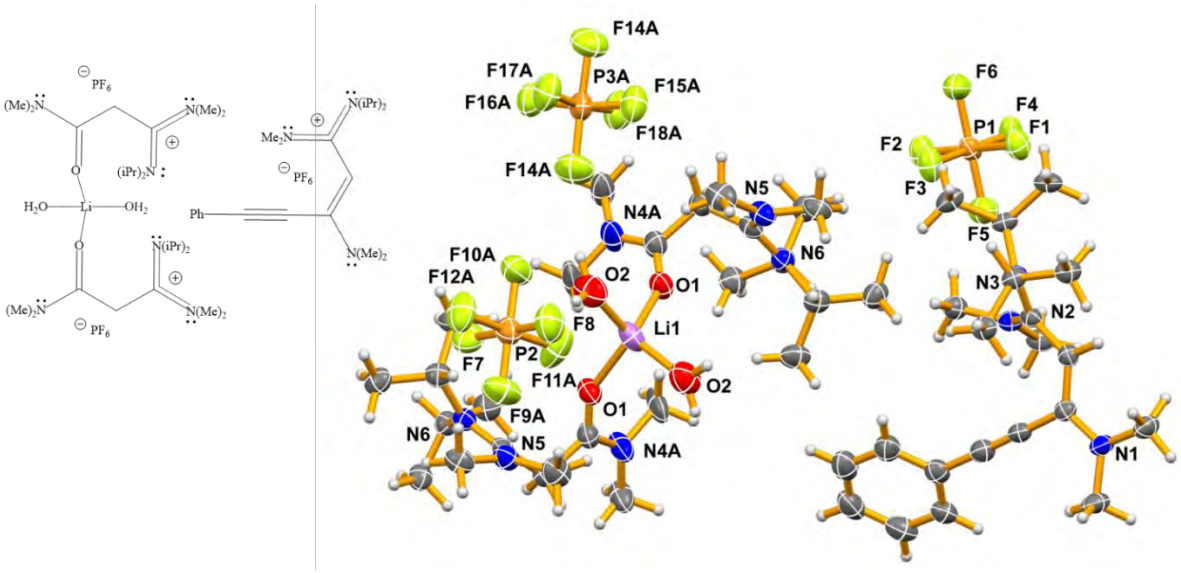

Figure 72: Solid state structure of lithium *bis*(((Z)-3-(diisopropylamino)-1-(dimethylamino)-3-(dimethyliminio)prop-1-en-1-yl)oxy)*bis*((E)-N-(1-(diisopropylamino)-3-(dimethylamino)-5-phenylpent-2-en-4-yn-1-ylidene)-N-methylmethanaminium) hexafluorophosphate(V) dihydrate, **UC3**. Disorder has been removed. Thermal ellipsoids are drawn at the 50% probability level. Only the non-hydrogen and non-carbon atoms have been labelled. Drawing of diagram has been included.

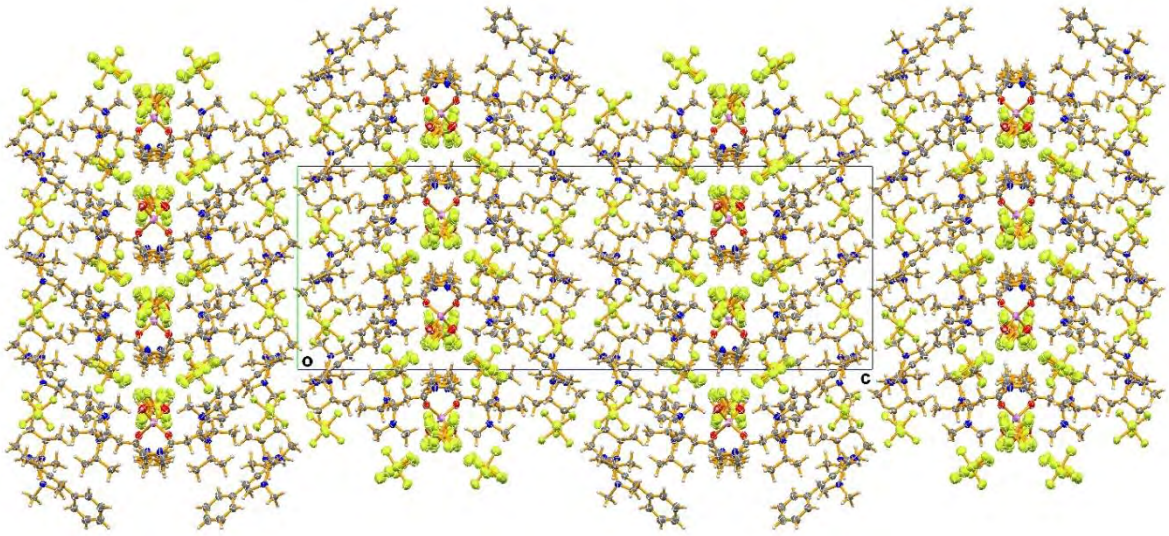

Figure 73: Solid state packing diagram of **UC3** viewed down the *X*-axis. Thermal ellipsoids are drawn at the 50% probability level.

From the structure, it appears that compound **UC3** was formed due to the presence of water in the system, which may have been present due to improperly dried THF. As can be seen from the structure, an intermediate equivalent to compound **7** was likely formed first from the reaction of **5a** with water. Two of these fragments then coordinate with one hydrated lithium ion, present from the *n*-butyl lithium in the reaction mixture, to give the more complex cation in the structure. The other two cations in the crystal structure are the expected product, equivalent to the cation in compound **8**. Overall, these can be thought of as forming a co-crystal with the lithium cation (and their respective anions) to give the overall structure of **UC3**. The unique portion of the unit cell of the crystal is composed of five PF_6 anions, two propargyl carbocations, and one complex hydrated lithium cation containing two hydrolyzed propargyl fragments.

In order to confirm the stereoselectivity of compound **8**, a new set of experiments was devised. It was now thought that a nucleophilic reagent would be necessary to initiate reaction at the C3 carbon. As it had been demonstrated that a hydrogen atom could be picked up from the solution, and added onto the C2 carbon, it would be possible to use a nucleophilic reagent to attack the C3 site. The chosen reactant for these reactions was the cyanide anion. The addition of cyanide to compound **5a** was done in two different ways. In the first reaction it was introduced as the potassium cyanide salt. In the second reaction a different source of cyanide was used, and it was added in the form of trimethylsilyl cyanide.

For the first reaction, compound **5a** was dissolved in acetonitrile. To this solution, an excess of potassium cyanide was added. The solution was heated to 50° C using a sand bath, and left to stir for 12 h. After cooling the solution was filtered through Celite. The

sample was left to slowly evaporate in order to grow crystals. This method did not yield crystals, thus the sample was dissolved in DCM and layered with hexanes. This was left at -15° C for 24 h which did yield crystals. The structure of the crystals showed them to be unwanted inorganic salts. They were redissolved in DCM and given an aqueous wash. New crystals were grown via solvent diffusion at -15° C. The structure of these crystals was determined using X-ray crystallography to be the expected product, (E)-N-(3-cyano-1,3-*bis*(dimethylamino)allylidene)-N-isopropylpropan-2-aminium, **9**.

Although the expected product was obtained, the crystal structure revealed that the product was not pure. There was partial methylation observed at the same position as the cyanide functional group had been added, giving a disordered crystal structure. The best model for the disorder during the refinement of the structure was an occupancy of 50% cyanide and 50% methyl at this position (C3). This co-product formed during the reaction, likely due to a reaction occurring with the acetonitrile solvent. The presence of large amounts of KCN could have promoted the fragmentation of the acetonitrile, which would have generated the methyl fragment that then reacted with **5a**. The acetonitrile solvent is the only likely source of a methyl group, unless the compound **5a** fragmented during the reaction, which is unlikely. The methylated product probably formed during the initial reaction, and the resulting aqueous wash removed enough of the inorganic salts for the methylated and cyanide salts to co-crystallize. There was still evidence of a double bond between the C2 and C3 carbons in the product. This indicates that there was no reaction to cause saturation of the compound, as had been observed in **7**. In order to generate a pure sample of compound **9**, the use of trimethylsilyl cyanide was explored.

For the second reaction, compound **5a** was also dissolved in acetonitrile. To this solution, a small excess of liquid trimethylsilyl cyanide was added. The sample was allowed to stir for 12 h, after which there was no visible precipitate. The sample was left to slowly evaporate, which did not yield crystals but instead gave an oil. This oil was washed with 3 x 5 mL of hexanes. The sample was then dissolved in DCM and layered with hexanes. It was left at -15° C for 24 h, which yielded crystals. The structure of the crystals was determined using X-ray crystallography to be the compound **9**. Unlike the reaction involving potassium cyanide, this structure did not show any unwanted methylation.

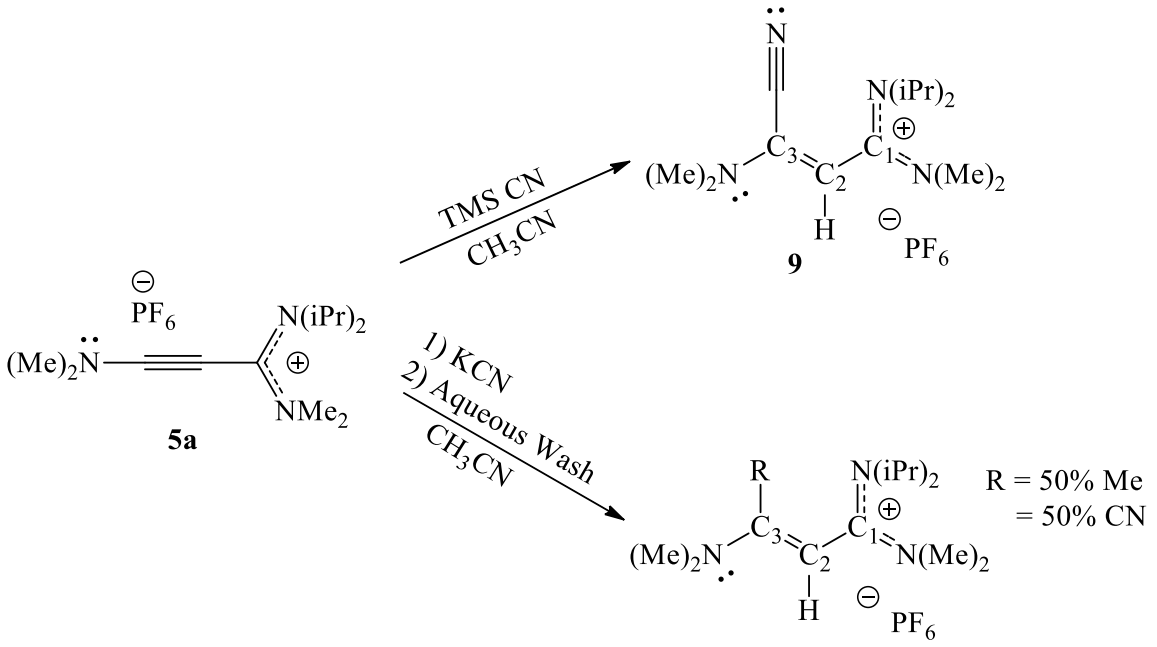

Scheme 23: Reaction conditions that led to the isolation of compound **9**, and the disordered product obtained from the reaction with KCN. The disordered product has 50% CN and 50% methyl occupancy at the C3 position.

Both of the synthetic routes to compound **9** resulted in the isolation of the cis isomer product. This is the same relative conformation as observed in the synthesis of compound

8, where nucleophilic attack on the C3 carbon was stereoselective giving only the cis product. This implies that it is not the specific reaction that leads to this stereoselectivity, rather it arises from the presence of the carbocation. If this is the case, a propargyl carbocation could be used to selectively form cis products in reactions that add across the CC triple bond.

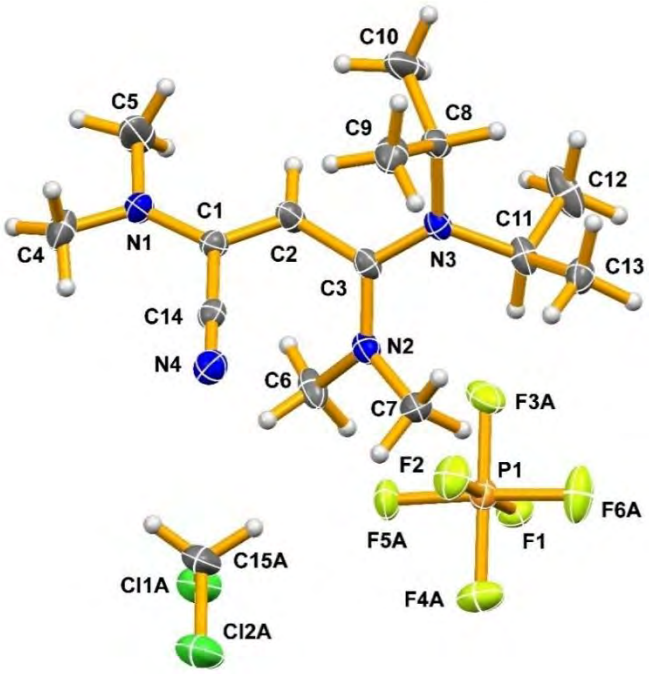

Figure 74: Solid state structure of (E)-N-(3-cyano-1,3-*bis*(dimethylamino)allylidene)-N-isopropylpropan-2-aminium hexafluorophosphate(V), **9**. Only the non-hydrogen atoms have been labelled. The structure is solvated with one molecule of DCM in the asymmetric unit. Disorder of the solvent has been removed in the diagram. Thermal ellipsoids are drawn at the 50% probability level.

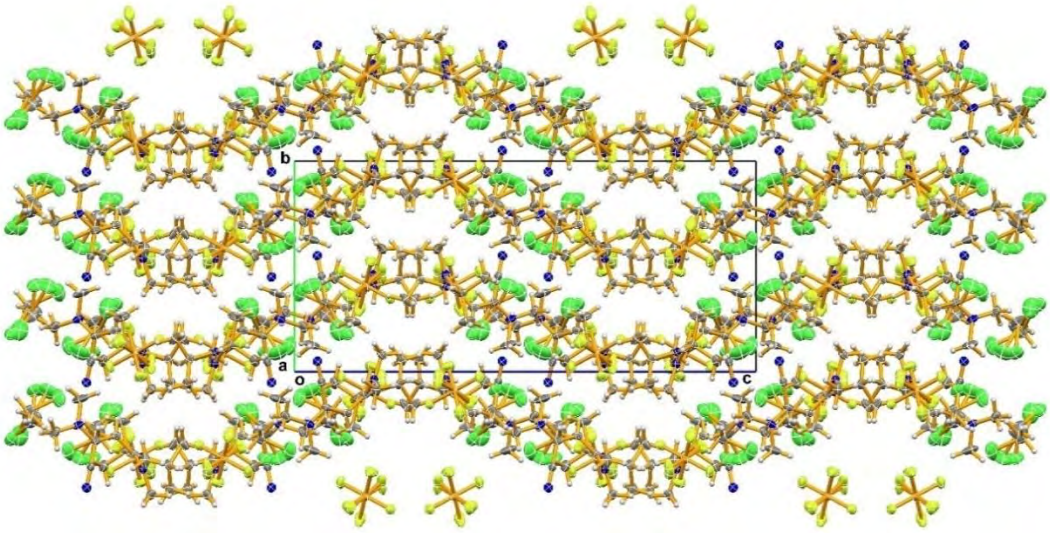

Figure 75: Solid state packing diagram of **9** viewed down the *X*-axis. Thermal ellipsoids are drawn at the 50% probability level.

In the packing of **9**, a wave pattern is observed perpendicular to the *X*-axis. There do not seem to be any channels in the structure where the DCM solvent and the hexafluorophosphate anion are able to fit, instead they appear to overlap with the cation of **9** in the packing diagram.

The same trend observed in **7** and **8** is also present within **9**, where the carbon-carbon bond lengths along the propenium backbone are consistent with bond orders of 1.5. This includes the C1C2 bond with a length of 1.4492(12) Å, and the C2C3 bond with a length of 1.3715(12) Å. The C2C3 bond length does show more double bond character compared to that in **8**, however, which is likely an effect from the lack of a CC triple bond adjacent to the C3 carbon. There is a C≡N triple bond located there instead, though it does not appear to donate as much electron density as the CC triple bond in **8**. This would make sense as the C14N4 bond length of the cyanide substituent is 1.1447(12) Å, which is typical of a nitrile.[108] The C3C14 bond also has a bond order of 1.5, instead of the expected single bond, at a length of 1.4506(12) Å. The sp^2 hybridization of the atoms is further observed

in the bond angles where the ∠C1C2C3 angle is 121.82(7)º, and the ∠C2C3C14 angle is 118.68(7)º, which are both close to the expected 120º. There do not appear to be any observable intermolecular forces which disrupt the nitrile group, as the ∠C1C14N4 angle has not significantly changed from the expected linear angle, at 177.26(10)º.

For compound **9**, a search of the CSD[58] was conducted in order to determine if there were any similar structures reported in literature. This search did not reveal any compounds that had been reported that contained three amino groups in close proximity to the nitrile, and were also non-cyclic in nature. A handful of compounds have been reported where the nitrile group had been added onto an aromatic ring, with amino groups in close proximity, however, those were not similar enough in structure to warrant a comparison.

It should be noted at this time that the attempted reaction of **5a** with inorganic azides, was not successful. The reactions with sodium azide, and azidotrimethylsilane were attempted on multiple occasions, each time not producing a crystal, or even enough evidence to warrant the belief that the reaction was proceeding. All reactions were performed in either DCM,[xlii,xliii] acetonitrile, or THF, at room temperature. When these reactions did not occur, later samples were heated to ~50ºC, which again, did not produce evidence that a reaction was occurring.

[xlii] When sodium azide was used with DCM, the reaction was performed in duplicate, one with only sodium azide, and a second with lithium chloride added to help increase the solubility of the sodium azide.
[xliii] A repeat of this reaction should NOT be performed, as the mixture of azides and halogenated solvents is dangerous.

5.2 Reactions of the IMes Propargyl Carbocation

Although two different metathesis reactions were successfully carried out with compound **6a**, the crystalline yields of the salts formed were not satisfactory enough to warrant using any of these derivatives over the powder (Br) form of compound **6a**. With this in mind, experimentation with compound **6a** could proceed as it had been definitively shown that the structure of compound **6a** is as depicted in Scheme 16. However, during one attempt to grow a higher quality (unsolvated) crystal of compound **6a**, it was discovered that the structure had undergone hydrolysis similar to that observed for compound **7**.

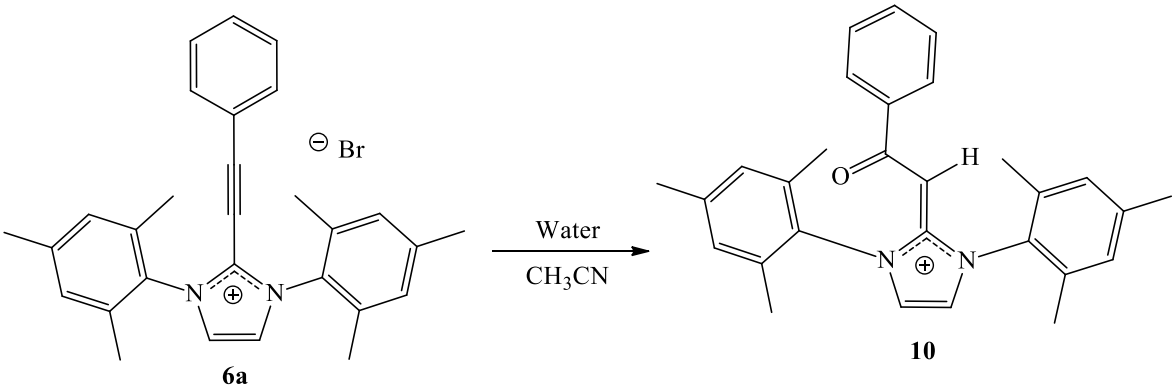

Scheme 24: Reaction conditions that led to the isolation of compound **10.**

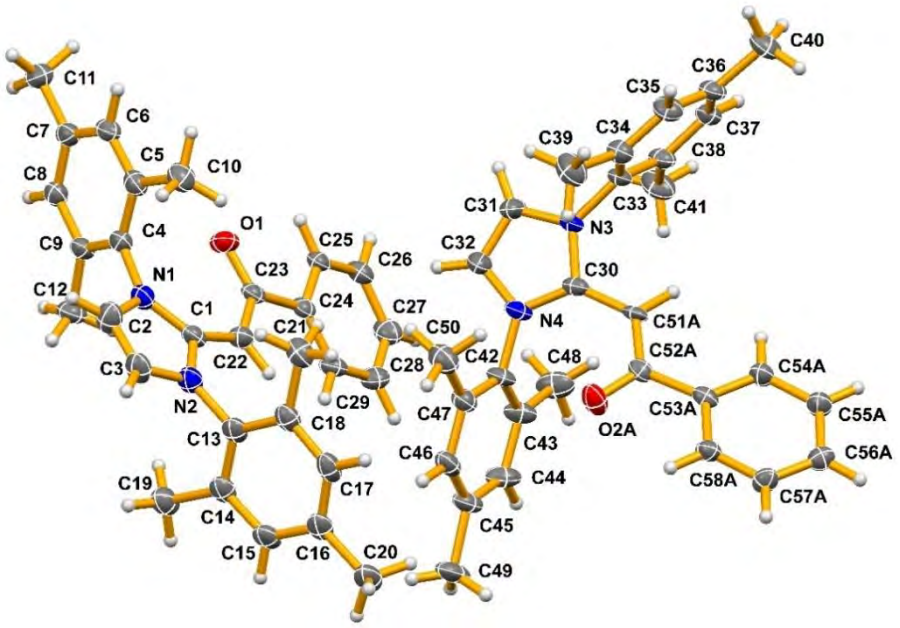

Figure 76: Solid state structure of 2-(1,3-dimesityl-1H-imidazol-2(3H)-ylidene)-1-phenylethanone, **10**. Only the non-hydrogen atoms have been labelled. Disorder in one of the cations has been removed. Two molecules are present in the asymmetric unit. Thermal ellipsoids are drawn at the 50% probability level.

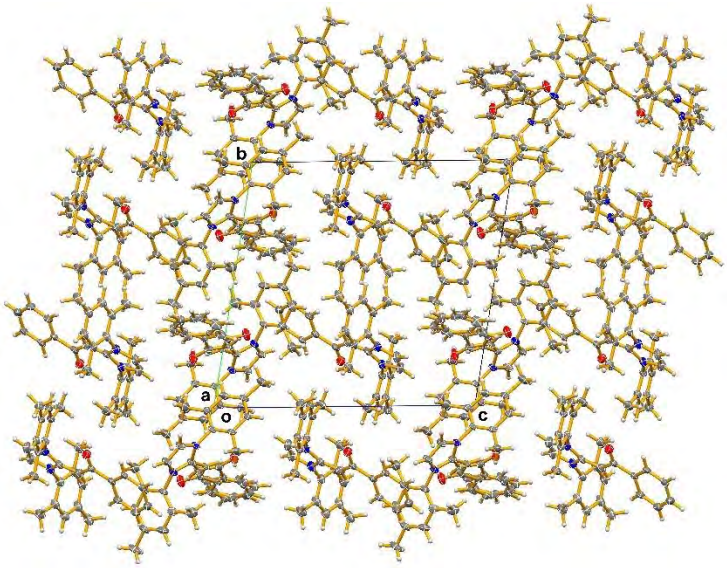

Figure 77: Solid state packing diagram of **10** viewed down the *X*-axis. Thermal ellipsoids are drawn at the 50% probability level**.**

Similar to compound **7**, compound **10** has undergone hydrolysis at the C3 carbon. There is, however, a striking difference between the two compounds. Compound **10** is a neutral complex with a CC double bond between the C1 and C2 carbons, while compound **7** is still an ionic salt with the C2 carbon fully saturated. This means that compound **6a** has had its carbocation disrupted either during the hydrolysis reaction or after. It is unclear whether compound **10** was initially an ionic compound, which later formed the above structure, or if the hydrolysis reaction itself disrupted the carbocation.

This compound was discovered accidentally during attempts to grow a higher quality crystal of compound **6a**. A direct hydration of compound **6a** was attempted, via reaction with water. However, no products were formed from that reaction, and thus it remains unclear how the carbocation was disrupted. It is possible that compound **6a** has less steric hindrance compared to compound **5a**, especially around the carbocation, which allows it to react more readily than compound **5a**.

Compound **10** has two molecules within the asymmetric unit, where one of those molecules has no disorder and the other one is statically disordered across the ethynylbenzene group (Figure 78). The source of this disorder seems to be the packing of the crystal structure. It does not appear that the direction of the attack from the water molecule forms different enantiomers of **10**, as the structure can be rotated 180º to give the same conformation. Instead it appears that the first molecule sets within the packing, and there is space for a second molecule, but it is disordered in either the A direction or the B direction. There is a 67.5% and 32.5% occupancy split between the A and B disorders, respectively.

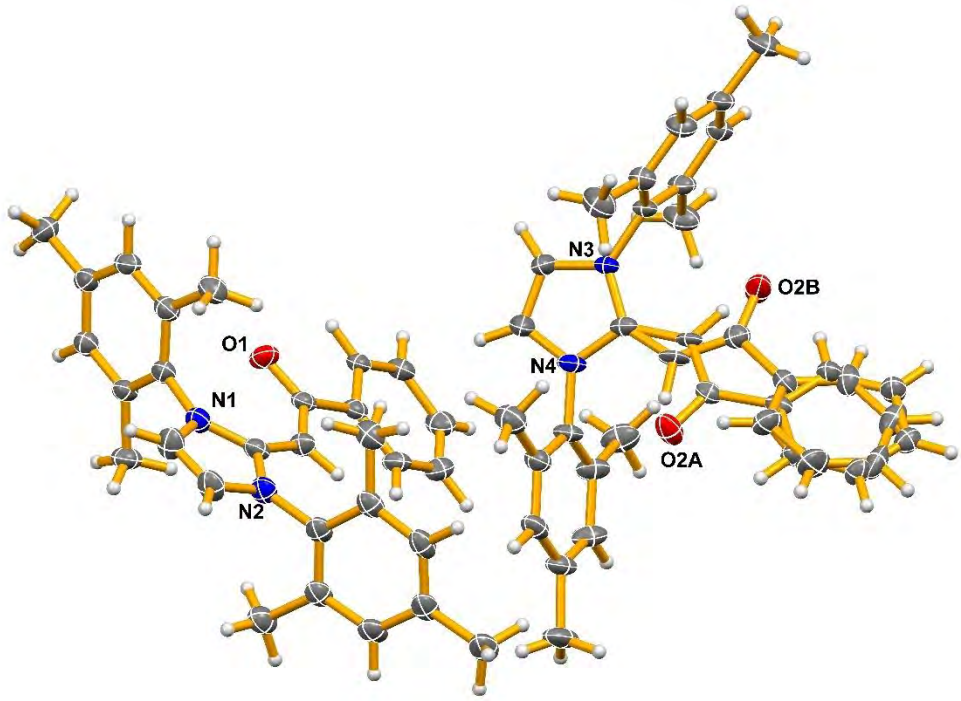

Figure 78: Disorder present within the crystal structure of compound **10**.

When examining the bond lengths of **10**, the non-disordered molecule has a C3O1 bond length of 1.244(2) Å, while in the disordered part A of molecule 2 it is 1.247(4) Å and in the disordered part B it is 1.230(6) Å. The bond lengths in the disordered molecule are not as well-determined as in the ordered molecule and so will not be discussed further. The C1C2 bond length is 1.398(3) Å, which is roughly a 1.5 bond order. It was expected that this would be a double bond, so electron density must have been removed in order to lengthen this bond, likely to the adjacent nitrogen atoms. The C2C3 bond is 1.413(3) Å, which is also a reflective of a 1.5 bond order instead of the expected single bond, implying that there is delocalized electron density across all of the C1C2C3 bonds. This does not extend to the phenyl ring, as the $C3C_i$ bond length is single, at 1.510(3) Å. The most efficient way to create such electron delocalization in this neutral molecule would be for a zwitterion to form through resonance (Scheme 25). The ∠C1C2C3 angle is 127.81(19)º,

which is slightly larger than the expected sp^2 hybridized angle of 120º. This is likely due to packing effects present within the structure. Compound **10** is rather different from **7**, due to the loss of the carbocation. **10** is sp^2 hybridized at C1 with a double bond formed there after the loss of the carbocation, while **7** still has the carbocation intact and is thus only sp^3 hybridized. **7** shows only CC single bond lengths across the C1C2C3 bonds, while there are bonds of order 1.5 present within **10**. Compound **7** shows this sp^3 hybridization with a ∠C1C2C3 angle of 109.58(8)º.

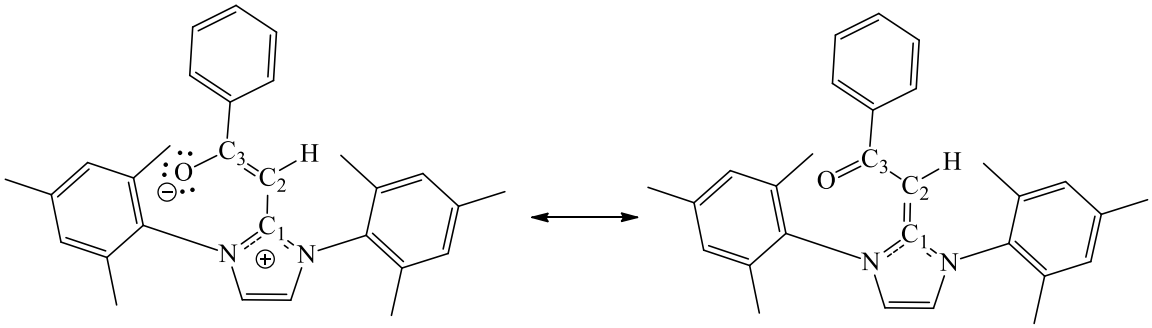

Scheme 25: Proposed resonance structures of compound **10**.

A number of reactions were performed on compound **6a**, to compare its responses with those of compound **5a**. Compound **6a** was reacted with potassium cyanide in an attempt to prepare a similar product to compound **9**. Such a reaction would also be able to help substantiate the theory that the propargyl carbocation undergoes nucleophilic attack to form the cis isomer stereoselectively. If the cyanide added to the C3 carbon while also giving the cis configuration in the carbocation product, this would be strong evidence that propargyl carbocations are stereoselective for addition reactions. Unfortunately, the reaction of compound **6a** with potassium cyanide did not yield a usable product.

Undeterred by the setback, however, another reaction that was of particular interest was attempted with compound **6a**. This reaction had not given an isolable product when it was carried out with compound **5a**. However, compound **6a** has less steric hindrance around the alkyne, compared to compound **5a**, so the experiment was tried in hopes that a reaction would occur. The reaction was carried out with sodium azide, in an attempt to perform a Huisgen cycloaddition. Though azide addition "click" reactions occur readily with terminal alkynes,[125,126,127] the same cannot be said for non-terminal alkynes; generally, the use of ruthenium catalysts and elevated temperatures are necessary for "click" reactions to occur with non-terminal alkynes. Here it was thought that the activation of the C3 carbon by the carbocation might allow a "click" reaction to proceed without the use of a catalyst.

To do this, compound **6a** was dissolved in acetonitrile. To the solution an excess of sodium azide was added and it was left to stir. It was noticed that after a few minutes that the colour of the solution changed from a deep red to orange. The sample was stirred for 12 h to ensure that the reaction went to completion. The sample was then filtered through Celite and left to slowly evaporate. Crystals grew from the evaporating solution. The crystals were examined using X-ray crystallography and the structure was confirmed to be 5-(1,3-dimesityl-1H-imidazol-3-ium-2-yl)-4-phenyl-1,2,3-triazol-1-ide, **11a**.

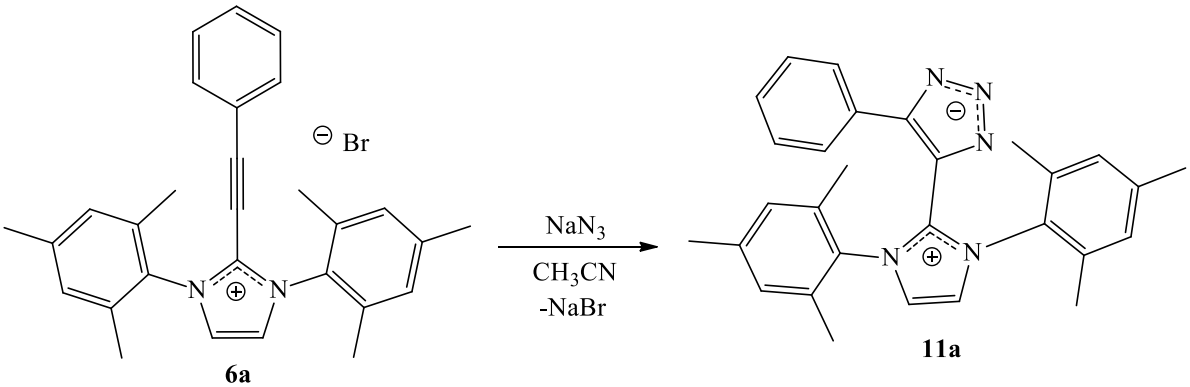

6a **11a**

Scheme 26: Synthesis of **11a**.

As the reaction was left over the course of 18 h, its true rate is unknown. This is important, as it would help determine if the Huisgen cycloaddition to a propargyl cation was a "click" reaction. The reaction did proceed in under 24 h with a modest yield of ~54%, so there is the possibility that it is. The reaction did occur at low temperatures which is evidence for "click" chemistry. As the propargyl carbocation has been seen to be stereoselective, there exists the possibility that this could also influence the stereoselectivity if an organic azide was used. If the propargyl carbocation produced a non-racemic mixture in a reaction with an organic azide, this would be further evidence that a "click" reaction is occurring. Additional experimentation and possibly computational studies will be necessary to provide further evidence. Regardless, the synthesis of compound **11a** demonstrates several things about the chemistry of propargyl carbocations. The first obvious observation is that compound **6a** was able to undergo a cyclic addition reaction without the use of a metal catalyst, while also being left at room temperature. Such a mild reaction has not commonly been observed in the literature for non-terminal alkynes. This reaction implies that propargyl carbocations are able to activate the alkyne, in a similar manner to the use of a catalyst, which allows for reactions that otherwise would not have been observed to occur.

From the structure of compound **11a**, it can be observed that a zwitterion has been formed, while the bromide anion has reacted with sodium from the added NaN_3 to produce sodium bromide. This has disrupted the classical salt-like properties, observed in the previous series of compounds, where the cation was intermolecularly coordinated to the

anion. Instead, compound **11a** is referred to as an inner salt, where the cation/anion pair is intramolecularly coordinated. Though the negative formal charge has been denoted on the N4 position in Scheme 26, it would be more correct to have the negative charge delocalized across the N3N4N5 positions of the triazole ring, which was formed after the azide addition (as denoted by the dashed lines in the diagram). Having a delocalized negative charge across the N3N4N5 positions by resonance is more favourable, instead of having it solely on a single nitrogen atom. This being said, there are multiple resonance structures that can be drawn for **11a**, including a neutral complex that is not a zwitterion, where there is an allene type bond distribution (analogous to previous examples) with a double bond to the carbenic carbon of the NHC. It is not known how much each of these individual resonance forms contribute to the overall structure.

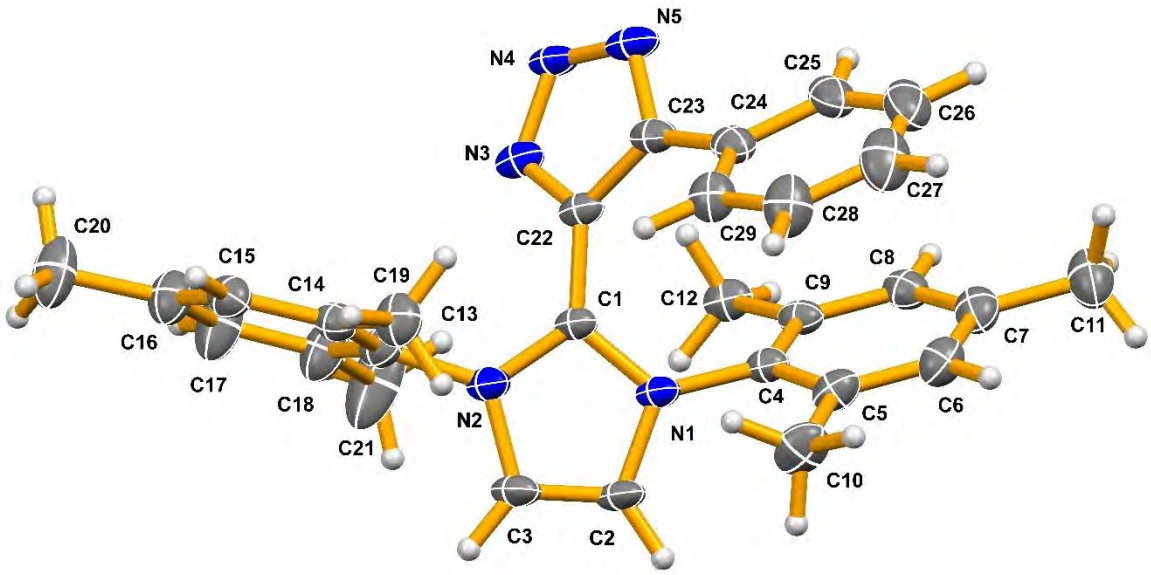

Figure 79: Solid state structure of 5-(1,3-dimesityl-1H-imidazol-3-ium-2-yl)-4-phenyl-1,2,3-triazol-1-ide, **11a**. Only the non-hydrogen atoms have been labelled. One molecule of disordered toluene solvent has been removed from the diagram. Thermal ellipsoids are drawn at the 50% probability level.

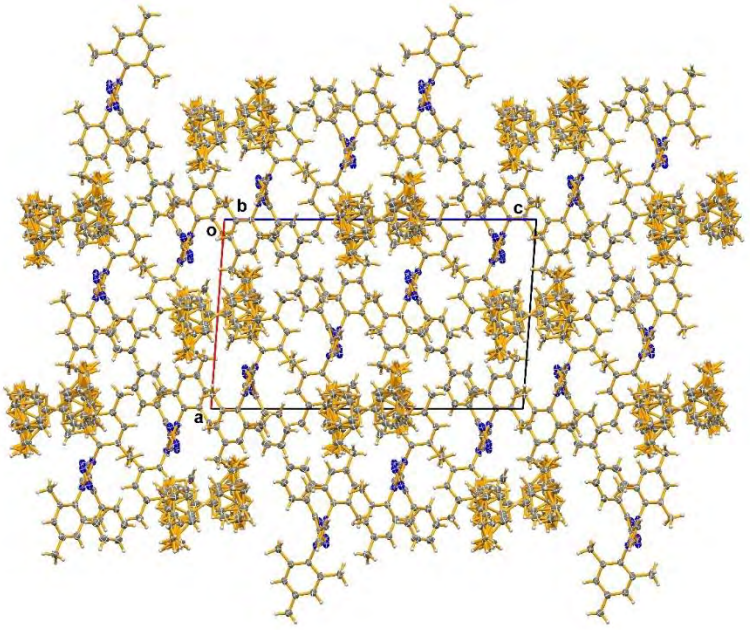

Figure 80: Solid state packing diagram of **11a** viewed down the *Y*-axis. Thermal ellipsoids are drawn at the 50% probability level.

Compound **11a** has shorter molecular bonds across the C1C2C3 atoms, compared to the single bonds depicted in the Lewis structure, likely due to the electron delocalization discussed earlier. The C1C2 bond length is 1.456(3) Å, which is a 1.5 order bond, as observed in the previous structures. The C2C3 bond length is 1.401(3) Å, and the $C3C_i$ bond length is 1.464(4) Å. This is all as expected for the bonds in the structure, further showing that there is a large amount of electron delocalization. The bond lengths for the C2N3 and C3N5 bonds are 1.362(3) Å, and 1.357(3) Å, respectively. These are in the range for an azole compound, where the expected bond length for a sp^2 carbon and a λ^2-nitrogen is 1.376 Å.[108] When looking at the N3N4 and N4N5 bond lengths, it would be expected that they should be nearly identical. They are expected to be 1.5 order bonds due to the delocalization of the double bond across them. The N3N4 and N4N5 bond lengths are 1.324(3) Å, and 1.315(3) Å, respectively, while the expected value for λ^2-nitrogen-nitrogen

bonds with an ortho-nitrogen atom in an aromatic system is 1.368 Å.[108] The observed bond lengths are slightly shorter than the expected value, which is likely due to the formal negative charge delocalized across these nitrogen atoms. This slight difference in bond length is likely not just chance variance, as the expected bond length under the same conditions (λ^2-nitrogen-nitrogen bonds in an aromatic system), but with an ortho-carbon atom would be 1.304 Å.[108]

Like the previous IMes structures discussed, the carbon atoms in the propenium chain in **11a** are sp^2 hybridized, and thus it would be expected that the C1C2C3 and C2C3C$_i$ angles would be 120°. The bond angle ∠C1C2C3 is 130.9(2)° and that of ∠C2C3C$_i$ is 131.4(2)°. These are both slightly larger than the expected 120°, which is likely due to the strain in the triazole ring. The electron delocalization around the ring gives bond orders between 1 and 2 for all of the CC, CN and NN bonds. The internal bond angles are all around 107°, not because of hybridization but rather from the geometry of the 5-membered ring itself. For the nitrogen atoms in the azole ring, the ∠C2N3N4, ∠N3N4N5, are ∠N4N5C3 are 105.7(2)º, 112.8(2)° and 107.4(2)º, respectively.

A new reaction was attempted in order to decrease the purification steps required in the preparation of **11a**. Instead of using sodium azide, **6a** was reacted with azidotrimethylsilane in DCM. Instead of forming the zwitterionic product, **11a**, a protonated cyclic azide structure was obtained. The structure was determined using X-ray crystallography and confirmed to be 1,3-dimesityl-2-(5-phenyl-1H-1,2,3-triazol-4-yl)-1H-imidazol-3-ium bromide, **11b**.

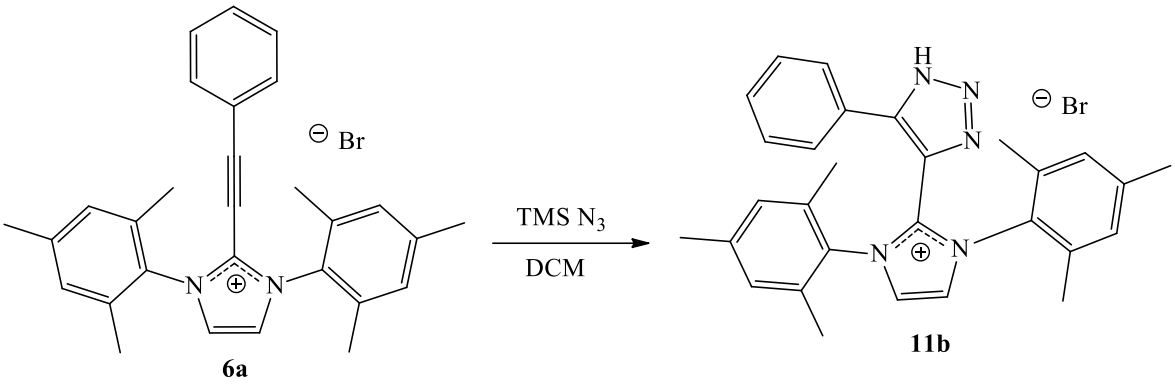

Scheme 27: Synthesis of **11b**.[xliv]

A poor choice of solvents was used for the reaction of **11b**, as the mixture of azides and halogenated solvents is dangerous. The reaction of **11b** should only be repeated in a more appropriate solvent. Unlike **11a**, compound **11b** is not a zwitterion, as the bromide anion is still present in the crystal structure. The proton of **11b** was likely acquired from the solvent. This also shows that the carbocation of **6a** was not disrupted in the reaction. The azide was still able to cyclize, as was seen with **11a**, however, the formal negative charge on the triazole ring in **11a**, has been neutralized by the addition of a proton at the N5 position of the ring (Scheme 27), which suggests that the N5 position is the most basic site. As the NH proton was not observed to have a partial occupancy within the crystal structure, and as it was located on the N5 nitrogen atom, there should be an NN double bond between the N3 and N4 nitrogen atoms, at least in the preferred Lewis structure shown. This double bond is longer than would be expected according to Allen *et al.*,[108] which indicates that there has to be some amount of electron delocalization still occurring around the ring. It is possible to draw Lewis structures that do allow delocalization of the

[xliv] A repeat of this reaction should NOT be performed, as the mixture of azides and halogenated solvents is dangerous.

electron density around the ring in this structure, particularly if the generation of a zwitterion is invoked.

Although the solid-state structure does show the proton having 100% occupancy on the N5 nitrogen, it should be noted that the structure could form a tautomer, with the proton on the N3 nitrogen in the liquid-state, as is also observed with the free PNP ligand in Chapter 2. This potential tautomeric structure, however, is not able to influence the solid state and cannot be the cause of the longer than expected NN double bond previously mentioned. The NH proton hydrogen bonds with a bromide anion, details of which can be seen in Table 18. The correct bromide anion is generated through symmetry using the *x*, *y*-1, *z* transformation.

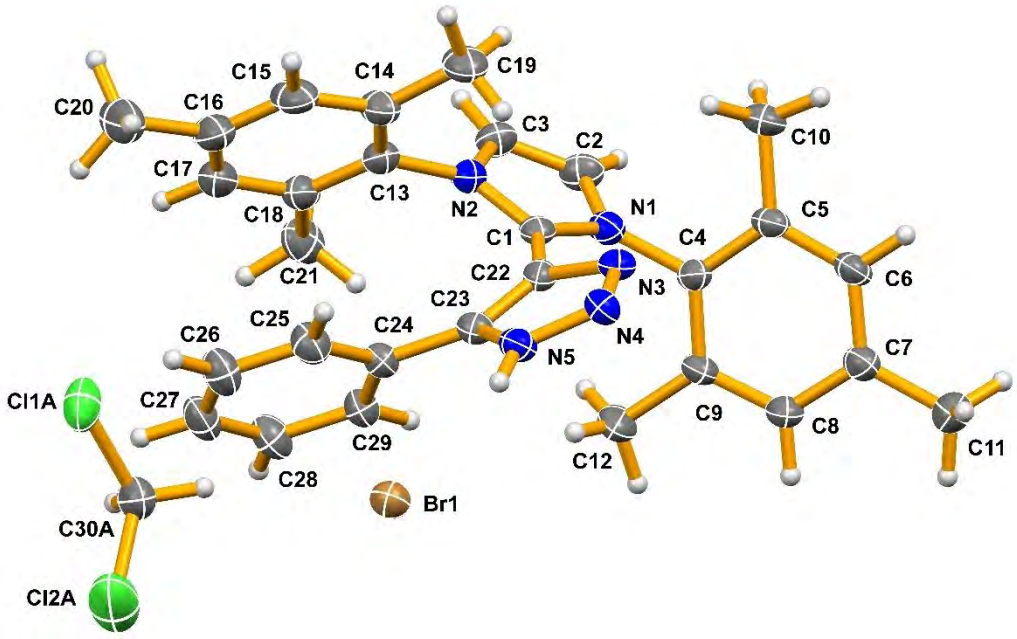

Figure 81: Solid state structure of 5-(1,3-dimesityl-1H-imidazol-3-ium-2-yl)-4-phenyl-1,2,3-triazol-1-ide, **11b**. Only the non-hydrogen atoms have been labelled. There is one molecule of DCM in the asymmetric unit. Disorder of the solvent has been removed. Thermal ellipsoids are drawn at the 50% probability level.

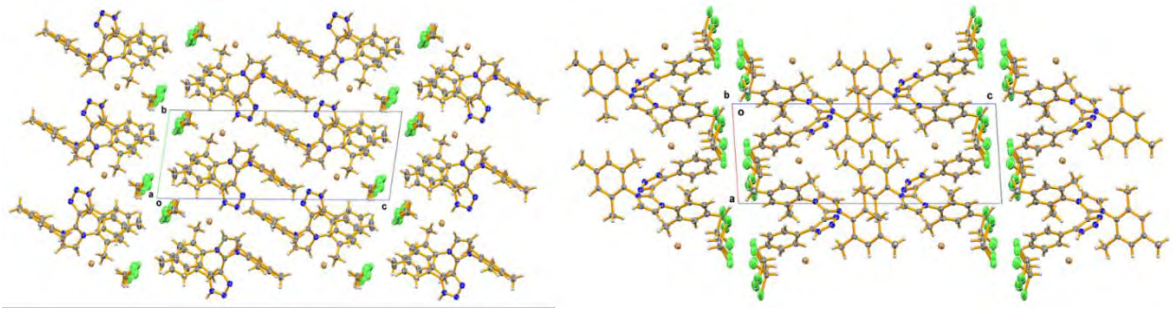

Figure 82: Solid state packing diagram of **11b** viewed down the *X*-axis (left) and the *Y*-axis (right). Thermal ellipsoids are drawn at the 50% probability level.

From the packing diagrams of **11b**, it can be seen that channels running along the *Y*-axis are formed for the DCM solvent to occupy. All of the DCM molecules are orientated to have the chlorine atoms directed towards each other in these channels. Viewed down the *X*-axis, it appears as if there are intermolecular stacking interactions between trimethylphenyl groups. This, however, is not observed when viewed down the *Y*-axis (Figure 82, right). Instead, there are only short intramolecular stacking contacts which occur within each molecule. These stacking interactions are from the center of gravity of a 6-membered ring, one of the trimethylphenyl groups (C13 to C18), to the center of gravity of the 6-member ring (C24 to C29) of the C≡C-Ph group and are equal to 3.614(3) Å.

With **11b** being a neutral complex, it would be expected to have slightly different bond lengths and angles when compared to **11a**. The C1C2 bond length is 1.438(6) Å, which is still a 1.5 bond order, as has been seen in the previous structures and in **11a**. The C2C3 bond length is 1.390(6) Å, and the $C3C_i$ bond length is 1.468(6) Å. There is no significant difference in the bond lengths of **11b** when compared to those of **11a** with respect to the carbon atoms of the propargyl chain. The C2N3 and C3N5 bond lengths are 1.377(6) Å, and 1.348(6) Å, respectively. These bond lengths again have no significant

changes in comparison to those in **11a**. When looking at the nitrogen atoms of the azole ring, the N3N4 bond has a length of 1.313(5) Å, and the N4N5 bond has a length of 1.344(5) Å. The N4N5 bond length is slightly longer when compared to that in **11a**, while the N3N4 bond length is slightly shorter. This makes sense, as the N-N bonds in **11a** were delocalized (bond order 1.5) across the nitrogen atoms. In the main Lewis structure drawn for **11b** there is a defined N-N single bond and an N=N double bond. The bond shortening observed for the N3N4 bond and lengthening for the N4N5 bond when compared to those in **11a** does imply that there is less delocalization in **11b**, although there is clearly some amount still present. It is also worth noting that these differences could also be due to the lack of a formal negative charge in **11b**, as the reduction in electron density would create less delocalization, which was responsible for the 1.5 bond orders in the azole ring of **11a**.

The observed bonds angle in **11b** for ∠C1C2C3 is 132.5(4)° and that of ∠C2C3C_i is 134.3(5)°. These bond angles are slightly more obtuse in **11b** compared to those in **11a**, which may be due to the difference in the azole ring geometry caused by protonation. As is observed with **11a**, all of the ring bond angles are around 107º, not because of hybridization but from the geometry of a 5-membered ring. When comparing the ∠C3N5N4 angle from **11a** to **11b**, the angles are 107.4(2)º and 112.5(4)º, respectively, which implies that the protonation of the N5 nitrogen slightly opens the bond angle.

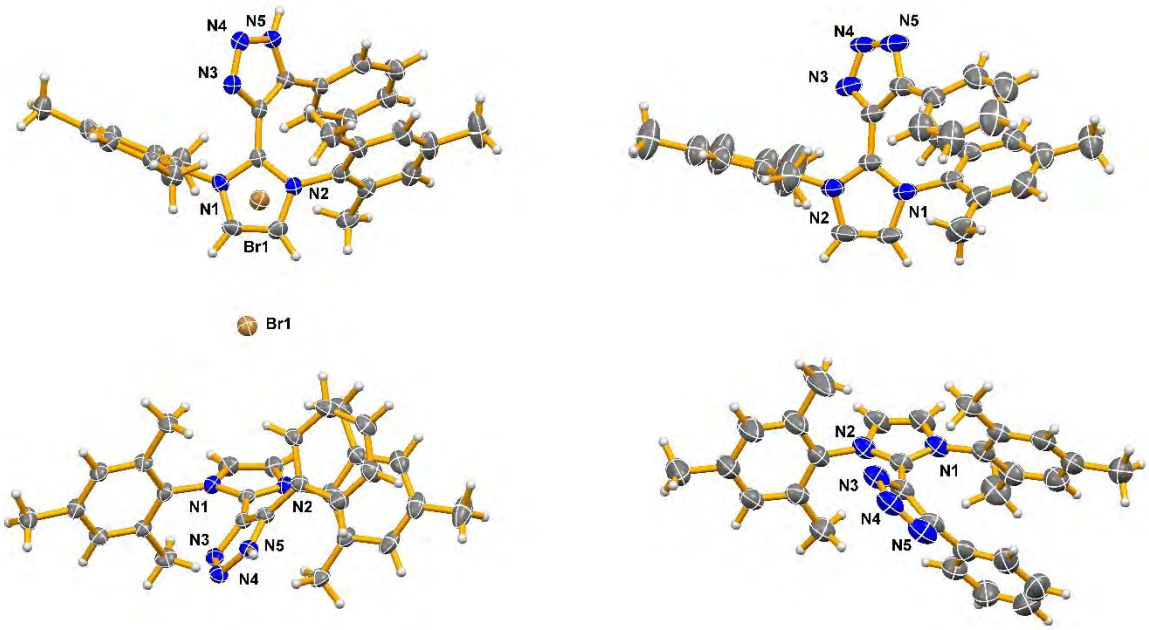

Figure 83: Comparison of the structures of **11a** (right) and **11b** (left), arranged in similar orientations. The bottom structures are rotated by 90° out of the plane of the page compared to the top structures.

As can be seen from Figure 83, there are a few notable differences between the compounds. The first apparent difference is how the CC triple bond has reacted with the azide. In the **11b (**top) structure, the cyclic azide is directed into the plane which also forces the orientation of the phenyl ring into that plane. The opposite is observed for the top **11a** structure, where the cyclic azide is directed out of the plane and thus forces the phenyl right out of the plane as well. For both of the structures, the azide is added across the triple bond to form what could be thought of as a cis complex, where the phenyl ring and the carbene residue are on the same side of the CC double bond in the triazole ring. In these structures, trimethylphenyl groups on the right in the diagram are oriented in opposite directions relative to each other; the trimethylphenyl in **11a** is twisted to tilt upwards, while in **11b** it tilts downwards. In the lower structures, the twisting of the cyclic azide becomes more apparent. The **11a** structure (right in Figure 83) has the phenyl group twisted to the 5

o'clock position, relative to the triazole ring. The **11b** structure (left in Figure 83) is similarly twisted except only to the 2 o'clock position, relative to the ring. When examining the torsion angles for the structure, this twisting effect can be seen quantitatively; the ∠C1C2C3C_i torsion in **11a** is -14.3(4)º and the same torsion angle for **11b** is 1.7(9)º. This shows a twist in the carbon chain in the region of the triazole ring. However, the difference of ~16º does not appear to account solely for the large differences seen in the structures in Figure 83. Looking at the ∠N1C1C2C3[xlv] torsion angles of **11a** and **11b** the values are -39.6(4) and 46.9(8) respectively. This torsion angle is best able to represent the twisting effect described earlier, and which was observed in Figure 83, as it amounts to a ~86º difference in the orientation of the triazole and phenyl rings relative to the orientation of the IMes carbocation in the two structures.

When looking at the planes for **11a** and **11b**, there are two interesting plane angle comparisons to discuss. The first is the angle that the plane of the triazole ring makes relative to the plane of the IMes five-membered ring. When comparing these plane angles, **11a** makes an angle of 45.4º, while **11b** has an angle of 46.7º. These angles are essentially the same, though the orientations in Figure 83 shows that the triazole rings are actually oriented opposite to each other relative to the IMes plane. When looking at the plane angles for the phenyl ring relative to the IMes five-membered ring, **11a** makes an angle of 116.6º, while **11b** has an angle of 66.4º. These angles show the relative orientations of the phenyl rings for both of the compounds, which are significantly different.

[xlv] From Figure 83, in **11a** the torsion angle should be denoted as ∠N2C1C2C3. The same angle is being discussed, though the denotation for **11b** will be the only one written for clarity.

When comparing the structures of **11a** and **11b** to structures found in the literature, there are only a few notable examples that need be discussed. The first is by Kantlehner *et al*.[123] and the other is by Golovanov *et al*.,[124] where the relevant structures are shown in Figure 84.

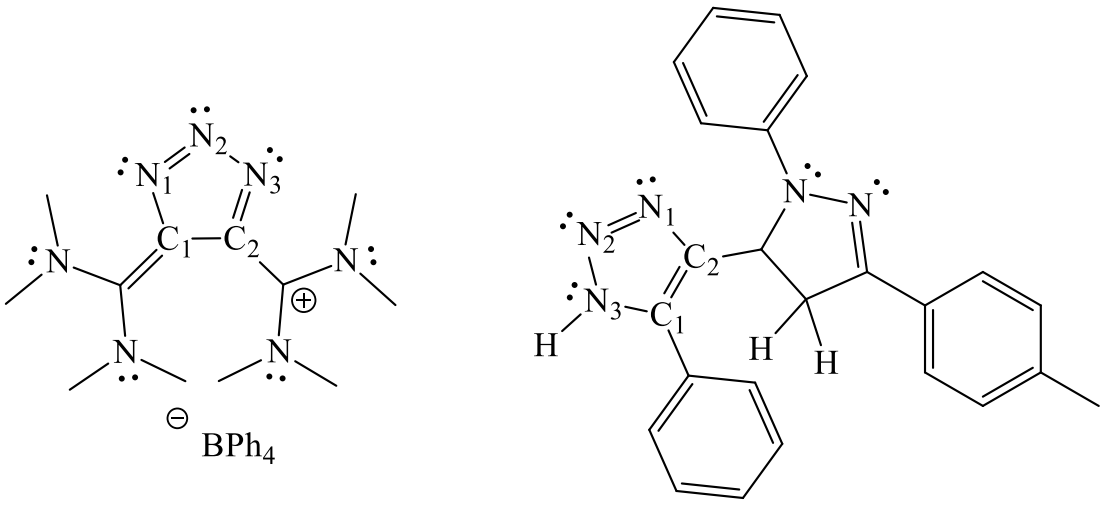

Figure 84: Lewis structures of literature compounds related to compounds **11a** and **11b**: Kantlehner *et al*.[123] (left) and Golovanov *et al*.[124] (right). Atomic labelling has been included for clarity of the discussion.

Due to the delocalization present in the **11a** and **11b** structures, it is difficult to determine exact similarities for bond lengths between the Kantlehner *et al*.[123] and Golovanov *et al*.[124] structures. Both of these literature examples have the ability to undergo resonance for electron delocalization; with the Kantlehner *et al*.[123] having more possible delocalization compared to the Golovanov *et al*.[124] structure. For **11b**, there is less electron delocalization within the structure compared to **11a**, however, there is still evidence that it occurs in the latter as well.

From the compounds in Figure 84, there are a few similarities that can be compared structurally to features in **11a** and **11b**, however, the focus here will be on the triazole rings.

Kantlehner *et al*.[123] report N1N2 and N2N3 bond lengths of 1.323(2) Å, and 1.348(2) Å, respectively. The ∠N1N2N3 angle is reported to be 111.41(13)º, which is more similar to that in the structure of **11a** (112.8(2)°). However, it was stated earlier that in the triazole rings all of the angles are attempting to be 107º due to ring strain. This also appears to the case with the structures of Kantlehner *et al*.[123] and Golovanov *et al*.[124] There does not appear to be any major differences between the Kantlehner *et al*.[123] structure and **11a** or **11b**.

In the structure of Golovanov *et al*.,[124] the N1N2 and N2N3 bond lengths are 1.330(6) Å, and 1.316(6) Å, respectively. These bonds are similar in length to those in **11b**, which is to be expected due to the similarity of the protonated triazole rings in the two structures. The ∠C1N3N2[xlvi] angle is reported to be 105.3(4)º, which is more similar to that in **11a**, where the ∠C3N5N4 angle is 107.4(2)º. **11b** has a ∠C3N5N4 angle of 112.5(4)º. This was unexpected, as it was believed that the Golovanov *et al*.[124] structure and **11b** would be the more similar due to their shared protonation of the triazole ring. It is unknown why the Golovanov *et al*.[124] structure has such a dissimilar ∠C3N5N4 angle compared to that of **11b**; it is unlikely to be a steric hindrance issue, as **11b** is the more sterically hindered of the two. This difference in the ∠C3N5N4 angle is likely due to the ring stain that the triazole is under. As mentioned before, the proton on the **11b** triazole ring seems to change the bond angles slightly from **11a**, and likely this is also the same change which creates the difference from the Golovanov *et al*.[124] structure. Besides this, however, there

[xlvi] This atomic labelling is based off the literature structures of Figure 84. It is the same as the ∠C3N5N4 denotation for the **11a** and **11b** structures.

does not appear to be any significant differences from the Golovanov *et al*.[124] structure and **11a** or **11b**.

After the synthesis of compounds **11a** and **11b**, it was important to continue to demonstrate that the reactivity observed for compound **6a** was similar (or not) to that of compound **5a**. The best way to confirm this was by repeating the types of reactions performed with compound **5a**. The same reaction that produced compound **8**, addition of lithium phenylacetylide, was thus repeated with **6a**. The reaction was performed using a method identical to that which generated compound **8**, however, crystals did not grow and the desired product could not be detected in spectroscopic studies. So, a reaction with trimethylsilyl cyanide was tried instead.

Compound **6a** was dissolved in acetonitrile. To this, a small excess (1.1 eq.) of trimethylsilyl cyanide was slowly added. The sample was stirred for 18 h, and then was filtered through Celite. The solution was left to slowly evaporate which resulted in the formation of an oily substance. This oil was washed with 3 x 5 mL of pentane, before being dissolved in DCM. The sample was layered with pentane and placed at -15°C. Crystals grew after a period of a few weeks. The structure of the crystals was determined using X-ray crystallography and confirmed to be (Z)-2-(2-cyano-2-phenylvinyl)-1,3-dimesityl-1H-imidazol-3-ium bromide, **12**.

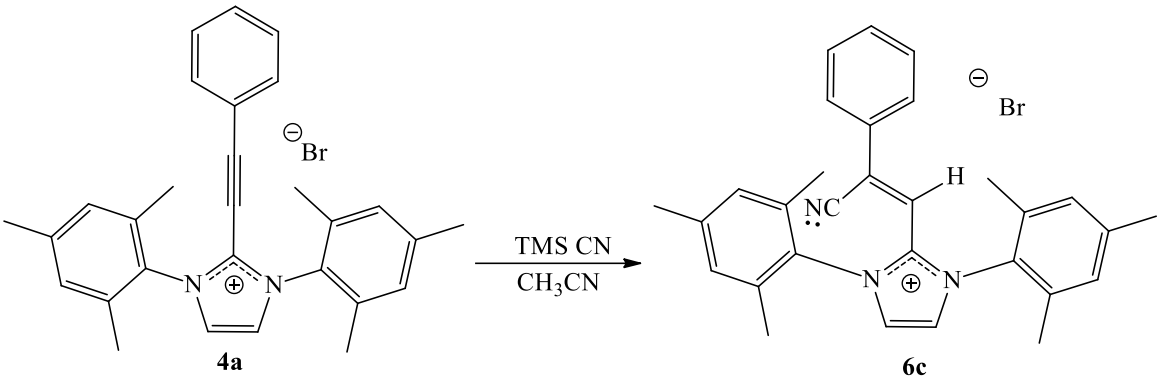

Scheme 28: Synthesis of **12**.

From the structure of compound **12**, two important things can be observed. The first is that the cyanide functional group has undergone a nucleophilic attack at the C3 carbon of the propargyl carbocation. This was also observed during the synthesis of compound **9**, which further indicates the nature of the carbocation is likely as was described in Scheme 11, Chapter 4; there is a resonance that forms an allene structure with the carbocation located at the C3 carbon. The second observation is that compound **12**, like compound **9**, crystallizes as the cis isomer. This shows that propargyl carbocations do seem to be stereoselective for cis isomers, as two different cations with different structures have given the same result. The formation of the cis isomer does not appear to be related to steric hindrance, but is more likely due to the chemical properties of the propargyl carbocation itself. If steric hindrance was a factor, then the trans isomer should have also been formed due to the difference in steric factors between compounds **5a** and **6a**. As no evidence of the trans isomer has been observed in any of the spectroscopic or crystallographic data, addition reactions on the C3 carbon of a propargyl carbocation appear to indeed be cis-stereoselective.

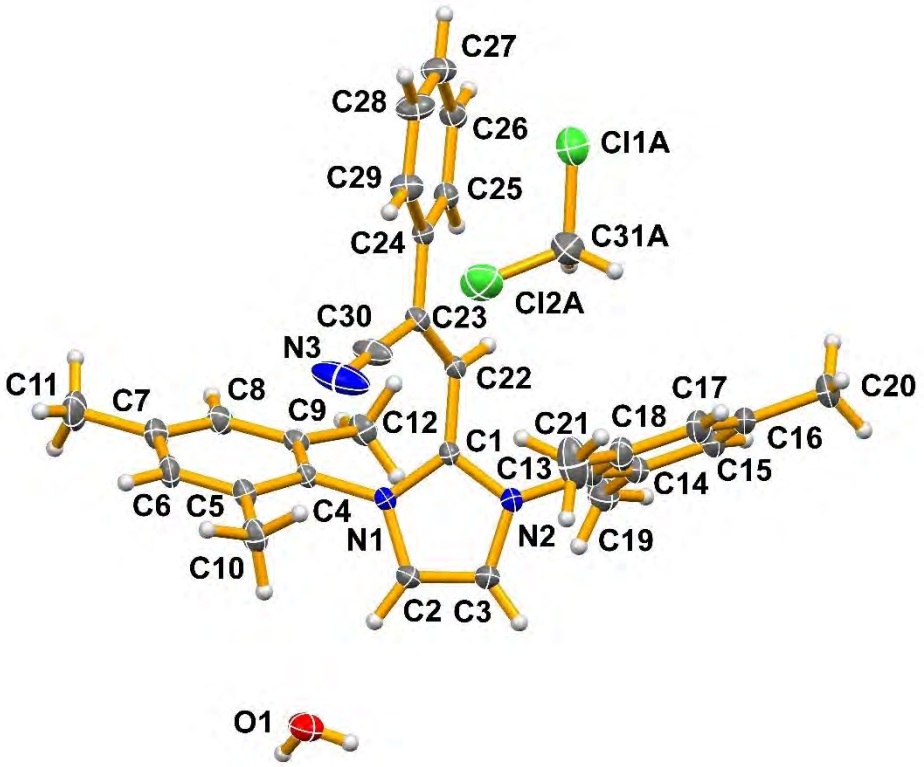

Figure 85: Solid state structure of (Z)-2-(2-cyano-2-phenylvinyl)-1,3-dimesityl-1H-imidazol-3-ium bromide, **12**. Only the non-hydrogen atoms have been labelled. Disorder of the DCM has been removed. The structure is solvated with one molecule each of DCM and water in the asymmetric unit. Thermal ellipsoids are drawn at the 50% probability level.

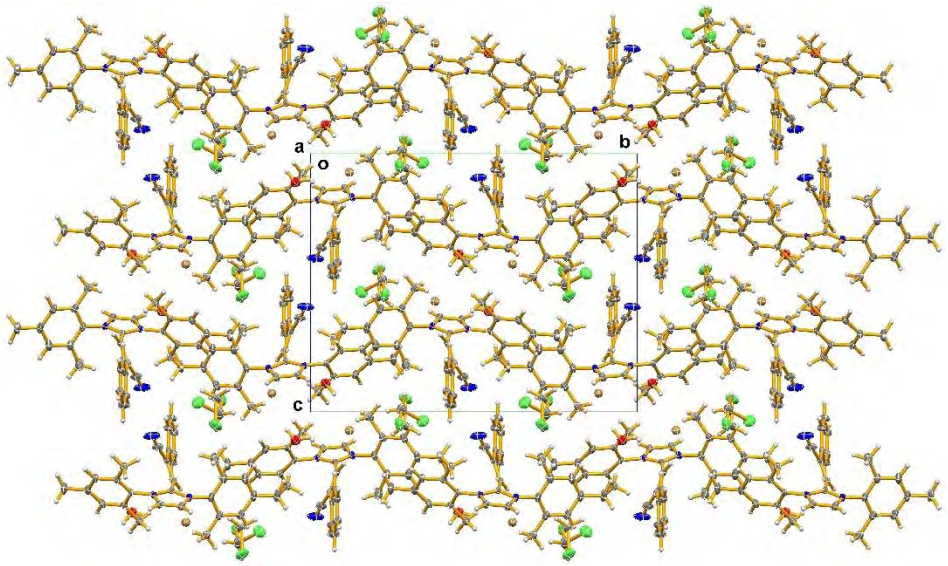

Figure 86: Solid state packing diagram of **12** viewed down the *X*-axis. Thermal ellipsoids are drawn at the 50% probability level.

From the previous structures discussed in this Section, it seemed reasonable to assume that there would be electron delocalization to form bonds of order 1.5 across the C1C2C3C$_i$ chain in **12**. This idea is only partially true, as the bond lengths for C1C2, C2C3, and C3C$_i$ are 1.460(2) Å, 1.344(2) Å, and 1.476(2) Å, respectively. The C2C3 bond does not appear to have substantial delocalization, to be considered as a 1.5 order bond, as it is the expected length for a double bond as given by Allen *et al.*[108] This would also imply that there cannot be much delocalization across the C1C2C3 bonds, if the C2C3 bond is not delocalized. It is possible that there are additional electron withdrawing effects present that are creating shorter than expected bond lengths for the C1C2 and C3C$_i$ bonds. Electron delocalization for the C3C$_i$ bond was not observed in compound **10**, which suggests that the oxygen atom is too electron withdrawing to allow for delocalization across this bond, in comparison to the nitrile group of **12**. The C3C30 bond length is 1.441(2) Å, which is also a 1.5 bond order. However, it is more likely this is a CC single bond, with the nitrile

group allowing a shorter C-C bond due to back-bonding occurring with the C≡N. The ∠C3C30N3 angle is 176.3(3)º which shows the linear characteristic of the nitrile group. The ∠C1C2C3 angle is 124.06(13)º which shows the expected the sp^2 hybridization at C2. The angles for ∠C2C3C_i and ∠C2C3C30 also support sp^2 hybridization of the C3 atom with values of 124.40(13)º and 118.55(14)º, respectively. There do not appear to be any significant differences in compound **12** compared to compound **9** in the region of the cyanide group. Compound **12** does show the same chemistry that was observed with **9**, where the nitrile formed with a cis-configuration, and a formal double bond was present across the C2C3 carbon atoms. There is also hydrogen bonding present in **12**, which is directed from the molecule of water to two different bromide anions (Table 18).

An interesting aspect of the structure of compound **12** can be seen when examining its plane angles. The plane of the C2C3C30N3 chain with respect to that of the IMes five-membered ring, makes an angle of 62.2º, which indicates that these planes are relatively perpendicular. This would make sense as the steric hindrance of the mesitylene groups would be greater if the nitrile was parallel to the plane. The phenyl ring plane and the IMes ring plane are also almost completely perpendicular (81.4°). When looking at the plane of the phenyl ring with respect to the C2C3C30N4 plane, there is an angle between them of only 8.6º, which indicates the phenyl ring is almost completely parallel to the plane of the cyanide region of the structure.

As with **9**, a search of the CSD[58] was conducted to determine if there were any structures similar to **12** reported in literature. Just like with **9**, this search did not reveal any compounds that were similar enough in structure to **12** to warrant a comparison.

In continuing attempts to acquire good crystal data for compound **6a**, an unintended compound was discovered from a solvent diffusion between DCM and hexanes left at -15°C. Crystals of what was believed to be compound **6a** were determined using X-ray crystallography and found instead to be 4-((1,3-dimesityl-1H-imidazol-2(3H)-ylidene)(phenyl)methyl)-3-mesityl-7,9-dimethyl-4,5-dihydroimidazo[1,2-a]quinolin-3-ium bromide, compound **13**.

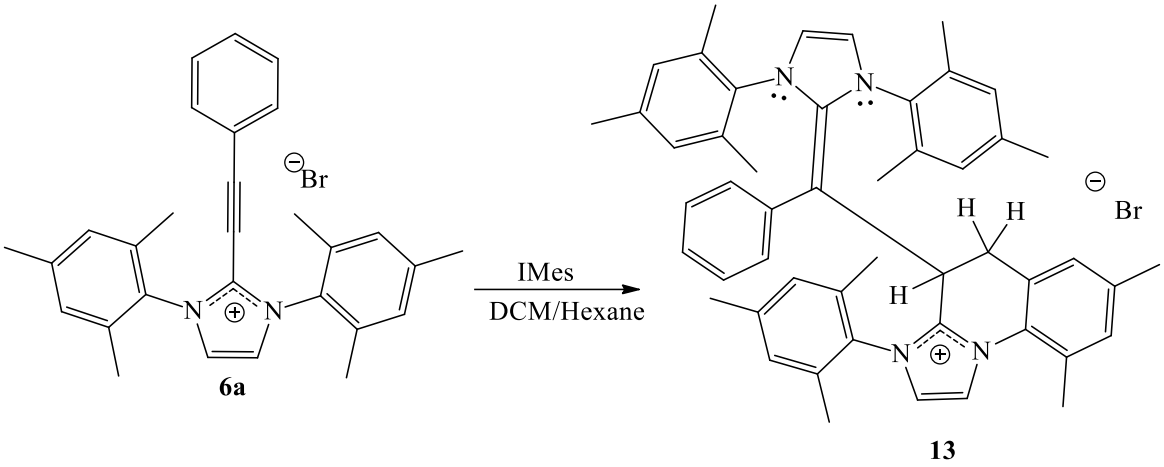

Scheme 29: Reaction conditions that led to the isolation of compound **13**. The bond between the C2 and C3 carbons has been elongated for clarity of the structure.

The formation of **13** likely results from unreacted IMes attacking the C_3 carbon of compound **6a** *in situ*. This would cause the carbenic carbon of the IMes to become electron deficient after the reaction of its electron pair and likely result in the formation of an allene intermediate across the propargyl C1C2C3 carbons. In turn, one of the methyl groups from the Mes could then perform a shift, filling the valance shell of the *i*-carbon. The C2 position of the propargyl carbocation, however, is also electron rich from the reaction at C3. Instead of reacting with the adjacent C1 carbon, the cationic carbon, it instead reacts with the methyl group that underwent the hydride shift. This results in a cyclization to form a piperidine ring, with the C1 and C2 carbons of the propargyl carbocation also included in

the ring structure (Scheme 29). What should also be noticed from the formation of **13** is that the IMes carbene forms a double bond with the C3 carbon, instead of there being one between the C2C3 carbons, as seen with previous structures. Due to this, it is impossible to determine the stereoselectivity of **13**, as the IMes is symmetrical in the cis and trans orientations.

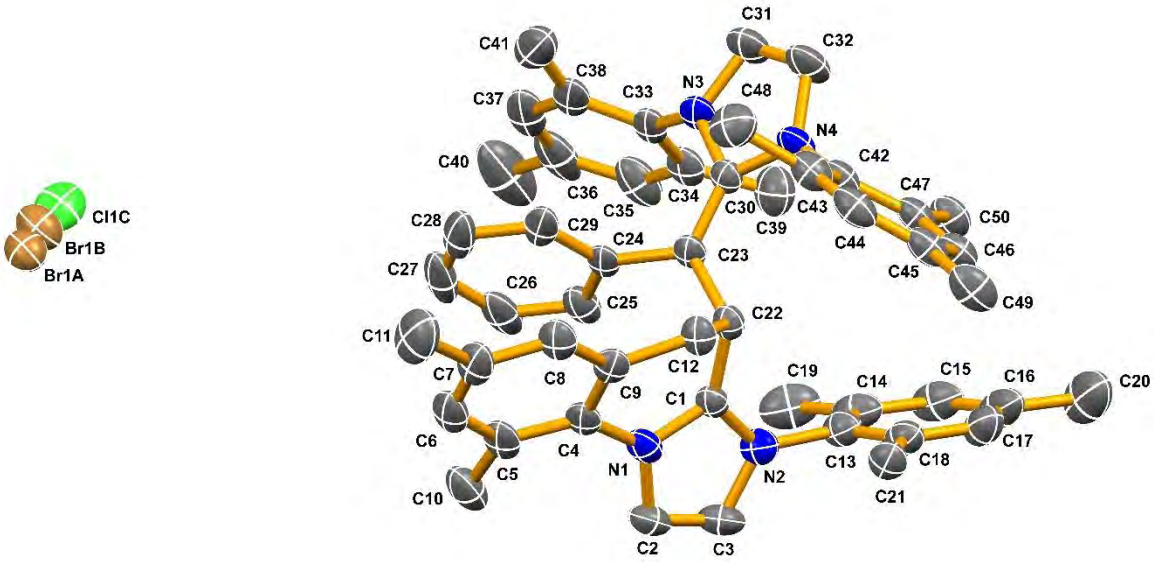

Figure 87: Solid state structure of Z)-4-((1,3-dimesityl-2,3-dihydro-1H-imidazol-2-yl) (phenyl)methylene)-3-mesityl-7,9-dimethyl-4,5-dihydroimidazo[1,2-a] quinolin-3-ium bromide, **13**. Only the non-hydrogen atoms have been labelled. Solvent was removed from the crystal structure during refinement using the Squeeze routine in the program Platon.[120] Disorder of the anions has not been removed. Thermal ellipsoids are drawn at the 50% probability level.

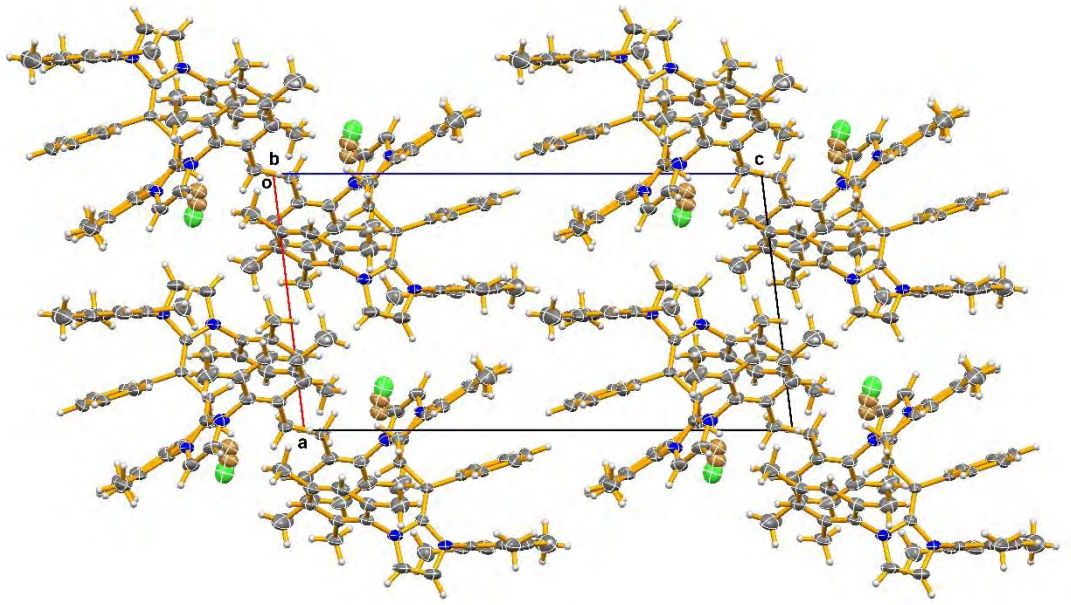

Figure 88: Solid state packing diagram of **13** viewed down the *X*-axis. Solvent was removed from the crystal structure during refinement using the Squeeze routine in the program Platon.[120] Thermal ellipsoids are drawn at the 50% probability level.

From the unit cell and the packing diagram, it is immediately apparent that there are intramolecular stacking interactions present in the structure of **13**. The stacking interactions involve three 6-membered rings; that from the center of gravity of one of the 6-membered rings (C4 to C9) of a mesityl group in the cation towards the center of gravity of the 6-membered ring (C24 to C29) of the phenyl ring is equal to 3.645(3) Å. There is also a stacking interaction from the center of gravity of the 6-membered phenyl ring towards the center of gravity of the 6-membered ring (C33 to C34) of the mesityl ring of the reacted IMes carbene which is equal to 3.519(3) Å. These interactions can be clearly seen in Figure 89.

Obtaining the crystal structure of **13** provided some challenges. It was determined that there was solvent within the crystal structure, however, the solvent could not be modelled properly. The routine Squeeze had to be implemented, using the program

Platon,[120] in order to remove the electron density of the solvent from the model of **13**. The potential solvent accessible volume in one-unit cell was calculated to be one void of 551 $Å^3$, which was 23% of the total cell volume. After 15 cycles of refinement, 153 electrons had been removed from the unit cell (153 electrons per void). No model could be found which would account for both the large number of electrons and the position of the top Fourier peaks in the final residual density map prior to SQUEEZE being applied. Additional information is needed (IR, NMR, EA) if the solvent is to be correctly identified and accounted for in the refinement model.

The anion of **13** also provided challenges for the crystallography. The anion of **13** should be bromide with 100% occupancy, however, when the occupancy of the bromine atom was refined it consistently came out to only roughly 90 %. Based totally on speculation, it seemed most reasonable that some of the bromide had been replaced with chloride generated most likely from the recrystallization solvent. A model using a mixture of both bromide and chloride (with the bromide split over two positions) gave the best statistical results. Whether the model chosen for the anion in the structure is strictly correct or not, it should have little effect on the cation, which is the portion of the structure of most interest.

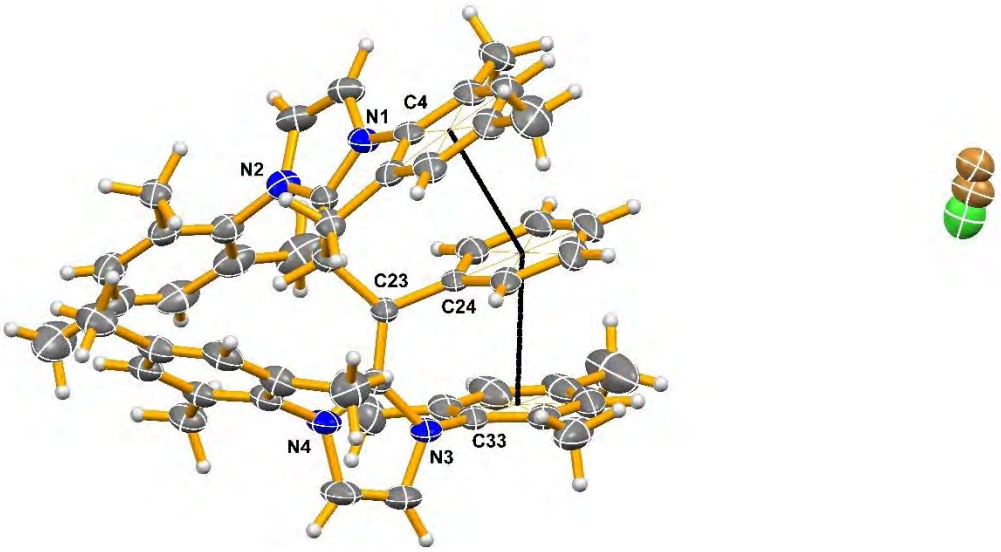

Figure 89: The close intramolecular stacking interactions observed in compound **13**. Only the non-hydrogen atoms have been labelled. Solvent was removed from the crystal structure during refinement using the Squeeze routine in the program Platon.[120] Thermal ellipsoids are drawn at the 50% probability level.

The C1C2 bond length in the cation is 1.478(6) Å, which implies that there is delocalization to a bond order greater than 1. This, as in previous structures, is different from the depicted Lewis structure of **13**, which predicts a C1C2 single bond. Unlike the previous compounds formed from the reaction of **6a**, the C2C3 bond length in **13** is 1.530(6) Å, which is representative of a single bond with no observed delocalization. As the C2C3 bond is single, this would imply that the C2 atom is sp^3 hybridized, compared to the sp^2 hybridization observed in previous structures. This sp^3 hybridization is substantiated by the ∠C1C2C3 angle of 112.6(4)°. For the piperidine ring, the angle at the site of its formation, the C2 atom (∠C1C2C12), is 103.5(4)°. This bond angle, however, is more acute than expected, which implies that there is ring strain across the 6-memebered piperidine ring, likely due to either steric hindrance or effects from the crystal packing. The torsion angle for ∠N1C1C2C3, which is 85.4(5)°, shows that the IMes group bonding to

the C3 carbon is twisted almost perpendicularly to the 5-membered ring of the cation. This helps to reduce the steric hindrance that would be present within such a bulky molecule. This also allows the phenyl and mesityl rings to align, forming the stacking interactions that were discussed earlier. When looking at the torsion for the ∠C1C2C3C30 angle, the observed value is -141.5(5)°. T This implies that the IMes carbene group is twisted to be almost 180° trans from the cation, which again, is likely to reduce the steric hindrance in the solid state. If the structure of **13** had a CC double bond between C2C3, this would be evidence against the cis isomer stereoselectivity of the propargyl carbocations. However, as the C2C3 bond is single, this arrangement is likely the conformation that has the least steric hindrance and strain on the piperidine ring. A mechanism for the formation of **13** is proposed in Scheme 30.

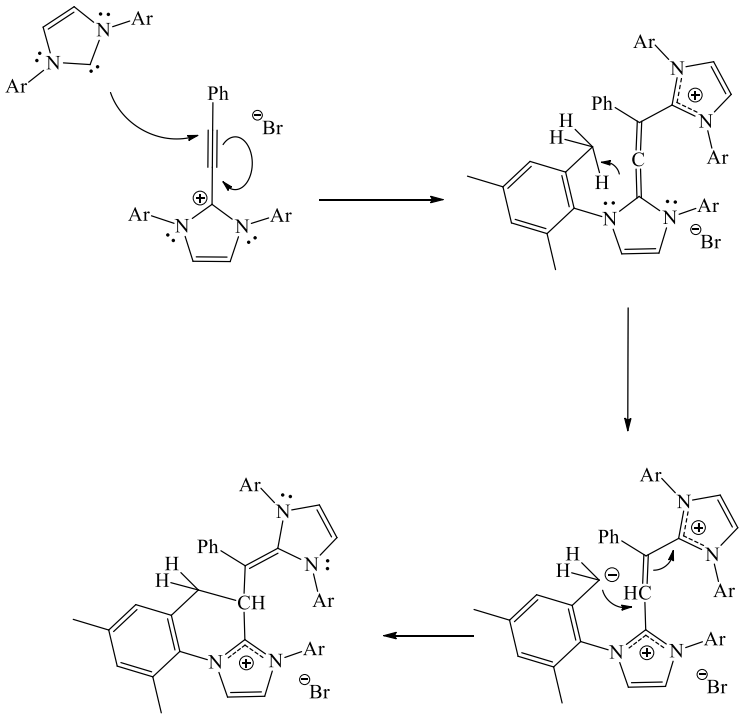

Scheme 30: Proposed mechanism for the formation of **13**, with carbon activation on the mesityl methyl group.

When comparing **13** to structures found in the literature, there is only one notable example, that of Frosch *et al*.,[128] which is shown in Figure 90. The structure of Frosch *et al*.[128] is also formed after carbon activation, where the carbenic carbon of an NHC residue reacts to form a piperidine ring with an activated methyl group of an isopropyl group on the 1,3-diisopropylbenzene substituent. The comparison between **13** and the structure of Frosch *et al*.,[128] will be focussed at the piperidine ring which is formed by the carbon activation. The bond lengths for C2C12 in **13** is 1.561(6) Å, while the bond length for C1C2 in Frosch *et al*.[128] is 1.483(2) Å. These lengths are for the bonds where the activated carbon has cyclized to form the piperidine ring. The Frosch *et al*.[128] structure has a shorter than expected single bond length, likely due to the formal positive charge on the nitrogen atom of the NHC. Unlike the structure of **13**, which has the formal charge on the C1 carbon,[47] the cation of Frosch *et al*.[128] has the charge localized on the N1 nitrogen, as the bond lengths for N1C1 and N2C1 differ, 1.346(2) Å, and 1.431(2) Å, respectively. For Frosch *et al*.[128] the ∠C1C2C3 angle is 104.57(14), while for **13** the ∠C2C12C9 angle is 111.5(4)°. This implies that the structure of Frosch *et al*.[128] is under more ring strain, compared to that in **13**. This is likely due to the ring in the structure of Frosch *et al*.[128] forming at the site of the carbene, along with the additional electronics of a cation within the ring system, both factors which are not present in **13**.

[47] It should be noted that the formal positive charge of the carbocation is more correctly depicted as delocalized across the N1C1N2 bond, but for ease of discussion, it is depicted formally on the C1 carbon.

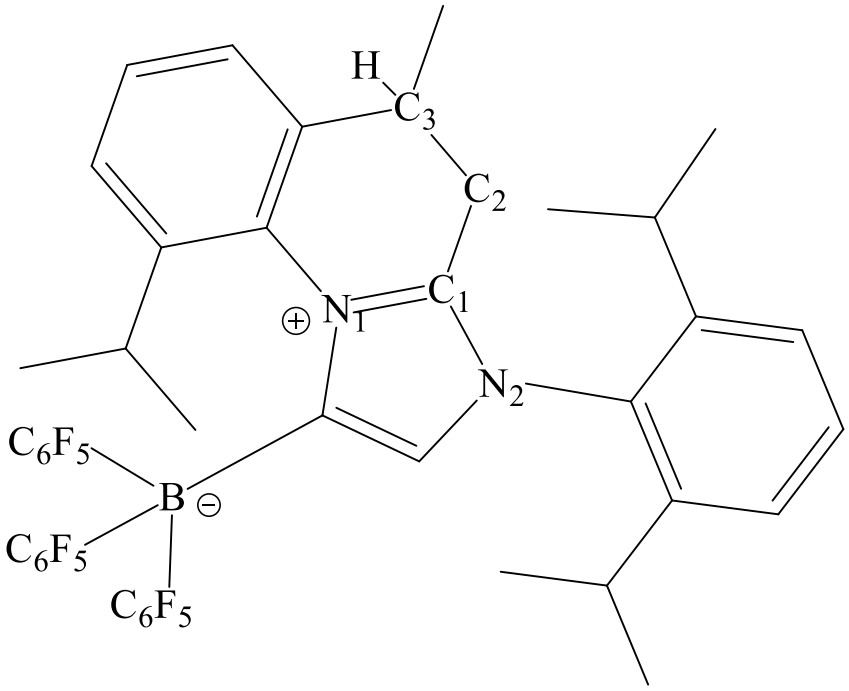

Figure 90: Structure of the carbon activated complex of Frosch *et al*.[128] Atomic labelling has been included for clarity of discussion.

From all of the reactions performed on the propargyl carbocations **5a** and **6a**, some preliminary conclusions that can be drawn as to their chemistry. The first is that the compounds are reactive enough to overcome steric hindrance. This can be seen with the structure of **8**, and especially with the structure of **13**, where large substituents are able to perform nucleophilic attacks on the C3 carbons of the propargyl cations, despite their also possessing bulky substituents. When the cations undergo nucleophilic attack, the C1C2C3 bonds are delocalized (bond order 1.5), instead of the expected C1C2 single bond and the C2C3 double bond. This shows that the first step of the nucleophilic attack is likely the formation of an allene across the C1C2C3 carbons, which would account for the delocalization of the electron density. This matches with the resonance structures proposed in Scheme 11, Chapter 4. Compound **5a** did not react with azides, despite **6a** being able to

perform this type of reaction. This is likely because **5a** could not reach the specific conformation required for the azide to react. In the products, **11a** and **11b**, the azide ring was found to be perpendicular to the plane of the 5-membered cation ring. Perhaps this was not possible in the reaction attempted with **5a**. It is unlikely that it is due to **6a** being able to perform a reaction that **5a** cannot, as they have been shown to undergo many of the same reactions, to give similar if not (respectively) identical products. The azide structure of **5a** may also have formed, but not crystallized, as only compounds that produced crystals have been discussed in this thesis. **6a** was observed to have stacking interactions across all of its derivatives, while **5a** did not. This was due to the presence of the mesityl groups in **6a**, which have the π-orbitals necessary to from stacking interactions and could help to stabilize the products formed.

Only in the structure of **10** was the carbocation disrupted and a neutral product obtained. Even the second hydrolysis product crystallized in this investigation, compound **7**, was ionic. This shows that the propargyl carbocations are able to sustain their cation under various conditions, but that is it also possible to form neutral complexes as well.

An important discovery from these reactions would be the cis-stereoselectivity observed in the reactions of **5a** and **6a**. Compounds **8**, **9**, and **12** formed cis-isomer products when undergoing nucleophilic attack. Structures **7**, **10**, and **13** did not have a double bond suitable for stereoisomers to occur. None of the spectroscopic or crystallographic data ever showed evidence of the trans isomers having been produced.

The azide structures of **11a** and **11b** are also notable, as these were concerted Huisgen cycloadditions over a non-terminal alkyne, without the use of catalysts. They also displayed another element of “click” chemistry as elevated temperatures were not used.

Additional research is needed into the work of propargyl carbocations, in order to determine precisely whether this azide cycloaddition is true "click" chemistry or not. The stereoselectivity of these reactions will have to be proven. Further azide reactions need to be performed with **5a** to try and isolate a solid product. Further reactions should also be carried out with the various products to see if propargyl carbocations could be used in other synthetic routes. Finally, computational studies should be performed on the synthesized molecules in order to determine the precise mechanisms of their production.

Table 16: Crystal Data and Structure Refinement Details of the Products from **5a** in Section 5.1

Identification code	**7**	**8**	**9**	**UC_3**
Empirical formula	$C_{13}H_{28}F_6N_3OP$	$C_{21}H_{32}F_6N_3P$	$C_{15}H_{29}Cl_2F_6N_4P$	$C_{68}H_{124}F_{30}LiN_{12}O_4P_5$
Formula weight	387.35	471.46	481.29	1905.57
Crystal system	Monoclinic	Triclinic	Orthorhombic	Orthorhombic
Space group	*$P2_1/n$*	*P-1*	*Pbca*	*Pbcn*
a (Å)	11.7060(18)	9.0247(3)	16.5508(7)	11.7592(4)
b (Å)	14.728(2)	10.6819(3)	11.2535(4)	16.3647(5)
c (Å)	11.9505(18)	14.0820(5)	24.6839(10)	46.4307(15)
α (°)	90	69.1000(10)	90	90
β (°)	118.5050(10)	72.3780(10)	90	90
γ (°)	90	75.6040(10)	90	90
Volume ($Å^3$)	1810.6(5)	1193.52(7)	4597.5(3)	8934.9(5)
Z	4	2	8	4
Density (calculated g/cm^3)	1.421	1.312	1.391	1.417
Absorption coefficient (mm^{-1})	0.216	0.174	0.408	0.216

F(000)	816	496	2000	3984
Crystal size (mm^3)	0.490 x 0.325 x 0.275	0.203 x 0.097 x 0.065	0.220 x 0.098 x 0.075	0.197 x 0.173 x 0.082
2Θ range for data collection (°)	2.004 to 28.928	2.191 to 36.318	2.058 to 36.368	2.133 to 25.350
Index ranges	$-15 \leq h \leq 15$	$-15 \leq h \leq 15$	$-27 \leq h \leq 27$	$-14 \leq h \leq 14$
	$-19 \leq k \leq 19$	$-17 \leq k \leq 17$	$-18 \leq k \leq 18$	$-19 \leq k \leq 19$
	$-15 \leq l \leq 15$	$-23 \leq l \leq 23$	$-41 \leq l \leq 41$	$-55 \leq l \leq 55$
Reflections collected	21707	59901	550573	185104
Independent reflections	4527	11560	11162	8173
R_{int}	0.0177	0.0327	0.0610	0.0352
Data/restraints/parameters	4527 / 30 / 262	11560 / 0 / 288	11162 / 16 / 355	8173 / 841 / 721
Goodness-of-fit on F^2	1.039	1.050	1.034	1.164
Final R indexes ($I > 2\sigma(I)$)	$R_1 = 0.0308$, $wR_2 = 0.0830$	$R_1 = 0.0427$, $wR_2 = 0.1081$	$R_1 = 0.0386$, $wR_2 = 0.0979$	$R_1 = 0.0770$, $wR_2 = 0.1818$
Final R indexes (all data)	$R_1 = 0.0345$, $wR_2 = 0.0860$	$R_1 = 0.0564$, $wR_2 = 0.1161$	$R_1 = 0.0586$, $wR_2 = 0.1134$	$R_1 = 0.0792$, $wR_2 = 0.1833$
Largest diff. peak and hole ($e.Å^{-3}$)	0.402/-0.295	0.490/-0.404	0.370/-0.447	1.428/--0.364

Table 17: Crystal Data and Structure Refinement Details of the Products from **6a** in Section 5.2

Identification code	**10**	**11a**	**11b**	**12**	**13**
Empirical formula	$C_{29}H_{30}N_2O$	$C_{36}H_{37}N_5$	$C_{30}H_{32}BrCl_2N_5$	$C_{31}H_{34}BrCl_2N_3O$	$C_{50}H_{53}Br_{0.75}Cl_{0.25}N_4$ +[solvent]
Formula weight	422.55	539.70	613.41	615.42	778.76
Crystal system	Triclinic	Monoclinic	Triclinic	Monoclinic	Triclinic
Space group	*P-1*	$P2_1/n$	*P*-1	$P2_1/n$	*P*-1
a (Å)	9.5936(4)	14.439(4)	7.9720(4)	9.4309(2)	10.5884(8)
b (Å)	15.5990(7)	8.759(5)	8.1458(4)	19.9956(5)	11.7673(7)
c (Å)	16.3071(7)	23.718(6)	22.9402(11)	15.9493(5	20.1129(14)
α (°)	79.255(2)	90	81.328(3)	90	80.778(2)
β (°)	82.192(2)	94.07(3)	85.875(3)	97.0370(10)	82.212(2)
γ (°)	79.838(2)	90	88.744(3)	90	83.475(2)
Volume (Å^3)	2346.55(18)	2992.1(19)	1468.76(10)	2985.01(14)	2439.9(3)
Z	4	4	2	4	2
Density (calculated g/cm^3)	1.196	1.198	1.387	1.369	1.060
Absorption coefficient (mm^{-1})	0.072	0.552	3.794	1.585	0.685
F(000)	904	1152	632	1272	823
Crystal size (mm^3)	0.250 x 0.172 x 0.116	0.135 x 0.110 x 0.062	0.094 x 0.050 x 0.024	0.220 x 0.163 x 0.068	0.198 x 0.119 x 0.023
2Θ range for data collection (°)	2.004 to 26.372	3.736 to 76.047	1.953 to 74.634	2.037 to 33.217	2.066 to 25.350

Index ranges	$-11 \leq h \leq 11$	$-18 \leq h \leq 18$	$-8 \leq h \leq 8$	$-14 \leq h \leq 14$	$-12 \leq h \leq 12$
	$-19 \leq k \leq 19$	$-10 \leq k \leq 10$	$-9 \leq k \leq 9$	$-30 \leq k \leq 30$	$-13 \leq k \leq 14$
	$-20 \leq l \leq 20$	$-29 \leq l \leq 28$	$-28 \leq l \leq 25$	$-24 \leq l \leq 24$	$-24 \leq l \leq 24$
Reflections collected	84682	43260	33789	148516	67680
Independent reflections	9585	6051	5602	11441	8930
R_{int}	0.0458	0.0770	0.1068	0.0546	0.0975
Data/restraints/parameters	9585 / 23 / 671	6051 / 1003 / 570	5602 / 76 / 409	11441 / 9 / 383	8930 / 469 / 526
Goodness-of-fit on F^2	1.040	1.067	1.036	1.019	1.059
Final R indexes ($I > 2\sigma(I)$)	$R_1 = 0.0585$, $wR_2 = 0.1477$	$R_1 = 0.0713$, $wR_2 = 0.1818$	R1 = 0.0644, wR2 = 0.1446	R1 = 0.0412, wR2 = 0.1066	R1 = 0.0879, wR2 = 0.2137
Final R indexes (all data)	$R_1 = 0.0741$, $wR_2 = 0.1576$	$R_1 = 0.0952$, $wR_2 = 0.1993$	R1 = 0.1136, wR2 = 0.1687	R1 = 0.0612, wR2 = 0.1193	R1 = 0.1255, wR2 = 0.2320
Largest diff. peak and hole ($e.Å^{-3}$)	0.952/-0.225	0.486/-0.309	0.579/-1.028	0.697/-0.661	0.570/-0.285

Table 18: Hydrogen Bonding [Å,°] in the Compounds of Chapter 5

Identification code	D(D-H)	D(H…A)	D(D…A)	<(DHA)
UC1 O(2)-H(2A)···F(11A)	0.86(2)	2.05(3)	2.874(5)	161(6)
UC1 O(2)-H(2A)···F(10B)	0.86(2)	1.91(4)	2.75(3)	167(6)
UC1 O(2)-H(2B)···F(13A)	0.87(2)	2.21(3)	3.050(14)	164(6)
UC1 O(2)-H(2B)···F(13B)	0.87(2)	1.87(3)	2.71(2)	164(6)
UC1* O(2)-H(2B)···F(14A)#	0.87(2)	2.22(3)	3.066(13)	167(6)
11b† N(5)-H(1N)···Br(1)#	0.91(6)	2.29(6)	3.173(4)	165(5)
12 O(1)-H(1O)···Br(1)	0.851(17)	2.498(19)	3.3237(15)	164(3)
12‡ O(1)-H(2O)···Br(1)#	0.800(17)	2.655(18)	3.4522(16)	174(3)

* The symmetry transformations used to generate equivalent atoms is -*x*,*y*,-*z*+1/2

† The symmetry transformations used to generate equivalent atoms is *x*,*y*-1,*z*

‡ The symmetry transformations used to generate equivalent atoms is -*x*,-*y*+1,-*z*+1

Conclusions

The work in this thesis describes the syntheses of a number of compounds, from the reaction of the PNP ligands, the bulky terphenyl compounds and the propargyl carbocations. It was shown that the PNP ligands do not react in the presence of 9-diazofluorene to form carbene complexes. Instead, there is a reaction which forms a diazene structure between the PNP ligand and 9-diazofluorene. The resulting structures have been shown to be either neutral or salts, always with two diazofluorene groups coordinated to one PNP ligand but with one or two of the fluorenes protonated, respectively. These products have the potential to be used for metal capture, as the crystal structures reveal a "bowl-like" cavity within some of the molecules, while others possess stacking of the 9-diazofluorene groups. Additionally, if a deprotonation reaction could be carried out at the H-N=N sites, then delocalization of electrons might occur across the entire structure.

The attempts to generate a bent allene form the terphenyl substituted compounds, though promising in concept, were unsuccessful. Instead the **4b** compounds were able to crystallize in five unique ways, each under separate sets of conditions. This shows two distinct things: The first is that the compound is highly unreactive across the propenium backbone, and the second is that it is able to have multiple conformations when crystallizing. It is likely that the **4b** compounds are able to reach an ideal packing arrangement regardless of the presence of solvent or anions, due to the observed twisting of the terphenyl groups. These minor changes between the terphenyl compounds must allow the cation to pack as efficiently as possible in the different structures. The overall

result is that the conformation of the cation changes very little in each of the structures studied.

The syntheses of the propargyl carbocations from halopropenium salts and carbenes were successful, and in high yields. For the propargyl carbocation generated from a halopropenium salt, **5a**, there were interesting comparisons that could be made with the work of Land.[26,35] The physical properties, such as bond lengths and angles, of the compounds were identical, which was to be expected. The crystal packing, however, was different for the compounds, as the structure of Land[26,35] (**5a-o**) only had a single cation/anion pair in the asymmetric unit, while **5a-m** had four cation/anion pairs in the asymmetric unit. It is believed that this is due to the structure of Land[26,35] taking more time to crystallize, and thus forming a more efficiently packed structure in comparison to **5a-m**. For the propargyl carbocation formed from a carbene, there was little difference between the structure of Barry *et al.,* [87] and the new cation generated in this thesis. This was to be expected as the technique used was adapted from that of Barry *et al.,* [87] with a different carbene employed. Interestingly, although the two propargyl carbocations were different in structure, they did display similar characteristics. They were both unreactive with air or water in the solid state for months at a time. There were also similar delocalization effects present in the compounds across the CCC bonds, which has been attributed to the resonance of the propargyl carbocation to the allene type structure.

From the reactions of the propargyl carbocations, a number of conclusions can be drawn. The first is that the cations undergo addition reactions at the C3 carbon, as was theorized from the activation created by the allene resonance structure. All addition reactions performed (water, cyanide, and bulky nucleophiles), attacked this C3 carbon with

no evidence of co-products being formed after attack at the C2 or C1 carbon atoms. This is also supported by the fact that the carbocation was never disrupted on the C1 carbon post reaction (with the exception of **10**). This implies that under attack from a strong nucleophile, the carbocation still persists and is not the site of attack. With the reactions that retained a C1C2 double bond in the product, it was noticed that the cis enantiomer was always the only one detected. This is important as it implies that the reactivity of the propargyl carbocation is cis-stereoselective; there was no evidence of a racemic mixture being formed in the solid-state structures or in the spectroscopic data.

The propargyl carbocation derived from an NHC was found to undergo a relatively rapid reaction with a non-organic azide, to form a triazole ring. This type of reaction is rare in the literature for a non-terminal alkyne, under mild conditions, with no heat supplied, and with no added catalyst. It is believed that the cation must be activating enough for the alkyne to undergo this reaction so readily. This reaction was only observed for the carbene derived cation, and not the halopropenium derived cation. Further study will be required to determine whether this Huisgen cycloaddition is a true “click” reaction. Mechanisms for the propargyl carbocation reaction have been proposed, however, as there is no computational or spectroscopic evidence to support them, they are purely speculative.

Future work

Although there were some important discoveries made with the compounds described in this thesis, several additional reactions or studies could be performed that would help to answer outstanding questions. This section will focus on the propargyl carbocations, as the chemistry in Chapters 2 and 3 does not have many avenues for progression. The first productive advancement for the propargyl carbocations would be to generate more of them, from either carbenes or halopropenium salts, in order to test if they can be tuned according to their degree of steric hindrance. Changing the substituents may allow for only certain reactions to proceed, while preventing others. This would help to explain why the halopropenium derived cation did not react with the inorganic azide, while the carbene derived cation did. Another thing that should be studied is the mechanisms of the performed experiments and those of any new experiments. Understanding the reaction mechanisms through computational study may help to shed light on if, or why, the propargyl carbocation is cis-stereoselective, and may also to help prove the proposed idea of allene formation through resonance. Focus should be increased even more for the azide reactions with the propargyl carbocation, as determining if this is a "click" reaction or not, would be useful. The reaction of the propargyl carbocation with a carbene should be repeated for both **5a** and **6a**. This would be important to determine whether the carbon activation that was observed for **13** is not only repeatable, but consistent for both compounds. The azide addition should be repeated for **5a** and for **8** (as there is a CC triple bond present) in order to determine if a cyclization can occur for the halopropenium derived cations.

Experimental

General Procedures

All preparations and reactions were carried out on the bench-top, under ambient conditions, unless otherwise stated. Air sensitive reagents were manipulated in an mBraun glove box, and air sensitive reactions were carried out using standard Schlenk line techniques and nitrogen gas (>99.998%) was provided by Praxair Inc. The condensers for all of the reactions that were heated to reflux were equipped with a $CaCl_2$ drying tube (or nitrogen gas, where noted). All reactions that were carried out at "room temperature" were performed under ambient conditions and the reaction temperatures were not monitored (22-28 °C). All of the yields are reported as isolated yields and not the reaction yield. If a yield is not reported, then the compound was not able to be isolated in sufficient purity to warrant a yield. All chemicals were obtained from commercial suppliers and were used as received, without further purification, unless otherwise stated. Magnesium sulfate ($MgSO_4$) and Hyflo Super Cel® (Celite) were dried/stored in a 135 °C oven prior to use. Hexane, toluene, chlorobenzene, tetrahydrofuran (THF), and dichloromethane (DCM) were purified using an mBraun MB-SPS-800 solvent purification system. Many of the compounds prepared for this thesis were purified *via* an *aqueous* workup. The general method for this workup is as follows; after the reaction mixture had cooled to room temperature, ~ 60 mL of deionized water was added to the mixture. The organic and *aqueous* phases were vigorously mixed, and the organic layer was extracted. The *aqueous* phase was washed with 2 x 30 mL portions of dichloromethane and the combined organic extracts were dried with $MgSO_4$. The volatiles were then removed *in vacuo* resulting in the crude product. The product was then further purified following the methods described in their specific sections.

Spectroscopic and Analytical Techniques

All NMR experiments were carried out at 298 K, unless stated otherwise, on a Bruker Ultrashield 300 MHz NMR spectrometer with a 7.05 Tesla magnet. The samples were prepared by dissolving a small amount of the compound into an aliquot of the deuterated solvent. All NMR solvents (D: ≥99%) were purchased from Cambridge Isotope Laboratories, Inc. The ^{1}H NMR (300 MHz) spectra were internally referenced to trace amount of non-deuterated solvent, which were referenced relative to TMS (δ = 0 ppm).[129] The deuterated solvent was used as an internal reference for ^{13}C{^{1}H} NMR (75 MHz), and referenced relative to TMS (δ = 0 ppm).[129] The ^{31}P NMR (121 MHz) chemical shifts are referenced to an external standard of 85% phosphoric acid (δ = 0 ppm). The data was processed using Bruker TOPSIN 3.6.[130]

The infrared spectra of all solid compounds were collected as neat samples using a Bruker Vertex 70 Infrared Spectrometer, at room temperature. The spectra of liquid compounds were collected by ATR on a Bruker Alpha Spectrometer. Data processing was completed using OPUS 6.0 software suite.

High-resolution mass spectrometry (HRMS) analyses were performed on a Bruker microTOF Focus Mass Spectrometer using electrospray ionization, at Dalhousie University, in Halifax. Analyses were performed using ~1 mg/mL solutions in HPLC grade acetonitrile, from Fisher Chemical.

The melting points were measured using a Mel-Temp melting point apparatus, with a heating rate of ~7 °C min^{-1} and are uncorrected. The melting point of primary standard benzoic acid (121 °C, Fisher Chemical) was found to be 121 °C, at the same heating rate.

All samples were prepared by filling a capillary tube with few milligrams of material, followed by sealing the capillary with silicon grease.

X-ray Crystallography

System 1 – Structures in Chapters 1 to 4 and Compound **7** of Chapter 5

The crystal chosen was attached to the tip of a MicroLoop with paratone-N oil. Measurements were made on a Bruker APEXII CCD equipped diffractometer (30 mA, 50 kV) using monochromated Mo Kα radiation (λ = 0.71073 Å) at 125 K.[131] The initial orientation and unit cell were indexed using a least-squares analysis of a random set of reflections collected from three series of 0.5° ω-scans, 10 to 30 seconds per frame and 12 frames per series, that were well distributed in reciprocal space. For data collection, four ω-scan frame series were collected with 0.5° wide scans, generally 30 second frames (depending on the crystal this time was sometimes increased or decreased to reach the resolution limit desired) and 366 frames per series at varying φ angles (φ = 0°, 90°, 180° and 270°). The crystal to detector distance was set to 6 cm and a complete sphere of data was collected. Cell refinement and data reduction were performed with the Bruker SAINT[132] software, which corrects for beam inhomogeneity, possible crystal decay, Lorentz and polarisation effects. A multi-scan absorption correction was applied (SADABS[133]).

System 2 – Structures in Chapter 5 and Compounds **6a** and **6b** from Chapter 4

The crystal chosen was attached to the tip of a MicroLoop with Paratone-N oil. Measurements were made on a Bruker D8 VENTURE diffractometer equipped with a PHOTON III CMOS detector using monochromated Mo Kα radiation (λ = 0.71073 Å) or Cu Kα radiation (λ = 1.54184 Å) from Incoatec micro-focus sealed tubes usually at 125 K[134]. The initial orientation and unit cell were indexed using a least-squares analysis of the reflections collected from a complete 360° phi-scan, 1 to 5 seconds per frame (depending on the data collection) and 1° per frame. For data collection, a strategy was calculated to maximize data completeness and multiplicity, in a reasonable amount of time, and then implemented using the Bruker Apex 3 software suite[134]. The crystal to detector distance was set to 4 cm. Cell refinement and data reduction were performed with the Bruker SAINT [135] software, which corrects for beam inhomogeneity, possible crystal decay, Lorentz and polarisation effects. A multi-scan absorption correction was applied (SADABS [136]).The structures were usually solved using SHELXT-2014 [137] and were refined using a full-matrix least-squares method on F^2 with SHELXL-2018.[137] The refinements were unremarkable unless otherwise noted. The non-hydrogen atoms were refined anisotropically. The hydrogen atoms bonded to carbon were included at geometrically idealized positions and were not refined. The isotropic thermal parameters of these hydrogen atoms were fixed at $1.2U_{eq}$ of the parent carbon atom or $1.5U_{eq}$ for methyl hydrogens. Any H(N) and H(O) hydrogen atoms were allowed to refine isotropically. The isotropic thermal parameters of these hydrogen atoms were either refined or fixed at $1.5U_{eq}$ of the nitrogen/oxygen atom to which they were bonded. Restraints on the O-H or N-H bond lengths were often added to keep them reasonable. Other details of individual refinements are given in the text.

Synthesis of Starting Materials

Synthesis and Spectroscopic Data for 9-Diazofluorene (starting material)

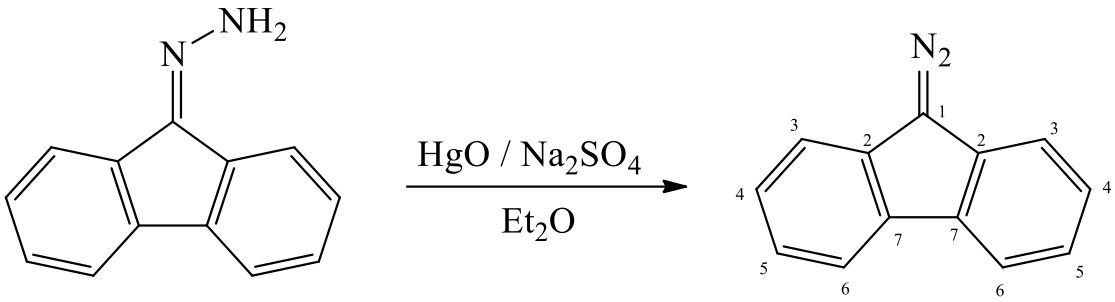

Fluorenone hydrazone (16.68 g, 85.91 mmol) was weighed and crushed in a mortar. To this, sodium sulfate (1 g, 7.04 mmol) was added, to keep the reaction dry, along with red mercury oxide (25.82 g, 119.21 mmol). The mixture was ground together for 10 minutes until it was a fine powder. The powder was transferred to a 250 mL round flask and 50 mL of diethyl ether was added. 5 mL of a weakly basic solution made from potassium hydroxide and ethanol was added dropwise. The solution was hand shaken for 5 minutes. A dark suspension formed then quickly became bright red. The solution was stirred for 1 hour. The resulting material was filtered through a fritted glass filter and washed 3x5 mL diethyl ether, which resulted in a red material. Red needle crystals were grown from both slow evaporation in dichloromethane and solvent diffusion of dichloromethane, layered with hexanes at -15°C. Mp = 86.0-88.1 °C. ^{1}H NMR (300 MHz, $CDCl_3$, ppm): δ 7.27 & 7.33 (td, 4H, $^{3}J_{HH}$ = 1.27 & 7.34 Hz, C<u>H</u> of C_4 and C_5), 7.44 (d, 2H, $^{3}J_{HH}$ = 7.31, C<u>H</u> of C_6), 7.88 (d, 2H, $^{3}J_{HH}$ = 7.31, C<u>H</u> of C_3). ^{13}C{^{1}H} NMR (75 MHz, $CDCl_3$, ppm): δ 63.47 (s, C_1),[104,105] 119.36 (s, C_5), 121.01 (s, C_4), 124.57 (s, C_3), 126.37 (s, C_6), 131.51 (s, C_7), 133.03 (s, C_2). IR (ATR, cm^{-1}): ν 3039 (w), 2084 (m), 2048 (vs), 1599 (m), 1436 (vs), 1372

(s), 1218 (s), 929 (m), 748 (vs), 718 (vs). HRMS calcd. For $[C_{13}H_8N_2]^+$: 192.07; found: 195.1.

Synthesis and Spectroscopic Data for 1,3-Dichloro-1,3-*Bis*(dimethylamino)propenium hydrogen dichloride **(**starting material)

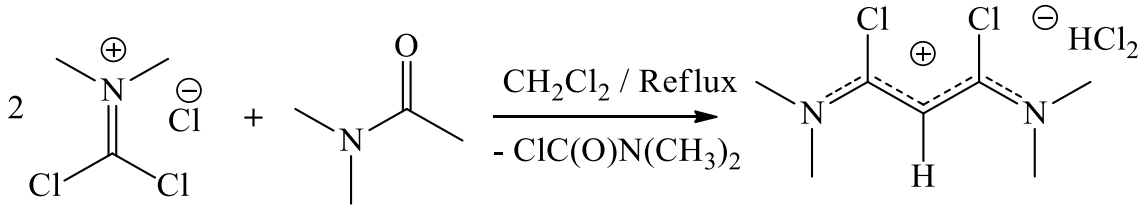

Known literature methods were used for the synthesis of 1,3-dichloromalonyl cyanine chloride.[30,31] A suspension of dichloromethylene-dimethyliminium chloride (15.02 g, 92.46 mmol) and *N,N*-dimethylacetamide (4.30 mL, 46.25 mmol) in 60 mL of dichloromethane was stirred at reflux for 4 h (or longer, if all the solids did not dissolve) protected from the atmosphere using a $CaCl_2$ drying tube. Solvent was removed *in vacuo* and the residual solids were rinsed with 5 x 30 mL portions of diethyl ether. The supernate, and the ether soluble by-product, dimethylcarbamoyl chloride, were removed by decantation, and the pale-yellow, insoluble, powder was dried under vacuum. Yield = 10.78 g (40.22 mmol, 87 %). Clear colourless crystals were grown from a 1:1 solution of dichloromethane and benzene in a -15 °C freezer overnight. Mp = 109 °C (dec), (lit.[1] = 114-116 °C). ^{1}H (300 MHz, CD_2Cl_2, ppm): δ 3.53 (s, 12H, NC<u>H</u>$_3$), 5.67 (s, 1H, C<u>H</u>), 11.01 (br s, 1H, <u>H</u>Cl_2). ^{13}C{^{1}H} (75 MHz, CD_2Cl_2, ppm): δ 44.92 (s, N<u>C</u>H$_3$), 89.83 (s, <u>C</u>H), 159.35 (s, <u>C</u>=N). IR (KBr, cm^{-1}): *v* 3693-2938 (s, br), 1562 (vs), 1430 (s), 1387 (m) 1312 (vs), 1132 (m), 1058 (w), 880 (m), 753(m), 673 (w), 573 (m). UV (CH_3CN): λ_{max} = 345

nm. EA calcd. for $C_7H_{14}Cl_4N_2$ [%]: C, 31.37; H, 5.27; N, 10.45; found [%]: C, 31.60; H, 5.24; N, 10.35. LRMS (ESI, +ve) cacld. for $[C_7H_{13}Cl_2N_2]^+$: 195.0 (100 %), 197.0 (64.0 %), 199.0 (10.4 %); found: 195.2 (100 %), 197.0 (69.1 %), 199.0 (12.6 %).

Synthesis and Spectroscopic Data 1,3-Dichloro-1,3-*Bis*(dimethylamino)propenium hexafluorophosphate (starting material)

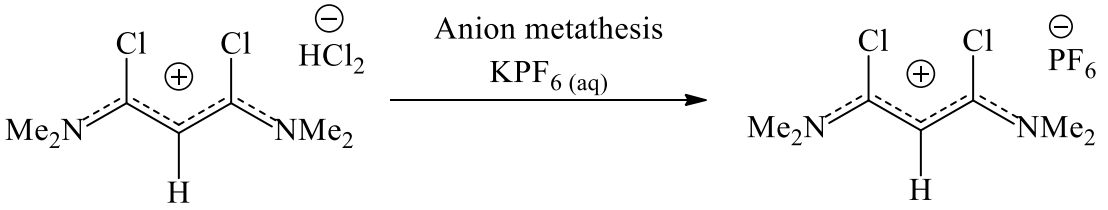

Synthesis was achieved following a modified literature method.[31, 138] Immediately following the synthesis and purification of 1,3-Dichloro-1,3-*Bis*(dimethylamino)propenium hydrogen dichloride (3.01 g, 11.23 mmol), the yellow powder was added to a saturated solution of potassium hexafluorophosphate in 200 mL of ice-cold water. The mixture was briefly stirred by hand resulting in the formation of a light-coloured precipitate, which was collected by filtration. On small scale syntheses (≤ 2 g), the material was washed with 3 x 5 mL portions of diethyl ether and dried *in vacuo*, without requiring further purifications. For larger scale syntheses, the material was dissolved in 50 mL of dichloromethane, and the *aqueous wash method* was employed. The organic phase was dried with $MgSO_4$, followed by filtration, and the volatiles of the filtrate were removed *in vacuo* giving a fine, pale-yellow powder. Yield = 3.44 g (10.116 mmol, 90 %). Clear and colourless thin rectangular plate crystals were grown by dissolving 60 mg of material in 3 mL chloroform, followed by layering with 1 mL benzene and storing in a -15 °C freezer for 48 h. Mp = 111-112 °C (lit.[31] = 140 °C). ^{1}H (300 MHz, $CDCl_3$, ppm): δ 3.47 (s, 12H,

NC$\underline{H}_3$), 5.51 (s, 1H, C$\underline{H}$). $^{13}C\{^1H\}$ (75 MHz, $CDCl_3$, ppm): δ 44.22 (s, N$\underline{C}H_3$), 89.43 (s, C$\underline{H}$), 159.08 (s, $\underline{C}$=N). ^{31}P NMR (121 Hz, $CDCl_3$, ppm): -144.47 (sept, $^1J_{PF}$ = 713.19 Hz, $\underline{P}F_6$). IR (KBr, cm^{-1}): *v* 2947 (w), 2886 (w), 1565 (vs), 1432 (s), 1388 (m) 1309 (vs), 1226 (m), 1136 (s), 1060 (m), 837 (vs), 736 (m), 556 (s). HRMS (ESI, +ve) calcd. for $[C_7H_{13}Cl_2N_2]^+$: 195.0451; found: 195.0444.

Synthesis and Spectroscopic Data for Compound **1a**

(Compound **2a** was obtained as a minor co-product in the synthesis of **1a** and is visible in its ^1H NMR and ^{13}C NMR spectra. (The two compounds could not be separated from each other and there is no characterization data other than the X-ray crystal structure available for **2a**.)

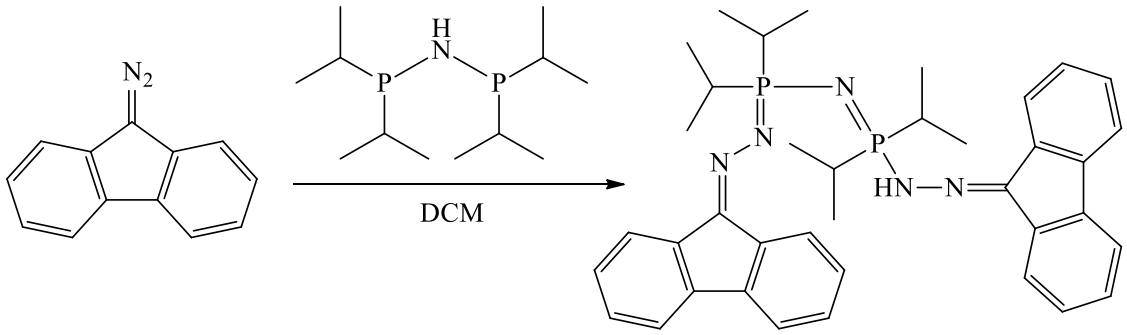

In a glovebox, *bis*(diisopropylphosphino)amine (0.12 g, 0.48 mmol) was weighed out and added to 9-diazoflorene (0.24 g, 1.25 mmol). The sample was dissolved in dichloromethane and stirred overnight. The sample was dried *in vacuo*, before crystals were grown from solvent diffusion with dichloromethane layered with hexanes at -15°C. Mp = 140°C (colour changed from yellow to orange at 125°C). ^1H NMR (300 MHz, CD_2Cl_2, ppm): δ 1.40 (m, 21H, C$\underline{H}_3$ of iPr groups), 2.52-2.83 (br s, 4H, C$\underline{H}$ of iPr), 6.5-8.37 (m, 37H, aromatic peaks of 9-diazofluorene). $^{13}C\{^1H\}$ NMR (75 MHz, CD_2Cl_2, ppm): The

sample was only weakly soluble and a sample with sufficient concentration for ^{13}C NMR was not obtained. ^{13}C NMR will have to be acquired at a later date. ^{31}P NMR (121 Hz, $CDCl_3$, ppm): 50.84 (s, N<u>P</u>N). IR (ATR, cm^{-1}): 3383 (w), 3309 (w), 3195 (w), 3051 (w), 2928 (w), 2052 (w), 1607 (w), 1574 (m), 1445 (m), 1185, (m), 777 (m), 726 (vs). HRMS calcd. for $[C_{38}H_{45}N_5P_2]^+$: 633.32; found: 634.3225.

Synthesis and Spectroscopic Data for Compound **1b**

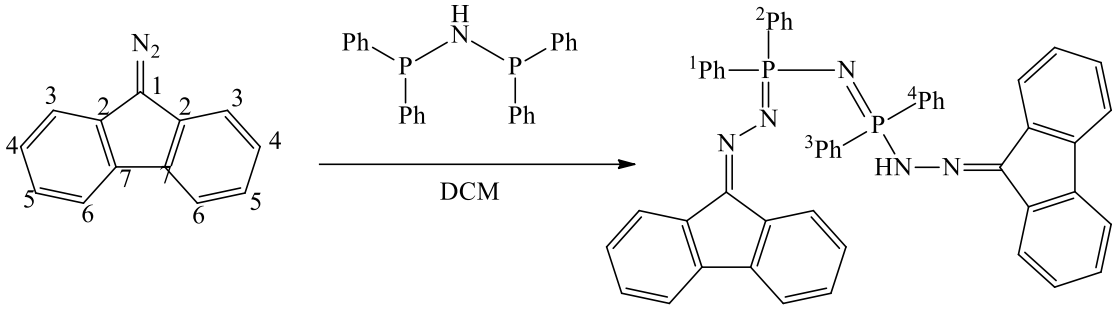

In a glovebox, *bis*(diphenylphosphino)amine (0.16 g, 0.41 mmol) was weighed out and added to 9-diazoflorene (0.22 g, 1.14 mmol). The sample was dissolved in dichloromethane and stirred overnight. The sample was dried *in vacuo*, before crystals were grown from solvent diffusion with dichloromethane layered with hexanes at -15°C. Mp = 168-170°C colour changed from yellow to orange. ^1H NMR (300 MHz, CD_2Cl_2, ppm): δ 6.73 (t, 2H, $^3J_{HH}$ = 7.63 Hz, *p*-C<u>H</u> of ^{1}Ph & ^{2}Ph), 6.96 (t, 2H, $^3J_{HH}$ = 7.51, *p*-C<u>H</u> of ^{3}Ph & ^{4}Ph), 7.14 (t, 4H, $^3J_{HH}$ = 7.29 Hz, *o*-C<u>H</u> of ^{1}Ph & ^{2}Ph, overlapping with signal at 7.17), 7.17 (t, 2H, $^3J_{HH}$ = 7.62 Hz, *o*-C<u>H</u> of ^{4}Ph, overlapping with signal at 7.17), 7.43 (t, 8H, $^3J_{HH}$ = 6.51 Hz, C<u>H</u> of C_4 and C_5), 7.51 (t, 4H, $^3J_{HH}$ = 7.36 Hz, *m*-C<u>H</u> of ^{1}Ph & ^{2}Ph, overlapping with signal at 7.53), 7.53 (t, 4H, $^3J_{HH}$ = 7.17 Hz, *m*-C<u>H</u> of ^{3}Ph & ^{4}Ph, overlapping with signal at 7.51), 8.04 & 8.08 (2d, 8H, $^3J_{HH}$ = 7.20 Hz, C<u>H</u> of C_3 and C_6, overlapping doublets), 8.19 (d, 2H,

$^{3}J_{HH}$ = 7.67 Hz, *o*-C<u>H</u> of ^{3}Ph). $^{13}C\{^{1}H\}$ NMR (75 MHz, CD_2Cl_2, ppm): δ 59.8 (s, *i*-<u>C</u> of fluorene),[104,105] 119.56 (s), 119.73 (s), 126.53 (s), 127.23 (s), 127.79 (s), 127.80 (s), 127.81 (s), 128.65 (s), 128.74 (s), 128.83 (s), 130.73 (s), 132.07 (s), 132.32 (s), 132.37 (s), 132.65 (s), 132.71 (s), 132.78 (s), 134.01 (s), 134.06 (s), 138.42 (s), 138.78 (s), 140.30 (s), 148.27 (s), 148.67 (s). ^{31}P NMR (121 Hz, CD_2Cl_2, ppm): 21.73 (s, N<u>P</u>N). IR (ATR, cm^{-1}): 3053 (w), 2083 (w), 2054 (s), 1527 (m), 1436 (s), 1225 (m), 1167 (m), 1154 (s), 1094 (s), 971 (m), 722 (vs), 688 (vs), 525 (s), 503 (s). HRMS calcd. for $[C_{50}H_{37}N_5P_2]^+$: 769.25; found: 770.2581.

Synthesis and Spectroscopic Data for Compound **2b**

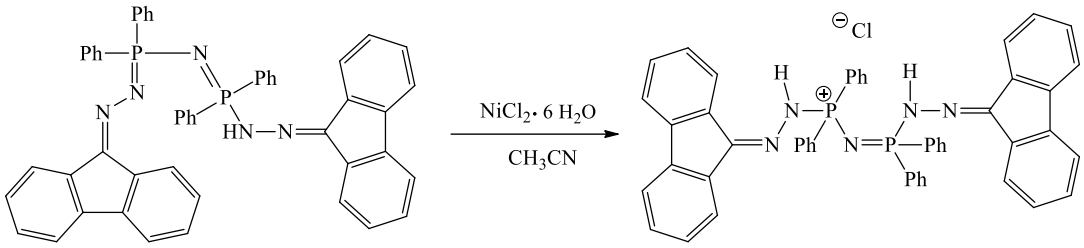

Sample **4b** (.0232 g, 0.03 mmol) was weighed out and dissolved in acetonitrile. To this, an excess of nickel (II) chloride hexahydrate (0.016, 0.067 mmol) was added. The sample was stirred overnight. The sample was decanted to remove unreacted nickel salt, and the blue solution was left to slowly evaporate at 8°C for 24 h. The solution became a yellow colour and two different types of crystals grew; dark red crystals (attributed to 9-diazoflourene) along with larger colourless crystals used for further analyses. Mp = 225°C (colour change from yellow to orange at 200°C). ^{1}H NMR (300 MHz, CD_2Cl_2, ppm): δ 7.09-7.19 (4d, 4H, $^{3}J_{HH}$ = 7.62 Hz, 6.15 Hz, 6.79 Hz, 7.62 Hz, C_3<u>H</u> & C_6<u>H</u> of single fluorene, four overlapping doublets that each integrate to 1H), 7.27-7.59 (m, 22H, 20H of

Ph groups, 2H of fluorene overlapping), 8.07-8.14 (2t, 8H, $^{3}J_{HH}$ = 5.60 Hz, 7.67 Hz, $C_4\underline{H}$ & $C_5\underline{H}$ of both fluorene, two triplets overlapping that each integrate to 4H), 8.50 (d, 2H, $^{3}J_{HH}$ = 7.67 Hz, $C_4\underline{H}$ & C_5H of single fluorene), 11.35 & 11.38 (s, 2H, NH, two overlapping singlets each integrating to 1H). $^{13}C\{^{1}H\}$ NMR (75 MHz, CD_2Cl_2, ppm): δ 59.88 (s, *i*-$\underline{C}$ of fluorene), 119.41 (s), 119.56 (s), 121.19 (s), 127.44 (s), 127.74 (s), 127.80 (s), 127.91 (s), 128.24 (s), 128.41 (s), 128.60 (s), 129.50 (s), 129.60 (s), 130.63 (s), 132.67 (s), 132.81 (s), 137.43 (s), 139.59 (s), 141.65 (s), 150.79 (s), 151.07 (s). ^{31}P NMR (121 Hz, CD_2Cl_2, ppm): 24.54 (s, N$\underline{P}$N). IR (ATR, cm^{-1}): 3040 (w), 2951 (m), 2922 (m), 2852 (m), 1617 (w), 1590 (w), 1453 (m), 1439 (m), 1370 (s), 1232 (vs), 1116 (s), 1026 (s), 776 (vs), 724 (vs), 690 (vs), 529 (s), 504 (s).

Synthesis and Spectroscopic Data for Compound **3**

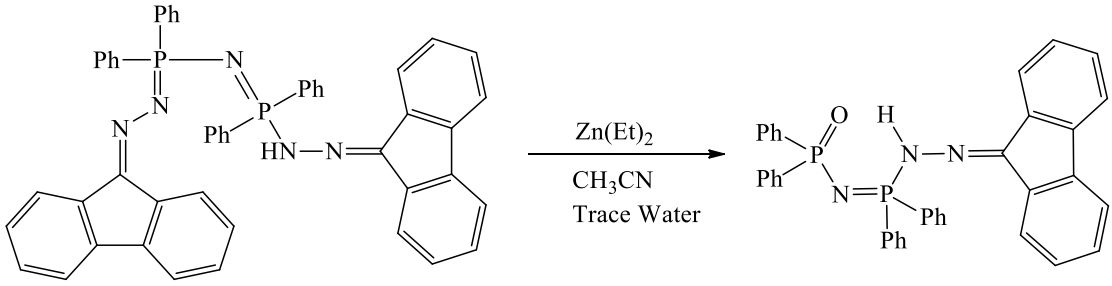

Sample **4b** (0.02 g, 0.03 mmol) was weighed out and dissolved in acetonitrile. To this, an excess (3-4 drops) of diethyl zinc was added and it was stirred overnight. A white precipitate formed in the solution, so the solvent layer was decanted to remove the powder (zinc oxide). The solvent layer was slowly evaporated which produced clear yellow thin-plate crystals. ^{1}H NMR (300 MHz, CD_2Cl_2, ppm): δ 7.18-8.48 (m, 28H, aromatic protons of 9-diazofluorene and phenyl groups), 9.76 (d, 1H, N$\underline{H}$---O, presence of the doublet is likely due to splitting from the hydrogen bonding). $^{13}C\{^{1}H\}$ NMR (75 MHz, $CDCl_3$, ppm):

δ 119.51 (s), 120.27 (s), 120.39 (s), 121.02 (s), 124.00 (s), 127.69 (s), 127.82 (s), 128.25 (s), 128.43 (s), 129.08 (s), 129.66 (s), 130.23 (s), 130.27 (s), 130.45 (s), 130.87 (s), 131.01 (s), 132.27 (s), 132.41 (s), 132.46 (s), 134.70 (s). ^{31}P NMR (121 Hz, CD_2Cl_2, ppm): 22.13 (s, N<u>P</u>N), 20.09 (<u>P</u>O). IR (ATR, cm^{-1}): 3056 (w), 2922 (w), 2851 (w), 1673 (w), 1618 (w), 1590 (w), 1436 (m), 1370 (s), 1234 (vs), 1171118 (s), 724 (vs), 690 (vs), 538 (s), 504 (s). HRMS calcd. For $[C_{37}H_{29}N_3P_2O]^+$: 593.18; found: 594.1872

Synthesis and Spectroscopic Data for Compound **4a**

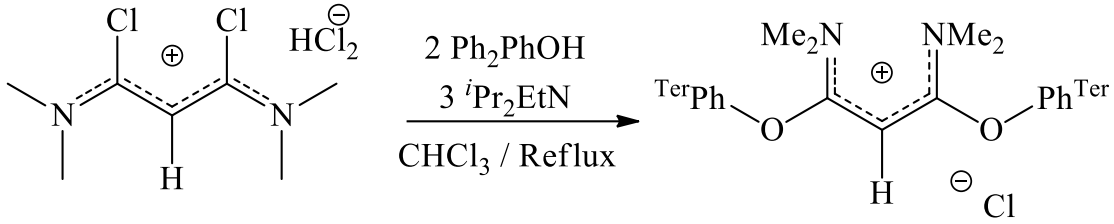

2,6-Diphenylphenol (7.39 g, 30 mmol) and *N,N*-diisopropylethylamine (8 mL, 45.93 mmol) were added to a solution of 1,3-Dichloro-1,3-*Bis*(dimethylamino)propenium hydrogen dichloride (4 g, 14.92 mmol) in 20 mL of chloroform and the mixture was heated at reflux for 18 h, under a $CaCl_2$ drying tube. After cooling to room temperature, the *aqueous* workup method was employed. The resulting waxy orange material was washed with 3x15 mL portions of diethyl ether and was dried *in vacuo*. The resulting light-pink powder was washed with 20 mL of THF forming a suspension with very fine, white solids. The solids were collected on a sintered glass Hirsch funnel and were washed with 2 x 5 mL portions of THF, and 2 x 5 mL portions of diethyl ether, and dried *in vacuo*. Yield = 6.77 g (10.4 mmol, 77 %). Clear and colourless cubic crystals were grown by dissolving 55 mg of the crude material in 5 mL of chloroform, followed by slow evaporation overnight. Mp:

turned blue-green at 248 °C then melted at 257-258 °C. ^{1}H NMR (300 MHz, CD_3CN, ppm): δ 0.61-2.07 (very br s, 6H, NC<u>H</u>$_3$), 2.07-3.48 (very br s, 6H, NC<u>H</u>$_3$), 2.53 (s, 1H, C<u>H</u>), 6.98 & 7.07 (br s, 8H, *o*-C<u>H</u> of *o*-Ph), 7.24 (br s, 6H, *p*-C<u>H</u> & *m*-C<u>H</u> of *o*-Ph), 7.43 (d, 4H, $^{3}J_{HH}$ = 7.7 Hz, *m*-C<u>H</u>), 7.52 (br s, 6H, *p*-C<u>H</u> & *m*-C<u>H</u> of *o*-Ph), 7.65 (t, 2H, $^{3}J_{HH}$ = 7.7 Hz, *p*-C<u>H</u>). ^{1}H NMR (300 MHz, CD_3CN, **353 K**, ppm): δ 2.21 (br s, 12H, NC<u>H</u>$_3$), 2.72 (s, 1H, C<u>H</u>), 7.04-7.12 (m, 8H, *o*-C<u>H</u> of *o*-Ph), 7.40 (br s, 12H, *p*-C<u>H</u> & *m*-C<u>H</u> of *o*-Ph), 7.45 (d, 4H, $^{3}J_{HH}$ = 7.6 Hz, *m*-C<u>H</u>), 7.68 (t, 2H, $^{3}J_{HH}$ = 7.6 Hz, *p*-C<u>H</u>). ^{13}C{^{1}H} NMR (75 MHz, CD_3CN, ppm): δ 39.58 (very br s, N<u>C</u>H$_3$), 64.81 (s, <u>C</u>H), 129.05 (s, *p*-<u>C</u>H), 129.24 (s, *p*-<u>C</u>H of *o*-Ph), 129.64 (s, *m*-<u>C</u>H of *o*-Ph), 130.14 (*o*-<u>C</u>H of *o*-Ph), 131.29 & 132.40 (two s, *m*-<u>C</u>H), 135.51, 136.37, 136.54 & 137.09 (four s, *o*-<u>C</u>Ph and *ipso*-<u>C</u> of Ph), 146.05 (s, *ipso*-<u>C</u>), 168.19 (<u>C</u>=N). IR (KBr, cm^{-1}): *v* 3646 (m), 3269 (m), 3183 (m), 3055 (m), 1970 (w), 1894 (w), 1830 (w), 1759 (w), 1619 (s), 1582 (vs), 1509 (vs), 1455 (s), 1415 (s), 1400 (s), 1344 (s), 1226 (vs), 1179 (vs), 1156 (s), 1032 (m), 921 (m), 848 (m), 810 (m), 761 (s) 702 (vs), 612 (m), 583 (m), 525 (m). HRMS (ESI, +ve) calcd. for $[C_{43}H_{39}N_2O_2]^+$: 615.3012; found: 615.2987.

Synthesis and Spectroscopic Data for Compound **4b**

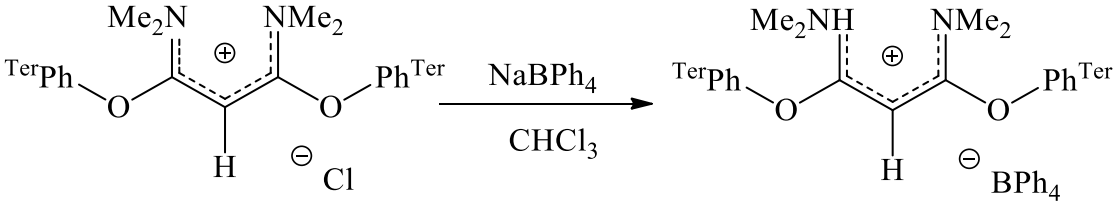

1,3-*Bis*(dimethylamino)-1,3-*bis*(2,6-diphenylphenolato)propenium chloride (0.13877 g, 0.1485 mmol) was dissolved in 10 mL of chloroform. To this, 82.45 mg of $NaBPh_4$ (0.241 mmol, 1.7 eq) was added and the mixture was stirred for 1 hour. The solution was

gravity filtered, and the unwanted precipitate was washed 3 x 5 mL with chloroform. The solution was left to slowly evaporate for 3 days, which resulted in the formation of clear colourless block crystals. Yield = 0.05297 g (0.0567 mmol, 75 %). ^{1}H NMR (300 MHz, $CDCl_3$, ppm): δ 0.61-2.07 (very br s, 6H, NC$\underline{H}_3$), 2.07-3.48 (very br s, 6H, NC$\underline{H}_3$), 2.53 (s, 1H, C$\underline{H}$), 6.71 (t, 4H, $^{3}J_{HH}$ = 7.17 Hz, *p*-C$\underline{H}$ of BPh_4), 6.85 (t, 8H, $^{3}J_{HH}$ = 7.2 Hz, *m*-C$\underline{H}$ of BPh_4), 6.97 & 7.03 (br s, 8H, *o*-C$\underline{H}$ of *o*-Ph), 7.21 (br s, 6H, *p*-C$\underline{H}$ & *m*-C$\underline{H}$ of *o*-Ph), 7.24-7.3 (very br s, 8H, *o*- C$\underline{H}$ of BPh_4), 7.49 (d, 4H, $^{3}J_{HH}$ = 7.7 Hz, *m*-C$\underline{H}$), 7.49 (br s, 6H, *p*-C$\underline{H}$ & *m*-C$\underline{H}$ of *o*-Ph), 7.63 (t, 2H, $^{3}J_{HH}$ = 7.7 Hz, *p*-C$\underline{H}$). ^{13}C{^{1}H} NMR (75 MHz, CD_3CN, ppm): δ 39.58 (very br s, N$\underline{C}H_3$), 64.81 (s, $\underline{C}$H), 121.66 (s, *p*-$\underline{C}$H of BPh_4), 125.47(q, $^{3}J_{BC}$ = 2.7 Hz, *m*-$\underline{C}$H of BPh_4), 125.83 (s, N$\underline{C}$≡C), 136.21 (m, *o*-CH of BPh_4), 129.05 (s, *p*-$\underline{C}$H), 129.24 (s, *p*-$\underline{C}$H of *o*-Ph), 129.64 (s, *m*-$\underline{C}$H of *o*-Ph), 130.14 (*o*-$\underline{C}$H of *o*-Ph), 131.29 & 132.40 (two s, *m*-$\underline{C}$H), 135.51, 136.37, 136.54 & 137.09 (four s, *o*-$\underline{C}$Ph and *ipso*-$\underline{C}$ of Ph), 146.05 (s, *ipso*-$\underline{C}$), 164.19 (q, $^{1}J_{BC}$ = 48.8 Hz, *i*-$\underline{C}$ of BPh_4), 168.19 ($\underline{C}$=N). ^{11}B NMR (96 Hz, $CDCl_3$, ppm): -6.7 (s, $\underline{B}Ph_4$). IR (KBr, cm^{-1}): *v* 3646 (m), 3269 (m), 3183 (m), 3055 (m), 1970 (w), 1894 (w), 1830 (w), 1759 (w), 1619 (s), 1582 (vs), 1509 (vs), 1455 (s), 1415 (s), 1400 (s), 1344 (s), 1226 (vs), 1179 (vs), 1156 (s), 1032 (m), 921 (m), 848 (m), 810 (m), 728 (s), 702 (vs), 612 (m), 583 (m), 525 (m).

It is important to note for **4b** that a variety of products were formed from the crude material. Each trial involved different reaction conditions in an attempt to form a bent allene from **4b**, however, none were successful. Each of these trials is described in Chapter 3, along with the different conformations of **4b** that were formed. The new products were only studied by X-ray crystallography as they were all identical to **4b,** with the differences between the structures only appreciable by this technique

Synthesis and Spectroscopic Data for Compound **5a**

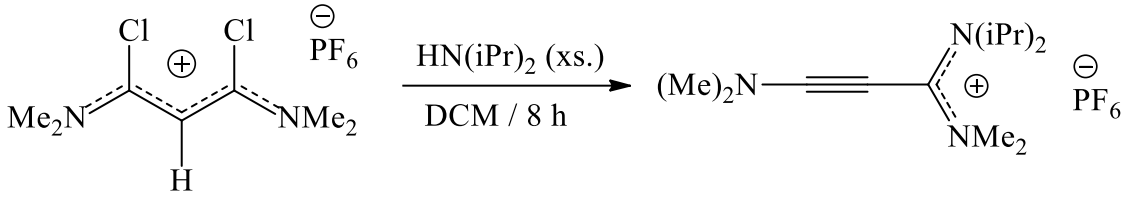

Diisopropylamine (2.2 g, 21.9 mmol) was added to a solution of 1,3-Dichloro-1,3-*Bis*(dimethylamino)propenium hexafluorophosphate (1.862 g, 5.476 mmol) in 30 mL dichloromethane. The resulting mixture was stirred at room temperature overnight. The *aqueous wash method* was employed, resulting in the isolation of a viscous orange oil. The oil was dried *in vacuo* for 4-5 h which resulted in a bright orange solid. Yield = 1.98 g (5.3665 mmol, 98%). Yellowish quartz-like crystals were grown by dissolving the crude material in 3 mL dichlorormethane, layering with 5 mL hexane, and storing at -15°C for 24 h. Mp = 116.7-118°C. ^{1}H NMR (300 MHz, $CDCl_3$, ppm): δ 1.407 (d, 12H, $^{3}J_{HH}$ = 6.8 Hz, C$\underline{H}_3$ of *i*Pr), 3.11 & 3.14 (two s, 12H, NC$\underline{H}_3$), 3.88 (sept, 2H, $^{3}J_{HH}$ = 6.8Hz, C$\underline{H}$ of *i*Pr). ^{13}C{^{1}H} NMR (75 MHz, $CDCl_3$, ppm): δ 21.95 (s, $\underline{C}H_3$ of *i*Pr), 42.56 & 43.03 (two s, N$\underline{C}H_3$), 51.90 (s, $\underline{C}$H of *i*Pr), 67.17 (s, C$\underline{C}$C), 126.20 (s, N$\underline{C}$≡C), 154.88 (s, N$\underline{C}$N). ^{31}P NMR (121 Hz, $CDCl_3$, ppm): -144.46 (sept, $^{1}J_{PF}$ = 713.19 Hz, $\underline{P}F_6$). IR (ATR, cm^{-1}): *v* 2979 (w), 2943 (w), 2178 (vs), 1567 (m), 1533 (s), 1396 (m), 1377 (m), 1330 (s), 1136 (m), 1082 (m), 829 (vs), 554 (s). HRMS calcd. for $[C_{13}H_{26}N_3]^+$: 224.2121; found: 224.2131.

Synthesis and Spectroscopic Data for Compound **5b**

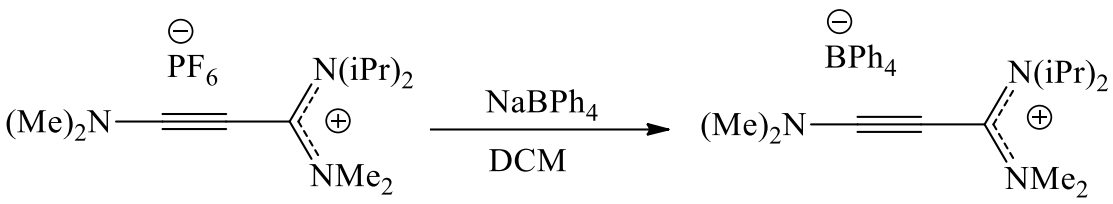

A sample of **5a** (0.97 g, 2.63 mmol) was added to a vial and dissolved in 5 mL of dichloromethane. To this, a small excess of sodium tetraphenyl borate was added and the reactants were mixed as a suspension overnight. The resulting solution was filtered through Celite and allowed to crystallize by slow evaporation. Yield = 1.16 g (2.13 mmol, 81.3%). Colourless cubic crystals were grown from the solution. Mp = 118.4-121.2 °C. ^{1}H NMR (300 MHz, $CDCl_3$, ppm): δ 1.261 (d, 12H, $^{3}J_{HH}$ = 6.8 Hz, C$\underline{H}_3$ of *i*Pr), 2.54 & 2.74 (two s, 12H, NC$\underline{H}_3$), 3.60 (sept, 2H, $^{3}J_{HH}$ = 6.8Hz, C$\underline{H}$ of *i*Pr), 6.88 (t, 4H, $^{3}J_{HH}$ = 7.2 Hz, *p*-C$\underline{H}$, of BPh_4), 7.02 (t, 8H, $^{3}J_{HH}$ = 7.2 Hz, *m*-C$\underline{H}$ of BPh_4), 7.41 (s, 8H, *o*-C$\underline{H}$, of BPh_4). $^{13}C\{^{1}H\}$ NMR (75 MHz, $CDCl_3$, ppm): δ 21.85 (s, C$\underline{H}_3$ of *i*Pr), 42.28 & 42.64 (two s, NC$\underline{H}_3$), 51.72 (s, C$\underline{H}$ of *i*Pr), 66.88 (s, C$\underline{C}$C), 121.66 (s, *p*-C$\underline{H}$ of BPh_4), 125.47(q, $^{3}J_{BC}$ = 2.7 Hz, *m*-C$\underline{H}$ of BPh_4), 125.83 (s, N$\underline{C}$≡C), 136.21 (m, *o*-CH of BPh_4), 154.12 (s, N$\underline{C}$N), 164.19 (q, $^{1}J_{BC}$ = 48.8 Hz, *i*-$\underline{C}$ of BPh_4). ^{11}B NMR (96 Hz, $CDCl_3$, ppm): -6.7 (s, $\underline{B}Ph_4$). IR (ATR, cm^{-1}): ν 3054 (w), 3039 (w)2999 (w), 2934 (w), 2170 (vs), 1567 (m), 1531 (s), 1389 (m), 1370 (m), 1317 (s), 1131 (m), 1077 (m), 833 (w), 730 (s), 700 (s).

Synthesis and Spectroscopic Data for Compound **6a**

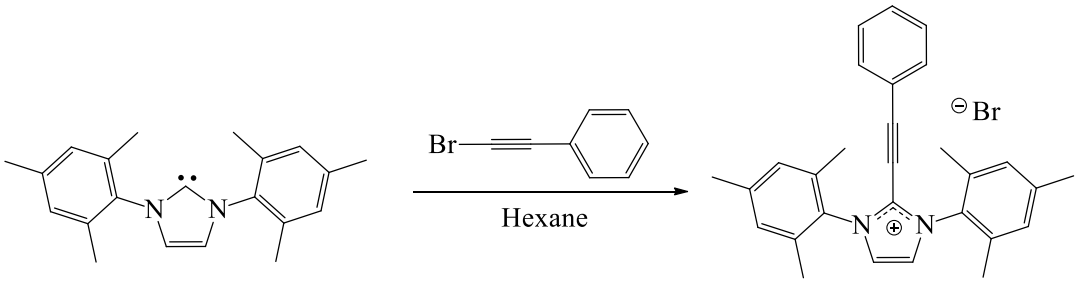

1,3-Dimesitylimidazol-2-ylidene (0.3 g, 0.98 mmol) was suspended in 5 mL hexanes. To this suspension, an excess (6 drops) of (bromoethynyl)benzene was added. The sample immediately turned bright pink from a yellow colour. The sample was stirred overnight to ensure complete reaction. The pink precipitate was filtered through a fritted glass filter and washed with 5 x 5 mL of hexanes. The sample was dried *in vacuo* for 4 h. Yield = 0.368 g (0.985 mmol, 77 %). Clear colourless plate crystals were grown by acetonitrile slow evaporation. Mp = 205 °C (turns black at 175 °C). ^{1}H NMR (300 MHz, $CDCl_3$, ppm): δ 2.16 (s, 12H, *o*-C$\underline{H}_3$ of Mes), 2.41 (s, 6H, *p*-C$\underline{H}_3$ of Mes), 7.04 (d, 2H, $^{3}J_{HH}$ = 7.47 Hz, NC$\underline{H}$C$\underline{H}$N), 7.10 (s, 4H, *m*-C$\underline{H}$ of Mes), 7.31 (d, 2H, $^{3}J_{HH}$ = 7.89 Hz, *o*-C$\underline{H}$ of Ph), 7.42-7.47 (m, 3H, *m*&*p*-C$\underline{H}$ of Ph). ^{13}C{^{1}H} NMR (75 MHz, $CDCl_3$, ppm): δ 17.61 (s, *o*-$\underline{C}H_3$ of Mes), 21.38 (s, *p*-$\underline{C}H_3$ of Mes), 69.7 (s, C$\underline{C}$Ph), 105.82 (s, $\underline{C}$CPh), 117.83 (s, N$\underline{C}$H$\underline{C}$HN), 127.63 (s, *i*-C of Ph), 128.45 (s, *o*-$\underline{C}$H of Ph), 129.00 (s, *i*-$\underline{C}$N of Mes), 130.09 (s, *o*-$\underline{C}CH_3$ of Mes), 130.37 (s, *p*-$\underline{C}$H of Ph), 132.09 (s, *m*-$\underline{C}$H of Ph), 132.47 (s, *p*-$\underline{C}CH_3$ of Mes), 134.39 (s, *m*-$\underline{C}$H of Mes), 141.94 (s, NCN). IR (ATR, cm^{-1}): 2976 (m), 2952 (m), 2916 (m), 2212 (m), 1673 (w), 1605 (m), 1553 (s), 1485 (vs), 1440 (s), 1378 (s), 1241 (s), 854 (s), 757 (s), 690 (s), 566 (s). HRMS calcd. For $[C_{29}H_{29}N_2]^+$: 405.23; found: 405.2338.

Synthesis and Spectroscopic Data for Compound **6b**

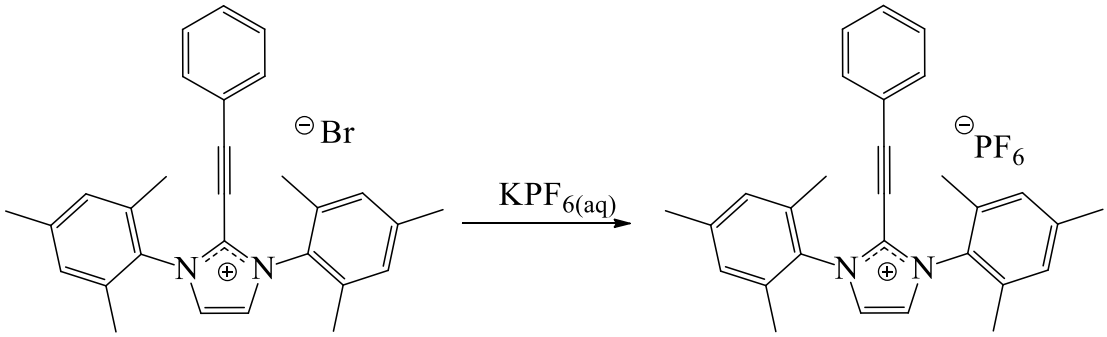

A sample of compound **6a** (0.15 g, 0.31 mmol) was dissolved in 5 mL dichloromethane. To this, an equal amount of a saturated aqueous potassium hexafluorophosphate solution was added. The sample was vigorously shaken for 10 minutes, using a separatory funnel and a method similar to that used for an extraction. Once finished, the organic layer was separated from the aqueous layer, and the aqueous layer was washed with more dichloromethane. The organic layers were combined and then dried *in vacuo*. The resulting solid material was redissolved in 5 mL dichloromethane and left to slowly evaporate. Colourless crystals were grown. ^{1}H NMR (300 MHz, $CDCl_3$, ppm): δ 2.16 (s, 12H, *o*-C$\underline{H}_3$ of Mes), 2.41 (s, 6H, *p*-C$\underline{H}_3$ of Mes), 7.04 (d, 3H, $^{3}J_{HH}$ = 7.47 Hz, NC$\underline{H}$C$\underline{H}$N, likely small overlapping peak present), 7.11 (s, 4H, *m*-C$\underline{H}$ of Mes), 7.29-7.78 (m, 3H, peaks likely from the phenyl ring but not able to be specifically attributed). ^{13}C{^{1}H} NMR (75 MHz, $CDCl_3$, ppm): δ 18.01 (s, *o*-$\underline{C}H_3$ of Mes), 20.99 (s, *p*-$\underline{C}H_3$ of Mes), 124.75 (s, *i*-C of Ph), 125.75 (s, *o*-$\underline{C}$H of Ph), 128.30 (s, *i*-$\underline{C}$N of Mes), 128.40 (s, *o*-$\underline{C}CH_3$ of Mes), 129.83 (s, *p*-$\underline{C}$H of Ph), 129.98 (s, *m*-$\underline{C}$H of Ph), 133.96 (s, *p*-$\underline{C}CH_3$ of Mes), 139.78 (s, *m*-$\underline{C}$H of Mes), 141.21 (s, NCN). Peaks for C$\underline{C}$Ph, $\underline{C}$CPh, and N$\underline{C}$H$\underline{C}$HN are not observed in the spectrum or are overlapping with other peaks. ^{31}P NMR (121 Hz, $CDCl_3$, ppm): -144.51 (sept, $^{1}J_{PF}$ = 713.19 Hz, $\underline{P}F_6$). IR (ATR, cm^{-1}): 3164 (w), 2925 (w), 2252 (w, possible bromoethynylbenzene

contamination), 2219 (m), 1608 (w), 1558 (m), 1488 (m), 1444 (m), 1382 (w), 1236 (m), 832 (vs), 760 (s), 690 (m), 556 (vs).

Synthesis and Spectroscopic Data for Compound **7**

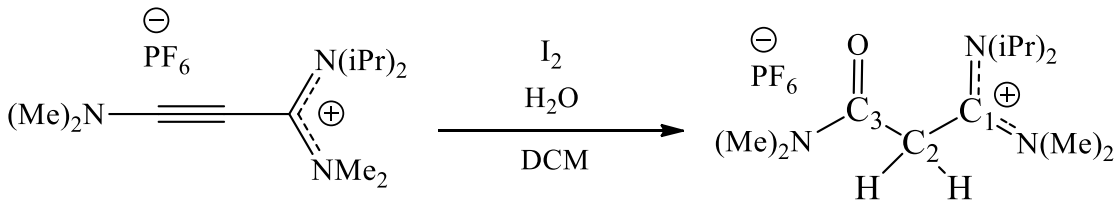

A sample of **5a** (112.63 mg, 0.3 mmol) was weighed out and dissolved in dichloromethane. To this, a solution of iodine (86.46 mg, 0.34) dissolved in dichloromethane was added dropwise. The resulting solution was allowed to stir overnight, before it was dried *in vacuo*. Colourless needle crystals were grown from solvent diffusion of dichloromethane layered with hexane at -15°C. Mp = 160°C. ^{1}H NMR (300 MHz, $CDCl_3$, ppm): δ 1.42 (d, 12H, $^{3}J_{HH}$ = 6.8 Hz, C$\underline{H}_3$ of *i*Pr), 2.97 & 3.11 (two s, 6H, OCNC$\underline{H}_3$), 3.19 (s, 6H, $^{+}$CNC$\underline{H}_3$), 3.95 (sept, 2H, $^{3}J_{HH}$ = 6.8Hz, C$\underline{H}$ of *i*Pr), 4.02 (s, 2H, OCC$\underline{H}_2$C^{+}). ^{13}C{^{1}H} NMR (75 MHz, $CDCl_3$, ppm): δ 22.37 (s, $\underline{C}H_3$ of *i*Pr), 35.54 (s, N$\underline{C}H_3$ of C_2), 37.44 (s, OCN$\underline{C}H_3$ of C_1), 38.68 (s, OC$\underline{C}H_2$) 43.48 (s, $^{+}$CN$\underline{C}H_3$), 53.44 (s, $\underline{C}$H of *i*Pr), 165.53 (s, N$\underline{C}$N), 174.37 (s, N$\underline{C}$OC). IR (ATR, cm^{-1}): *v* 2979 (w), 2951 (w), 1652 (m), 1604 (m), 1497 (w), 1427 (w), 1129 (m), 827 (vs), 555 (s). HRMS calcd. for $[C_{13}H_{28}N_3O]^{+}$: 242.22; found: 242.2221.

Synthesis and Spectroscopic Data for Compound **8**

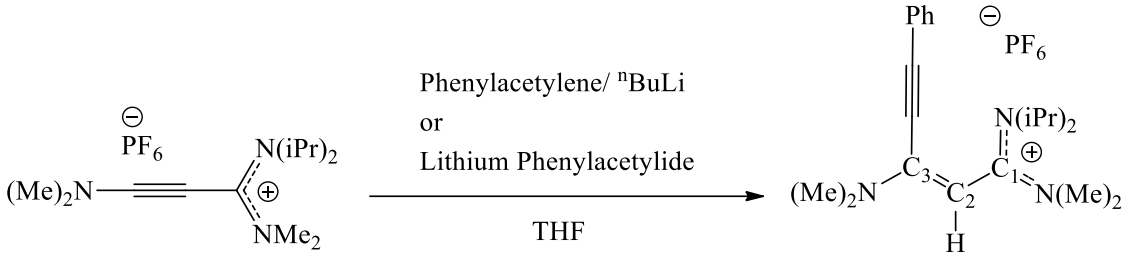

A sample of **5a** (0.1 g, 0.27 mmol) was weighed out and dissolved in tetrahydrofuran. To this, an excess (4-5 drops) of phenylacetylene was added, along with a catalytic amount of 2.5 M n-butyl lithium in hexanes. The addition of the n-butyl lithium resulted in the appearance of a purple colour which immediately dissipated. The solution was stirred overnight which resulted in a green/brown oily liquid. About 10 mL of hexanes were added which immediately precipitated a brown/orange material. The solid material was dried *in vacuo*. Pale yellow rectangular prism crystals were grown from slow evaporation in acetonitrile. Mp = 145°C, ^{1}H NMR (300 MHz, CD_3CN, ppm): δ 1.34 (d, 12H, $^{3}J_{HH}$ = 6.8 Hz, C<u>H</u>$_3$ of *i*Pr), 3.08 & 3.22 (two s, 6H, NC<u>H</u>$_3$), 3.82 (sept, 2H, $^{3}J_{HH}$ = 6.8Hz, C<u>H</u> of *i*Pr), 4.94 (s, 1H, CC<u>H</u>C), 7.42-7.61 (m, 5H, CC<u>Ph</u>). ^{13}C{^{1}H} NMR (75 MHz, CD_3CN, ppm): δ 22.93 (s, <u>C</u>H$_3$ of *i*Pr), 41.63 & 41.66 (two s, N<u>C</u>H$_3$), 43.56 (s, <u>C</u>H of *i*Pr), 82.21 (s, C<u>C</u>CPh), 91.54 (s, CC<u>C</u>Ph), 99.90 (s, NC<u>C</u>C$^+$), 121.20 (s, *i*-<u>C</u> of Ph), 129.99 (s, *m*-<u>C</u>H of Ph), 131.64 (s, *p*-<u>C</u>H of Ph), 132.97 (s, *o*-<u>C</u>H of Ph), 147.23 (s, N<u>C</u>CC$^+$), 170.13 (s, N<u>C</u>N). IR (ATR, cm^{-1}): 2971 (w), 2934 (w), 2216 (w), 1539 (m), 1506 (m), 1443 (m), 1405 (m), 1300 (m), 831 (vs), 759 (m), 555 (s). HRMS calcd. For $[C_{21}H_{32}N_3PF_6]^+$: 326.26; found: 326.2593.

Synthesis and Spectroscopic Data for Compound **9**

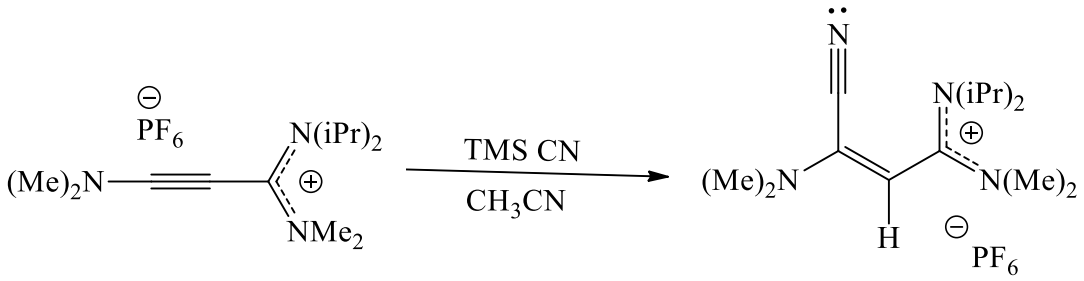

A sample of **5a** (0.1 g, 0.27 mmol) was dissolved in 5 mL acetonitrile. To this solution, a small excess (3 drops) of trimethylsilyl cyanide was added. The sample was allowed to stir overnight. The solution showed no visible precipitate, so it was slowly evaporated, then washed with 3 x 5mL of hexanes. A smaller sample of the crude product was dissolved in dichloromethane, layered with hexanes, and left at -15°C, which yielded pale yellow rectangular prism crystals. Yield = 0.06 g (0.15 mmol, 55.91%). Mp = 133.6-136.7 °C. ^{1}H NMR (300 MHz, $CDCl_3$, ppm): δ 1.388 (d, 12H, $^{3}J_{HH}$ = 6.8 Hz, C$\underline{H}_3$ of *i*Pr), 3.17 & 3.24 (two s, 12H, NC$\underline{H}_3$), 3.86 (sept, 2H, $^{3}J_{HH}$ = 6.8Hz, C$\underline{H}$ of *i*Pr). ^{13}C{^{1}H} NMR (75 MHz, $CDCl_3$, ppm): δ 22.53 (s, $\underline{C}H_3$ of *i*Pr), 41.54 (s, $^{+}$CN$\underline{C}H_3$), 43.76 (s, N$\underline{C}H_3$), 53.01 (s, $\underline{C}$H of *i*Pr), 96.08 (s, C$\underline{C}$HC^{+}), 112.24 (s, C$\underline{C}$≡N), 135.39 (s, $\underline{C}$C≡N), 167.83 (s, N$\underline{C}$N). IR (ATR, cm^{-1}): 2977 (w), 2940 (w), 2239 (w), 1581 (m), 1547 (m), 1514 (m), 1402 (m), 1365 (m), 1309 (m), 1246 (m), 1129 (m), 1031 (m), 829 (vs), 772 (m), 555 (s). HRMS calcd. For $[C_{14}H_{27}N_4]^{+}$: 251.22; found: 251.2228.

Synthesis and Spectroscopic Data for Compound **11a**

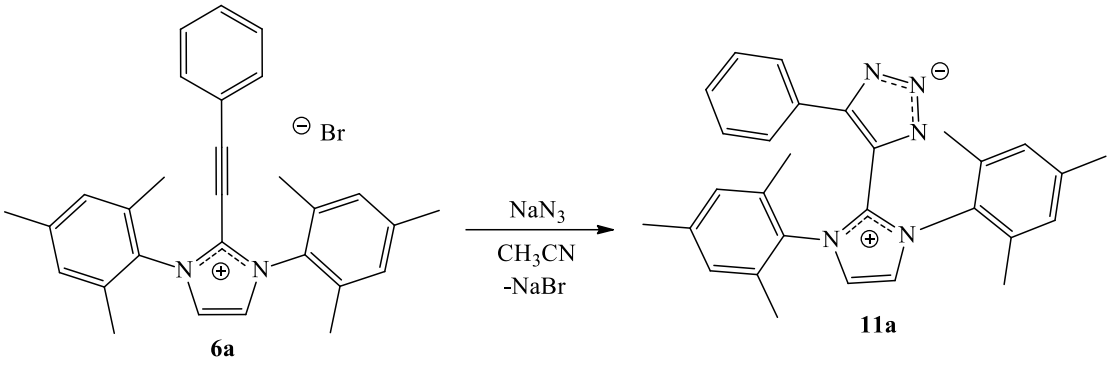

6a **11a**

A small sample of compound **6a** (0.05 g, 0.103 mmol) was dissolved in 5 mL acetonitrile. To this, an excess of sodium azide (0.02 g, 0.31 mmol) was added. This was left to stir, and after a few minutes, the colour changed from red to orange. The sample was stirred overnight, then filtered through Celite and left to slowly evaporate. Colourless rectangular prism crystals grew from the evaporating solution. Yield = 0.025 g (0.056 mmol, 54.34%). Mp = The sample did not melt; over the range of 186-253°C, the sample decomposed with no residue. ^{1}H NMR (300 MHz, CD_2Cl_2, ppm): δ 1.97 (s, 12H, *o*-C<u>H</u>$_3$ of Mes), 2.27 (s, 6H, *p*-C<u>H</u>$_3$ of Mes), 6.84 (d, 2H, $^{3}J_{HH}$ = 7.47 Hz, NC<u>H</u>C<u>H</u>N), 6.86 (s, 4H, *m*-C<u>H</u> of Mes), 7.08-7.13 (m, 5H, C<u>H</u> of Ph). ^{13}C{^{1}H} NMR (75 MHz, CD_3CN, ppm): δ 17.41 (s, *o*-<u>C</u>H$_3$ of Mes), 20.02 (s, *p*-<u>C</u>H$_3$ of Mes), 124.54 (s, N<u>C</u>H<u>C</u>HN), 126.26 (s, *i*-C of Ph), 127.90 (s, *i*-<u>C</u>N of Mes), 128.63 (s, *m*-<u>C</u>H of Ph), 128.77 (s, *o*-<u>C</u>H of Ph), 129.42 (s, C<u>C</u>CPh), 130.15 (s, *m*-<u>C</u>H of Mes), 132.56 (s, *o*-<u>C</u>CH$_3$ of Mes), 134.91 (s, *p*-<u>C</u>CH$_3$ of Mes), 135.68 (s, *p*-<u>C</u>H of Ph), 141.21 (s, NCN), 147.86 (s, CC<u>C</u>Ph). IR (ATR, cm^{-1}): 3152 (w), 3023 (w), 2954 (m), 2918 (m), 2858 (w), 1608 (m), 1573 (s) 1553 (w), 1487 (vs), 1445 (s), 1379 (m), 1228 (s), 850 (s), 768 (vs), 731 (s), 695 (vs), 466 (s). HRMS calcd. For $[C_{29}H_{29}N_5]^+$: 447.24; found: 448.2488.

Synthesis and Spectroscopic Data for Compound **11b**

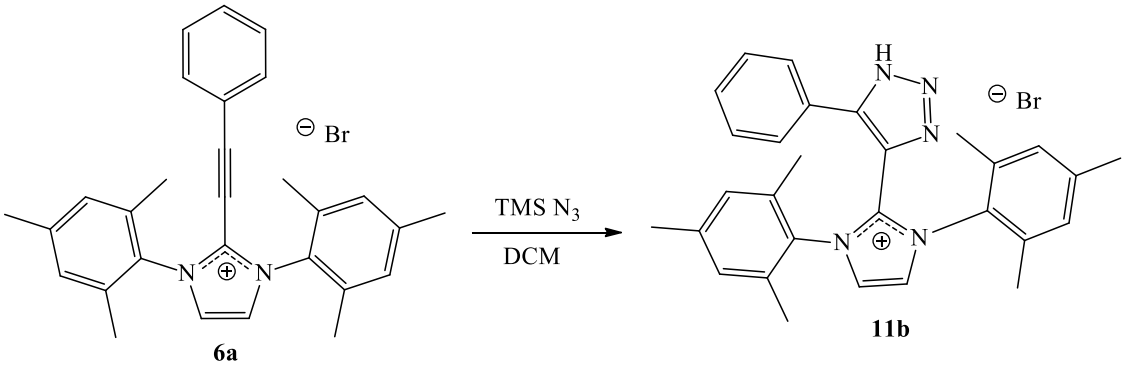

A sample of **6a** (0.05 g, 0.103 mmol) was dissolved into 5 mL DCM. An excess of azidotrimethylsilane (0.02 g, 0.174 mmol) was added to the sample. The resulting solution was left to stir, and after a few minutes, the colour changed from red to orange. The sample was stirred overnight; then it was filtered through Celite and left to slowly evaporate. Clear colourless triangular plate crystals grew from the evaporating solution. ^{1}H NMR (300 MHz, CD_2Cl_2, ppm): δ 1.91 (s, 12H, *o*-C<u>H</u>$_3$ of Mes), 2.24 (s, 6H, *p*-C<u>H</u>$_3$ of Mes), 6.76 (s, 4H, *m*-C<u>H</u> of Mes), 6.88 (d, 2H, $^{3}J_{HH}$ = 7.43, *o*-Ph), 7.18 (t, 2H, $^{3}J_{HH}$ = 7.60, *m*-Ph), 7.31 (t, 1H, $^{3}J_{HH}$ = 7.60, *p*-Ph), 7.85 (s, 2H, NC<u>H</u>C<u>H</u>N), 10.30 (s, NNN<u>H</u>). ^{13}C{^{1}H} NMR (75 MHz, CD_3CN, ppm): δ 17.41 (s, *o*-<u>C</u>H$_3$ of Mes), 20.02 (s, *p*-<u>C</u>H$_3$ of Mes), 124.54 (s, N<u>C</u>H<u>C</u>HN), 126.26 (s, *i*-C of Ph), 127.90 (s, *i*-<u>C</u>N of Mes), 128.63 (s, *m*-<u>C</u>H of Ph), 128.77 (s, *o*-<u>C</u>H of Ph), 129.42 (s, C<u>C</u>CPh), 130.15 (s, *m*-<u>C</u>H of Mes), 132.56 (s, *o*-<u>C</u>CH$_3$ of Mes), 134.91 (s, *p*-<u>C</u>CH$_3$ of Mes), 135.68 (s, *p*-<u>C</u>H of Ph), 141.21 (s, NCN), 147.86 (s, CC<u>C</u>Ph). IR (ATR, cm^{-1}): 3150 (m), 3007 (m), 2952 (m), 2656 (s), 2629 (s), 2589 (s), 1608 (s), 1556 (m), 1489 (vs), 1448 (s), 1379 (s), 1238 (vs), 993 (vs), 854 (vs), 772 (vs), 737 (vs), 694 (vs), 548 (s), 463 (m).

Synthesis and Spectroscopic Data for Compound **12**

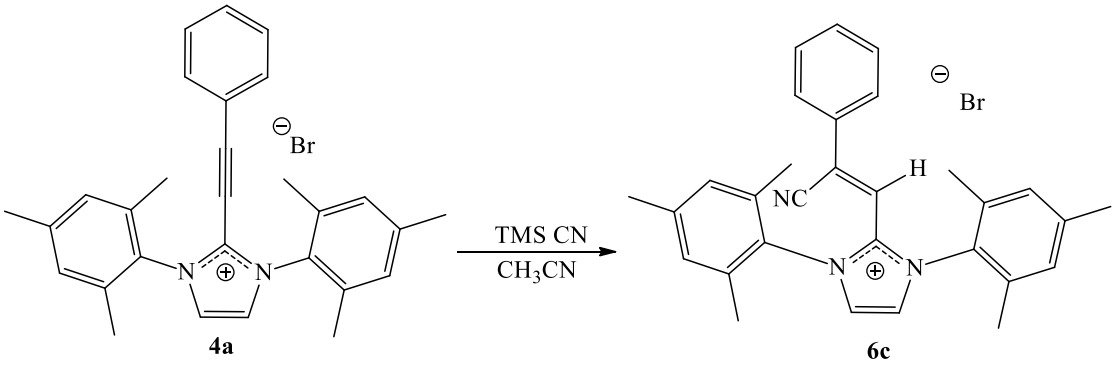

4a **6c**

Compound **6a** (0.11 g, 0.226 mmol) was dissolved in 5 mL acetonitrile. To this, an excess of azidotrimethylsilane (0.034 mL, 0.243 mmol) was added. The sample was left to stir overnight. It was then filtered through Celite and left to slowly evaporate. The oil which resulted was washed with 3 x 5 mL of pentane. It was dissolved in DCM, layered with pentane and placed at -15°C. No crystals grew, but the sample did slowly evaporate over the course of 4 months. This produced an oil which yielded a single crystal which was used for X-ray analysis. As only a single crystal grew over the course of months, additional spectroscopy, in the form of ^{1}H NMR, ^{13}C NMR, and IR, could not be performed. Attempts were made to repeat the experiment and grow additional crystals, but they were unsuccessful. The solids from the unsuccessful crystallization attempts were washed and purified to try and generate a sample which would provide clean spectroscopic data, however, this too was unsuccessful. Due to time restrictions, only the crystal structure of **12** is reported here.

A number of unexpected products came from reactions that were carried out to generate better samples of compound **6a**. The structures of **10** and **13** were determined from crystals that came from these unintended but significant reactions. Just like the **UC** compounds, they are not included in this experimental. Only single crystals of **10** and **13** were grown, and thus, like **12**, additional spectroscopic data could not be collected.

References

[1] Stang, P. J. *In Carbocation chemistry*; Olah, G. A., Prakash, G. K. S., Eds.; Wiley: New York, **2004**; pp 1–6.
[2] Jencks, W. *Acc. Chem. Res.* **1980**, *13*, 161-169.
[3] Norris, J. *J. Am. Chem. Soc.* **1901**, *25*, 117-122.
[4] Kehrmann, F.; Wentzel, F. *Ber. Dtsch. Chem. Ges.* **1901**, *34*, 3815-3819.
[5] Gomberg, M. *Ber. Dtsch. Chem. Ges.* **1900**, *33*, 3150-3163.
[6] Wagner, G. *J. Russ. Phys. Chem. Soc.* ***1899****, 31, 690.*
[7] Meerwein, H. *Liebigs Annalen.* **1914**, *405*, 129-175.
[8] Corey, E.; Casanova, J. *J. Am. Chem. Soc.* **1963**, *85*, 165-169.
[9] Corey, E.; Casanova, J.; Vatakencherry, P.; Winter, R. *J. Am. Chem. Soc.* **1963**, *85*, 169-173.
[10] Roberts, J.; Mazur, R. *J. Am. Chem. Soc.* **1951**, *73*, 2509-2520.
[11] Gleicher, G.; von R. Schleyer, P. *J. Am. Chem. Soc.* **1967**, *89*, 582-593.
[12] Schleyer, P. *J. Am. Chem. Soc.* **1964**, *86*, 1856-1857.
[13] Sustmann, R.; Williams, J.; Dewar, M.; Allen, L.; Schleyer, P. *J. Am. Chem. Soc.* **1969**, *91*, 5350-5357.
[14] Olah, G. *J. Am. Chem. Soc.* **1965**, *87*, 1103-1108.
[15] Olah, G.; Tolgyesi, W.; Kuhn, S.; Moffatt, M.; Bastien, I.; Baker, E. *J. Am. Chem. Soc.* **1963**, *85*, 1328-1334.
[16] Saunders, M.; Telkowski, L.; Kates, M. *J. Am. Chem. Soc.* **1977**, *99*, 8070-8071.
[17] McMurry, J.; Lectka, T.; Hodge, C. *J. Am. Chem. Soc.* **1989**, *111*, 8867-8872.
[18] Reich, H. 8-TECH-5 The Saunders Equilibrium Isotope Perturbation Experiment https://www.chem.wisc.edu/areas/reich/nmr/08-tech-05-saunders.htm (accessed Nov 8, 2018).
[19] Balzer, H.; Berger, S. *J. Phys. Org. Chem.* **1997**, *10*, 187-189.
[20] Olah, G. *J. Am. Chem. Soc.* **1972**, *94*, 808-820.
[21] Winstein, S.; Trifan, D. *J. Am. Chem. Soc.* **1949**, *71*, 2953-2953.
[22] Olah, G.; Prakash, G.; Saunders, M. *Acc. Chem. Res.* **1983**, *16*, 440-448.
[23] Viehe, H. G.; Janousek, Z. *Angew. Chem. Int. Ed.* **1973**, *12*, 806–818.
[24] Janousek, Z.; Viehe, H. G.; Viehe, H. G. Chemistry of Dichloromethyleniminium Salts (Phosgeniminium Salts). In *Iminium Salts in Organic Chemistry Part 1. Advances in Organic Chemistry*; Bohm, H., Viehe, H. G., Eds.; John Wiley & Sons: New York, **1976**; Vol. 9, pp 343–419.
[25] Viehe, H. G. *Chem. Ind.* **1977**, 386–395.
[26] Land, M. A Reinvestigation of the Reactivity of the 1,3-Dihalo- 1,3-*bis*(dimethylamino)propenium Salts with EH Bonds (E = N, P, O, S), MSc, Saint Mary's University, Halifax, NS, **2018**.
[27] Yarovenko, N. N.; Vasil'eva, A. S. *Zh. Obs. Khim.* **1959**, *29*, 3786–3787.
[28] Vilkas, M.; Qasmi, D. *Synth. Commun.* **1990**, *20*, 2769–2773.
[29] Gauthier, P.; Senet, J. P. Process for Synthesis of Phosgene-Iminium Chloride. French Patent. 2849026 A1, **2004**.
[30] Janousek, Z.; Viehe, H. G. *Angew. Chem. Int. Ed.* **1971**, *10*, 574–575.
[31] Regnier, V.; Planet, Y.; Moore, C. E.; Pecaut, J.; Philouze, C.; Martin, D. *Angew. Chem. Int. Ed.* **2017**, *56*, 1031–1035.
[32] Land, M.; Huo, B.; Robertson, K.; Ylijoki, K.; Lee, P.; Areephong, J.; Vidović, D.; Clyburne, J. *Dalton Trans.* **2018**, *47* (30), 10195-10205.
[33] Do, D.; Keyser, A.; Protchenko, A.; Maitland, B.; Pernik, I.; Niu, H.; Kolychev, E.; Rit, A.; Vidovic, D.; Stasch, A.; Jones, C.; Aldridge, S. *Chem. Eur. J.* **2017**, *23* (24), 5830-5841.
[34] De Voghel, G. J.; Eggerichs, T. L.; Janousek, Z.; Viehe, H. G. *J. Org. Chem.* **1974**, *39*, 1233–1235.
[35] Land, M. Saint Mary's University, Halifax, NS. Unpublished work, **2018**.
[36] Furstner, A.; Alcarazo, M.; Krause, H. *Org. Synth.* **2009**, *86*, 298–305.
[37] Hopkinson, M.; Richter, C.; Schedler, M.; Glorius, F. *Nature* **2014**, *510* (7506), 485-496.
[38] Nesterov, V.; Reiter, D.; Bag, P.; Frisch, P.; Holzner, R.; Porzelt, A.; Inoue, S. *Chem. Rev.* **2018**, *118*, 9678-9842.
[39] Hopkinson, M.; Richter, C.; Schedler, M.; Glorius, F. *Nature* **2014**, *510*, 485-496.
[40] Hahn, F. *Chem. Rev.* **2018**, *118*, 9455-9456.

[41] Wanzlick, H.; Schönherr, H. *Angew. Chem. Int. Ed.* **1968**, *7*, 141-142.
[42] Öfele, K. *J. Organomet. Chem.* **1968**, *12*, P42-P43.
[43] Cardin, D.; Cetinkaya, B.; Lappert, M.; Manojlović-Muir, L.; Muir, K. *J. Chem. Soc.* **1971**, *0*, 400-401.
[44] Wanzlick, H.; Schikora, E. *Angew. Chem.* **1960**, *72*, 494-494.
[45] Igau, A.; Grutzmacher, H.; Baceiredo, A.; Bertrand, G. *J. Am. Chem. Soc.* **1988**, *110*, 6463-6466.
[46] Arduengo, A.; Harlow, R.; Kline, M. *J. Am. Chem. Soc.* **1991**, *113*, 361-363.
[47] Tomioka, H.; Iwamoto, E.; Itakura, H.; Hirai, K. *Nature* **2001**, *412* (6847), 626-628.
[48] Itoh, T.; Nakata, Y.; Hirai, K.; Tomioka, H. *J. Am. Chem. Soc.* **2006**, *128* (3), 957-967.
[49] Vellé, A.; Cebollada, A.; Macías, R.; Iglesias, M.; Gil-Moles, M.; Sanz Miguel, P. *ACS Omega* **2017**, *2* (4), 1392-1399.
[50] Janousek, Z.; Huys, F.; René, L.; Masquelier, M.; Stella, L.; Merényi, R.; Viehe, H. *Angew. Chem. Int. Ed.* **1979**, *18* (8), 616-617.
[51] Bertrand, G.; Reed, R. *Coord. Chem. Rev.* **1994**, *137*, 323-355.
[52] Riley, R. The Chemistry of *Bis*-phosphinoamine Ambidentate Ligands and a Rare Example of *Bis*muth Catenation. Undergraduate, Saint Mary's University, Halifax, NS, **2019**.
[53] Caminade, A. M.; Ocando, E.; Majoral, J. P.; Cristante, M.; Bertrand, G. *Inorg. Chem.* **1986**, *25* (5), 712–714.
[54] Housecroft, C. E.; Sharpe, A. G. *Inorganic chemistry*; Pearson: New York, **2018**.
[55] Nöth, H.; Fluck, E. *Z. Naturforsch.* **1984**, *39* (6), 744-753.
[56] Ritch, J.; Chivers, T.; Ahmad, K.; Afzaal, M.; O'Brien, P. *Inorg. Chem.* **2010**, *49* (3), 1198-1205.
[57] Dickie, D.; Coker, E.; Kemp, R. *Inorg. Chem.* **2011**, *50* (22), 11288-11290.
[58] CCDC. CSD web interface – intuitive, cross-platform, web-based access to CSD data. Cambridge Crystallographic Data Centre, Cambridge, UK **2017**.
[59] Taylor, D. *Chem. Rev.* **1967**, *67*, 317-359.
[60] Patel, D.; Bharatam, P. *J. Org. Chem.* **2011**, *76*, 2558-2567.
[61] Ma, S. *Acc. Chem. Res.* **2009**, *42*, 1679-1688.
[62] Price, J.; Johnson, R. *Tetrahedron* **1986**, *27*, 4679-4682.
[63] Fernández, I.; Dyker, C.; DeHope, A.; Donnadieu, B.; Frenking, G.; Bertrand, G. *J. Am. Chem. Soc.* **2009**, *131*, 11875-11881.
[64] Dyker, C.; Lavallo, V.; Donnadieu, B.; Bertrand, G. *Angew. Chem. Int. Ed.* **2008**, *47*, 3206-3209.
[65] Christl, M.; Engels, B. *Angew. Chem. Int. Ed.* **2009**, *48*, 1538-1539.
[66] Lavallo, V.; Dyker, C.; Donnadieu, B.; Bertrand, G. *Angew. Chem. Int. Ed.* **2009**, *48*, 1540-1542.
[67] Kaufhold, O.; Hahn, F. *Angew. Chem. Int. Ed.* **2008**, *47*, 4057-4061.
[68] Skell, P.; Klebe, J. *J. Am. Chem. Soc.* **1960**, *82*, 247-248.
[69] Jahn, H.; Teller, E. *Proc. Math. Phys. Eng. Sci.* **1937**, *161*, 220-235.
[70] Herges, R.; Mebel, A. *J. Am. Chem. Soc.* **1994**, *116*, 8229-8237.
[71] Seburg, R.; DePinto, J.; Patterson, E.; McMahon, R. *J. Am. Chem. Soc.* **1995**, *117*, 835-836.
[72] Land, M. Structure, Detection, and Generation, of Small, Unsaturated, Organic Molecules. Undergraduate, Saint Mary's University, Halifax, NS, **2017**.
[73] Defrees, D.; McLean, A. *ApJ.* **1986**, *308*, L31.
[74] Mohajeri, A.; Jenabi, M. *J. Mol. Struct.: THEOCHEM* **2007**, *820*, 65-73.
[75] Osborn, D.; Vogelhuber, K.; Wren, S.; Miller, E.; Lu, Y.; Case, A.; Sheps, L.; McMahon, R.; Stanton, J.; Harding, L.; Ruscic, B.; Lineberger, W. *J. Am. Chem. Soc.* **2014**, *136*, 10361-10372.
[76] Miller, J.; Klippenstein, S.; Georgievskii,, Y.; Harding, L.; Allen, W.; Simmonett, A. *J. Phys. Chem. A* **2010**, 114 (14), 4881-4890.
[77] Fischer, I. *Chem. Soc. Rev.* **2003**, *32* (2), 59-69.
[78] Huisgen, R. *Proc. Chem. Soc.***1961**, 357.
[79] Singh, M.; Chowdhury, S.; Koley, S. *Tetrahedron* **2016**, *72*, 5257-5283.
[80] Diels, O.; Alder, K. *Liebigs Annalen.* **1928**, *460*, 98-122.
[81] Kolb, H.; Finn, M.; Sharpless, K. *Angew. Chem. Int. Ed.* **2001**, *40* (11), 2004-2021.
[82] Cenini, S.; Ragaini, F.; Gallo, E.; Caselli, A. *Curr. Org. Chem.* **2011**, *15* (10), 1578-1592.
[83] Diels-Alder Reaction https://www.organic-chemistry.org/namedreactions/diels-alder-reaction.shtm (accessed Dec 13, **2018**).
[84] Dai, M.; Sarlah, D.; Yu, M.; Danishefsky, S.; Jones, G.; Houk, K. *J. Am. Chem. Soc.* **2007**, *129*, 645-657.

[85] Hilt, G.; Danz, M. *Synthesis* **2008**, *2008*, 2257-2263.
[86] O'Connor, J.; Casey, C. *Chem. Rev.* **1987**, *87*, 307-318.
[87] Barry, B.; Soper, R.; Hurmalainen, J.; Mansikkamäki, A.; Robertson, K.; McClennan, W.; Veinot, A.; Roemmele, T.; Werner-Zwanziger, U.; Boeré, R.; Tuononen, H.; Clyburne, J.; Masuda, J. *Angew. Chem. Int. Ed.* **2018**, *57*, 749-754
[88] Bach, R.; Su, M.; Aldabbagh, E.; Andres, J.; Schlegel, H. *J. Am. Chem. Soc.* **1993**, *115*, 10237-10246.
[89] Deardorff, C.; Eric Sikma, R.; Rhodes, C.; Hudnall, T. *ChemComm.* **2016**, *52*, 9024-9027.
[90] Mahoney, J.; Jazzar, R.; Royal, G.; Martin, D.; Bertrand, G. *Chem. Eur. J.* **2017**, *23*, 6206-6212.
[91] Mahoney, J.; Martin, D.; Moore, C.; Rheingold, A.; Bertrand, G. *J. Am. Chem. Soc.* **2013**, *135*, 18766-18769.
[92] Hansmann, M.; Melaimi, M.; Bertrand, G. *J. Am. Chem. Soc.* **2017**, *139*, 15620-15623.
[93] Veinot, A.; Todd, A.; Robertson, K.; Masuda, J. *Can. J. Chem.* **2018**, *96* (1), 8-17.
[94] Montgomery, L.; Huffman, J.; Jurczak, E.; Grendze, M. *J. Am. Chem. Soc.* **1986**, *108*, 6004-6011.
[95] Barry, B.; Dickie, D.; Murphy, L.; Clyburne, J.; Kemp, R. *Inorg. Chem.* **2013**, *52* (15), 8312-8314.
[96] Dickie, D.; Kemp, R. *Organometallics* **2014**, *33* (22), 6511-6518.
[97] Dickie, D.; Barker, M.; Land, M.; Hughes, K.; Clyburne, J.; Kemp, R. . *Inorg. Chem.* **2015**, *54* (23), 11121-11126.
[98] Dickie, D.; Chadha, U.; Kemp, R. . *Inorg. Chem.* **2017**, *56* (12), 7292-7300.
[99] Ross, B.; Reetz, K. *Chemische Berichte* **1979**, *112* (5), 1756-1762.
[100] Elder, P.; Chivers, T.; Thirumoorthi, R. *Eur. J. Inorg. Chem.* **2013**, *2013* (16), 2867-2876.
[101] Grasse, P.; Brauer, B.; Zupancic, J.; Kaufmann, K.; Schuster, G. *J. Am. Chem. Soc.* **1983**, *105* (23), 6833-6845.
[102] Riley, R.; Dickie, D.; Land, M.; Kemp, R.; Macdonald, C.; Werner-Zwanziger, U.; Robertson, K.; Clyburne, J. *Chem. Eur. J.* **2020**.
[103] Riley, R. Saint Mary's University, Halifax, NS. Unpublished work, **2018**.
[104] Myers, E.; Raines, R. *Angew. Chem. Int. Ed.* **2008**, *48* (13), 2359-2363.
[105] Davis, P.; Harris, L.; Karim, A.; Thompson, A.; Gilpin, M.; Moloney, M.; Pound, M.; Thompson, C. *Tetrahedron* **2011**, 52 (14), 1553-1556.
[106] *Mercury*, version 2020.2.0; Software for crystal structures; Cambridge Crystallographic Data Centre, Cambridge, UK.
[107] Kawano, M.; Hirai, K.; Tomioka, H.; Ohashi, Y. *J. Am. Chem. Soc.* **2007**, *129* (8), 2383-2391.
[108] Allen, F.; Kennard, O.; Watson, D.; Brammer, L.; Orpen, A.; Taylor, R. *J. Am. Chem. Soc. ,* **1987**.
[109] Dannenberg, J.; Haskamp, L.; Masunov, A. *J. Phys. Chem. A.* **1999**, *103* (35), 7083-7086.
[110] Bethell, D.; Brown, M.; Harding, M.; Herbert, C.; Khodaei, M.; Rios, M.; Woolstencroft, K. *Acta Crystallogr. B.* **1992**, *48* (5), 683-687.
[111] Wang, J.; Kubicki, J.; Hilinski, E.; Mecklenburg, S.; Gustafson, T.; Platz, M. *J. Am. Chem. Soc.* **2007**, *129* (44), 13683-13690.
[112] Frenking, G.; Tonner, R. *Wiley Interdiscip. Rev. Comput. Mol. Sci.* **2011**, *1*, 869–878.
[113] Goldfogel, M. J.; Roberts, C. C.; Meek, S. J. *J. Am. Chem. Soc.* **2014**, *136*, 6227–6230.
[114] Roberts, C. C.; Matías, D. M.; Goldfogel, M. J.; Meek, S. J. *J. Am. Chem. Soc.* **2015**, *137*, 6488–6491.
[115] Schwesinger, R. *Angew. Chem.* **1987**, *99*, 1209–1210.
[116] Saalfrank, R. W.; Maid, H. *Chem. Commun*. **2005**, 5953.
[117] *Spartan*, version 18; Software for molecular modelling; Wavefunction, Inc.: Irvine, CA.
[118] Clyburne, J. Saint Mary's University, Halifax, NS. Unpublished work, **2018**.
[119] Olah, G.; Donovan, D. *J. Am. Chem. Soc.* **1977**, *99* (15), 5026-5039.
[120] Spek, A.L. (**2009**) *Acta Cryst*., D65, 148–155.
[121] Arduengo III, A.; Dias, H.; Harlow, R.; Kline, M. *J. Am. Chem. Soc.* **1992**, *114* (14), 5530–5534.
[122] Giffin, N.; Hendsbee, A.; Masuda, J. *Acta Crystallogr. E.* **2010**, *66* (9), o2194-o2194.
[123] Kantlehner, W.; Edelmann, K.; Frey, W. *Z. Naturforsch.* **2012**, *67* (9), 913-920.
[124] Golovanov, A.; Odin, I.; Bekin, V.; Vologzhanina, A.; Bushmarinov, I.; Zlotskii, S.; Gerasimov, Y.; Purygin, P. *Russ. J. Org. Chem.***2016**, *52* (3), 414-420.
[125] Huisgen, R. *Proc. Chem. Soc.***1961**, 357.
[126] Singh, M.; Chowdhury, S.; Koley, S. *Tetrahedron* **2016**, *72*, 5257-5283.
[127] Kolb, H.; Finn, M.; Sharpless, K. *Angew. Chem. Int. Ed.* **2001**, *40* (11), 2004-2021.

[128] Frosch, J.; Freytag, M.; Jones, P.; Tamm, M. *J. Organomet. Chem.* **2020**, *918*, 121311.
[129] Fulmer, G. R.; Miller, A. J. M.; Sherden, N. H.; Gottlieb, H. E.; Nudelman, A.; Stoltz, B. M.; Bercaw, J. E.; Goldberg, K. I. *Organometallics* **2010**, *29*, 2176–2179.
[130] *Topspin*, version 3.6.1; Software Nuclear Magnetic Resonance Collection And Processing; Bruker: Billerica, MA.
[131] APEX II (Bruker, **2008**) Bruker AXS Inc., Madison, Wisconsin, USA.
[132] SAINT (Bruker, **2008**) Bruker AXS Inc., Madison, Wisconsin, USA.
[133] SADABS (Bruker, **2009**) Bruker AXS Inc., Madison, Wisconsin, USA.
[134] APEX 3 (Bruker, **2018**) Bruker AXS Inc., Madison, Wisconsin, USA.
[135] SAINT (Bruker, **2016**) Bruker AXS Inc., Madison, Wisconsin, USA.
[136] SADABS (Bruker, **2016**) Bruker AXS Inc., Madison, Wisconsin, USA.
[137] Sheldrick, G.M. (**2008**) *Acta Cryst*., A64, 112-122; Sheldrick, G.M. (**2015**) *Acta Cryst*., A71, 3-8; Sheldrick, G.M. (**2015**) *Acta Cryst*., C71, 3-8.
[138] Furstner, A.; Alcarazo, M.; Krause, H. *Org. Synth.* **2009**, *86*, 298–305.